

TECHNISCHE UNIVERSITÄT MÜNCHEN

Lehrstuhl E23 für Technische Physik
Walther-Meißner-Institut für Tieftemperaturforschung der Bayerischen
Akademie der Wissenschaften

Crystal growth and normal state transport of electron doped high temperature superconductors

Michael Lambacher

Vollständiger Abdruck der von der Fakultät für Physik der Technischen
Universität München zur Erlangung des akademischen Grades eines

Doktors der Naturwissenschaften

genehmigten Dissertation.

Vorsitzender: Univ.-Prof. Dr. R. Netz

Prüfer der Dissertation: 1. Univ.-Prof. Dr. R. Gross
2. Univ.-Prof. Chr. Pfeleiderer, Ph. D.

Die Dissertation wurde am 04.08.2008 bei der Technischen Universität
München eingereicht und durch die Fakultät für Physik am 13.10.2008
angenommen.

Abstract

The present thesis deals with the improvement of the growth and annealing parameters as well as the influence of oxygen impurities on the structural and electronic properties of $\text{Re}_{2-x}\text{Ce}_x\text{CuO}_4$ (Re = La, Pr, Nd, Sm) single crystals. For transport measurements a sample set of high quality single crystals of $\text{Nd}_{2-x}\text{Ce}_x\text{CuO}_4$ was available, which covers the major part of the phase diagram on the electron doped side of the cuprate high temperature superconductors. The resulting unusual transport data of the optimally doped and overdoped crystals can be explained within conventional Boltzmann transport theory when applying a two-band model with anisotropic scattering rates.

Zusammenfassung

In der vorliegenden Arbeit werden verbesserte Wachstumsbedingungen und Temperaturparameter sowie der Einfluss von Sauerstoffstörstellen auf die strukturellen und elektronischen Eigenschaften von $\text{Re}_{2-x}\text{Ce}_x\text{CuO}_4$ (Re = La, Pr, Nd, Sm) Einkristallen diskutiert. Für die Transportmessungen stand ein hochreiner $\text{Nd}_{2-x}\text{Ce}_x\text{CuO}_4$ Probensatz zur Verfügung, der einen großen Bereich des elektron-dotierten Phasendiagramms der Kuprat Hochtemperatursupraleiter abdeckt. Die sich ergebenden ungewöhnlichen Transportdaten im optimalen und überdotierten Bereich können im Rahmen konventioneller Boltzmann-Transporttheorie erklärt werden, indem ein Zwei-Band Modell mit anisotropen Streuraten angewandt wird.

Contents

1	Introduction	1
I	Growth of high quality electron doped cuprate single crystals	5
2	The electron doped and hole doped cuprate superconductors	7
2.1	Similarities and differences in the phase diagram	7
2.1.1	Hole doped side of the phase diagram	9
2.1.2	Electron doped side of the phase diagram	10
2.2	Appropriate sample sets for probing the whole phase diagram . . .	11
2.3	The electron doped compounds	15
2.3.1	Crystal structure	15
2.3.2	Magnetic behavior	16
3	Growth of electron doped cuprate single crystals	19
3.1	The composition phase diagram of incongruently melting compounds	19
3.1.1	Differential thermal analysis (DTA)	19
3.1.2	Travelling solvent floating zone technique (TSFZ)	26
3.2	Experimental setup: the mirror furnace	28
3.3	Crystal growth	30
3.3.1	Preparation of the feed rods	30
3.3.2	Growth process and growth parameters	31
4	Characterization of the grown crystals	39
4.1	The annealing treatment of the grown crystals	39
4.2	The superconducting properties of $\text{Nd}_{2-x}\text{Ce}_x\text{CuO}_4$ and $\text{Pr}_{2-x}\text{Ce}_x\text{CuO}_4$	42
4.2.1	Transition curves of 214-cuprates	42
4.2.2	Testing bulk superconductivity	45
4.3	X-ray analysis	48
4.4	The role of oxygen in electron doped high temperature superconductors	52
4.4.1	Determination of the oxygen concentration of as grown and annealed crystals	52

4.4.2	Magnetization measurements: Testing the microscopic homogeneity of the crystals	54
4.4.3	Oxygen as co-dopant and source of disorder	57
II	Transport properties of $\text{Nd}_{2-x}\text{Ce}_x\text{CuO}_4$ single crystals	59
5	Theory: The normal state transport	61
5.1	Phenomenology of the normal state transport in cuprate superconductors	61
5.1.1	Transport properties of hole doped cuprates	61
5.1.2	Transport properties of electron doped cuprates	63
5.2	Models for explaining the anomalous normal state transport	64
5.2.1	The two-lifetime picture of Anderson	64
5.2.2	The marginal Fermi liquid model of Varma	65
5.2.3	Boltzmann theory in combination with an anisotropic scattering rate	65
5.3	Modeling the normal state transport of electron doped cuprates	69
5.3.1	Boltzmann transport theory	69
5.3.2	Fermi surface topology	75
6	Experimental techniques	79
6.1	Preparation of the single crystals	79
6.1.1	In-plane transport with a standard six-terminal Hall bar	79
6.1.2	Measuring technique	81
6.1.3	Collection of data	84
6.2	Out-of-plane transport	85
7	Magnetotransport properties of high quality $\text{Nd}_{2-x}\text{Ce}_x\text{CuO}_4$ single crystals	87
7.1	The in-plane and out-of-plane resistivity	87
7.2	The upturn behavior at low temperatures	94
7.3	The Hall effect and magnetoresistance	99
7.3.1	The Hall resistivity	99
7.3.2	The transverse magnetoresistance	101
7.4	Simulation of the normal state transport	103
7.4.1	The two-band model	104
7.4.2	Discussion	117
8	Summary	121

Chapter 1

Introduction

More than 20 years of intensive research on the cuprate high temperature superconductors has provided a deep insight into a rich variety of exciting new phenomena of modern solid state physics. Nevertheless, the fundamental question of the underlying pairing mechanism of the charge carriers is still open and discussed controversially. The reason for this lies in the complexity of the material system, which is reflected in a rich doping dependent phase diagram. As for other transition metal oxides, such as the colossal magnetoresistance manganites, the physics of the cuprate superconductors is controlled by the subtle interplay of electronic, spin and orbital degrees of freedom, resulting in a complex behavior and fascinating physical properties. The superconducting state is only one facet of the entire phase diagram, which is characterized by several competing and/or coexisting ordering phenomena. Thus, there is a general agreement that the detailed understanding of the nature of the superconducting state can only be achieved by developing a solid understanding of the whole phase diagram.

At present, a thorough understanding of the phase diagram of the cuprates is still missing. In past, this was caused by inconsistent and sometimes controversial experimental results, depending on the details of the investigated cuprate compounds and experimental techniques. In particular, the question of what is generic and what is material specific (influence of crystal structure, defects and inhomogeneities) in the phase diagram is an important aspect, which can only be solved by including material specific questions in the research efforts. On the electron doped side of the phase diagram, for instance, the appearance of the superconducting state with increasing Ce doping strongly depends on material specific aspects such as the rare earth elements as well as the preparation conditions and thus, the question of the effective doping of the CuO_2 unit arises. In addition, there is a noticeable asymmetry between the hole and electron doped side of the phase diagram, which turned out to be intrinsic, which is not completely understood so far.

Reliable experimental studies of the cuprate superconductors require high quality materials with reproducible properties. Until today, the fabrication of a high quality cuprate sample set covering the entire phase diagram is the main problem

for probing the phase diagram, which was also the main motivation for the present thesis. However, the growth of a set of electron doped crystals was not only motivated by the lack of available pure crystals, but also by its dichotomy in the electronic properties with respect to the hole doped compounds. An example for this is the complementary doping dependent evolution of the Fermi surface and, presumably related to it, the different physical behavior in the slightly doped regime. The electron doped compounds are particular suitable for studying the effect of "doping into a Mott insulator", as the doped charge carriers lie above the band gap (in the so-called upper Hubbard band (UHB)), which is induced by strong correlation effects, while for hole doped compounds only states below the gap (in the lower Hubbard band (LHB)) are involved. In addition, the relative simple crystal structure, which is similar to that of the hole doped $\text{La}_{2-x}\text{Sr}_x\text{CuO}_4$, makes both sides of the phase diagram comparable.

During the last years the research activities were primarily focused on the lightly and heavily doped regime of the cuprates, as remarkable progresses in the crystal preparation and annealing treatment allowed to access also these regions of the phase diagram. In the underdoped regime the pseudogap phenomenon (gap in the normal state) is still considered as a central issue towards the understanding of the cuprate phase diagram. The pseudogap crossover is observed on both sides of the phase diagram [1–3]. Its physical origin, its relation to different ordering phenomena (charge, spin ordering) as well as its impact on the formation of superconductivity as competing phase or precursor phase (preformed pairs without long range phase coherence) are up to now controversially discussed.

On increasing the doping level, the transition from the peculiar pseudogap state into a Fermi liquid-like metal in the heavily doped regime of the cuprates is intimately connected with the change in the Fermi surface topology. Both electron and hole doped cuprates show a crossover from a fragmented surface to a large closed surface with hole-like character for the electron doped compounds and electron-like character for the hole doped compounds [1, 4]. Recently, it could be shown for several hole doped compounds that the transport data in this regime can be explained successfully within the framework of conventional Boltzmann transport theory [5, 6]. For the hole doped cuprates there are new attempts to extend the Fermi liquid picture to the underdoped region and to interpret the unusual underdoped transport data at moderate temperatures within Boltzmann transport theory. This new approach is supported by the markedly metallic behavior of the in-plane transport in the far underdoped regime close to the Mott insulator state. In this case the observed Fermi arcs are interpreted as the manifestation of those regions of an underlying, large Fermi surface, where the quasiparticles are coherent with a finite scattering time. The states on the Fermi surface outside the arcs are incoherent and do not contribute to the transport. The picture of an underlying, large Fermi surface, which is gapped at certain regions due to antiferromagnetic interactions is also supported by recent photoemission studies on $\text{La}_{2-x}\text{Sr}_x\text{CuO}_4$ [4], where it could be shown that the large Fermi surface satisfies Luttinger's theorem.

Very recently it became evident that the doping dependent shape and evolu-

tion of the Fermi surface has to be reviewed again, especially for the hole doped cuprates. The traditional interpretation of the Fermi arcs (based on observations by angle resolved photoemission spectroscopy) as a new topological state in the momentum space, where the conventional Fermi liquid picture fails, has recently been challenged by the observation of quantum oscillations in underdoped $\text{YBa}_2\text{Cu}_3\text{O}_{6.5}$ single crystals [7, 8]. These new transport experiments provided evidence for small Fermi surface pockets which behave Fermi liquid-like. Furthermore, they underlined once more, that the improvement of the crystal growth process and annealing treatment is the key towards a better understanding of this class of materials.

On the electron doped side of the phase diagram a two-band model is clearly confirmed by angle resolved photoemission spectroscopy [9, 10]. While for small electron doping the photoemission spectroscopy data and Hall measurements seem to reflect in the same way the small electron pockets in the Brillouin zone, the transition from fragmented pieces to a large hole-like Fermi surface for heavily electron doped crystals is difficult to extract from transport data. In this context, a possible Fermi surface reconstruction accompanied by a magnetic quantum phase transition at a Ce doping of $x = 0.165$ has previously been suggested arising from a discontinuity of the low temperature Hall coefficient in $\text{Pr}_{2-x}\text{Ce}_x\text{CuO}_4$ thin films [11].

In this thesis the reconstruction of the Fermi surface in electron doped cuprates is reviewed carefully. For that purpose the growth process and annealing treatment for electron doped cuprates was improved and a sample set of high quality $\text{Nd}_{2-x}\text{Ce}_x\text{CuO}_4$ single crystals with Ce doping $x \leq 0.17$ was grown. The analysis of the transport data has revealed that, in contrast to photoemission experiments, the two-band model with small Fermi surface pockets persists up to a Ce doping of $x = 0.17$. A possible transition to a reconstructed, large Fermi surface is expected for Ce doping beyond the superconducting dome. In addition, for Ce doping $x \geq 0.15$ it was for the first time possible to explain the unusual normal state transport properties of electron doped cuprates within conventional Boltzmann transport theory.

The thesis consists of two parts. Part I, comprising Chapter 2 to 4, deals with the growth and characterization of electron doped cuprate single crystals. In Chapter 2 the general phase diagram of the electron doped and hole doped cuprates is reviewed. In addition, the important question of appropriate sample sets for probing the entire phase diagram with respect to crystal quality and accessible doping range is discussed. The crystal structure and magnetic behavior of the electron doped compounds is summarized explicitly. In Chapter 3 the compositional phase diagram of the electron doped cuprate superconductors is introduced. On the basis of the compositional phase diagram the growth process and growth parameters are described. Thereafter, in Chapter 4, the annealing treatment as well as the characterization of the grown single crystals is presented.

Part II of the thesis is devoted to the normal state magnetotransport properties of the grown series of high quality $\text{Nd}_{2-x}\text{Ce}_x\text{CuO}_4$ single crystals. For the interpretation of the transport data the theoretical background is described in Chapter

5. Chapter 6 deals with the experimental techniques for the Hall measurements on the $\text{Nd}_{2-x}\text{Ce}_x\text{CuO}_4$ single crystals. The transport data are presented in Chapter 7 and discussed within a two-band model. Finally, the most important results are summarized in Chapter 8.

Part I

Growth of high quality electron doped cuprate single crystals

Chapter 2

The electron doped and hole doped cuprate superconductors

2.1 Similarities and differences in the phase diagram of electron doped and hole doped cuprate superconductors

The schematic phase diagram of the electron and hole doped cuprate superconductors is shown in Figure 2.1. This material class is characterized by a variety of phase transitions and ordering phenomena [2, 12–16]. Intensive investigations on both sides of the phase diagram are still going on and hence, the outlined phase diagram cannot be considered to be final. It is rather a summary of generally accepted and still discussed experimental facts, obtained from various experiments. The undoped parent compounds are a suitable starting point for a qualitative discussion of the phase diagram. The CuO_2 unit provides a half filled molecular orbital of antibonding $\sigma_{x^2-y^2}^*$ character, resulting from a strong covalent bonding between the $3d_{x^2-y^2}$ and $2p_x$ orbitals [28]. Thus, according to band theory, the conduction band is semi-filled and the parent compounds are expected to show a metallic behavior. However, this is not the case, as conventional band theory does not account for the strong on-site Coulomb repulsion U , which is characteristic for the cuprates. The resulting strong correlation effects are responsible for the splitting of the $\sigma_{x^2-y^2}^*$ band into a fully occupied lower and an empty upper Hubbard band. Therefore, the parent compounds are Mott insulators with considerable energy gaps [28, 29]. Since the Cu one-site repulsion U dominates the hopping energy t ($U \gg t$) and because of the strong covalent bonding, the antiferromagnetic ordering (AFM) of the Cu sites ($3d^9$ configuration) arises due to a super-exchange with $J \approx 130$ meV (see [12, 29] and the references therein). Typical values measured for the Néel temperature T_N are between 250 K and 400 K for the hole doped parent compounds [12] and come up to about 250 K for the undoped Nd_2CuO_4 compound [30, 31], which are moderate values compared to the high value for J . By means of electron

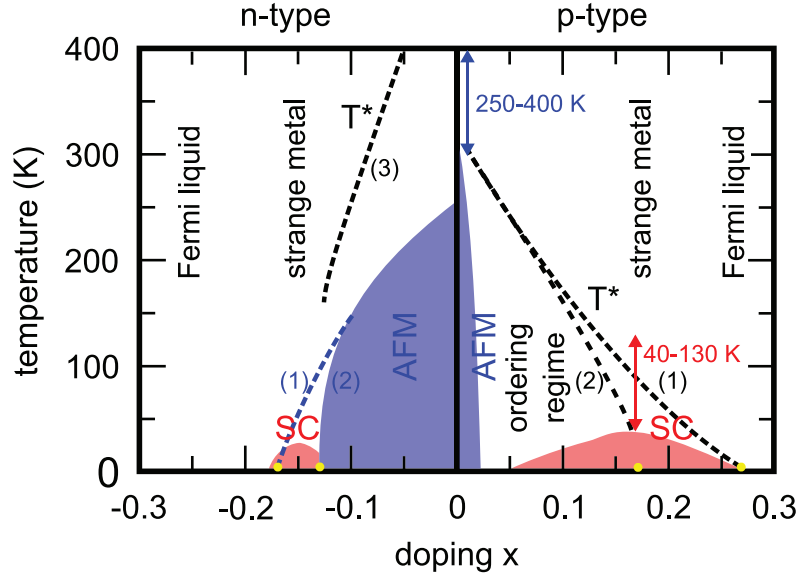


Figure 2.1: Schematic phase diagram of the electron doped and hole doped cuprate high temperature superconductors. The doping dependent evolution of the long-range antiferromagnetic order (AFM) and the superconducting phase (SC) are sketched by the blue and red areas, respectively. The transition temperatures (Néel temperature T_N and superconducting transition temperature T_c) depend on the various compounds. T_N for the undoped and T_c for the optimally hole doped compounds amount to 250 – 400 K [12] and 40 – 130 K [17], respectively. The phase diagram corresponds to the experimental results obtained from hole doped $\text{La}_{2-x}\text{Sr}_x\text{CuO}_4$ [6, 18–23] and electron doped $\text{Nd}_{2-x}\text{Ce}_x\text{CuO}_4$ [1, 2, 24–27]. Proposed crossovers ($T^*(x)$, black dashed lines) and quantum critical points (QCP, yellow dots) are discussed in the text. The doping x , plotted on the abscissa, corresponds to the effective charge carrier number p per Cu ion for the hole doped compounds. On the electron doped side (and also for the 214 compound $\text{La}_{2-x}\text{Sr}_x\text{CuO}_4$) x might differ slightly from the real carrier concentration n due to possible oxygen co-doping (see also discussion in Chapter 4.4.3). In literature and the underlying thesis, the following terminology is common: the doping x_{opt} with maximal $T_{c,max}$, is called optimal doping, whereas crystals with doping $x < x_{opt}$ and $x > x_{opt}$ are called underdoped and overdoped, respectively.

or hole doping of the undoped compounds the long-range AFM ground state vanishes gradually and the AFM state is replaced by a superconducting one. Hence, both sides of the phase diagram comprise these phase transitions. For both sides of the phase diagram the maximum transition temperature T_c of the superconducting phase is obtained at similar doping levels of $x \approx 0.16$ charge carriers per Cu site. Despite these general similarities, the hole/electron asymmetry in the phase diagram dominates. Therefore, it is worth discussing both sides separately, in order to extract the differences in more detail. In this thesis the following terminology is used for the discussion, which is also common in literature: the doping x_{opt} , corresponding to maximum $T_{c,max}$, is called optimal doping, whereas crystals with doping $x < x_{opt}$ and $x > x_{opt}$ are called underdoped and overdoped, respectively.

2.1.1 Hole doped side of the phase diagram

Despite the various hole doped compounds, which differ in the absolute values of T_c [17] and T_N [12, 30], it is generally accepted that the long-range ordered three dimensional AFM phase is destroyed rapidly with hole doping of the CuO_2 planes and disappears at $x = 0.02$ [12, 22]. In addition, the parabolic superconducting dome, which extends over the broad doping interval of $x = [0.05, 0.27]$ with a maximum T_c at $x_{opt} \approx 0.16$, is generic for all hole doped cuprates [18, 20]. The d-wave nature of the superconducting state was confirmed by ARPES [32, 33] and tricrystal experiments [34]. The region between AFM and optimal doping shows a variety of new features in complementary experiments. The origin of these features and the underlying physics is up to now controversially discussed. A short-range disordered AFM state is reported from μSR ¹ experiments [22] for doping $x > 0.02$, which extends into the superconducting regime. In addition, neutron scattering experiments show that the long-range Bragg peaks are replaced by incommensurate magnetic peaks when crossing the AFM phase boundary [19]. These experimental facts are interpreted in terms of the formation of charge and spin superstructures [35], the so called stripes. This microscopic magnetic ordering can be static or dynamic and the degree of charge and spin ordering depends upon the material system and on its purity. A fluctuating order is common to all hole doped cuprates for doping levels up to optimal doping [12, 36]. Microscopic ordering phenomena might also be the reason for the so called $x = 1/8$ anomaly [35], at which T_c is reduced or even suppressed, resulting in a deviation from the parabolic $T_c(x)$ behavior [19, 21, 37]. The origin of these stripes, their possible impact on the formation or suppression of the superconducting state as well as their relation to the so called pseudogap phenomenon are still unknown.

The pseudogap phenomenon shows up in an impressive way in ARPES measurements as a suppression of the single-particle density of states in the normal state and the absence of the single-particle coherence peak [3, 38]. For the optimally doped and underdoped region the SC gap does not collapse while moving through T_c , but is replaced by a gap in the normal state, the pseudogap. It is anisotropic in momentum space and maximal in $(\pi, 0)$ direction. It becomes zero within a certain region around the nodal (π, π) direction, leaving behind the so called Fermi arcs [12, 14, 38–41]. Recently, it has been shown that the anisotropy of the pseudogap evolves with T/T^* and that the related Fermi surface shrinks linearly onto four nodal points for $T \rightarrow 0$ [37, 41]. The temperature T^* , at which the crossover into the pseudogap regime appears, is illustrated qualitatively by the dashed lines in Figure 2.1. Up to now, there is no general agreement concerning the doping evolution of this crossover, its physical origin and its impact on the formation of superconductivity. Recently, two scenarios have been discussed, which are summarized in [14–16]:

- In the first scenario, the crossover matches the T_c line on the overdoped side

¹ μSR is the abbreviation of muon Spin Rotation.

(curve 1 in Figure 2.1, p-type), and the pseudogap phase is interpreted as a precursor phase to the superconducting one (preformed pairs) without global phase coherence, from which both the AFM and SC phase arise.

- In the second scenario (curve 2 in Figure 2.1, n-type) the T^* line meets the SC dome at a doping value of $x \approx 0.16$ and the pseudogap state is interpreted as a competing phase to the superconducting one.

Experimental results, however, seem to favor the first scenario, where the pseudogap is interpreted as pairing gap [37, 38].

Unusual normal state behavior over the whole doping range can also be observed in transport measurements [21, 42]. Especially the strong temperature dependence of the Hall signal cannot be explained within a conventional Fermi liquid theory. It is obvious that the gaped Fermi arcs do not allow for an usual Fermi liquid. Nevertheless, with increasing doping the Fermi surface evolves from disconnected arcs to a closed surface in the momentum space on the overdoped side [4]. In this case the strongly doped cuprates might behave more like a normal metal. In fact, a coherent quasi three-dimensional Fermi surface was found for heavily overdoped $\text{Tl}_2\text{Ba}_2\text{CuO}_{6+\delta}$ [5], and it was shown for different overdoped compounds that the transport data can be understood within a Fermi liquid picture, if an anisotropic scattering rate is assumed [5, 6, 43–45].

2.1.2 Electron doped side of the phase diagram

In contrast to the hole doped side, the extended AFM region and the reduced superconducting dome are the most prominent differences on the electron doped side of the phase diagram. The doping dependent evolution of the Néel temperature T_N is controversially discussed so far. μSR [24] and elastic neutron scattering [26] show a parabolic decrease of T_N , approaching zero at doping $x = 0.16$. At this doping level evidence for an antiferromagnetic/paramagnetic quantum phase transition was found in transport measurements [11, 13] (see curve 1 with the quantum critical point in Figure 2.1 (n-type)). In a recent INS² study [27] the evolution of the AFM curve was corrected. It was shown that long-range ordered AFM disappears at $x \approx 0.13$, where superconductivity first sets in (curve 2 in Figure 2.1 (n-type)). Therefore, in the superconducting regime the samples show only short-range spin ordering rather than a coexistence of AFM and superconductivity [24]. A d-wave symmetry for the superconducting order parameter was deduced from various experiments [46–48]. Due to the robustness of the AFM phase, the electron doped phase diagram does not comprise such a variety of ordered states in the underdoped region. Stripe and charge ordering phenomena might be suppressed.

Evidence for a pseudogap in the electron doped cuprates is provided by ARPES [1, 9] and optical conductivity measurements [2, 25] (curve 3 in Figure 2.1 electron doped). In contrast to hole doped cuprates the normal state gap opens at the nodal

²INS is the abbreviation for inelastic neutron scattering.

position in the k -space, causing therefore the fragmentation of the Fermi surface into two electron-like pockets around $(\pi, 0)$. At the AFM/SC boundary this gap is filled-in abruptly and the Fermi surface is reconstructed towards a large hole-like one in the overdoped region [1]. Because of the large energy scale of the pseudogap and its correspondence to the spin correlation length, the pseudogap in the electron doped compounds might be of magnetic origin [1, 2].

During the last two decades of intensive research, the asymmetry in the hole doped and electron doped cuprate phase diagram turned out to be intrinsic, even though its origin is not yet understood. A rather qualitative explanation is given by [30], which states that the doped holes reside primarily on the oxygen site in the CuO_2 plane, leading to an effective frustration of the AFM order, whereas doped electrons are located on the Cu site, which causes only a dilution of the AFM order. It turned out, however, that a random dilution picture of a spin-1/2 model is not fully consistent with the experimental data [26].

2.2 Appropriate sample sets for probing the whole phase diagram

Succeeding the short discussion of the complex phase diagram of the cuprate high temperature superconductors in the previous section, appropriate sample sets of single crystals for probing the whole phase diagram are now discussed in more detail. As this thesis deals primarily with the growth and characterization of high quality single crystals, which are also provided for different experiments (spectroscopy, transport, etc.) within the research unit *FOR538*, the discussion of the following fundamental questions seems to be important:

- Which cuprate family is suitable for the growth of high quality single crystals?
- Is there a compound for probing the whole phase diagram?
- Do the single crystals meet the different requirements of the various experiments?
- Which properties of the cuprates are intrinsic, and which ones are related to structural aspects (material issues)?

The last question is crucial for outlining a generic phase diagram and for understanding its doping dependent phase transitions.

It must be emphasized that the growth of high quality cuprate single crystals is not straightforward, as they are complex compounds consisting of several elements. Hence, due to material or technical reasons, only a few systems are suitable for probing the whole phase diagram, although a multitude of cuprate superconductors is known. The cuprate compounds, which are commonly used for probing both sides of the phase diagram, are illustrated in Figure 2.2.

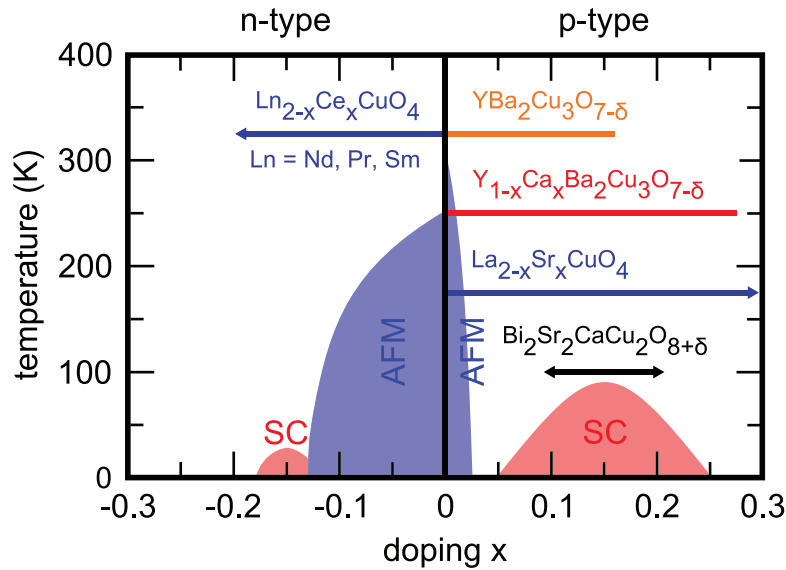


Figure 2.2: Illustration of prominent cuprate compounds for probing the hole doped and electron doped side of the phase diagram. The bars mark the doping region in the phase diagram, covered by a specific compound. The listed compounds are discussed in the text.

1. **$\text{YBa}_2\text{Cu}_3\text{O}_{7-\delta}$ system:** Generally, $\text{YBa}_2\text{Cu}_3\text{O}_{7-\delta}$ is the ideal compound for probing the hole doped side of the phase diagram. As it is a stoichiometric compound, disorder and crystal imperfections are expected to be strongly reduced in comparison to compounds that form solid solutions.

The compound has two crystallographically well defined states: the nonsuperconducting tetragonal state with $\delta = 1$, which corresponds to a vacant O(1) site, and the superconducting orthorhombic structure with full occupation of the O(1) site within the copper-oxygen chains. The effective hole doping is a function of both the oxygen deficiency δ and its ordering within the chains [49]. Due to improved growth procedures using BaZrO_3 crucibles [50] and further developments in the annealing treatment [51, 52], crystals of highest quality and oxygen ordering over a broad doping range are available. These crystals offer for the first time the opportunity to see quantum oscillations in cuprates by using ortho-II ordered $\text{YBa}_2\text{Cu}_3\text{O}_{6.5}$ single crystals³ [7, 53].

As the maximum T_c is reached for $\delta \approx 0.08$, i.e. for almost full oxygenation, the (far) overdoped region in the phase diagram is not accessible by this compound. In addition, the interesting region around the AFM/SC boundary, with the formation of spin-charge-ordered states [54–57], is difficult to probe due to homogeneity problems in the microscopic oxygen distribution. In order to separate extrinsic effects, caused by oxygen inhomogeneities and related structural problems, the partial substitution of bivalent Ca on the Y site is a suitable

³In the ideal ortho-II phase the dopant oxygen occupies completely every second copper-oxygen chain, resulting in a superstructure of alternating full and empty chains in the basal plane.

approach for overcoming the doping problems in the far underdoped and overdoped region. Ca co-doping up to 15% is feasible, leading to an extension of the doping region and giving access to the overdoped side up to $x \approx 0.30$. In addition, with Ca co-doping of the fully reduced $\text{YBa}_2\text{Cu}_3\text{O}_6$ the underdoped region is accessible with crystals of well defined oxygen content, resulting in new experimental insights in the formation of stripes [54–56].

Nowadays, even detailed spectroscopic experiments on natural, flux-free surfaces as well as bulk sensitive experiments, such as INS [57], are performed successfully due to the quality and quantity of available $\text{YBa}_2\text{Cu}_3\text{O}_{7-\delta}$ crystals. However, the main drawback lies in the difficulties of producing cleaved surfaces. It was shown [58] that the cleavage leads to a charge transfer and thus, to an “electronic reorganization” of the surface, leaving behind an overdoped surface layer which is nearly independent of the oxygen content δ . This might also be the reason, why comprehensive ARPES experiments on $\text{YBa}_2\text{Cu}_3\text{O}_{7-\delta}$ are missing so far.

2. **$\text{La}_{2-x}\text{Sr}_x\text{CuO}_4$ system:** This 214 solid solution is a promising alternative to $\text{YBa}_2\text{Cu}_3\text{O}_{7-\delta}$ for probing the phase diagram on the hole doped side. The doping occurs due to bivalent Sr substitution of the parent compound. Systematic transport measurements [21, 59–61] as well as ARPES measurements [4, 62] have been performed over the whole doping range, giving a deep insight into the doping dependent evolution of the Fermi surface of the hole doped cuprates. Particularly the accessibility of the (far) overdoped regime, where high quality cuprate crystals are rare, and in this context the proof of the Fermi liquid theory [42] makes this family very attractive. The solubility limit of Sr for single crystals is close to the doping level $x = 0.30$. Furthermore, due to its simple crystal structure, which is closely related to the crystal structure of the electron doped 214 compounds, one has the unique opportunity to compare both sides of the phase diagram with compounds of similar structure. The growth of larger quantities in mirror furnaces can be performed considerably easier than for the electron doped counter parts. Therefore, and due to the $^1\text{S}_0$ state of the La cations, $\text{La}_{2-x}\text{Sr}_x\text{CuO}_4$ might be very attractive for neutron scattering experiments, as well.

As for $\text{YBa}_2\text{Cu}_3\text{O}_{7-\delta}$, the disadvantage of this crystal family is given by the difficulty to prepare clean surfaces for spectroscopy and STM⁴ measurements. In addition, the appearance of twin boundaries in the underdoped region – due to an orthorhombic distortion of the lattice [59, 63, 64] – complicates the experimental work. Generally, the doping [63, 64] and temperature dependent [65, 66] phase transitions from a tetragonal to an orthorhombic structure and – closely related to this – the rotation and tilt of the copper-oxygen octahedra must be taken into account in order to exclude structural effects when interpreting results such as spin or charge ordering (stripes) data.

⁴STM is the abbreviation for scanning tunneling microscopy.

3. **Bi₂Sr₂CaCu₂O_{8+δ} system:** In general, the Bi-family Bi₂Sr₂Ca_{n-1}Cu_nO_{2n+4+δ} consists of three slightly different compounds. Depending on the number $n = 1, 2, 3$ of copper-oxide layers within the conventional unit cell, they are denoted as single layer ($T_c \approx 40$ K), double layer ($T_c \approx 90$ K) and three-layer ($T_c \approx 110$ K) Bi-compound. The crystal structure consists of an alternating stacking of metal-oxide and copper-oxide layers along the c axis of the unit cell, where the bonds between adjacent layers are extremely weak. Due to the weakness of these bonds, the crystals can be cleaved easily by using a knife. The opportunity to get large, clean surfaces without complications (surface recombination, charge transfer) and with only a minimum of experimental effort as well as the appearance of high transition temperatures have led to an intensive study of this system by means of spectroscopic methods (ARPES, Raman spectroscopy, ellipsometry), followed by a tremendous number of publications [17, 67–71]. Concerning crystal structure, growth and doping control, the Bi-family is the most difficult system, even though some effort in crystal synthesis using the TSFZ⁵ method [72–74] has been made.
- The double layer compound Bi₂Sr₂CaCu₂O_{8+δ} is the most promising candidate of the family with the highest crystal quality [73]. Nevertheless, also in this compound the quality is limited by the intergrowth of the three phases as well as the partial solubility of Bi on the Sr site. The fact that stoichiometric Bi₂Sr₂CaCuO_{8+δ} is very difficult to grow and instead of it a Bi:Sr nonstoichiometry of $x = 2.1:1.9$ is generally used [17], shows that the stacked oxide layers are hardly compatible to each other, resulting in corrugations and deformations of the layers. These modulations of the orthorhombic structure, which can easily be observed in X-ray diffraction, as well as the inherent cation disorder [17] and broad rocking curves are a clear hint for the low crystallographic quality of this family. Especially experiments performed on Bi-crystals, which are substituted by Pb in order to stabilize the bismuth-oxide layers [68], must be reviewed critically, as a large part of Pb evaporates during the growth process and only a small amount is crystallized, which might cause additional disorder [75, 76]. There is another drawback, which concerns the doping (see Figure 2.2). Doping is performed by varying the oxygen content δ of the bismuth-oxide layers while only a limited region around optimal doping is accessible [77]. Consequently, despite of the excellent processability, the Bi-family is not suitable for systematic studies of the phase diagram due to the limited doping regime as well as structural problems.
4. **214 compounds on the electron doped side:** On the electron doped side of the phase diagram only the so called 214 compounds Ln_{2-x}Ce_xCuO₄ are available. In this context Ln represents various rare earth elements. Similar to the La_{2-x}Sr_xCuO₄ system, the doping is performed by partial substitution of the trivalent rare earth ions with tetravalent Ce ions. Consequently, also on the electron doped side a precise doping control over the whole phase diagram should be possible.

⁵TSFZ is the abbreviation for traveling solvent floating zone technique.

However, these compounds reveal more than a different sign of their charge carriers. The doping dependent evolution of the Fermi surface, pseudogap and transport properties are complementary to those of the hole doped compounds. Furthermore, due to a completely different behavior in the underdoped region with its robust AFM phase, these “exotic” cuprates might play an important role for the understanding of the Mott state. In addition, effects caused by bilayer splitting or CuO chains, which might complicate the interpretation, are absent. The main disadvantage of the electron doped 214 compounds is given by the complicated growth process and annealing treatment of single crystals, which hampers strongly the performance of experiments. Considering crystal preparation for various experiments the same argumentation is valid as for the $\text{La}_{2-x}\text{Sr}_x\text{CuO}_4$ system.

2.3 The electron doped compounds

2.3.1 Crystal structure

Like the hole doped compounds the electron doped cuprates consist of an alternating stack of CuO_2 and rare earth oxide layers. The electronic properties are governed primarily by the CuO_2 sheets, whereas the rare earth oxide layers act as charge carrier reservoir and spacer for the CuO_2 sheets. Hence, the single crystals are characterized by a strong in-plane to out-of-plane electronic anisotropy (see Chapter 7.1). The electron doped 214 compounds crystallize in the body centered (bc) tetragonal T' structure with space group $I4/mmm$. The crystal structure is illustrated in Figure 2.3. Note, that adjacent CuO_2 sheets are shifted to each other along the in-plane diagonal by $(1/2, 1/2)$, and hence, the conventional unit cell is doubled. The oxygen atoms occupy two distinct sites: the so called O(1) site, which is the position within the CuO_2 sheets, and the O(2) site, which denotes the out-of-plane oxygen in the rare earth sublattice. The rare earth sublattice $\text{Ln}_2\text{O}_2^{2+}$ has the fluorite structure with an oxygen coordination number of 8 for the rare earth ion Ln, leaving vacant the apex position directly below and above the Cu ions. This is a potential impurity site, which might be occupied partially [78, 79] during crystal growth. Because of steric considerations, the apex occupation leads to a strong, local lattice distortion with considerable influence on the physical properties of the electron doped compounds.

The arrangement of the O(2) oxygen and hence, the planar coordination of Cu in the electron doped cuprates is unique, whereas the related hole doped 214 compound $\text{La}_{2-x}\text{Sr}_x\text{CuO}_4$ crystallizes in the more common T structure (Figure 2.3 (right)). The T structure is characterized by the apex occupation of the O(2) oxygen. In this case the Cu site is sixfold coordinated with the oxygen forming an octahedral environment. The $\text{La}_2\text{O}_2^{2+}$ layers show rock salt structure with an oxygen coordination number of nine for the La ion. Compared to the T structure, the T' structure is stable at low temperatures. There are no structural phase transitions [66], which influence the electronic properties. The crystallization in T or T' de-

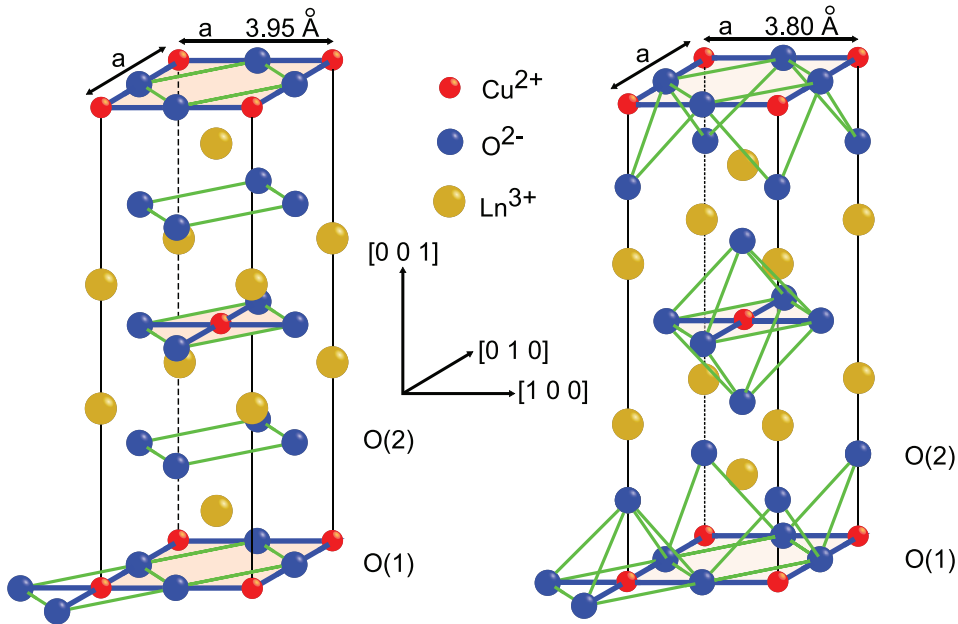


Figure 2.3: **Left:** T' structure with its characteristic fourfold planar coordination of the Cu ions. The vacant apex site, which is the position directly below and above the Cu ion, acts as effective impurity site when occupied by oxygen [78, 79]. All electron doped compounds crystallize into the T' structure. **Right:** The T structure is favored by 214 compounds, where La is used as rare earth element. In this case the out-of-plane oxygen O(2) occupies the apex position, resulting in a sixfold oxygen coordination of the Cu ions. Both structures are tetragonal with space group $I4/mmm$. Note, that adjacent CuO_2 layers are shifted to each other by $(1/2, 1/2)$ along the in-plane diagonal. Hence, the conventional unit cell is doubled.

depends on the rare earth ionic radii [80]. 214 crystals with smaller lanthanides favor the T' structure, whereas the compound $\text{La}_{2-x}\text{Ce}_x\text{CuO}_4$ cannot be crystallized in the T' structure. Concerning single crystal growth, the system $\text{La}_{2-x}\text{Ce}_x\text{CuO}_4$ has an additional problem: growth experiments have shown that the dopant Ce is precipitated on the surface and cannot be incorporated into the crystal structure. Thus, although $\text{La}_{2-x}\text{Ce}_x\text{CuO}_4$ might be the ideal compound for comparative studies with $\text{La}_{2-x}\text{Sr}_x\text{CuO}_4$, this system can only be grown in thin film form [81].

2.3.2 Magnetic behavior

As in this thesis the main focus lies on $\text{Nd}_{2-x}\text{Ce}_x\text{CuO}_4$ single crystals, the magnetic properties of this compound are discussed primarily. The magnetism of the electron doped 214 compounds is characterized by both the AFM ordering of the CuO_2 sublattice and the magnetism of the rare earth ions.

The three dimensional AFM ordering of the Cu spins below T_N is governed by the weak interplanar exchange coupling of $J_{\perp} = 5 \cdot 10^{-3}$ meV, which is by a

factor of $2.5 \cdot 10^4$ smaller than the in-plane coupling ($J_{\parallel} = 126$ meV) [31, 82]. Hence, the structural anisotropy leads also to a strong anisotropy in the exchange coupling, and above T_N a two dimensional Spin-1/2 Heisenberg model is suitable for the theoretical description [83]. T_N and spin stiffness evolve with doping and are strongly reduced for as grown optimally doped 214 compounds [84]. For $T < T_N$, $\text{Nd}_{2-x}\text{Ce}_x\text{CuO}_4$ shows a series of spin reorientation transitions [82, 84–87], which are absent for the $\text{Pr}_{2-x}\text{Ce}_x\text{CuO}_4$ system. Below T_N the Cu spins are ordered into the La_2NiO_4 type structure (phase-I, Figure 2.4 (a)), followed by a spin rotation of 90° about the c axis at $T \approx 75$ K (phase-II, Figure 2.4 (b)), and a subsequent transition into the primary La_2NiO_4 order at $T = 30$ K (phase-III) [82, 85]. The Cu spins show a noncollinear structure [86, 87], i.e. the AFM spin orientation of adjacent layers is orthogonal to each other. By applying a magnetic field of $\mu_0 H \approx 4$ T parallel to the CuO_2 planes, the noncollinear spin structure can be transformed into a collinear one [86] (Figure 2.4 (c)). In phase-III, at temperatures

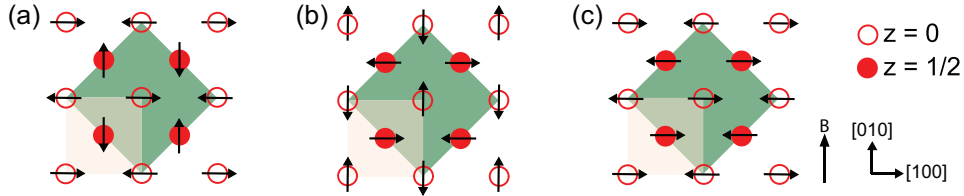


Figure 2.4: Illustration of the Cu spin orientation below T_N [82, 84, 86]. The unit cell is projected onto the in-plane area (highlighted square). For clarifying reasons, only the Cu ions of adjacent CuO_2 planes (open circles: $z = 0c$, closed circles: $z = 1/2c$) are shown. The unit cell of the AFM lattice is situated along the diagonal direction (highlighted diamond) with lattice constants of $a_m = \sqrt{2} \cdot a$ and $c_m = c$. (a) In zero field below T_N the Cu spins order into a noncollinear type-I structure. (b) At $T \approx 75$ K a spin rotation by 90° is observed (type-II). For symmetry reasons, configuration (a) and (b) are different and the spin structure (a) cannot be transformed into the structure (b) by a simple rotation of the crystal. Below 30 K the type-I structure is restored and the Nd^{3+} moments start participating in the magnetic order. (c) With applied in-plane magnetic field the noncollinear structure can be switched to a collinear one [86]. The collinear configuration in (c) is obtained from (b) by applying an in-plane field along the [010] direction.

below 30 K, the Nd^{3+} ions start participating in the magnetic order due to the coupling between the Nd moments and the second nearest neighbor Cu^{2+} spins. Because of tetragonal symmetry the nearest neighbor interaction is canceled [82, 87].

The magnetic susceptibility of the electron doped 214 compounds is governed by the magnetism of the rare earth ions. At high temperatures a Curie-Weiss behavior prevails (especially for the in-plane magnetic susceptibility χ_{ab}), whereas at lower temperatures the anisotropy between χ_{ab} and χ_c is high. Figure 2.5 shows the temperature dependence of the in-plane and out-of-plane susceptibility for Nd_2CuO_4 and Pr_2CuO_4 , respectively.

Nd_2CuO_4 crystals have an isotropic χ for temperatures $T > 100$ K. From the

shown fit, according to the Curie-Weiss law, an effective magnetic moment of $\mu_{eff \parallel} = \mu_{eff \perp} = 3.72\mu_B$ per Nd ion is evaluated, which is slightly higher than the value of $\mu = 3.62\mu_B$ for a free Nd^{3+} ion with ground state $^4I_{9/2}$. For $T < 100$ K a deviation from Curie-Weiss behavior arises due to the crystal field splittings of the J multiplet [88] and the increasing antiferromagnetic Nd-Nd interaction. In susceptibility data, there is no evidence for a magnetic order of the Nd^{3+} ions at low temperatures, as no phase transition can be seen in the data. However, it was shown [88, 89] that the observed Schottky anomaly in specific heat at $T \leq 1.6$ K can be interpreted assuming a crystal field doublet ground state and an antiferromagnetic transition in the Nd^{3+} sublattice. Hence, an AFM order of the Nd moments induced by Cu-Nd interaction at $T \leq 1.6$ K is deduced. The susceptibility data for $\text{Nd}_{2-x}\text{Ce}_x\text{CuO}_4$ are almost doping independent. Experimental data (not shown in Figure 2.5) on an overdoped $\text{Nd}_{1.83}\text{Ce}_{0.17}\text{CuO}_4$ crystal show an identical susceptibility curve for $T < 100$ K, whereas the effective magnetic moment is slightly lower due to the diamagnetic Ce^{4+} ions, amounting to $\mu_{eff \parallel} = \mu_{eff \perp} = 3.55\mu_B$ per Nd ion.

For the magnetic behavior of the rare earth sublattice of other 214 compounds, the same explanations are valid as for Nd_2CuO_4 . Differences arise from the different magnetic ground states of the rare earth ions. The values for T_N are below 10 K [89]. The out-of-plane susceptibility of Pr_2CuO_4 (Figure 2.5 (b)) does not obey a Curie-Weiss law for temperatures up to 320 K. From the in-plane data, μ_{eff} is estimated to be $3.75\mu_B$ per Pr ion, which is about 5% higher than the value of $3.58\mu_B$, obtained by Hund's rule for Pr^{3+} .

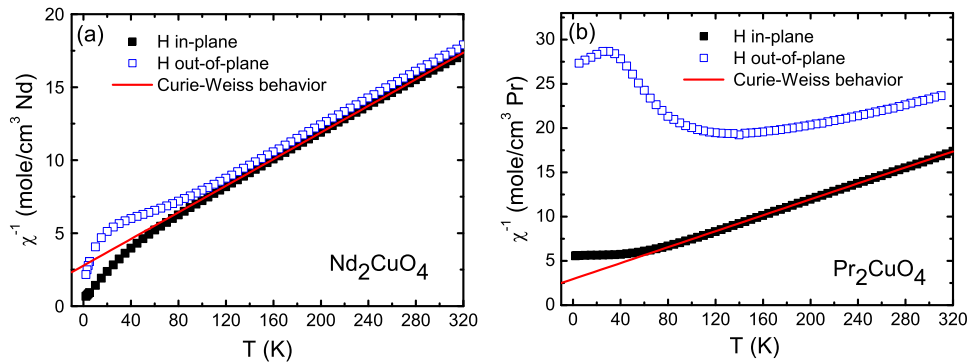


Figure 2.5: Temperature dependence of the inverse magnetic susceptibility for annealed Nd_2CuO_4 (a) and Pr_2CuO_4 (b) single crystals. The magnetic susceptibility is governed by the magnetism of the rare earth ions. Hence, the AFM ordering of the CuO_2 sublattice cannot be seen. The applied magnetic field amounts to $\mu_0 H = 0.5$ T. Characteristic for both systems is the strong anisotropy between the in-plane and out-of-plane configuration, especially for temperatures $T < 100$ K, which is a clear indication of the crystal-field splitting of the J multiplets.

Chapter 3

Growth of electron doped cuprate single crystals

The availability of homogeneous, high purity single crystals covering the whole phase diagram is a basic requirement in order to elucidate the doping dependent appearance and interplay of the different phenomena in cuprates, already reviewed in Chapter 2.1. While the growth process of hole doped cuprates - especially the $\text{YBa}_2\text{Cu}_3\text{O}_{7-\delta}$ and $\text{La}_{2-x}\text{Sr}_x\text{CuO}_4$ sample set - has been continuously improved over the last two decades (see discussion in Chapter 2.2 and the references therein), the growth of high quality electron doped 214 single crystals and their annealing process represents a particular challenge and the results obtained are not always satisfying [90–96]. The growth process of electron doped high temperature superconductors is optimized and discussed in the following chapter. Thereby, the main focus lies on the $\text{Nd}_{2-x}\text{Ce}_x\text{CuO}_4$ and $\text{Pr}_{2-x}\text{Ce}_x\text{CuO}_4$ system. Moreover, other rare earth 214 sample sets are grown to some extent using the same growth technique and experimental setup.

3.1 The composition phase diagram of incongruently melting compounds

Before growing crystals it is inevitable to discuss the temperature-composition phase diagram of the 214 compounds in order to find the optimal composition of the flux and temperature, at which the crystallization of the 214 phase takes place.

3.1.1 Determination of the phase diagram by means of differential thermal analysis (DTA)

The characteristic compositional phase diagram of the 214 cuprates is shown in Figure 3.1. The binary compositional diagram describes the appearance and regions of coexistence of thermodynamic stable phases as well as phase transformations as a function of the state variables. The state of a phase is well-defined by the

state variables pressure p , temperature T and the concentration variable x of the mixed starting components Ln_2O_3 and CuO .

For the thermodynamical description of the compositional phase diagram the Gibbs free energy

$$G = U + pV - TS = H - TS \quad (3.1)$$

is the appropriate thermodynamic potential. In this context, U represents the internal energy, V the volume, S the entropy, and H the enthalpy of the system. Applying the first law of thermodynamics

$$dU = \delta Q - pdV + \sum_i \mu_i dN_i \quad (3.2)$$

the total derivative of G is given by

$$dG = dU + d(pV) - d(TS) = dH - d(TS) = -SdT + Vdp + \sum_i \mu_i N dx_i, \quad (3.3)$$

where μ_i and $dN_i = N dx_i$ are the chemical potentials and the number of particles of each component i , respectively. Neglecting any particle loss during phase transition and assuming given constant state variables, the system is in the thermodynamic equilibrium, when G is minimal, i.e.

$$dG = dH - TdS = 0. \quad (3.4)$$

From Equation 3.4 one can see that a small variation in G is given by two contributions, namely the change in the enthalpy H and the variation in the entropy S of a system. For constant volume V , the enthalpy H represents the internal energy, whereas the entropy S is a measure of disorder of the system. Generally speaking, at low temperatures the contribution of H prevails over the entropy term, whereas at high temperatures the importance of TdS increases. Therefore, for certain T and p those phases are stable and appear in the compositional phase diagram as a function of x , which minimize the Gibbs free energy G .

In practice the Gibbs free energy G as well as the entropy S of a system cannot be expressed in terms of absolute values. The quantities to be measured are differences of the thermodynamic potentials, which arise during phase transitions or transitions from one equilibrium state to another. Therefore, the thermal analysis in combination with X-ray powder diffraction is an appropriate experimental approach in order to determine the equilibrium states of a mixture as a function of T , p and x . The X-ray analysis gives information about the phase formation, whereas in the thermal analysis first-order phase transitions such as chemical reactions, crystallographic phase transitions, melting, peritectic and eutectic transformations, spinodal decomposition etc. are detected. Note, that first-order phase transitions are characterized by the absorption or release of latent heat¹. The heat

¹According to Ehrenfest, phase transitions are classified using the discontinuity in the lowest derivative of the Gibbs free energy G [97]. A newer classification distinguishes between first-order and second-order phase transitions depending on whether latent heat is involved or not.

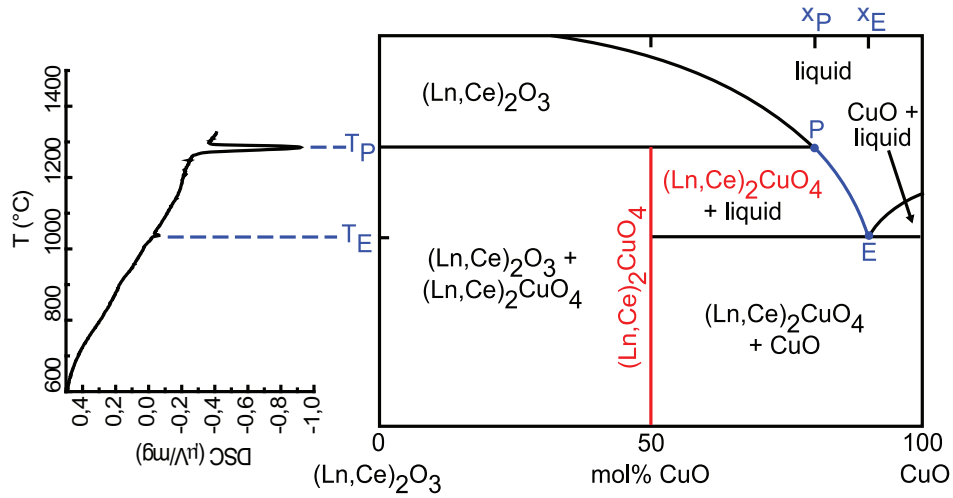


Figure 3.1: **Left:** Typical curve of a differential thermal analysis (DTA) of a $Pr_{2-x}Ce_xCuO_4$ pellet. Two endothermic peaks, which represent the eutectic and peritectic phase transformation, are clearly visible. Using DTA in combination with X-ray powder diffraction the binary phase diagram of the system $Ln_2O_3 - CuO$ can be explored. **Right:** Sketch of the binary compositional phase diagram of the $(LnCe)_2O_3 - CuO$ system with $Ln = La, Pr, Nd, Sm$ etc. The superconducting phase $Ln_{2-x}Ce_xCuO_4$ undergoes a peritectic decomposition at temperatures greater than 1200 °C and therefore, the growth is restricted to a small window between the peritectic point P and eutectic point E (blue liquidus line).

(enthalpy change ΔH) consumed or released by a substance during a phase transition is determined in the differential thermal analysis (DTA) experiment. Thereby, the quantity to be measured is the temperature difference

$$\Delta T = T_s - T_r \quad (3.5)$$

between the substance (s) and a reference substance (r) as a function of the temperature T or the heating rate $\beta = dT_r/dt$ of the furnace. With the definition of the specific heat for an isobaric process

$$C = \left(\frac{\delta Q}{dT} \right)_p = T \left(\frac{dS}{dT} \right)_p, \quad (3.6)$$

which is a measure of the heat quantity δQ required for an infinitesimal temperature change dT of the substance, and the relation between specific heat and heat flow

$$\Phi = \frac{\delta Q_{s,r}}{dt} = C_{s,r} \frac{dT}{dt}, \quad (3.7)$$

one can deduce the specific heat capacity C_s and the enthalpy of transition ΔH of the sample from the signal ΔT . Figure 3.2 shows the DTA setup with the different contributions of the heat flow as well as the corresponding thermal resistances R .

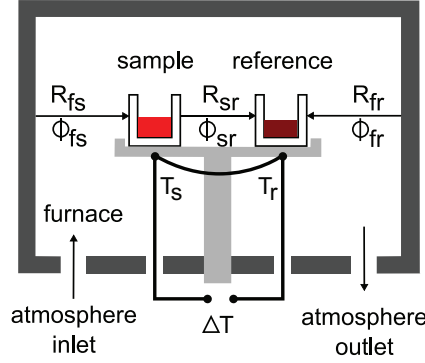


Figure 3.2: Illustration of the DTA setup with the corresponding heat flows and thermal resistances.

The heat flow between furnace and sample/reference as well as between sample and reference is proportional to the relative temperature difference and the inverse thermal resistance

$$\Phi_{fs,r} = \frac{T_f - T_{s,r}}{R_{fs,r}} \quad \text{and} \quad \Phi_{sr} = \frac{T_s - T_r}{R_{sr}} . \quad (3.8)$$

Considering Φ_{fs} as the heat flow from the furnace to the sample and Φ_{re} as the heat flow due to the reaction, the following equation arises:

$$C_s \frac{dT_s}{dt} = \Phi_{fs} - \Phi_{re} - \Phi_{sr} = C_s \frac{dT_r}{dt} + C_s \frac{d\Delta T}{dt} . \quad (3.9)$$

The corresponding relation for the reference sample is given by

$$C_r \frac{dT_r}{dt} = \Phi_{fr} + \Phi_{sr} . \quad (3.10)$$

By calculating the difference between Equation 3.9 and 3.10 one obtains

$$\Phi_{fs} - \Phi_{fr} - \Phi_{re} - 2\Phi_{sr} = (C_s - C_r) \frac{dT_r}{dt} + C_s \frac{d\Delta T}{dt} . \quad (3.11)$$

For a symmetric setup $R_{fs} \approx R_{fr} = R$ and with Equations 3.8 and 3.5 one can rewrite Equation 3.11 according to

$$-\Delta T \left(\frac{1}{R} + \frac{2}{R_{sr}} \right) - \Phi_{re} = (C_s - C_r) \frac{dT_r}{dt} + C_s \frac{d\Delta T}{dt} . \quad (3.12)$$

With the thermal resistance $R^* = \left(\frac{1}{R} + \frac{2}{R_{sr}} \right)$ the measured signal ΔT is finally given by the following equation:

$$\Delta T = -R^* \Phi_{re} - R^* (C_s - C_r) \beta - C_p R^* \frac{d\Delta T}{dt} . \quad (3.13)$$

The first term on the right hand side describes the change in ΔT due to the first-order phase transition, the second one is an offset contribution due to the differences in the heat capacity of reference and sample $C_{r,s}$. The third term describes the relaxation of the system after a first order phase transition. If no first order phase transition occurs during a temperature ramp, the measured temperatures of sample and reference are equal (provided $C_s = C_r$) and therefore, $\Delta T = 0$. If there is a first order phase transition of the substance, the temperature of the sample is retarded or advanced with respect to the reference temperature during an uniform T sweep, depending on whether an endothermic or exothermic reaction occurs. If the experimental setup is calibrated properly² one can extract the specific heat capacity C_s and the enthalpy of transition ΔH , which is equal to the area around the ΔT peak as a function of β . For the calculation of ΔH the base line is subtracted and the ΔT peak is integrated over the time period of the transition

$$\Delta H = \int_{t_1}^{t_2} \Phi dt = -\frac{1}{R^*} \int_{t_1}^{t_2} \Delta T dt . \quad (3.14)$$

The measuring setup for thermal analysis consists basically of a furnace as heat source, which can be evacuated and used with different atmospheres (Figure 3.2). This furnace encloses a sample holder with a platinum/rhodium bearing area. On the bearing area two Al_2O_3 crucibles for sample and reference are mounted and on the rear side two thermocouples are fixed closely to the crucibles. The thermocouples are connected in difference to each other and therefore, in case of thermal symmetry the resulting voltage signal is zero. In addition to the determination of the enthalpy ΔH or the specific heat capacity C_s , the change in weight Δm of a substance as a function of β might be important. This method of thermal analysis is called thermogravimetry analysis (TGA). The information of weight loss or gain due to a reaction in an atmosphere with a certain oxygen partial pressure p_{O_2} gives hint of the reduction or oxygenation state of a phase. For this purpose the sample holder is connected with a balance. In general, TGA and DTA experiments are carried out at the same time³.

As shown in Figure 3.1, the 214 compounds are incongruently melting solid solutions. This means that the 214 phase does not melt uniformly at a certain temperature, but it decomposes at the peritectic point P into a Ln_2O_3 phase and a CuO rich liquid. Generally, the formation of a peritectic phase takes primarily place in systems, where the melting point of the different component phases differs strongly. This is also the case in the sesquioxides Ln_2O_3 - CuO system, where the melting point arises at temperatures of $T > 2300$ °C [99] and 1100 °C [100], respectively⁴. However, for the further discussion only the quasi-binary system $(\text{LnCe})_2\text{CuO}_4$ - CuO is of importance. The 214 phase, which is stable at room temperature, can only be grown along the liquidus line (blue line in Figure 3.1)

²For detailed information about thermal analysis see also [98] and the references therein.

³The DTA and TGA experiments were carried out using a Netzsch STA 409 apparatus.

⁴The exact values for the melting temperature are obviously dependent on the oxygen partial pressure p_{O_2} .

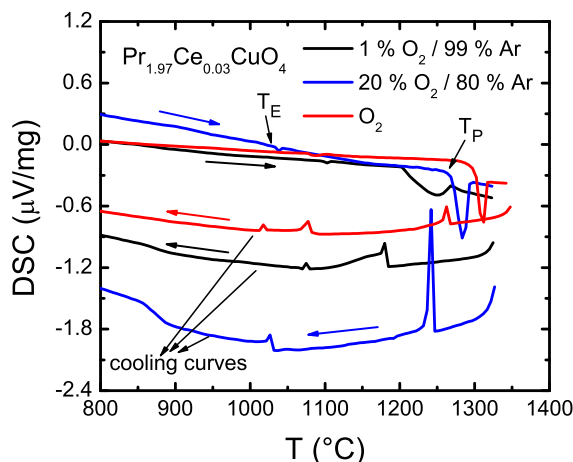


Figure 3.3: DTA curves of $\text{Pr}_{1.97}\text{Ce}_{0.03}\text{CuO}_4$ under different atmospheres in order to determine the eutectic and peritectic temperature. For the estimation of T_E and T_P the heating curves are used (upper three curves) as the temperature controlled cooling curves are much more difficult to interpret due to supercooling and crucible corrosion effects. The curve measured in an atmosphere of 1% O_2 / 99% Ar shows a broadening of the peritectic transition, which reflects the reduction/oxygenation of the melt.

between the peritectic point P and the eutectic point E. The eutectic point E in the phase diagram is characterized by a temperature T_E and an eutectic mixture x_E , at which the component mixture melts/crystallizes simultaneously. T_E is the lowest melting temperature in the phase diagram.

With DTA, T_P and T_E are determined using a 20 mg pellet of pre-reacted 214 phase, which is heated up to 1350 $^\circ\text{C}$ with a constant temperature ramp of 10 $^\circ\text{C}/\text{min}$. After the heating a short dwell time of 10 minutes and a subsequent temperature controlled cooling with the same rate are applied. The DTA curves are recorded for both the heating-up and cooling down. For the experimental determination of T_E and T_P the onset point⁵ of the endothermic peaks is used. The values for $\text{Nd}_{2-x}\text{Ce}_x\text{CuO}_4$ and $\text{Pr}_{2-x}\text{Ce}_x\text{CuO}_4$ in atmospheres with different p_{O_2} are summarized in Table 3.1. For the curves recorded during heating, only two endothermic peaks, which can be assigned to the eutectic and peritectic point, are clearly visible (cf. Figure 3.3). In the curves recorded during cooling one can see that the onset point for the peritectic transition is shifted to lower temperatures and especially for pure oxygen atmospheres the exothermic eutectic peak is splitted up into two peaks. The discrepancy between heating and cooling curves can be explained in terms of non-equilibrium reactions which can occur in a dynamical measuring method such as DTA. This means that the temperature rate β is so fast that at a certain T the system has not enough time for relaxation into the equilibrium state and an intermediate state is recorded. For example, the shift of the

⁵The onset point is defined by the intersection point of the tangents, which represent the slope of the background curve before the phase transition and the slope of the peak curve.

DTA atmosphere	T_E (°C)	T_P (°C)	T_E (°C)	T_P (°C)	T_E (°C)	T_P (°C)
$\text{Pr}_{2-x}\text{Ce}_x\text{CuO}_4$	$x = 0$		$x = 0.03$		$x = 0.15$	
O_2	1083	1305	1075	1295	1081	1290
20 % O_2 / 80 % Ar	1035	1275	1034	1270	1038	1274
1 % O_2 / 99 % Ar	–	1197	1097	1203	1060	1220
$\text{Nd}_{2-x}\text{Ce}_x\text{CuO}_4$	$x = 0$		$x = 0.03$		$x = 0.15$	
O_2	1075	1300	–	–	1081	1326
20 % O_2 / 80 % Ar	1040*	1253	–	–	1040*	1300
1 % O_2 / 99 % Ar	1070*	1200	–	–	1054*	1218

Table 3.1: Onset temperatures T_E and T_P of the eutectic and peritectic transformation determined from the heating curves of differential thermal analysis (DTA) for the $\text{Nd}_{2-x}\text{Ce}_x\text{CuO}_4$ and $\text{Pr}_{2-x}\text{Ce}_x\text{CuO}_4$ system. Data marked by an asterisk are determined from cooling curves. For all measurements, Al_2O_3 crucibles were used, the gas flow was set to 4 l/h and the temperature was ramped up to 1340 °C with rates of 10 °C/min. The error of measurement is estimated to be $\Delta T_{E,P} = 10$ °C.

peritectic peak to lower temperatures and the sudden onset of the exothermic reaction is a signature of a supercooling of the melt. The appearance of two or more peaks rather than a single transition at T_E might be due to the strong reaction of the flux with the Al_2O_3 crucible. The wall of the crucible is coated to some extent by the flux and a strong corrosion process can be observed leading to a partial dissolution of Al into the melt and the formation of a PrAlO_3 phase, which can clearly be seen in X-ray powder diffraction. This strong crucible corrosion due to the aggressive CuO melt⁶ is responsible for the variation of the composition of the melt and therefore, cooling curves can lead to misleading temperature-composition diagrams.

The use of furnace atmospheres with diminishing p_{O_2} leads to a modification of the CuO rich melt into an oxygen deficient melt of $\text{CuO}/\text{Cu}_2\text{O}$, while T_P is decreasing continuously. The curves recorded in an atmosphere of 1 % O_2 in Ar show a strong broadening at the peritectic transition. This broadening is associated with the reduction/oxygenation of the melt and can also be seen in the weight loss/gain of the simultaneous TG measurement. Within the estimated error of measurement there is no Ce dependence of T_P and T_E , which differs from earlier measurements [100, 102]. The eutectic and peritectic mixture x_E and x_P amount to 78 mol % and 92 mol % [100, 102], respectively, with deviations of ± 2 mol%. The general phase diagram, presented in Figure 3.1, with a liquidus line between E = (X_E, T_E) and P = (X_P, T_P) is valid for all rare earth 214 compounds. Only in the La_2O_3 - CuO system the appearance of a stable $\text{La}_2\text{Cu}_2\text{O}_5$ is reported [103], which decomposes peritectically at 40 °C above T_E into La_2CuO_4 . It is reported that the values for T_P decrease with increasing ionic radius of the rare earths [90] resulting in a narrower liquidus line, while x_E and x_P are almost independent of the rare earth ion.

⁶Problems of crucible corrosion and their impact on DTA results are also discussed in [101].

3.1.2 The growth of high quality single crystals using the travelling solvent floating zone technique (TSFZ)

From the detailed discussion of the compositional phase diagram of the 214 high temperature superconductors in Section 3.1.1, it can easily be deduced that a growth of the 214 phase can only be performed within the peritectic and eutectic point along the liquidus line.

The growth of $\text{Nd}_{2-x}\text{Ce}_x\text{CuO}_4$ and $\text{Pr}_{2-x}\text{Ce}_x\text{CuO}_4$ single crystals in crucibles out of a CuO rich melt is reported in prior publications [90, 92, 104]. In this growth experiments a mixture with the composition ratio $\text{Nd}_{2-x}\text{Ce}_x\text{CuO}_4/\text{CuO} = x = 70/30$ is completely molten in a crucible at temperatures higher than $T(x)$ of the liquidus line, followed by a slow cooling of the melt until the eutectic temperature is reached, at which the growth process of the 214 phase is finished and the remaining flux is crystallized eutectically. Two major problems arise when using this method, which are the crucible corrosion already mentioned in Chapter 3.1.1 and the effective distribution coefficient⁷ k_e^A .

For the $\text{Nd}_{2-x}\text{Ce}_x\text{CuO}_4$ system 0.02 at./f.u. Pt impurities on the Cu site are found when Pt crucibles are used during crystal growth [92]. This small substitution is sufficient to suppress superconductivity completely. Corrosion problems due to the reactive oxide melts are observed in all cuprate systems for different commercially available crucible materials, such as Al_2O_3 or Y stabilized ZrO_2 [50]. The second problem of container grown crystals is the observed inhomogeneity or variation from the nominal value of the Ce doping [92, 104], as deviations in k_e^A from unity change continuously the composition of the melt, giving rise to gradients in the dopant concentration.

The improvement in crystal quality is closely connected with the solution of these two main problems. One possibility to solve the problems is the use of a container-free growth method. This method is called travelling solvent floating zone (TSFZ) technique. The functional principle of this technique is shown in Figure 3.4. The system consists of a feed and seed rod and a local solvent zone in-between. This vertical floating zone is only held by surface tension and has a composition x between E and P in the steady state growth process of the 214 phase. During growth polycrystalline feed material is dissolved continuously at the solid-liquid interface on the top and the material is transported within the solvent by diffusion and convection to the second phase interface at the bottom side where the crystallization occurs. As a result the solvent traverses slowly the feed rod leaving behind a single crystalline rod. There are two possibilities to obtain the appropriate

⁷The effective distribution coefficient is defined as the ratio of the concentration of a component A in two phases. Let $[A]_{\text{liquid}}$ be the concentration of the considered component in the liquid phase and $[A]_{\text{solid}}$ the concentration in the crystallized phase. The definition of k_e^A is: $k_e^A = [A]_{\text{solid}}/[A]_{\text{liquid}}$. Note, that the growth process initiates a linear movement of the phase interface with velocity v and therefore, k_e^A is primarily governed by the growth kinetics and the transport processes in the system, which depend on the growth parameters. For each component of a mixture one can define a k_e . In practice only the crystallization behavior of a dopant or impurity is of importance. A detailed description of k_e^A is given in [105].

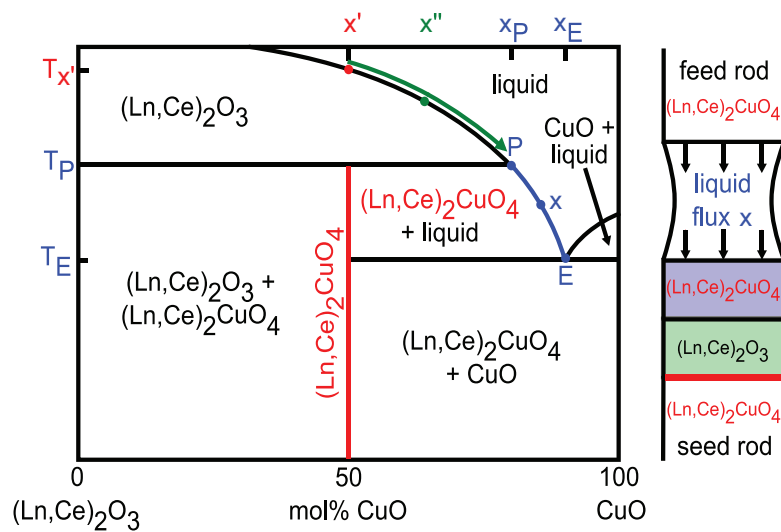


Figure 3.4: Explanation of the TSFZ growth technique by means of the 214 compositional phase diagram. A local vertical solvent zone of composition x is held by surface tension between the seed and feed rod (“floating zone”). The 214 phase from the polycrystalline feed rod is dissolved continuously into the melt on the upper solid-liquid interface and crystallized on the lower liquid-solid interface. In equilibrium state the solvent traverses the polycrystalline feed rod (“travelling solvent”) and on its bottom side the 214 single crystal is grown. When using a flux pellet of composition x between P and E, steady state growth conditions can be reached from the beginning of the growth process. Otherwise, when starting with the 214 phase, $(\text{Ln,Ce})_2\text{O}_3$ is grown at first and simultaneously the solvent composition becomes richer of CuO, moving from x' via x'' to x_P (green arrow), where the crystallization of the 214 phase sets in. The underlying color represents the composition of the solvent zone at a given stage of the growth process.

flux composition for a stable 214 growth process between E and P:

1. The flux can be generated by melting the end of the feed rod at $T > T_{X'}$. In this case, at the beginning, the liquid has the same composition as the rod and according to the phase diagram only the $(\text{Ln,Ce})_2\text{O}_3$ phase can be crystallized. Simultaneously the composition of the melt will be changed towards a CuO richer one. Therefore, it is possible to move along the liquidus line in Figure 3.4 (green arrow) while the temperature is gradually lowered until the peritectic point P is reached. At P the 214 phase starts crystallizing⁸.
2. Alternatively, one can place a polycrystalline flux pellet of composition x between x_P and x_E on the top of the seed rod. The weight of the used flux pellet should correspond to the one of the molten zone. In this case the growth of a 214 single crystal is possible from the beginning, provided that

⁸This example shows how flexible and powerful the TSFZ method is. In principle, one can use the TSFZ method in combination with X-ray powder diffraction and EDX analysis in order to determine the composition phase diagram of a system [106].

a monocrystalline seed is used. This approach is also applied in this thesis.

From the discussion above it is obvious that the modern TSFZ method has many advantages compared to flux growth methods using a crucible. The purity of the crystals is only affected by the purity of the starting materials and the contamination problems due to crucible corrosion are avoided. In addition, by using suitable growth conditions (oxygen partial pressure p_{O_2} , flux composition x , temperature T , growth velocity v) one can overcome the problem of an inhomogeneous Ce distribution and large, bulky crystals of several centimeters in length can be grown under exactly the same conditions. This is the basic requirement for homogeneous crystals. Crucible grown crystals, however, have usually a plate like structure and the crystal yield is small, which is a serious problem for experiments such as neutron scattering, where bulky crystals are indispensable.

3.2 Experimental setup: the mirror furnace

For the crystal growth using the TSFZ method a mirror furnace⁹ was used. The experimental setup is shown in Figure 3.5.

The mirror furnace consists of four half ellipsoidal mirrors with halogen projector lamps located on their first focus. The four mirrors are arranged symmetrically within a horizontal plane with an angle of 90° to each other around the vertical axis of the furnace. The radiation is focused on one point in the center of the furnace, at which the second focus of all four mirrors overlaps. Hence, only a small localized zone is strongly heated up and there is a large temperature gradient in vertical direction. The advantage of four mirrors, compared to older setups using a single or double mirror system, is given by an improvement of the homogeneity of the horizontal temperature distribution¹⁰, which is crucial for a well defined and stable growth process. The mirrors are made up of Al coated glass which provides high reflectivity and low costs compared to gold coated brass systems. Another important factor, influencing the size and the stability of the local solvent zone, is the choice of appropriate lamps. For the 214 cuprates small 300 W halogen lamps are adequate in order to achieve the desired temperatures of the solvent zone between T_E and T_P . Compared to xenon arc lamps, which are also often used especially for higher melting compounds, halogen lamps are much more stable. Additionally, the used lamps have a flat, rectangular filament design, which improves the

⁹A commercial 4-mirror furnace from CSI corporation (Japan), type FZ-T-10000-H-VI-VP was available.

¹⁰There are several other types of mirror furnaces, such as the vertical single mirror furnace. In this configuration an ellipsoidal mirror with high eccentricity is mounted vertically and the feed rod is located within the mirror, providing therefore a homogeneous horizontal temperature distribution. The disadvantage of this configuration is given by the limitation in the growth length due to the setup. It is clear that furnaces with one or two opposing mirrors in horizontal configuration have a nonuniform in-plane temperature distribution, as not each surface element of a feed rod is facing the heat source at the same time. Rotation of the rods might reduce this effect. With a horizontal 4 mirror setup differences in the in-plane temperature can be suppressed below 10°C .

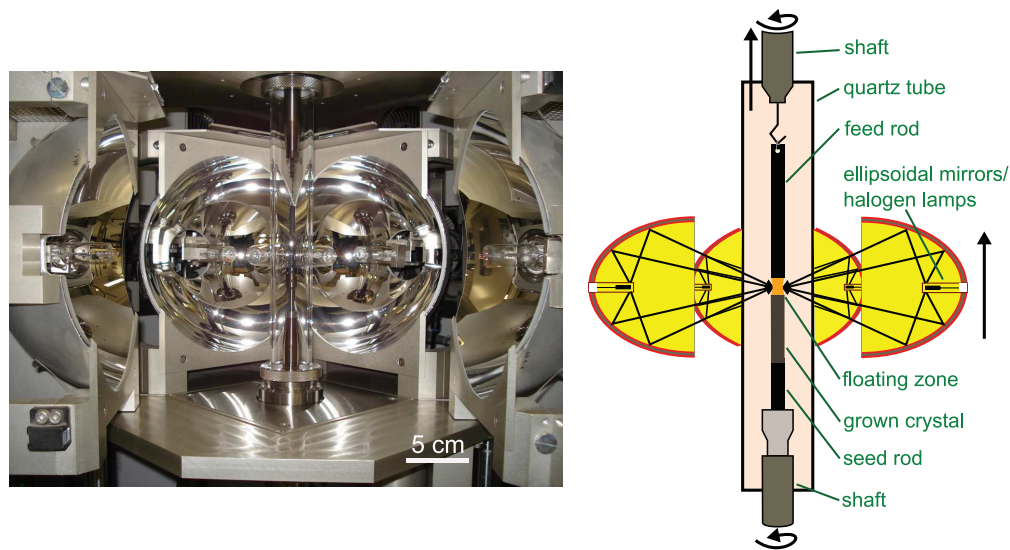


Figure 3.5: **Left:** Opened 4-mirror furnace with sample space (vertical quartz tube). **Right:** Illustration of the operating mode of the furnace. The furnace consists of four half ellipsoidal mirrors with halogen projector lamps on their first focus, arranged in a 2π configuration around the vertical center line of the system. The radiation produced by the four lamps with their angular separation of 90° to each other is focused on one point in the centre of the furnace, at which the feed and seed rod are vertically mounted along the axis of the setup. The rods with suspension are surrounded by a quartz tube providing the possibility to grow under arbitrary atmospheres. The growth velocity v is given by the external movement of the mirror system in vertical direction (black arrow). Additional degrees of freedom of the setup are the vertical translation and rotation of the shafts.

homogeneity of the horizontal temperature distribution as well as the formation of a steep temperature gradient in vertical direction. With this setup temperatures of 2200°C can be generated. The temperature of the solvent zone is given by the output power of the four lamps, which is controlled by a silicon current regulator. There is no possibility to measure the temperature of the solvent directly. In order to estimate the real temperature of the solvent zone, one has to monitor, at which power the eutectic melt and the total dissolution occur and to compare these values to the temperature values obtained by DTA. The molten zone can be observed in real time using an integrated CCD camera. Of course, the real temperature of the solvent depends on how effective the radiation is absorbed and converted to heat. For example high purity Al_2O_3 or CaWO_4 polycrystalline rods are nearly “transparent”, i.e. the absorption of the light is small and occurs primarily via impurities. In addition, effects of thermal convection have to be taken into account when atmospheres with higher pressures are applied during the growth process.

The feed and seed rods are attached vertically onto two shafts and they are aligned exactly along the vertical center line of the system. Both shafts can be rotated, while the rotation speed can be continuously adjusted from 0 to 60 rpm.

The upper shaft and the mirror system can be moved in vertical direction with two different velocities. The high speed mode with velocities from 5 to 60 cm/min is used for the vertical adjustment of the rods, whereas the low speed mode with velocities from 0.1 to 18 mm/h is used during the growth process. Note, that the growth velocity v of the crystal is given by the velocity of the external parallel translation of the mirrors and is an important growth parameter. The maximum growth length of a crystal rod is limited to the maximum mirror translation of 15 cm. In addition to the many degrees of freedom making this furnace very flexible, the use of different atmospheres can sometimes be essential. This can be realized by using a quartz tube of highest purity together with an appropriate sealing system, which surrounds the rods with suspension. The sample space generated in this way can be evacuated and used under different atmospheres and pressures up to 10 bar.

In conclusion, it can be stated that due to its high flexibility in the adjustment of appropriate growth conditions such as temperature range, atmosphere, pressure, additional degrees of freedom in the parallel translation and the real time observation of the floating zone, the mirror furnace setup used for this thesis is very suitable for growing a multitude of incongruently and congruently melting oxide compounds. As already discussed above, this approach is not suitable for compounds which are "transparent" for the light radiation. However, this is certainly not the case for the cuprate compounds with their black color. On the other hand, the use of a light source in the floating zone approach offers a simple opportunity to melt poorly electroconductive substances, where the use of a HF induction coil fails.

3.3 Crystal growth

In order to grow high quality single crystals, not only appropriate growth parameters are important but also a careful preparation of the polycrystalline feed rods must be ensured.

3.3.1 Preparation of the feed rods

High quality feed rods are characterized by their homogeneity and uniformity in density and shape. Furthermore, phase purity and homogeneous distribution of the dopant are important as otherwise the small solvent zone changes continuously its composition during the growth process along the vertical feed rod, thereby affecting the stability of the floating zone and the crystallization. Rods of high density avoid the penetration of a larger quantity of liquid flux into the feed rod and hence, leading to a well defined upper solid-liquid interface.

At first, the 214 phase is prepared by solid state reaction. For this purpose the corresponding rare earth oxide and CuO powders with a purity of 99.99 % are mixed together according to the desired stoichiometric composition. The phase is generated via a fivefold pre-reaction of the mixture at temperatures of 900 °C, 920

°C, 950 °C and 980 °C (twice) for 10 h in air. Between each cycle the powder is homogenized using a ball mill. The multiple calcination steps improve the homogeneity. After the calcination the phase formation is checked by X-ray powder diffraction.

Thereafter, the phase pure polycrystalline powder is pressed hydrostatically into rods of 5 – 7 mm in diameter and up to 140 mm in length. In order to increase the density, the rods are sintered in O₂ at temperatures of 1050 °C, 1100 °C and 1200 °C for 5 h, respectively. As the sintering temperature is close to T_P a special vertical furnace is used, in which the rods are suspended on one end via a Pt wire on a holder. In this way, contaminations caused by the furnace tube or a supporting plate are avoided. During sintering the long rod is rotated and moved uniformly around the position of the highest temperature ensuring that each segment of the rod undergoes the same sintering conditions.

The rods used for flux pellets with the component fraction $(0.5 \cdot (2-x) \cdot \text{Ln}_2\text{O}_3 + x \cdot \text{CeO}_2)/\text{CuO} = 15/85$ are pre-reacted in the same way as the feed rods and are sintered at 1010 °C for 10 h in air.

3.3.2 Growth process and growth parameters

A sequence of the growth process of 214 single crystals is shown in Figure 3.6. For the first growth of electron doped 214 crystals a polycrystalline seed is used, at which a flux pellet of 0.35 – 0.4 g is fixed. The radiation power is increased slowly and the flux, which is simply a mixture of the 214 phase with CuO, starts melting at T_E . At this stage the vertically mounted feed rod is moved from the top towards the flux pellet, closing the gap in-between. The initial melt starts coating the feed and seed rod (Figure 3.6 (a)). Thereafter, the power is increased further on until the flux pellet is completely dissolved at T_x and a floating zone, which is only held by surface tension is established. In order to promote the homogenization of the floating zone, feed and seed rod are rotated in opposite direction to each other with rotational speeds of 20 and 15 – 20 rpm, respectively. At this point the growth process is started by setting a constant velocity of 0.5 mm/h for the motion of the mirror stage along the feed rod in vertical direction. Note, that the small growth velocity v of 0.5 mm/h corresponds to a total growth time of circa 10 days for one growth cycle. During the first day of growth the system is balanced by adjusting the power of the lamps and the vertical movement of the feed rod in order to get an equilibrium between dissolution and growth rate on both solid-liquid interfaces. This initial stage of the growth process is also used to get rid of any surplus of melt (in case the amount of used flux was too high) and to taper the seed to a small diameter (so called neck). This provides an effective natural grain selection when beginning with a polycrystalline seed (Figure 3.6 (c)). For the growth of a neck one has to keep the major part of the liquid flux on the feed rod side, which is only possible when a small amount can penetrate for 1 – 2 mm into the feed rod. In addition, this penetration of the CuO rich flux assists the dissolution of the feed

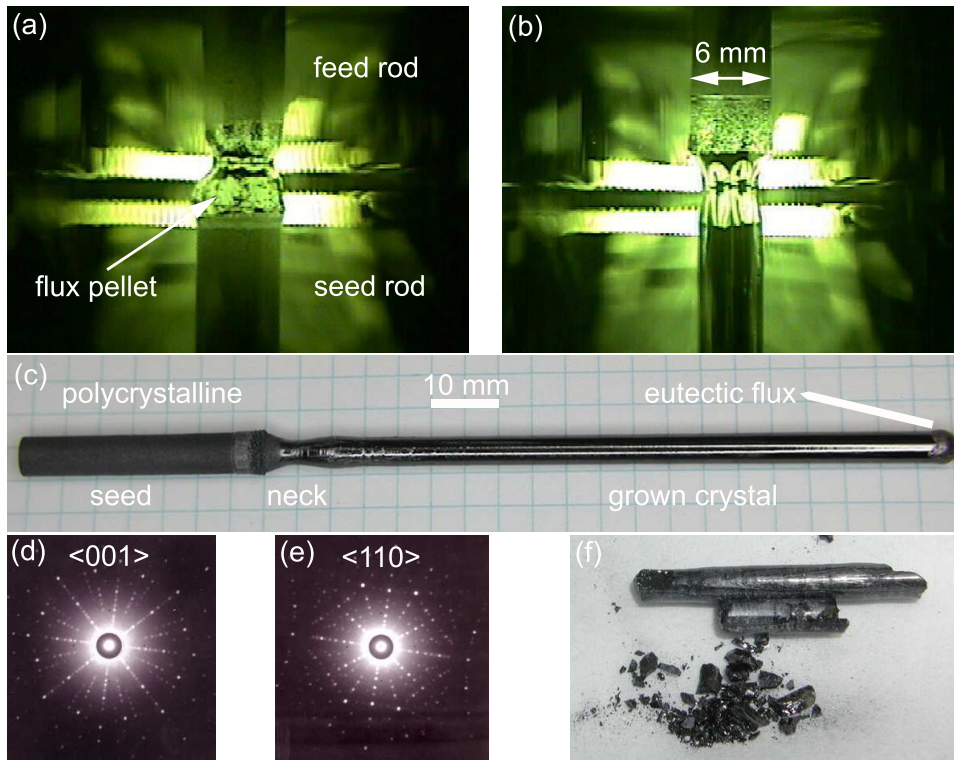


Figure 3.6: Illustration of the single crystal growth of 214 high temperature superconductors. The growth process starts with the generation of the floating zone of an appropriate composition by melting a flux pellet (a). The growth velocity usually amounts to 0.5 mm/h. After a few days stable conditions are obtained. In (b) a snapshot after 7 days of successful growth is provided, illustrating the 6 mm thick polycrystalline feed rod with a small region of flux penetration, the stable floating zone of 4.5 mm in length with a slightly concave crystallization line and the grown single crystal rod with its shiny surface. The whole rod ($\text{Nd}_{1.85}\text{Ce}_{0.15}\text{CuO}_4$) is shown in (c). Note the neck at the beginning, which is useful for the natural selection of grains when starting with a polycrystalline seed, and the facet emerging from the end. The residual flux is crystallized eutectically on the top. Laue back scattering shows that the facet is a (001) face (d) and the growth occurs along the crystallographic [110] or [100] axis (e), which are the directions of highest growth rate. In (f) a $\text{Nd}_{2-x}\text{Ce}_x\text{CuO}_4$ crystal rod, decomposing slowly after a couple of months when grown in an inappropriate atmosphere, is shown.

material into the floating zone¹¹. Once a stable growth process is established (Figure 3.6 (b)), the crystal growth is brought to a termination with exactly the same growth parameters. Especially for the electron doped 214 crystals small variations in parameters during this growth stage cause the formation of new nuclei, CuO precipitations and in worst case a possible break down of the floating zone.

Concerning the growth of single crystals when starting with a polycrystalline seed the following considerations should be made: The crystal growth is characterized by the competition of different neighboring grains, which tend to become larger and larger. As the growth direction and growth rate are predetermined by the setup, only those grains survive and continue to grow, which have the most favorable orientation with respect to the growth direction, i.e. the vertical direction. The most favorable orientation is the crystallographic [100] or [110] axis, as the growth rate in this direction is enhanced compared to that in [001] direction¹². Therefore, it is not surprising that the remaining single crystal at the end of a boule shows [100] or [110] orientation along the grown rod and [001] orientation in radial direction (Figure 3.6 (d, e)). This grain selection is a slow process and diminishes the utilizable part of a boule. The slow elimination of a smaller grain on the surface of the boule is also visible in Figure 3.6 (c). The remaining grain has a (001) facet on the end of the rod. Of course, the natural grain selection can be forced by tapering the crystal to small diameters, which has also been tested in this thesis. The use of monocrystalline seed rods was successful in the $\text{La}_{2-x}\text{Sr}_x\text{CuO}_4$ compounds, where the grown crystals have immediately adopted the [100] orientation of the seed.

At the electron doped 214 compounds, however, it was not possible to benefit from the predefined orientation of the monocrystalline seed and a multiple nucleation occurs at the beginning, as it is very difficult to find the exact amount of flux and growth parameters from beginning. In general, the growth experiments have shown that the growth along the crystallographic [001] axis is reduced with increasing doping, resulting often in a coexistence of several plate like grains within a rod. In this case the separation of the different grains using a polarizing microscope and a wire saw is a time consuming and difficult task. The frequent appearance of two or more coexisting grains with a slightly different orientation throughout the whole rod is a serious problem of this method and cannot be avoided by simple means.

After conversion of all polycrystalline material, the growth process is finished by a slow cooling of the melt and the simultaneous separation of both rods, the crystal boule and the remaining feed end. The residual flux is thereby crystallized eutectically (Figure 3.6 (c)). In order to improve the crystal quality, the influence of the Ce doping on the growth parameters has to be investigated for the whole doping range of a 214 system. All parameters for $\text{Nd}_{2-x}\text{Ce}_x\text{CuO}_4$ and $\text{Pr}_{2-x}\text{Ce}_x\text{CuO}_4$ are summarized in Table 3.2 and 3.3.

The adjustment of the oxygen partial pressure p_{O_2} of the growth atmosphere to

¹¹Nevertheless, it is important to prepare feed rods of high density as otherwise the whole liquid would be absorbed.

¹²The different growth rates between in-plane and out-of-plane direction are also reflected in the plate like shape of cuprate crystals when grown in crucibles.

compound	doping x	atmosphere	pressure	flow rate	power
$\text{Nd}_{2-x}\text{Ce}_x\text{CuO}_4$	0	O_2	4 – 5 bar	0.2 l/min	70 %
	$0 < x \leq 0.15$	8 % O_2 / 92 % Ar	3 – 4 bar	0.2 l/min	64 %
	$x > 0.15$	3 % O_2 / 97 % Ar	3 – 4 bar	0.2 l/min	63 %
$\text{Pr}_{2-x}\text{Ce}_x\text{CuO}_4$	0	O_2	4 – 5 bar	0.2 l/min	68 %
	$0 < x \leq 0.08$	8 % O_2 / 92 % Ar	3 – 4 bar	0.2 l/min	58 %
	$x > 0.08$	1 % O_2 / 99 % Ar	3 – 4 bar	0.2 l/min	57 %

Table 3.2: Summary of the used growth atmospheres. The choice of an appropriate atmosphere is the most important parameter and depends on the doping x. It affects the oxygenation and the temperature of the floating zone. A gas flow rate of 0.2 l/min and an excess pressure of 3 – 5 bar is used, in order to suppress CuO evaporation from the melt. The growth temperature is given by the percentage of the output power of the lamps (100 % corresponds to $4 \cdot 300$ W).

the Ce concentration of the crystal results in a quantum leap for the improvement of the crystal quality. In literature the doping independent growth in pure oxygen atmospheres [26, 95, 96] is often proposed, but also growth studies in a pure Ar environment and Ar/ O_2 mixtures for certain doping levels are reported [90, 107–109]. In contrast to the floating zone growth of silicon single crystals, where inert atmospheres of Ar or Ar/ H_2 are used in order to avoid oxygen impurities [105], such atmospheres cannot be the solution for single crystals based on copper oxides. Crystals grown in pure Ar show a strong tendency to form inclusions and segregations of the component phases and they decompose after only a short time [107, 109]. The use of a pure oxygen atmosphere, however, is only adapted successfully for the undoped parent compounds Pr_2CuO_4 and Nd_2CuO_4 , where Ar/ O_2 mixtures of any composition cause a nonuniform dissolution and crystallization behavior resulting in unstable solvent zones. In this case, the molten zone has an oxygen deficiency and the segregation of metastable LnCuO_2 , rare earth oxides and Cu_2O phases occurs. The formation of the floating zone for Nd_2CuO_4 using atmospheres of 1 % O_2 in Ar and pure O_2 is shown in Figure 3.7. Interestingly, the situation is opposite for the doped 214 crystals and hence, with increasing doping, p_{O_2} has to be lowered.

These experimental facts provide a clear indication of a Ce-assisted increased oxygen solubility in the molten zone¹³, which causes the segregation of Ln_2O_3 and CeO_2 particles at the crystallization interface. These precipitations do not only deteriorate the grown crystal but also affect strongly the stability of the floating zone, inhibiting thereby a long-lasting growth experiment. The precipitation of rare earth oxide particles due to an additional oxygen enrichment from the surrounding gas phase could also explain the inhomogeneous Ce distribution in radial direction with

¹³As the ratio of surface area to volume of the molten zone is relatively high, the oxygenation or reduction of the zone should be very effective.

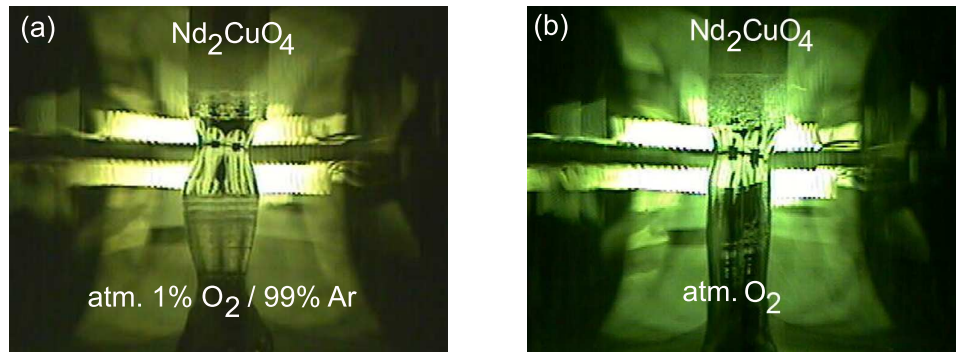


Figure 3.7: By means of real time observation of the floating zone it can be seen how strongly the stability of the vertical melt is influenced by the applied oxygen partial pressure p_{O_2} . For the undoped Nd_2CuO_4 the molten zone is highly unstable in oxygen reduced atmospheres (a) and only in pure O_2 the growth can be performed (b). With Ce doping the situation is vice versa.

higher Ce concentration at the surface of the boules as well as a high effective distribution coefficient of Ce [108, 109], and the slow decomposition of the grown crystals after a longer time, when grown in a pure oxygen atmosphere. Figure 3.6 (f) illustrates the decomposition of a $\text{Nd}_{1.87}\text{Ce}_{0.13}\text{CuO}_4$ boule grown in an atmosphere of 20 % O_2 in Ar at a pressure of 2 bar. Although the boule consists of only two grains and the crystal matrix looks promising at the first view, the crystal has started decomposing after a few weeks due to unstable rare earth segregations. In addition, by means of EDX¹⁴ analysis a slight inhomogeneity in the Ce distribution has been found.

Apart from a suitable, doping dependent growth atmosphere, a pressure of 3–4 bar at a constant gas flow of 0.2 l/min is applied in order to suppress Cu evaporation from the solvent. Nevertheless, a small amount of Cu evaporates and coats the quartz tube, as the vapor pressure of CuO is fairly high at these growth temperatures. The application of even higher pressures leads to an unfavorable thermal convection within the atmosphere and an augmented heat transport away from the floating zone region, causing therefore additional problems in the temperature distribution of the floating zone in radial and vertical direction and hence, its stability is reduced. A simple estimation from the measured weight loss of the whole system after the growth process on overdoped $\text{Nd}_{1.83}\text{Ce}_{0.17}\text{CuO}_4$, where the evaporation was at highest, shows that the change of the flux composition is smaller than 2 mol %. This means that the composition of the molten zone shifts only slightly towards the peritectic point and the evaporation problem can easily be balanced by the flux itself. A compensation of this evaporation by means of feed rods comprising a surplus of 1 – 2 mol % CuO has been suggested in literature [60, 95]. Growth experiments, however, show clearly that the CuO surplus complicates the finding of appropriate growth parameters at the beginning, and several readjustments have

¹⁴EDX is the abbreviation for Energy Dispersive X-ray.

to be made during the growth over several days. Readjustments, however, change the obtained equilibrium.

growth rate v	0.50 mm/h
feed, vertical movement v_f	0.10 – 0.20 mm/h
rotation feed / seed R	20 / (15 – 20) rpm
weight of flux pellet m	0.35 – 0.45 g
diameter of starting rods	5 – 6 mm

Table 3.3: Summary of the setup-related growth parameters. Parameters such as the diameter of the starting rods, the corresponding amount of flux and the ratio v_f/v are related particularly to the shape and dimension of the filament of the lamps. Consequently, when using another setup, these parameters might vary.

In addition to an appropriate atmosphere and pressure, which affect strongly the crystallization behavior and hence, the stability of the floating zone, there are additional parameters which are associated with the experimental setup and which are summarized in Table 3.3. The maximum length of the floating zone is limited by the vertical dimension of the image of the planar designed filaments and amounts to about 5 mm. Within this region the temperature can easily be adjusted by radiation power, whereas beyond the filament image the effective temperature decreases rapidly and is also affected by the effectiveness of the thermal conductivity within the melt and the solid. Generally, the thermal conductivity of the melt and of the grown crystal as well as the ratio of heat conduction in the boules to the radiation of heat from the surface of the zone are important factors, which govern the temperature distribution within the floating zone and therefore, the shape of both solid-liquid interfaces. The best growth results are obtained by using feed rods of 5 – 6 mm in diameter, which are elongated during growth by moving the feed to the top with 0.10 – 0.20 mm/h (at a given growth rate of 0.5 mm/h) resulting in a stable floating zone of 4.5 mm in diameter and 4 – 4.5 mm in length and a relatively flat crystallization interface (see Figure 3.6 **(b)** and 3.7 **(b)**). Thicker feed rods lead to a strongly cone-shaped upper solid-liquid interface, as the radial temperature gradient increases. With thinner feed rods the stability and flexibility of the molten zone decrease dramatically, as the length of the zone cannot be longer than its diameter and therefore, the solvent zone must be scaled in vertical direction, as well. Generally, the length of a melt column, which is only held by surface tension against gravitational and centrifugal forces, cannot be larger than its diameter even if the latter forces are neglected [105].

Finally, the applied power of the lamps has to be adjusted carefully to the grown 214 system and the corresponding atmosphere. As DTA measurements have shown, there is a dependency of the peritectic temperature T_P on the oxygen partial pressure p_{O_2} . By taking into account the geometrical dimensions of the system, the above mentioned thermal conductivity as well as radiation effects, one has to ensure that the real temperature of the melt is not too close to T_E and T_P , as small

local temperature fluctuations would favor the formation of rare earth oxide or CuO nuclei.

Concluding this chapter it can be summarized that the challenge in growing 214 compounds consists in finding the appropriate growth parameters, which are all strongly related to each other. Parameters, which are closely related to the setup must be linked to those which are specific of the compound. Only with the right parameters one can obtain crack and inclusion free homogeneous single crystals.

Chapter 4

Characterization of the grown crystals

After the detailed discussion of the doping dependent growth parameters in the previous chapter, the following chapter focuses on the fundamental properties of the electron doped 214 single crystals. Concerning superconductivity of the electron doped cuprates with T' structure an unusual feature is reported in literature [26, 91, 93, 95, 110–114], which is absent in the hole doped compounds: electron doping of the CuO₂ sheets by substituting only tetravalent Ce⁴⁺ for trivalent Ln³⁺ is not sufficient in order to induce superconductivity. An additional annealing step at high temperatures in oxygen poor atmospheres is required in order to make the crystals superconductive. The impact of this oxygen reduction step on the crystal structure as well as on their physical properties such as superconductivity, Néel temperature, transport properties etc. is up to now controversially discussed [26, 78, 79, 87, 94, 113, 115–122].

As oxygen co-doping poses a problem for all cuprate solid solutions (as well as for the hole doped La_{2-x}Sr_xCuO_{4+δ}) and the real charge carrier concentration n per Cu ion is difficult to determine unambiguously, the phase diagrams in this thesis are plotted over the dopant concentration x . Thereby, one must be aware of the fact that the dopant concentration x of Ce or Sr can differ slightly from the real doping level n or p of the crystal.

In this chapter an improved annealing treatment as well as the role of the oxygen in the crystal as a source of co-doping or disorder are discussed. For this purpose the overall value of the oxygen content of as grown and annealed single crystals is determined by TG measurements and the microscopic distribution is analyzed by magnetization measurements.

4.1 The annealing treatment of the grown crystals

The annealing treatment of the 214 single crystals after the growth process has two effects: Firstly, it reduces tensions in the crystal as well as disorder in the rare

earth sublattice and secondly, the oxygen content can be adjusted depending on the annealing parameters. Unlike in $\text{YBa}_2\text{Cu}_3\text{O}_{7-\delta}$ and the rare earth 123 superconductors, where the oxygen content can be continuously varied within the interval $\delta = [0, 1]$ (see discussion in Chapter 2.2 and the references therein), in the 214 crystals only a tiny amount of oxygen in the range of $\delta = 0.02 - 0.06$ can be removed/added without decomposition [94, 95, 112, 123]. Nevertheless, this small amount of oxygen affects strongly the Néel temperature as well as the transition temperature in the superconducting state [94, 95], although the doping is primarily governed by the Ce substitution.

In the past many annealing experiments were carried out in order to improve T_c in the superconducting state [26, 93–96, 111, 115, 124]. Nevertheless, it was not possible to give a clear answer to fundamental questions such as the onset, shape and doping range of the superconducting dome, the overall oxygen content of as grown and annealed samples and the reversibility of the reduction step. The general consensus of all these studies is that bulk superconductivity and sharp transition curves are only obtained by a severe reduction treatment very close to the stability limit of the compounds.

In order to verify the different results the whole sample set of $\text{Nd}_{2-x}\text{Ce}_x\text{CuO}_4$ and $\text{Pr}_{2-x}\text{Ce}_x\text{CuO}_4$ is annealed in the following way: as grown single crystals are annealed for 20 h in an atmosphere of flowing Ar 4.8 ($\text{O}_2 \leq 3$ ppm) gas at constant temperatures close to the stability limit. The used temperatures depend on the doping and the rare earth element Ln and is plotted in Figure 4.1 (a). For higher

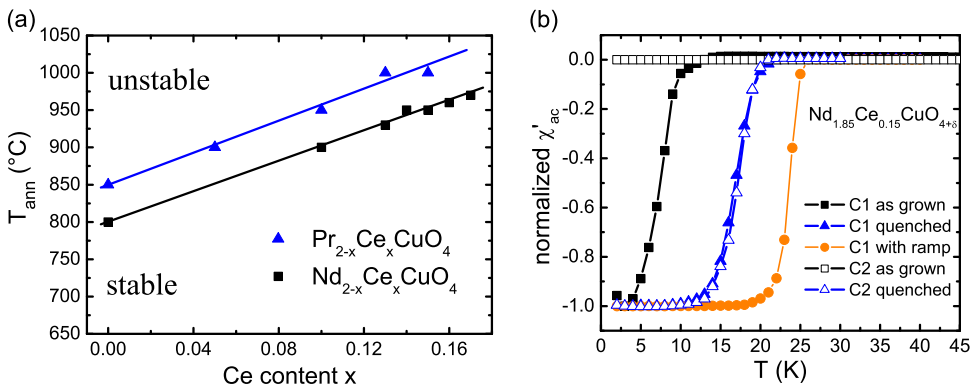
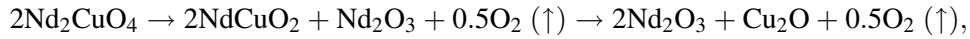


Figure 4.1: (a) Doping dependent annealing temperatures T_{ann} applied to the 214 systems $\text{Nd}_{2-x}\text{Ce}_x\text{CuO}_4$ and $\text{Pr}_{2-x}\text{Ce}_x\text{CuO}_4$. All crystals are annealed in a flow of pure Ar 4.8 ($\text{O}_2 \leq 3$ ppm) for 20 h. Under these conditions crystals start decomposing partially when T_{ann} is greater than the temperature, marked by the solid lines. (b) Normalized transition curves of $\text{Nd}_{1.85}\text{Ce}_{0.15}\text{CuO}_4$ single crystals of two different batches. Superconducting behavior in the as grown state is found in the batch C1, grown in a low oxygen atmosphere of $p_{\text{O}_2} = 0.03$ bar, whereas batch C2, grown as described in Chapter 3.3.2, is not superconducting. Crystals quenched to room temperature after the standard annealing show broader and lower transitions curves (open triangle Δ and closed triangle \blacktriangle) compared to those which are cooled down with moderate cooling rates (closed circle \bullet).

temperatures more distant from the marked solid lines, the crystals start decomposing into the corresponding rare earth oxides and a cuprite phase. The undoped Nd_2CuO_4 , for example, decomposes according to the following equation



where NdCuO_2 is metastable. This phase decomposition can clearly be detected by X-ray powder diffraction as shown in Figure 4.2 for a Nd_2CuO_4 single crystal, which was annealed at 1000°C .

For the annealing treatment the crystals are enclosed in polycrystalline crucibles of the same material in order to provide a homogeneous environment and to protect the crystal surface. After the dwell time of 20 h the crystals are cooled down to room temperature with moderate cooling rates of $50 - 100^\circ\text{C/h}$. The quenching from high temperatures [95] might induce new tension into the crystal lattice resulting in considerably broader and lower transition curves, as one can see in Figure 4.1 (b).

It is also reported that the annealing treatment depends on the sample size [26, 95], and that a subsequent annealing after the reduction step in pure O_2 at moderate temperatures of $500 - 600^\circ\text{C}$ for 10 h increases T_c [26, 93, 115]. For the cut crystals with a typical weight in the range of $50 - 250$ mg, there is no size effect observable in the transition curves, confirming therefore that the oxygen diffusion coefficient $D(T)$ and hence, the diffusion length $l = \sqrt{D(T)t_{ann}}$, is large enough at the applied annealing temperatures. In addition, a short O_2 treatment at moderate temperatures complicates the control of the oxygen content and its microscopic homogeneity within the crystal, as $D(T)$ might vary by some orders of magnitude at

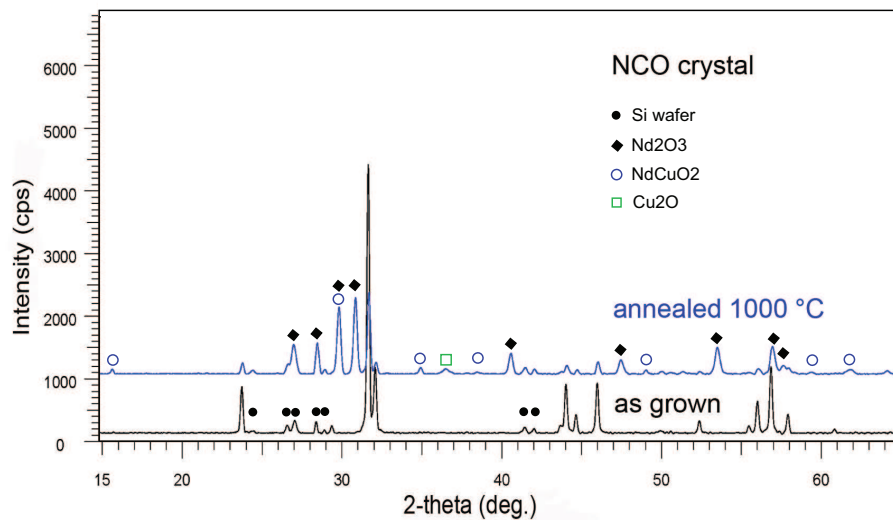


Figure 4.2: X-ray powder diffraction of an as grown and annealed Nd_2CuO_4 single crystal. The annealing at a temperature of 1000°C leads to the partial decomposition of the crystal into Nd_2O_3 , Cu_2O and the metastable NdCuO_2 phase.

these high and moderate annealing temperatures¹. As there are no reliable studies concerning the kinematics of the oxygen diffusion process for the 214 systems, the interpretation of annealing experiments under different atmospheres, temperatures and time scales is speculative. Diffusion studies on single crystals using TG analysis failed due to sensitivity problems, as the oxygen variation per formula unit is in the range of $\delta = 0.02 - 0.04$. Studies on large ceramic samples [123] are misleading, since the in- and out-diffusion is governed by grain boundaries, micro-cracks and other imperfections in the samples.

Hence, the annealing parameters are optimized in a way that the crystals show doping dependent sharp transition curves, as depicted in Figure 4.3. Another experimental observation disagrees with many publications [26, 93, 122] but might be of importance, when trying to understand the role of the reduction treatment and the related appearance of superconductivity:

As grown, optimally doped $\text{Nd}_{1.85}\text{Ce}_{0.15}\text{CuO}_4$ crystals are already superconducting with a broad transition with $T_c < 10$ K, when grown in an atmosphere of low oxygen partial pressure of $p_{\text{O}_2} = 0.03$ bar. However, $\text{Nd}_{1.85}\text{Ce}_{0.15}\text{CuO}_4$ crystals grown in atmospheres as described in Chapter 3.3.2 are not superconducting (compare the transition curves in Figure 4.1 for the crystal batches C1 and C2). Unfortunately, for atmospheres with low p_{O_2} the CuO evaporation is high and the growth process is not stable enough resulting in crystals with medium quality. As grown $\text{Pr}_{2-x}\text{Ce}_x\text{CuO}_4$ crystals are not superconducting even at low p_{O_2} .

4.2 The superconducting properties of $\text{Nd}_{2-x}\text{Ce}_x\text{CuO}_4$ and $\text{Pr}_{2-x}\text{Ce}_x\text{CuO}_4$

So far, the shape and the doping evolution of the transition temperature T_c could only be determined roughly [94, 96, 126]. In contrast to the hole doped compounds there is no doping interval, in which the superconducting dome of the different electron doped compounds coincides. The doping levels, where superconductivity first appears, as well as the doping range in which superconductivity is established, differ slightly depending on the rare earth composition of the 214 compounds.

4.2.1 Transition curves of 214-cuprates

The doping dependent transition curves for $\text{Nd}_{2-x}\text{Ce}_x\text{CuO}_4$ and $\text{Pr}_{2-x}\text{Ce}_x\text{CuO}_4$ are illustrated in Figure 4.3. The superconducting transition is obtained by measuring

¹From diffusion studies of $\text{YBa}_2\text{Cu}_3\text{O}_{7-\delta}$ and rare earth RE-123 crystals it is well known that $D(T)$ varies over several orders of magnitude [125]. Certainly, the O_2 diffusion in $\text{YBa}_2\text{Cu}_3\text{O}_{7-\delta}$ occurs along the CuO chains and the residual crystal, such as the CuO_2 planes, remains unaffected. Thus, results from $\text{YBa}_2\text{Cu}_3\text{O}_{7-\delta}$ cannot directly be applied to the 214 crystals, where the diffusion seems to be a three dimensional process, and where much higher temperatures must be applied in order to activate the oxygen diffusion.

the ac-susceptibility² of the annealed crystals in an oscillating field of $\mu_0 H_{osc} = 5 \cdot 10^{-4}$ T with a frequency of 19.8 Hz. From the transition curves the superconducting dome as a function of Ce content x is derived and plotted in Figure 4.3 (b) and (d). The midpoint of the transition curve (drop of 50 %) is taken as T_c (closed squares) and the transition widths, defined as $\Delta T_c = T_c(90\%) - T_c(10\%)$, are illustrated by the vertical bars.

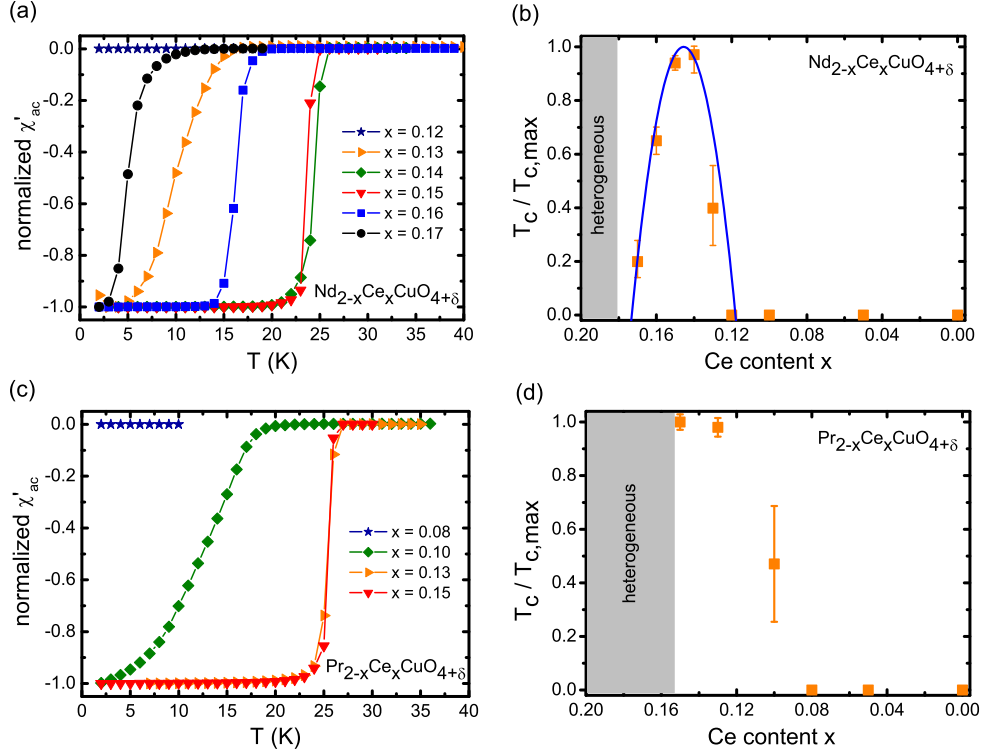


Figure 4.3: Transition curves obtained from ac-susceptibility measurements ($\mu_0 H = 5 \cdot 10^{-4}$ T) on $\text{Nd}_{2-x}\text{Ce}_x\text{CuO}_4$ (a) and $\text{Pr}_{2-x}\text{Ce}_x\text{CuO}_4$ (c) single crystals. The crystal weight varies from 100 to 250 mg. Because of demagnetization effects the diamagnetic susceptibilities are set to unity for a better comparison. The derived superconducting dome for both compounds is illustrated in (b) and (d), respectively. Note the common notation of the x-axis: x is plotted to the left for electron doping, whereas for hole doping, x is plotted to the right. The closed squares denote T_c at 50 % of the transition normalized to $T_{c,max}$. The transition width defined as $\Delta T_c = T_c(90\%) - T_c(10\%)$ is given by the vertical bars. The solid line in the $\text{Nd}_{2-x}\text{Ce}_x\text{CuO}_4$ map (b) represents an empirical fit of the overdoped $\text{Nd}_{2-x}\text{Ce}_x\text{CuO}_4$ data according to the quadratic function $T_c/T_{c,max} = 1 - 1317(x - 0.146)^2$. The whole superconducting dome is accessible for $\text{Nd}_{2-x}\text{Ce}_x\text{CuO}_4$ crystals, whereas the $\text{Pr}_{2-x}\text{Ce}_x\text{CuO}_4$ system is limited to the optimally and underdoped region due to the low solubility limit of Ce, which is found to be close to the doping level $x = 0.15$.

²The ac-susceptibility is defined as $\chi_{ac} = \frac{\partial M}{\partial H} = \chi' + i\chi''$. The real part χ' describes the shielding of the sample and amounts to -1 in the superconducting state. The imaginary part χ'' describes the dissipative contribution of the ac-susceptibility in the Shubnikov state.

Compared to previous studies on $\text{Nd}_{2-x}\text{Ce}_x\text{CuO}_4$ single crystals [26, 94, 96] the resolution of the doping dependent evolution of T_c within the superconducting region is improved considerably. The transition widths are small, especially in the optimally doped and overdoped region. In this region, T_c can be well described by the empirical quadratic function $T_c/T_{c,max} = 1 - 1317(x - 0.146)^2$ with $T_{c,max} = 25.1$ K (solid line in Figure 4.3 (b)). According to this fit, T_c peaks at $x = 0.146$ and becomes zero at the Ce doping of $x = 0.118$ and $x = 0.173$. Of course, these experimentally determined doping values might vary within an estimated error of a few %, resulting from the fact that the determination of the exact doping without destroying the crystals by EDX analysis is in the range of 5 %. Nevertheless, the fact that all samples with different doping levels are annealed in the same way (which is important in order to neutralize the contribution coming from the oxygen state) and that the deviation of T_c at a certain doping level of other crystals is in the range of ΔT_c , is a clear hint for the correctness of the determined superconducting dome. From the steep slope on the overdoped side one can also estimate the homogeneity of the Ce distribution within the specimen. For example, a T_c of approximately 5 K with a transition width of $\Delta T_c > 3$ K is expected for a crystal with a nominal doping of $x = 0.17$ and a variation in the homogeneity of only $\Delta x = 0.002$. Hence, it is not surprising that in literature relatively sharp transition curves are only found around the optimal doping, where $\Delta T_c/\Delta x$ is almost zero, whereas for the overdoped and underdoped crystals the transition curves are often very broad. The underdoped region behaves quite differently. Superconductivity suddenly sets in at $x = 0.13$ and T_c increases rapidly to $T_{c,max}$, which is expected at $x = 0.146$. The transition curves are always broad, independent from the annealing treatment, and it is not clear whether this broadening is due to homogeneity problems of the Ce distribution or due to an intrinsic effect. However, problems of homogeneity should be reduced by moving away from the solubility limit and the asymmetry in the superconducting dome might be a hint for influences coming from the neighboring AFM phase. The microscopic behavior at the phase boundary AFM/SC is up to now controversially discussed (see discussion in Chapter 2.3). The $\text{Nd}_{2-x}\text{Ce}_x\text{CuO}_4$ system meets the requirement for probing the whole electron doped phase diagram, as the solubility limit for Ce is beyond the superconducting dome at $x = 0.18$.

The $\text{Pr}_{2-x}\text{Ce}_x\text{CuO}_4$ system is less suitable for a comprehensive study as the lower solubility limit at $x = 0.15$ cuts off the overdoped region. In addition, the AFM/SC transition is shifted to the lower doping level $x = 0.10$, where superconductivity sets in abruptly and the transition curves behave in the same way as for the $\text{Nd}_{2-x}\text{Ce}_x\text{CuO}_4$ system at the doping $x = 0.13$. The optimal doping at $x = 0.15$ coincides approximately with the doping of the $\text{Nd}_{2-x}\text{Ce}_x\text{CuO}_4$ and $\text{Sm}_{2-x}\text{Ce}_x\text{CuO}_4$ system and a trend towards lower transition temperatures is clearly visible (Figure 4.4), when rare earth cations with increasing ionic radius are used. The broader superconducting region in $\text{Pr}_{2-x}\text{Ce}_x\text{CuO}_4$, which becomes already apparent when comparing the slope of the $T_c(x)$ curve in the underdoped regime of both compounds, is also found in the related system $\text{LaPr}_{1-x}\text{Ce}_x\text{CuO}_4$ [126, 127].

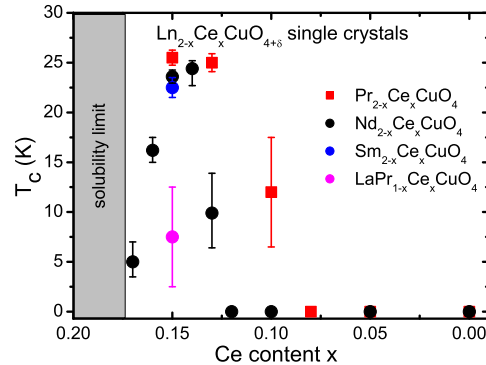


Figure 4.4: Summary of the critical temperatures T_c and transition widths ΔT_c as a function of the Ce doping x for all grown electron doped 214 compounds. There is a trend to lower transition temperatures when using rare earth cations with increasing ionic radius. The compound $\text{LaPr}_{1-x}\text{Ce}_x\text{CuO}_4$ has an extended superconducting region with its maximum T_c around the doping level 0.10 [126, 127]. Crystals with $x = 0.15$ are already far overdoped with a T_c below 10 K.

$\text{LaPr}_{1-x}\text{Ce}_x\text{CuO}_4$ has the advantage that the doping level with highest T_c is shifted to $x = 0.10$, avoiding therefore the Ce solubility problems in the overdoped region. Indeed, a grown $\text{Pr}_{0.85}\text{LaCe}_{0.15}\text{CuO}_4$ rod (Figure 4.4) shows broad transition curves with a T_c of only 7.5 K, whereas $T_{c,max}$ amounts to 26 K for $x \approx 0.10$ [127], which is equal to $T_{c,max}$ of $\text{Pr}_{2-x}\text{Ce}_x\text{CuO}_4$ at $x = 0.15$. Although $\text{LaPr}_{1-x}\text{Ce}_x\text{CuO}_4$ is characterized by a broader overdoped region, which is also accessible with single crystals, the growth of this sample set was not performed for a simple reason: the microscopic homogeneity of the metal sublattice might suffer from the additional substitution of the La^{3+} sites by Pr^{3+} cations. Concerning the superconducting dome the inconsistent published results [126, 127] clearly reveal the homogeneity problems of this system. In addition, the difference in the shape and doping range of the $T_c(x)$ curves for $\text{Nd}_{2-x}\text{Ce}_x\text{CuO}_4$ and the Pr based 214 compounds cannot only be explained by the modality of the reduction step and the appearance of a related, epitaxially grown $(\text{Ln,Ce})_2\text{O}_3$ impurity phase (see Chapter 4.3), as the performed annealing treatment is identical for both systems and all doping levels. The appearance of superconductivity already at lower doping x in the Pr based 214 compounds is a clear material specific issue and might arise from a small Pr co-doping, although X-ray analysis shows that the Pr cation is trivalent.

4.2.2 Testing bulk superconductivity

For the $\text{Nd}_{2-x}\text{Ce}_x\text{CuO}_4$ sample set bulk superconductivity is reported within the doping range $0.14 \leq x \leq 0.17$ [96]. The measurement of shielding curves³ can

³Shielding curves correspond to the zero-field-cooled (ZFC) recorded magnetization measurements. For that purpose the sample is cooled down in a zero field below T_c and the magnetic field is turned on afterwards.

be misleading, as in principle a small, closed superconducting skin around a non-superconducting core is sufficient in order to screen the whole interior, resulting in a nearly perfect diamagnetic response. A non-uniform reduction of the core and shell [26] as well as the appearance of two superconducting phases with different T_c due to the annealing treatment [95] can be excluded for all doping levels. Susceptibility measurements on annealed cylindrical crystal boules and on small pieces cut from the interior of the same cylinder show clearly the same transition behavior and are compared with each other for $\text{Pr}_{1.85}\text{Ce}_{0.15}\text{CuO}_4$ in Figure 4.5 (a). The Meissner fraction, determined from the field-cooled (FC) magnetization measurement via the relation $f_M = -M_{FC}/H_a \cdot 100\%$, amounts to 72 % for $\text{Pr}_{1.85}\text{Ce}_{0.15}\text{CuO}_4$. The determination of the Meissner fraction on high temperature superconductors is not straightforward, as the measurement depends on many factors, such as vortex-pinning, size effects and the strength of the applied magnetic field H_a [128]. In general, deviations from the perfect diamagnetic value as well as broader superconducting transition curves are not related a priori to the real superconducting fraction and the homogeneity of the sample. As the 214 systems are type-2 superconductors, flux pinning might play an important role in determining f_M . Hence, f_M is larger for powdered samples than for single crystals [93], and it decreases with increasing external fields. Values close to unity in $\text{La}_{2-x}\text{Sr}_x\text{CuO}_4$ high quality crystals are only reported for very small fields of $\mu_0 H < 10^{-4}$ T [128]. In addition, the sample size influences the magnetization measurements due to the demagnetization effect. Figure 4.5 (b) illustrates the obtained FC and ZFC curves for a $\text{Pr}_{1.85}\text{Ce}_{0.15}\text{CuO}_4$ single crystal slab in a dc field of $5 \cdot 10^{-5}$ T applied in c direction. The expected perfect diamagnetism of $\chi = -1$ is marked by the horizontal line. As already mentioned above, the Meissner fraction is diminished by

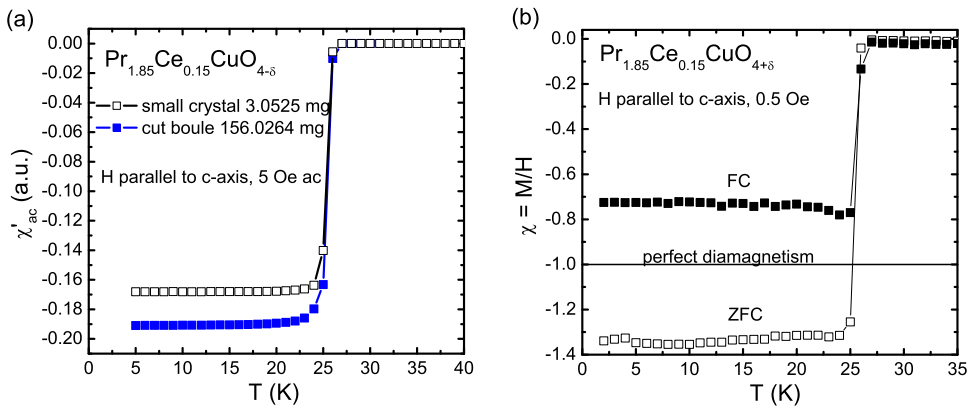


Figure 4.5: (a) Susceptibility measurements on a cut boule of a $\text{Pr}_{1.85}\text{Ce}_{0.15}\text{CuO}_4$ rod and on a small bar from the interior of the same piece. There is no evidence for a core/shell effect due to a non-uniform reduction. The crystals are perfectly homogeneous. (b) Meissner (FC) and shielding curve (ZFC) of a $\text{Pr}_{1.85}\text{Ce}_{0.15}\text{CuO}_4$ slab ($a \times b \times c = 1 \times 1 \times 0.5 \text{ mm}^3$) at an applied field of $\mu_0 H_a = 5 \cdot 10^{-5}$ T in c direction. The Meissner fraction amounts to 72 %.

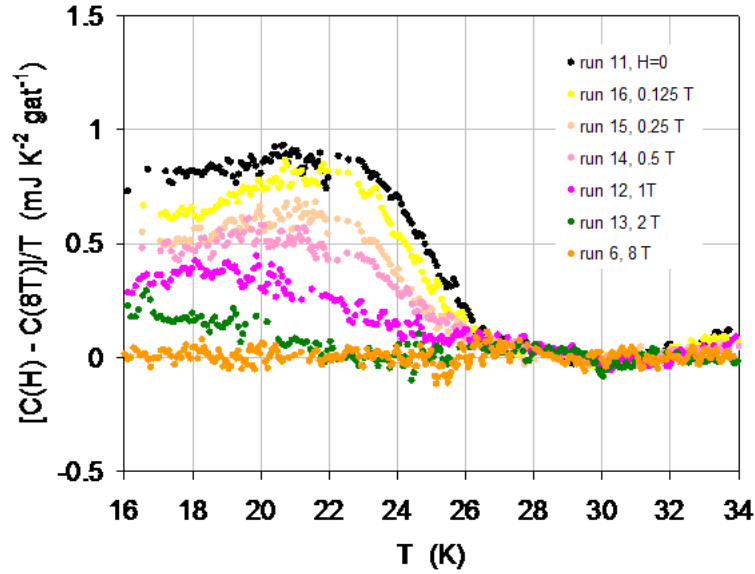


Figure 4.6: Specific heat measurement on a $\text{Pr}_{1.85}\text{Ce}_{0.15}\text{CuO}_4$ single crystal (100.5 mg). $\Delta C/T$ is plotted against the temperature T . The field is applied in c direction. The high field data at $H = 8$ T, where superconductivity is fully suppressed, is used as background. A jump with onset point at $T = 26$ K is clearly visible. For comparison, the corresponding transition curves obtained from susceptibility measurements are shown in Figure 4.5. (The specific heat measurement was performed by A. Junod, Geneva).

28% whereas the shielding signal is larger than the expected value, which can be explained by the demagnetization effect.

An appropriate, but very complex experimental method to test the bulk superconductivity is the measurement of the specific heat change at T_c due to the difference in the free energy between the superconducting and the normal state. Thereby, the problem for high temperature superconductors is primarily given by the dominating phononic contributions to the specific heat of the system at T_c as well as by a significant contribution from unpaired electrons even at low temperatures, due to the nodes in the energy gap Δ . The electron doped 214 compounds, however, have moderate upper critical fields H_{c2} when the magnetic field is applied perpendicular to the CuO_2 sheets. For $\text{Pr}_{1.85}\text{Ce}_{0.15}\text{CuO}_4$, $\mu_0 H_{c2}$ amounts to 8 T (estimation from resistivity curves) and the curve recorded at this field is used as background. Curves at lower and zero field are subtracted from the normal state curve at 8 T in order to eliminate the normal state contribution to the specific heat

$$\Delta C = C_S - C_N = C(H) - C(8 \text{ T}) . \quad (4.1)$$

In Figure 4.6 $\Delta C/T$ is plotted against T . Starting at $T \simeq 26$ K an increase in $\Delta C/T$ of approximately $1 \text{ mJ}/(\text{K}^2 \text{gat})$, which corresponds to $7.0 \text{ mJ}/(\text{K}^2 \text{mole})$, is clearly visible. For comparison, the total specific heat of the sample amounts to $304.50 \text{ mJ}/(\text{K}^2 \text{mole})$ at a temperature of 28 K.

The measured value for $\Delta C/T$ is about 13 % higher than the value for optimally doped $\text{Pr}_{1.85}\text{Ce}_{0.15}\text{CuO}_4$ reported in literature [129]. $\Delta C/T_c$ has been found to amount to 6.1 mJ/(K²mole), from which a condensation energy E_c of 568 mJ/mole was calculated, which corresponds to only 70 % of the BCS d-wave prediction.

4.3 X-ray analysis

X-ray powder diffraction confirms the phase purity and T' structure of the grown $\text{Nd}_{2-x}\text{Ce}_x\text{CuO}_4$ and $\text{Pr}_{2-x}\text{Ce}_x\text{CuO}_4$ single crystals. The diffraction pattern for the undoped and optimally doped 214 crystals is shown in Figure 4.7. The lattice constant c of the tetragonal unit cell decreases linearly with increasing doping x . Between undoped and optimally doped crystals the contraction in c amounts to 7.5 ‰ and 6.5 ‰ for $\text{Nd}_{2-x}\text{Ce}_x\text{CuO}_4$ and $\text{Pr}_{2-x}\text{Ce}_x\text{CuO}_4$, respectively (see Figure 4.8). The linear decrease of c as a function of the doping x is interpreted as evidence for the oxidation state of 4 of the dopant, since the ionic radius of the tetravalent Ce is smaller than the radius of the corresponding trivalent rare earth ions [80, 130, 131]. In principle, one can use this linear relationship for estimating the doping concentration in a grown crystal. Further evidence for the formal Ce oxidation state of 4 rather than 3 was derived from X-ray absorption spectroscopy (XAS) studies [132]. Interestingly, the in-plane lattice parameter a increases slightly with doping (≈ 1 ‰), although one would expect a steady decrease for the same considerations of the ionic radius size. This lengthening of a might result from the weakening of the Cu-O bond due to electron doping into the CuO_2 sheets. The Cu-O bonds have

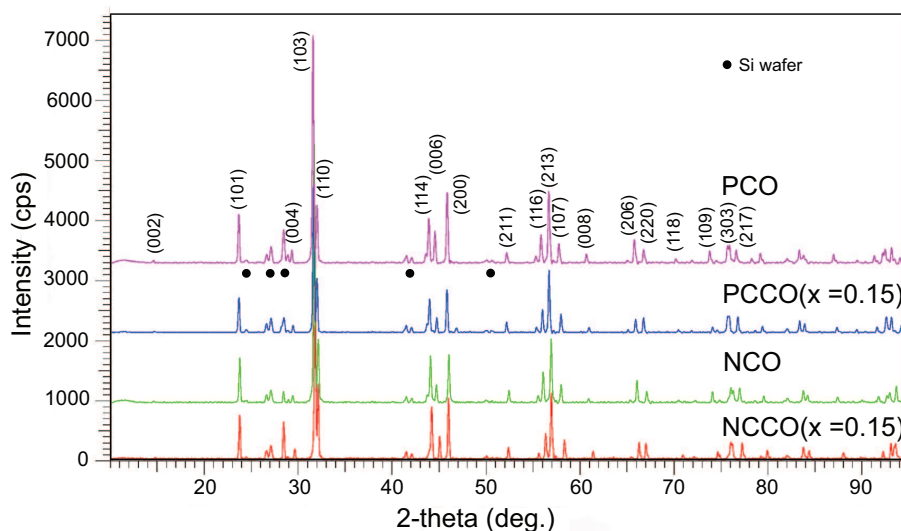


Figure 4.7: X-ray diffraction pattern ($2\theta - \theta$ scan) of grinded as grown single crystals, confirming the tetragonal T' structure and the phase purity of the grown crystals.

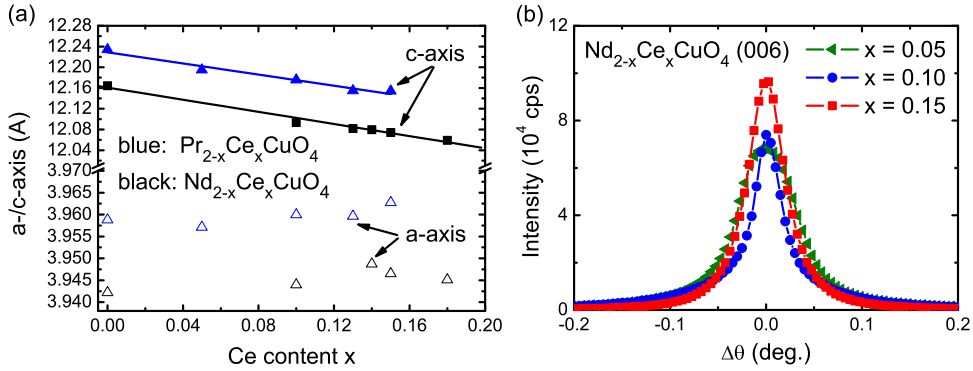


Figure 4.8: (a) Doping dependent evolution of the lattice parameters a and c , obtained from X-ray powder diffraction on as grown single crystals of the $\text{Pr}_{2-x}\text{Ce}_x\text{CuO}_4$ and $\text{Nd}_{2-x}\text{Ce}_x\text{CuO}_4$ sample set. The lattice constant c decreases linearly with increasing doping, which is interpreted as an evidence for the oxidation state Ce^{4+} of the dopant [80]. The lattice parameter a increases slightly with increasing doping. (b) X-ray (006) rocking curves for $\text{Nd}_{2-x}\text{Ce}_x\text{CuO}_4$ single crystals with a full width at half maximum (FWHM) of less than 0.08° .

antibonding $\sigma_{x^2-y^2}^*$ character and thus, doped electrons are added into the antibonding band orbital, causing therefore the weakening of the Cu-O bonds [28, 131]. The elimination of electrons from the CuO_2 sheets (hole doping) strengthens the CuO bond (i.e. shortens the bond length), as electrons from the antibonding orbital are removed. This implies that electron doping is favored in the T' structure, whereas hole doping is found in the T structure. Concerning the mosaicity as a measure of crystal quality, rocking curves for both systems of different doping levels have been recorded. Figure 4.8 (b) shows the (006) curves for $\text{Nd}_{2-x}\text{Ce}_x\text{CuO}_4$. The full width of half maximum (FWHM) of the (006) reflex is less than 0.08° , which is the lowest value reported so far.

The annealing treatment does not influence the lattice parameters and the rocking curves, but can cause the intergrowth of a small $(\text{Ln,Ce})_2\text{O}_3$ impurity phase [26, 122]. The volume fraction of the impurity phase depends on the annealing treatment and is roughly estimated to be in the range of $\leq 1\%$ [26]. Additional peaks after annealing were detected at first in systematic neutron scattering experiments and were attributed to coherent atomic displacements and oxygen vacancy superstructures [95]. However, it could be shown [26] by means of systematic X-ray and neutron scattering that the additional peaks can be assigned to a parasitic $(\text{Ln,Ce})_2\text{O}_3$ phase, which grows epitaxially in $[110]$ direction onto the CuO_2 layers. The $(\text{Ln,Ce})_2\text{O}_3$ phase has a cubic bixbyite structure (C-type) with a lattice constant of $a_c \approx c/1.1 \approx a2\sqrt{2}$. Because of the nearly perfect in-plane lattice matching of the cubic lattice constant (subscript c) and the diagonal of the CuO_2 planes (Figure 4.9 (a)), but a mismatch of $\approx 10\%$ in c direction, the growth of the parasitic phase is almost two-dimensional. Typical values for the in-plane and out-of-plane dimensions of the parasitic phase amount to $1\ \mu\text{m}$ and a few unit cells,

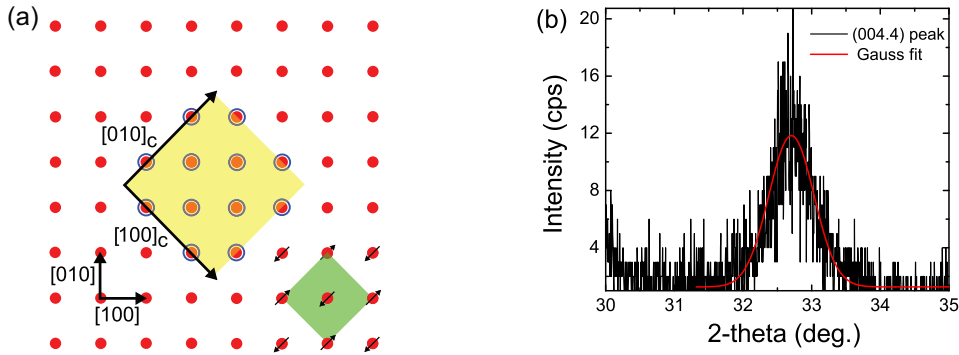


Figure 4.9: (a) Illustration of the epitaxial intergrowth of the $(\text{Ln,Ce})_2\text{O}_3$ phase onto the CuO_2 plane. Note, that for clarifying reasons only the Cu^{2+} ions are shown (red dots). The unit cell of the parasitic phase is highlighted as yellow diamond. For comparison the magnetic unit cell is illustrated as well (green diamond). (b) (004.4) reflex of the epitaxial intergrown parasitic phase. From the full width at half maximum (FWHM) of the Gauß fit a thickness of 13 nm in the out-of-plane direction is estimated.

respectively [26]. An estimation of the real thickness d of the parasitic phase can be obtained from the full width at half maximum (FWHM) of the additional broad peaks by using the Scherrer relation [133]:

$$d = \frac{K \cdot \lambda_{\text{Cu}, K\alpha}}{\text{FWHM} \cdot \cos \theta}, \quad (4.2)$$

where $K = 0.94$ is the Scherrer constant, $\lambda_{\text{Cu}, K\alpha} = 0.154056$ nm is the X-ray wavelength and θ the diffraction angle at the maximum of the peak. The impurity peaks are well fitted with a Gauß function (Figure 4.9 (b)), from which the value of the FWHM is determined. The calculated thickness d , derived from the (004.4) and (008.8) peaks, amounts to 13 nm, which is in good agreement with reported averaged values of 8 nm and 6 nm [26], respectively. Note, that in the Scherrer formula the values for the FWHM are given in radian. As the FWHM values of the peaks are in the range of $0.7^\circ - 0.8^\circ$, the influence of the apparatus resolution is negligible.

The in-plane Bragg reflections from the impurity phase appear at commensurate positions, whereas along the c direction the incommensurability increases according to the Miller index transformation $l = 1.1l_c = 0, \pm 1.1, \pm 2.2, \pm 3.3, \dots$ (compare the position of the impurity peaks with respect to the $(00L)$ peaks of the single crystal in Figure 4.10). This incommensurability in the c direction shows clearly that the additional peaks are not due to a three-dimensional superstructure but due to a parasitic phase with the same c orientation but different lattice constant.

Recently, a microscopic model was suggested [122] in order to explain the annealing-assisted formation of the epitaxial intergrowth. According to this model the as grown single crystals have a Cu deficiency of a few percent. Due to the reduction process, oxygen vacancies in the rare earth oxide layers arise, which drive the phase separation into the Cu free C-type rare earth minority phase and the Cu repaired T' majority phase. As a result of a partial decomposition Cu does not segregate within the crystal, but it repairs the vacancies of adjacent CuO_2 layers. Hence, the Cu deficiency must be equal to the volume fraction of the $(\text{Ln,Ce})_2\text{O}_3$

minority phase and the annealing treatment must be fully reversible. In fact, it has been reported [122] that the rare earth interlayer disappears with oxygenation and reappears with reduction. Surprisingly, the stability of the T' structure seems to be uncritical against a small amount of Cu and oxygen deficiency due to the strong three-dimensional interconnections of the rare earth-oxygen sublattice.

The reversibility of the appearance/disappearance of the parasitic phase and – related to this – the occurrence of superconductivity was checked by annealing experiments on an optimally doped $\text{Nd}_{1.85}\text{Ce}_{0.15}\text{CuO}_4$ single crystal. After each annealing treatment a $2\theta - \theta$ scan along the $(00L)$ direction is recorded, which is shown in Figure 4.10. The scan along L is sufficient for identifying unambiguously the parasitic phase, as Bragg reflections are expected at the above mentioned incommensurate positions, whereas X-ray powder diffraction is not sensitive enough. Surprisingly, the additional peaks disappear upon oxygenation and the crystal is not superconducting anymore, confirming therefore the proposed model of a reversible rearrangement within the crystal. In addition, after annealing the appearance of the parasitic phase is found to be independent from doping for most crystals.

Based on this microscopic model an attempt was made in order to explain the impact of oxygen on the physical properties and the appearance of superconductivity in electron doped cuprates [122]. From the ambiguous experimental data, obtained from X-ray diffraction, neutron scattering and TG measurements on $\text{LaPr}_{1-x}\text{Ce}_x\text{CuO}_4$, it was concluded that the Cu deficiency of a few % in the as grown state weakens enormously the electron doping of Ce, whereas the recovery

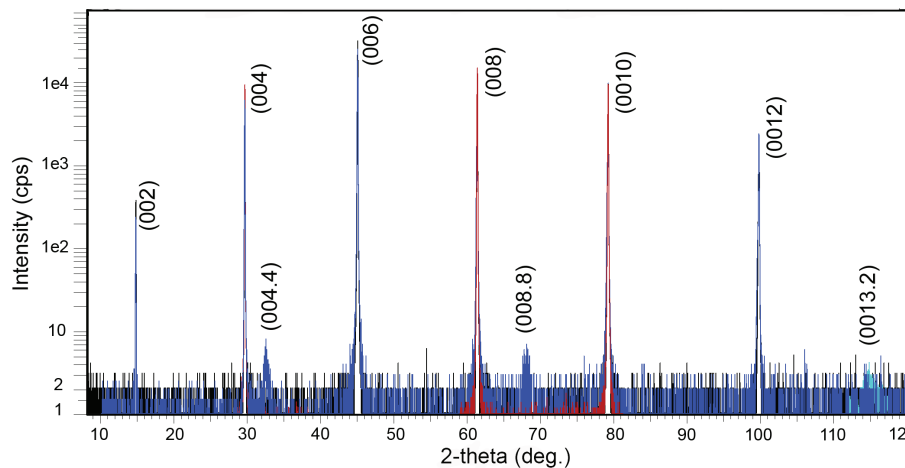


Figure 4.10: X-ray $(00L)$ scan on a $\text{Nd}_{1.85}\text{Ce}_{0.15}\text{CuO}_4$ single crystal after standard annealing (blue curve) and re-oxygenation at 900°C for 20 h in a pure oxygen atmosphere (black and red curve). The red curve represents a scan with an integration time of 10 s around the (008.8) peak, in order to minimize the background. After the reduction step additional broad peaks at the incommensurate positions (004.4) , (008.8) and (0013.2) arise. The corresponding lattice parameter of the impurity phase amounts to $a_c = 1.100\text{ nm} \approx c/1.1$. The intergrowth is fully reversible, as the additional peaks disappear with re-oxygenation.

of the full occupation of the Cu site promotes the electron number in the CuO_2 sheets. In addition to this doping effect of the annealing treatment, the healing out of Cu vacancies might increase the charge carrier mobility as these point defects break the translation symmetry of the CuO_2 planes and therefore, charge carriers are scattered effectively on these impurities. Simultaneously, in comparison to the as grown state, an increase of O(1) vacancies was found in the annealed samples, whereas the O(2) site was assumed to be fully occupied. This additional induced disorder in the CuO_2 sheets is inconsistent with the argumentation of increased mobility by repairing the CuO_2 planes. In addition, the datasets, on which this microscopic model is based, are not fully consistent with each other and the tiny deviations from the nominal occupation of the Cu and O(1) site obtained by Rietveld refinement are model dependent and questionable.

4.4 The role of oxygen in electron doped high temperature superconductors

X-ray analysis on a high quality $\text{Nd}_{2-x}\text{Ce}_x\text{CuO}_4$ single crystal confirms the oxygen-driven formation of a rare earth oxide impurity phase, which is absolutely reversible with annealing. The proposed model for the microscopic reorganization seems to be adequate, but its implications on the physical properties are inconsistent. Therefore, for further characterization of the crystals, the crucial overall oxygen content is determined as a function of doping and is compared to the results of [122].

4.4.1 Determination of the oxygen concentration of as grown and annealed crystals

In literature there are contradicting observations of the real overall oxygen content of as grown and annealed crystals. In [123, 134–137] stoichiometric oxygen for the as grown $\text{Nd}_{2-x}\text{Ce}_x\text{CuO}_{4+\delta}$ system (i.e $\delta = 0$) is proposed. In addition, the T' structure is found to be stable against a small oxygen deficiency of a few % due to reduction. For the deviation from stoichiometry an upper limit of $\delta = -0.07$ in $\text{Nd}_2\text{CuO}_{4+\delta}$ was found before decomposition sets in. Simultaneously, oxygenation experiments showed that δ does not become greater than zero [123]. These observations are inconsistent with studies primarily based on neutron diffraction, which have found an excess of oxygen ($\delta \approx 0.1$), which occupies the apical position [78, 79]. The apical oxygen is removed partly during the reduction treatment.

In order to determine the overall oxygen content, TG experiments in combination with X-ray powder diffraction on high quality as grown single crystals were performed. Since, according to the above mentioned studies, the deviation from oxygen stoichiometry is expected to be very small, only crack- and inclusion-free single crystals⁴ of 100 – 200 mg were investigated in order to minimize errors in

⁴A major part of the previous studies was carried out on polycrystalline samples and hence, the real oxygen content of the phase determined by TGA or titration experiments might be misleading due to some contributions arising from grain boundaries and small inclusions. In addition, the re-

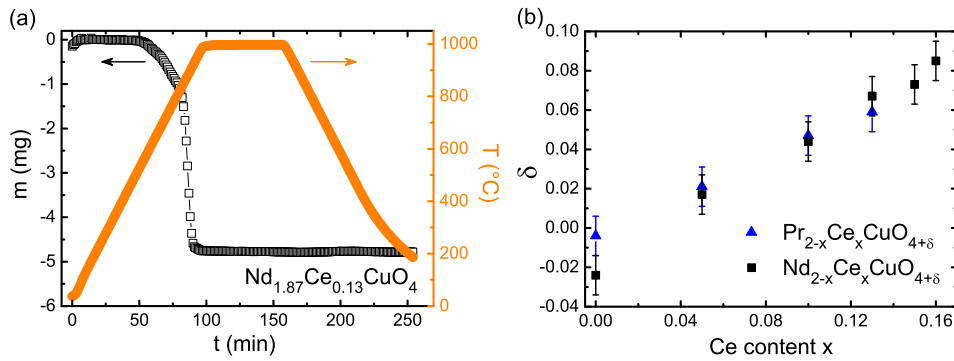
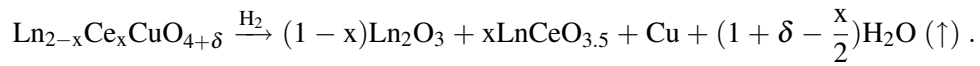


Figure 4.11: (a) Illustration of the TG experiment carried out on an as grown $\text{Nd}_{1.87}\text{Ce}_{0.13}\text{CuO}_{4+\delta}$ single crystal ($m = 123.182$ mg). The weight loss (open squares) during the reduction in an inert gas flow of $\text{H}_2/\text{N}_2 = 15/85$ for 1 h at 1000°C is recorded, from which the oxygen content of the crystal can be calculated. The used temperature ramps are shown as well (closed squares). (b) Plot of the measured overall oxygen content of the as grown 214 crystals as a function of the Ce content x .

the results. The oxygen content is calculated from the measured weight loss during the reduction in a gas flow of $\text{H}_2/\text{N}_2 = 15/85$ for 1 h at 1000°C . A typical TG measurement is shown in Figure 4.11. The crystals are heated with $10^\circ\text{C}/\text{min}$, held for 1 h at 1000°C and cooled to room temperature with the same rate. The crystals starts decomposing at $\approx 500^\circ\text{C}$ according to the following equation:



Subsequent X-ray powder diffraction clearly confirms the perfect transformation of the 214 phase into elemental copper and the corresponding rare earth oxides. For comparison, the phase transformation for a $\text{Nd}_{1.87}\text{Ce}_{0.13}\text{CuO}_{4+\delta}$ single crystal is illustrated in Figure 4.12. In general, the rare earths form thermodynamically very stable oxides, which cannot be cracked by the used reactive atmosphere and temperature. X-ray analysis has confirmed the valency of 3 for Nd and Pr as well as the valency of 4 for Ce. From the weight of the nonvolatile reaction product one can calculate the oxygen content of the as grown crystal. The corresponding result is plotted in Figure 4.11 (b) for both compounds. Undoped, as grown crystals show nearly stoichiometric oxygen content, which is in good agreement with [123] and in disagreement with neutron data [78]. Upon doping a small oxygen surplus δ is found, which increases linearly with $x/2$. A total error of measurement of $\Delta\delta = \pm 0.01$ is estimated from the uncertainties in measuring the oxygen weight loss. Small variations in doping of $\Delta x < 0.005$ do not affect the result. This is the first systematic investigation on the evolution of the oxygen content as a function of doping, as previous experiments were mostly limited to one specific doping

duction and oxygenation of polycrystalline samples behave differently as diffusion of any kind is increased along the grain boundaries.

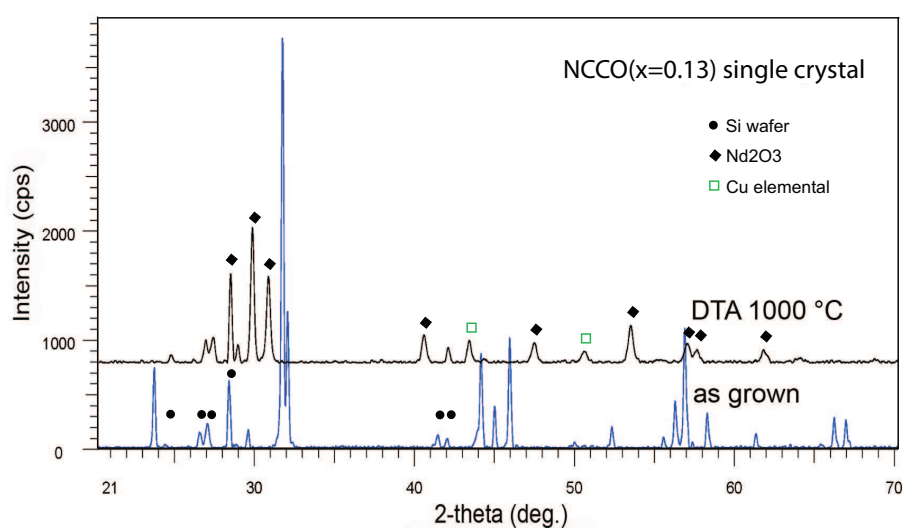


Figure 4.12: X-ray pattern of a crystal before and after the TGA experiment. The $\text{Nd}_{1.87}\text{Ce}_{0.13}\text{CuO}_4$ phase is completely transformed into the corresponding rare earth oxides and elemental Cu.

level. The oxygen content does not depend on the used growth atmosphere. If it were the case, the undoped compound, grown in a pure O_2 environment, should show the highest value for δ . The correlation of δ and the growth parameters (cf. discussion in Section 3.3.2) with the Ce doping is a clear signature of a doping assisted oxygen enrichment within the crystal. Although TGA experiments are not site sensitive, this additional oxygen must occupy the apex position, which is the only available impurity site in the T' structure. Finally, the oxygen content of the annealed crystals is given by subtracting the nearly doping independent oxygen loss which amounts to 0.020 ± 0.003 for $\text{Nd}_{2-x}\text{Ce}_x\text{CuO}_4$ and 0.030 ± 0.003 for $\text{Pr}_{2-x}\text{Ce}_x\text{CuO}_4$, when using the annealing described in Section 4.1. Thus, only a part of the excess oxygen is reduced by annealing.

4.4.2 Magnetization measurements: Testing the microscopic homogeneity of the crystals

After the determination of the overall oxygen content of as grown and annealed crystals, the role of oxygen has to be clarified, especially with respect to the appearance of superconductivity in the electron doped 214 compounds. This is a difficult task, as reduction/oxygenation experiments for 214 single crystals at the inevitable high temperatures are difficult to control, resulting often in phase separations and irreversible rearrangements in the metal lattice [95].

So far, there are no systematic data concerning the evolution of the superconducting phase as a function of the oxygen variation per formula unit $\Delta\delta$ and their reversibility with reduction/re-oxygenation of the crystals. In addition, depend-

ing on the investigation method, the change in the oxygen content of $\approx 5\%$ due to annealing experiments is often close to the detection limit of the method, resulting therefore in contradicting models. In thin film samples the reversible oxygenation/reduction process is much easier to control and it is reported that oxygen removal has a similar effect as Ce doping [113, 138, 139] and hence, oxygen is believed to act as co-dopant.

In order to clarify this issue, a slab of an overdoped $\text{Nd}_{1.84}\text{Ce}_{0.16}\text{CuO}_{4+\delta}$ high quality single crystal of 51.5288 mg is used for oxygenation experiments. Overdoped crystals are expected to be very sensitive to small variations in the oxygen content $\Delta\delta$ due to the steep slope of $T_c(x)$ on the overdoped side (Figure 4.13 (a)). Additionally, the effects of doping and disorder of a small oxygen variation $\Delta\delta$ within the crystal can only be separated from each other in the overdoped regime, as disorder always inhibits superconductivity, whereas oxygen co-doping in electron doped superconductors is directly opposed to the Ce doping. These two competing doping effects can be described within a simple ionic model. Assuming the valencies for the constituents to be $\text{Ln}(+3)$, $\text{Ce}(+4)$, $\text{O}(-2)$ and $\text{Cu}(v)$, the nominal oxygen contribution fraction to the total charge carrier concentration per Cu ion n_{Cu} is obviously given by the relation:

$$n_{\text{Cu}} = v - 2 = -x + 2\Delta\delta, \quad (4.3)$$

with the formal valency v for the copper. Thus, in the overdoped region disorder causes a decrease in T_c , whereas oxygen co-doping leads to an increase in T_c . In the underdoped region, however, co-doping and disorder lead to a decrease in T_c . The impact of oxygenation and reduction on T_c is shown in Figure 4.13 (a). In principle, by starting with an annealed overdoped single crystal, one should be able to move on the $T_c(x)$ curve towards the underdoped region and back by fractional oxygenation/reduction of the crystal. Note, that for this experiment the absolute

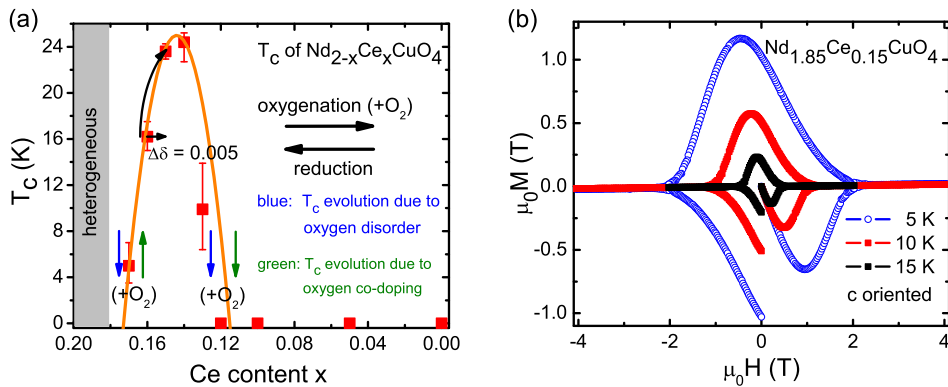


Figure 4.13: (a) Demonstration of the oxygenation/reduction experiment on an overdoped $\text{Nd}_{1.84}\text{Ce}_{0.16}\text{CuO}_{4+\delta}$ crystal and its implications to superconductivity. (b) Magnetization curves recorded after the standard reduction process of an as grown $\text{Nd}_{1.85}\text{Ce}_{0.15}\text{CuO}_{4+\delta}$ crystal.

value of oxygen content of the annealed crystals is of secondary importance as only relative changes in T_c and δ are measured.

The $\text{Nd}_{1.84}\text{Ce}_{0.16}\text{CuO}_{4+\delta}$ crystal was annealed according to the following sequence, the corresponding results are shown in Figure 4.14 (**a, b**): At first the crystal is reduced by using the standard reduction procedure. From the weight loss, $\Delta\delta = -0.018$ is estimated. T_c amounts to 16.2 K with a transition width ΔT of 2 K. In the subsequent annealing step a small amount of oxygen of $\Delta\delta = +0.005$ is added. According to the ionic model for explaining the oxygen co-doping and the assumption that the samples have nearly stoichiometric oxygen content after the first reduction treatment of the as grown crystals, one would expect a strong increase in T_c towards $T_c(x = 0.15)$, as the electron carrier concentration n_{Cu} should be changed by +0.01 (cf. Figure 4.13 (**a**)). The transition curve, however, is diminished by 1 K and the absolute value of the susceptibility at low temperatures is decreased dramatically. In order to check the reversibility of the system, the reduction step with the same parameters as in the first reduction step is repeated. The oxygen loss amounts to $\Delta\delta = -0.006$ and the transition curve of annealing 1 (compare the curves for annealing 1 and 3 in Figure 4.14 (**a**)) is reproduced. The reversibility of the oxygenation/reduction step shows clearly that the rare earth sublattice remains unaffected by the oxygenation experiment. There are no microscopic CeO_2 precipitations or rearrangements in the metal lattice, which might be responsible for the change in the transition curve. Thus, the experiment shows that oxygen co-doping cannot explain completely the evolution of superconductivity in the electron doped 214 single crystals. The decreased value in the susceptibility after oxygenation suggests rather an augmentation of disorder, which is responsible for a decreasing effective repulsion of the field within the sample. Note, that the volume of the sample does not change during the experiment.

Concerning the microscopic homogeneity, the measurement of hysteresis loops of magnetization is very informative. It is reported [50] that there is an unambiguous relation between the microscopic homogeneity and the evolution of the magnetization curve. For example the appearance of a second peak in the hysteresis loop (the so-called fishtail effect) and its temperature dependence can be related to microscopic inhomogeneities in the crystal. Due to the short coherence length in high temperature superconductors, local deviations from the dopant or oxygen content, as well as inhomogeneities in the rare earth sublattice lead to an effective field induced pinning, which influences the magnetization curves. In fact, the magnetization curves, recorded at 10 K for applied fields along the c axis, show a second peak effect after oxygenation (annealing 2 in Figure 4.14 (**b**)). This effect is absent after re-reducing the crystal and was never observed in crystals of different doping and size after standard annealing (Figure 4.13 (**b**)). Thus, the appearing/vanishing second peak is clearly related to the partial oxygenation of the crystal. Hence, it is an unambiguous confirmation of an augmented, oxygen induced disorder within the crystal, which gradually destroys superconductivity.

The reduced/injected oxygen might be associated with the oxygen fraction, which occupies the apex position. Because of steric considerations the occupation

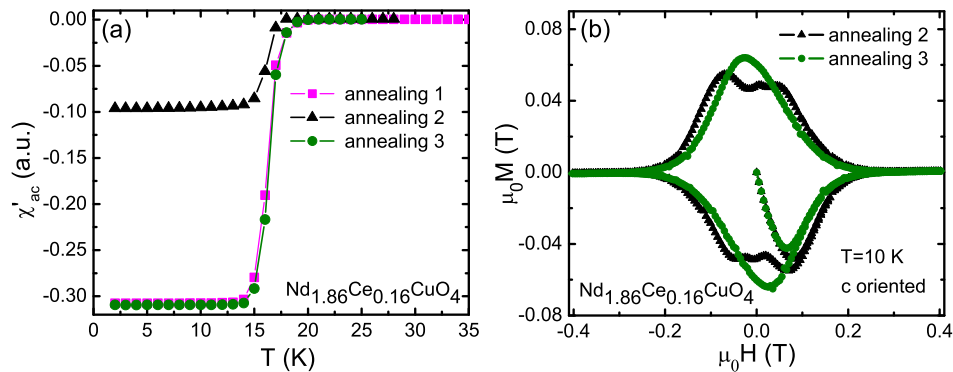


Figure 4.14: Annealing experiments on a c oriented $\text{Nd}_{1.84}\text{Ce}_{0.16}\text{CuO}_{4+\delta}$ crystal of 51.5288 mg. Annealing 1: Standard reduction of the as grown crystal in an argon gas flow at 960°C for 20 h ($\Delta\delta = -0.018$). Annealing 2: Oxygenation of the reduced sample in a gas flow of $\text{O}_2/\text{Ar} = 0.1\%$ at 750°C for 70 h ($\Delta\delta = +0.005$). Annealing 3: Repetition of annealing 1 with the same parameters ($\Delta\delta = -0.006$). (a) The ac-susceptibility curves confirm the reversibility of the annealing steps. The transition curve after oxygenation shows a reduction of T_c by 1 K and the absolute value of the response decreases by a factor of $1/3$. (b) Magnetization curves recorded at 10 K after the annealing 2 and 3. The partial oxygenation causes a broader magnetization curve with irregularities. This fluctuation, which appears/disappears with oxygenation/reduction, is a clear sign for oxygen induced disorder, which gradually destroys superconductivity.

of this impurity site might lead to a local deformation of the crystal lattice and hence, to a distortion of the CuO_2 plane. This oxygen induced disorder in the CuO_2 planes might behave pair breaking and influences strongly the electronic properties of the 214 crystals. During reduction the removal of oxygen on the apex site should be favored in comparison to a removal of the stronger bound oxygen, occupying the O(1) and O(2) site. Of course, it cannot completely be excluded that some small fraction of O(1) and O(2) oxygen is also removed at such high reduction temperatures. However, the removal/incorporation of oxygen on the regular lattice sites O(1) and O(2) implies the creation/reduction of disorder, which should also affect superconductivity. Thus, if oxygen of the O(1) site were mainly removed due to the reduction step, the disorder would increase, which is inconsistent with the observation that superconductivity appears upon reduction.

4.4.3 Oxygen as co-dopant and source of disorder

From the oxygenation/reduction experiments as well as from the oxygen determination experiments the following conclusions can be drawn:

1. The crystals contain a slight, doping dependent surplus of oxygen and only the parent compounds Pr_2CuO_4 and Nd_2CuO_4 have a nearly stoichiometric oxygen content. This experimental result obtained from TG measurements agrees with Raman results [117] and is in contrast to the finding of a small

oxygen deficiency of the doped, as grown crystals in [122]. The surplus of oxygen has to occupy the apex position, which is the only impurity site in the tetragonal T' structure.

2. The purpose of annealing is the reduction of tensions in the crystal structure and the removal of the surplus of oxygen. Because of the high annealing temperatures not only the apex oxygen, but also the oxygen of the O(1) and O(2) side is mobile. Thus, the removal of a small amount of the O(1) and O(2) oxygen and consequently, the formation of a reversible parasitic phase cannot be excluded [27, 117, 118]. Nevertheless, superconductivity occurs only in the stoichiometric T' phase, and the appearance of the impurity phase is rather a structural by-product than a prerequisite for superconductivity.
3. The oxygen nonstoichiometry of the crystals dopes the crystals only marginally and is primarily a source of disorder. This is an unambiguous result of the oxygenation/reduction experiments on the overdoped side, where the influence of oxygen co-doping on superconductivity can be separated clearly from disorder effects. This important result agrees with recently published transport data on overdoped $\text{Pr}_{2-x}\text{Ce}_x\text{CuO}_4$ thin films [140], where additional oxygen is found to affect the mobility of the charge carriers rather than the band filling. However, the result disagrees with prior publications [27, 139], which have deduced an effective oxygen co-doping from oxygenation experiments on optimally doped thin films.
4. From the magnetization measurements on an overdoped, oxygenated/reduced $\text{Nd}_{1.84}\text{Ce}_{0.16}\text{CuO}_{4+\delta}$ single crystal and the corresponding evolution of T_c it can be concluded, that the apical oxygen is removed during reduction, resulting in a decrease of disorder in the crystal lattice. Recent publications [117, 122] suggest that the apical oxygen (provided that there is an apical oxygen) is unaffected by reduction and only the oxygen in the CuO_2 planes O(1) is removed. This picture is inconsistent, as one would not expect the establishment of superconductivity with increasing disorder in the CuO_2 planes.
5. A suggested small Cu deficiency of a few % in as grown crystals [122] cannot be the main reason for the absence of superconductivity in electron doped compounds. In addition, the Cu deficiency cannot be simply related to the CuO evaporation during crystal growth, as this small evaporation can be balanced easily by the Cu rich flux. Experiments have shown that as grown $\text{Nd}_{1.85}\text{Ce}_{0.15}\text{CuO}_{4+\delta}$ single crystals, grown in an atmosphere of $\text{O}_2/\text{Ar} = 1\%$, are superconducting with $T_c < 10$ K, although the CuO evaporation is noticeably higher compared to the standard grown crystals. The Cu nonstoichiometry is expected to be negligible and the incorporated, additional oxygen influences strongly the as grown behavior of the crystals.

Part II

Transport properties of $\text{Nd}_{2-x}\text{Ce}_x\text{CuO}_4$ single crystals

Chapter 5

Theory: The normal state transport

The electron and hole doped cuprate high temperature superconductors reveal unusual transport properties, which cannot be understood within conventional Fermi liquid theory. For both sides of the phase diagram (electron and hole doped side) the compounds are characterized by an unusual, strong temperature and doping dependent evolution of the Hall coefficient R_H . A sign change in R_H at higher doping levels is reported for both types of doping [141, 142]. In addition, unusual features are also observed in the behavior of the normal state resistivity and magnetoresistance, which are incompatible with the established transport theory of normal metals. At low temperatures the normal state resistivity shows a remarkable doping dependent upturn behavior, whose origin is up to now controversially discussed. Additionally, fluctuation effects must be kept in mind – especially for the hole doped cuprates with their high upper critical fields B_{c2} – when analyzing the low temperature normal state transport data.

In this chapter the characteristic normal state transport properties are reviewed briefly. Afterwards proposed theoretical models for explaining the transport data are introduced and discussed in terms of their applicability.

5.1 Phenomenology of the normal state transport in cuprate superconductors

In this section the most prominent results of DC transport – based on transport measurements of more than 20 years – are summarized separately for electron and hole doped cuprates.

5.1.1 Transport properties of hole doped cuprates

The T dependence of the in-plane resistivity of hole doped cuprates shows a clear evolution with doping. The often reported linear T dependence of the in-plane

resistivity

$$\rho_{xx} \propto T \quad (5.1)$$

over a broad doping interval [5, 141] from the underdoped to the optimally doped region is inconsistent with newer measurements. It was shown on underdoped high quality single crystals of $\text{YBa}_2\text{Cu}_3\text{O}_{7-\delta}$ and $\text{La}_{2-x}\text{Sr}_x\text{CuO}_4$ that ρ_{xx} obeys a T^2 rather than a T dependence [21] and thus, the in-plane resistivity shows the same power law as the inverse Hall angle

$$\cot \theta_H \propto T^2. \quad (5.2)$$

Consequently, the transport in the underdoped regime, carried by the quasiparticles on the Fermi arcs (see illustration in Section 5.3.2), behaves similar as in a conventional Fermi liquid. Nevertheless, it seems to be difficult to reconcile a Fermi liquid model for lightly hole doped cuprates with an arc-like topology of the Fermi surface as observed by ARPES [4, 62] and a strong violation of the Mott limit¹ [21, 143]. At moderate temperatures even for the almost undoped compounds a metallic behavior in ρ_{xx} (i.e. $d\rho_{xx}/dT > 0$) was found [23], although the Mott limit is strongly violated and, hence, Boltzmann transport theory is not applicable. It was estimated for $\text{La}_{2-x}\text{Sr}_x\text{CuO}_4$ [143] that the mobility of the holes changes only by a factor of 3 from far underdoped crystals with $x = 0.01$ to overdoped samples with $x = 0.17$. This metallic behavior of the underdoped compounds is a remarkable feature which is not understood so far. As there is a correlation between the inverse mobility of $\text{La}_{2-x}\text{Sr}_x\text{CuO}_4$ and the AFM correlation length ξ_{AFM} with varying doping level x , a not clearly specified stripe assisted transport mechanism has been suggested [143].

The unambiguous observation of crossovers in the transport data of underdoped cuprates such as the pseudogap is difficult and often not reliable. A crossover temperature T^* was deduced from the inflection point of the slightly “S-shaped” $\rho_{xx}(T)$ curves by taking the second derivative $d^2\rho_{xx}/dT^2$. The observed change in curvature was interpreted in terms of a partial reduction of an inelastic scattering channel in the pseudogap state. From resistivity measurements on different hole doped cuprates an about linear decrease of T^* with increasing doping level x was observed, terminating near optimal doping [23].

A linear T dependence in resistivity for all temperatures $T > T_c$ was only found in a small region around optimally doping [5, 21, 23]. This linearity seems to be a characteristic feature of optimally hole doped cuprates. Its physical origin might be rather attributed to electron correlation effects than to phonon interactions. A similar linear T dependence of the resistivity for temperatures $T \rightarrow 0$ was found in the system YbRh_2Si_2 [144] exactly at the position of a quantum critical point (QCP). However, the interpretation of the linear T dependence as a signature for

¹The Mott limit states whether a material behaves metallic or not. For metallic transport the Fermi wave length λ_F of the Bloch electrons must be larger than the mean free path l , or equivalently: $l \cdot k_F \geq 2\pi$. For 1% doped $\text{La}_{2-x}\text{Sr}_x\text{CuO}_4$ a value of $l \cdot k_F \approx 0.1$ at $T = 300$ K is estimated [143].

quantum criticality in the hole doped cuprates is up to now controversially discussed. From negative intercepts of the extrapolated $\rho_{xx}(T)$ curves [145] as well as from explicit measurements of $\rho_{xx}(T)$ at high magnetic fields [146] a deviation from a strict linear T dependence to higher powers in T has been found for $T \rightarrow 0$. In the overdoped regime the purely linear $\rho_{xx}(T)$ behavior is replaced by a power law behavior $\rho_{xx} \propto T^\alpha$ at moderate temperatures [23], where α increases continuously, starting with 1 at optimal doping up to 2 in the far overdoped region beyond the superconducting dome. For non-superconducting, strongly overdoped $\text{La}_{1.7}\text{Sr}_{0.3}\text{CuO}_4$ samples a strict T^2 behavior was observed for temperatures $T < 50$ K and interpreted as Fermi liquid ground state [147], whereas at higher temperatures deviations from T^2 towards smaller exponents were found.

The unusual doping and temperature dependence of the Hall coefficient is another intriguing feature of high temperature superconductors. For weakly doped $\text{La}_{2-x}\text{Sr}_x\text{CuO}_4$ samples, R_H was found to scale with $1/x$ [21, 148], which disagrees with Luttinger's theorem for the "normal" Fermi surface, stating a scaling with $1/(1+x)$. This discrepancy was associated with a reduced Fermi surface (Fermi arcs) containing exactly the carrier number given by the nominal doping x [21]. In the far overdoped region of $\text{La}_{2-x}\text{Sr}_x\text{CuO}_4$ the sign change of R_H is meanwhile well established and explained consistently within theoretical models [6]. Instead of R_H , the quantity $\cot \theta_H$ is often discussed due to its characteristic T^2 dependence observed over a wide doping range [21]. Although both quantities, ρ_{xx} and $\cot \theta_H$, are in the same way related to the scattering rate Γ , they differ in the T dependence, suggesting two independent scattering rates [149].

Concerning the orbital magnetoresistance, Boltzmann transport theory predicts the proportionality $\Delta\rho/\rho \propto (\omega_c \tau)^2$. If τ changes only by a \vec{k} independent function $f(T)$ due to a temperature variation, the magnetoresistance curves for different temperatures must collapse on a temperature independent straight line when plotted versus $(B/\rho)^2$. This scaling behavior is known as Kohler's rule. However, it has been reported that Kohler's rule is strongly violated in hole doped cuprates [150], and that $\Delta\rho/\rho$ follows the T dependence of the Hall angle $\tan^2 \theta_H$. Hence, Kohler's rule can be modified by plotting $\Delta\rho/\rho$ versus $m \cdot \tan^2 \theta_H$, where m is a constant. Only in the far overdoped $\text{La}_{2-x}\text{Sr}_x\text{CuO}_4$ a recovery of Kohler's rule could be observed [151].

5.1.2 Transport properties of electron doped cuprates

On the electron doped side of the phase diagram systematic transport measurements have been carried out primarily on $\text{Pr}_{2-x}\text{Ce}_x\text{CuO}_4$ thin films [11, 141, 152–156]. The in-plane resistivity has been reported to be doping independent over a wide doping range at moderate temperatures [141]. This doping independent behavior in resistivity is believed to arise primarily from the charge carriers of the electron-pockets. At lower temperatures ($T < 100$ K) the normal state resistivity is highly doping dependent with crossovers to insulating behavior (upturn) [156]. The temperature dependence of the resistivity obeys roughly a quadratic behavior

$\rho_{xx} \propto T^2$ [11].

The deduced Hall angle $\tan \theta_H$ has been reported to depend strongly on the doping level. With increasing doping level, $\tan \theta_H$ is initially negative for underdoped samples and shows a turning point followed by a sign change at low temperatures, when doping levels close to $x = 0.15$ are reached. Obviously, the same dependence on x and T is also displayed by the Hall coefficient R_H [11]. In the overdoped region, R_H becomes positive over the whole temperature range [11]. It has been tried to explain the doping evolution as well as the sign change in R_H by invoking a two band model [11, 139, 157]. Further experimental evidence for two electronic bands caused by the interactions with a spin-density-wave (SDW) state [158] was obtained from ARPES measurements [1, 10, 159, 160]. At low temperature R_H shows a kink at $x = 0.16$ when plotted over doping, which was interpreted in terms of a quantum phase transition (QPT) [11] into a SDW ordered state. High field measurements of $\rho_{xy}(B)$ have been reported to deviate from linearity [152], which was ascribed to a possible \vec{B} field induced suppression of the SDW gap Δ , and consequently, to a reconstruction of the Fermi surface.

Concerning magnetoresistance it was shown that for optimally doped $\text{Nd}_{1.85}\text{Ce}_{0.15}\text{CuO}_4$ samples, Kohler's rule holds for $T > 50$ K [139]. At low temperatures and depending on doping, $\Delta\rho/\rho$ shows a complicated field dependence with possible negative magnetoresistance and saturation effects at high magnetic fields [152].

5.2 Models for explaining the anomalous normal state transport

It was tried to explain the unusual normal state transport within different models based on Fermi liquid theory, or by involving a non-Fermi liquid scenario. While in electron doped compounds some doping and temperature dependent features can be understood qualitatively within a two band model, the transport in hole doped compounds is governed by a single band and the apparent "separation" of lifetimes is difficult to explain within a Fermi liquid approach.

5.2.1 The two-lifetime picture of Anderson

In the phenomenological model of Anderson [149] two different lifetimes τ_{tr} and τ_H are introduced, which are assigned to two different many-particle excitations, called holons and spinons. The latter comprise only the spin of the electrons while the charge is carried by the holons. The normal state resistivity is dominated by the holons scattered on spinons with a scattering rate of $\Gamma_{tr} = \tau_{tr}^{-1} \propto T$, while the temperature evolution of the Hall angle is determined by spinon-spinon scattering with the Hall scattering rate of $\Gamma_H = \tau_H^{-1} \propto T^2$. Note, that in a conventional Fermi liquid there is no "separation" of lifetimes, thus $\tau_{tr} = \tau_H$. With the introduced transverse and longitudinal scattering rates the T dependence of the transport

properties (at least for optimally hole doped cuprates) is explained quantitatively by

$$\rho_{xx} \propto \Gamma_{tr} \propto T, \quad (5.3)$$

$$\cot \theta_H \propto (\omega_c \tau_H)^{-1} \propto \Gamma_H \propto A + BT^2, \quad (5.4)$$

$$\Delta\rho/\rho \propto (\omega_c \tau_H)^2 \propto \frac{1}{(A + BT^2)^2}, \quad (5.5)$$

where A and B are free parameters determined by the experimental data. The model of Anderson comprehends only the experimental results of optimally doped cuprates. It does not explain the very important aspect of the doping evolution of the transport quantities. Furthermore, it is not applicable to electron doped cuprates.

5.2.2 The marginal Fermi liquid model of Varma

Varma and Abrahams [161–163] have proposed a marginal Fermi liquid (MFL) model for the description of the “bad metal” behavior of cuprates. In contrast to the two-lifetime picture of Anderson, this MFL model assumes a single scattering rate Γ , which consists of two parts: an elastic, T independent, anisotropic scattering rate Γ_i and a T linear, isotropic, inelastic scattering rate Γ_M :

$$\Gamma = \Gamma_M + \Gamma_i \approx B \cdot T + \tau_i^{-1} \cdot \cos^2(2\theta). \quad (5.6)$$

The modeling of the scattering rate was deduced from ARPES results, which give evidence for an isotropic linear T dependence of the scattering rate. The physical origin of Γ_i was ascribed to small angle scattering off impurities, which are located at a certain distance D from the CuO_2 sheets. The theory provides a modified expression for the Hall angle, which consists of a dominating term which is proportional to the square of the particle lifetime. Consequently, the observed T and T^2 dependence of ρ_{xx} and $\cot \theta_H$ is also predicted by this theory. The introduced small angle scattering accounts for the unconventional T dependence of the magnetotransport quantities.

Note, that the MFL theory is confined to optimal doping, as well. While the term comprising the squared lifetime in the Hall angle is responsible for a doping independent lifetime separation in the different transport quantities, recent experiments show a convergence of the transport and Hall lifetime in the overdoped and underdoped regime of hole doped cuprates [21]. Hence, this theory also seems not to be suitable to explain the observed experimental results.

5.2.3 Boltzmann theory in combination with an anisotropic scattering rate

Recently, a more generalized phenomenological model was proposed by Hussey [5]. The basic idea consists in using standard Boltzmann transport theory in combination with a doping dependent anisotropic scattering rate Γ , and the application

of the Mott-Ioffe-Regel (MIR) limit. The Boltmann transport theory is discussed in Section 5.3.1. The aim of this section is the discussion of the expression for the scattering rate. Based on experimental results [43, 45, 164, 165] the following assumptions are made for the scattering rate Γ in hole doped compounds.

1. The scattering rate is anisotropic in the basal plane with fourfold symmetry. The anisotropy is already introduced in the elastic term $\Gamma_0(\phi)$ of the scattering rate. For the parameterizations a sinusoidal ansatz of the form

$$\Gamma_0 = G_0 \cdot [1 + \chi \cdot \cos^2(2\phi)] , \quad (5.7)$$

or an ansatz according to Abrahams and Varma (AV) [161]

$$\Gamma_0 = \frac{\beta}{v_F(\phi)} \quad (5.8)$$

is used. G_0 , χ and β are free fit parameters and ϕ describes the angle between the Fermi vector k_F and the Cu-O-Cu bond direction. The strong anisotropy of the elastic scattering rate is an essential assumption in order to explain the pronounced T dependence of R_H , which increases for $T \rightarrow 0$, as well as the angle dependent magnetoresistance data [165]. Abrahams and Varma have suggested that this anisotropy might arise from small-angle scattering off impurities away from the CuO_2 layers [161]. In this case the scattering rate of the charge carriers is proportional to the density of states (DOS), which is proportional to v_F^{-1} , and the characteristic scattering angle $\delta\theta \approx D^{-1}$, where D is the characteristic distance of such impurity from the basal plane.

2. For the inelastic scattering, which has a similar anisotropy as Γ_0 , the following ansatz is made [164, 166]:

$$\Gamma_T = G_1 \cdot \cos^2(2\phi) \cdot T + G_2 \cdot T^2 , \quad (5.9)$$

where G_1 and G_2 are again free parameters in the model. The inelastic term consists of an isotropic T^2 scattering term, which might be associated with electron-electron scattering, and an anisotropic part, which is linear in T . The nature of the anomalous linear term in T is unknown and might have a magnetic origin [167]. A doping dependent study of the evolution of the anisotropy might elucidate the underlying scattering mechanism. The total scattering rate is therefore given by

$$\Gamma_{tot} = \Gamma_0 + G_1 \cdot \cos^2(2\phi) \cdot T + G_2 \cdot T^2 . \quad (5.10)$$

3. Application of the Mott-Ioffe-Regel (MIR) limit: The MIR limit states that the quasi-particle mean-free-path l cannot be smaller than the in-plane lattice constant a :

$$l \geq a . \quad (5.11)$$

If l was smaller than a , coherent transport within the basal plane and hence, Boltzmann transport theory would break down. The MIR limit is introduced by using a “parallel resistor” model with a maximum scattering rate Γ_{max} , at which the condition $l = a$ is attained [5, 168]. The maximum scattering rate is given by the parameter free term [6]

$$\Gamma_{max} = \frac{\langle v_F \rangle}{a}. \quad (5.12)$$

According to the model one can introduce an effective scattering rate Γ_{eff} , which comprises the total scattering rate, which is shunted by a saturation scattering rate Γ_{max}

$$\frac{1}{\Gamma_{eff}} = \frac{1}{\Gamma_{tot}} + \frac{1}{\Gamma_{max}}. \quad (5.13)$$

Finally, Γ_{eff} is the expression, which is inserted into an appropriate Boltzmann transport expression (Equation 5.23 in Section 5.3.1) for calculating the conductivity tensor. The observation of resistivity saturation at higher temperatures and its explanation within a “parallel resistor” model was also reported for A-15 superconductors [168]. In [169] an explanation for the necessity of a minimum conductivity (thus, a maximum scattering rate) is given. One has to keep in mind that a perfect periodic lattice does not give rise to scattering of Bloch electrons. Scattering in a crystal occurs only due to deviations from the perfect periodicity due to imperfections of the lattice, phonons, etc. Hence, the distance between potential scattering centers cannot be smaller than the lattice constant itself, which characterizes the spatial periodicity. Note, that for hole doped cuprates with their pronounced anisotropy in the mean-free-path l , the impact of the MIR limit on the effective scattering rate Γ_{eff} is different for the various regions of the Fermi surface at a given temperature. For increasing temperature the MIR limit attenuates the degree of anisotropy between nodal and antinodal direction and the system becomes more isotropic [5].

By using Equation 5.13 for the scattering rate in the Boltzmann transport theory, Hussey et al. [5] could explain straightforwardly the lifetime separation of ρ_{xx} and $\cot \theta_H$ for optimally doped Tl2201 and Bi2212 compounds. The scattering rate Γ_{eff} was assumed to be purely T^2 dependent (no linear term in T) and the linear behavior in resistivity of the optimally doped compounds turned out to be the result of the T^2 contribution in nodal direction, which is shunted by the MIR limit. In antinodal direction $(\frac{\pi}{a}, 0)$ the MIR limit is already achieved at temperatures of $T \approx 90$ K where the quasiparticles lose their coherence, while in nodal direction $(\frac{\pi}{a}, \frac{\pi}{a})$ the model suggests a MIR limit at much higher temperatures at approximately $T = 600$ K. Hence, in nodal direction coherent quasi-particles exist over a wide temperature interval, whereas in antinodal direction the quasi-particles lose their coherence already at low temperatures. This finding is in perfect agreement with the loss of the quasiparticle peak in antinodal direction

in ARPES² results [3, 170]. The anisotropy in the effective scattering rates in nodal/antinodal direction is also reflected by the temperature evolution of the Hall coefficient $R_H(T)$. Upon doping the amount of anisotropy, which is described by the parameters χ and G_1 , decreases. This suggests that an increasing part of the Fermi surface is effectively contributing to the transport [5].

Recently, the transport data of strong overdoped $\text{La}_{1.70}\text{Sr}_{0.30}\text{CuO}_4$ were explained successfully by using the same approach [6]. The anisotropy in the scattering rate was introduced by using the AV ansatz for the elastic part of the scattering rate. The inelastic scattering rate was assumed to be isotropic and only T^2 dependent. In addition, the MIR limit was implemented. Hence, the used model consists only of two free fit parameters β and G_2 , which are already determined one-to-one by the $\rho_{xx}(T)$ curve. For the measured quantities R_H and $\Delta\rho/\rho$ there is no free parameter in the model. With the values of $\beta = 4.0 \cdot 10^{18} \text{ ms}^{-2}$ and $G_2 = 1.6 \cdot 10^9 \text{ s}^{-1}\text{K}^{-2}$, Narduzzo et al. were able to reproduce all characteristic features in ρ_{xx} , R_H and $\Delta\rho/\rho$ of the far overdoped $\text{La}_{1.70}\text{Sr}_{0.30}\text{CuO}_4$ samples. ρ_{xx} shows a pure T^2 dependence in the low temperature regime and a transition to a linear T -behavior at moderate temperatures (influence of the MIR limit). $R_H(T)$ and $\Delta\rho/\rho$ are reflecting the Fermi surface topology and the anisotropy of the mean-free-path l . The sign change in R_H clearly reflects the different curvatures in the Fermi surface (hole-like in nodal, electron-like in antinodal direction, obtained from ARPES measurements [4]) and the corresponding anisotropy in l on different segments of the Fermi surface. In the case of $\text{La}_{1.70}\text{Sr}_{0.30}\text{CuO}_4$, the mean-free-path l must be larger in nodal direction than in antinodal direction, as otherwise a sign change cannot occur for topological reasons (cf. discussion in Section 5.3.1). There is no need of the incorporation of an anisotropic linear T term in the scattering rate, which might be a sign of a pure Fermi liquid-like ground state.

The application of the described approach to experimental data of various hole doped compounds [5, 6] has shown, that hole doped cuprates from optimally doped to the far overdoped region behave more like a Fermi liquid as one would expect when having a first look at the data. Fermi liquid-like behavior was also deduced from transport data in the underdoped cuprates [21], and there are first attempts [171] to explain the transport data within a Fermi liquid picture by introducing a factor $p = \frac{L_{\text{arc}}}{L_{\text{full}}}$ in the conductivity expressions, which accounts for the real length of the Fermi arcs with respect to the underlying whole Fermi surface.

²From the imaginary part of the quasiparticle self energy $\Sigma = \Sigma'(\omega) + i \cdot \Sigma''(\omega)$ a scattering rate can be deduced from the FWHM of the quasiparticle peak. $\Gamma = \frac{1}{\tau} = |2\text{Im}\Sigma| = \hbar\Delta k v_F$. v_F is the unrenormalized Fermi velocity.

5.3 Modeling the normal state transport of electron doped cuprates

The successful description of the normal state transport properties of hole doped cuprates using Boltzmann transport theory in combination with an anisotropic scattering rate $\Gamma(\phi)$ gives the motivation to apply the same model to electron doped cuprates. For doing so one has to calculate the conductivity tensor by using an appropriate band dispersion $E(\vec{k})$ and an expression for $\Gamma(\phi)$.

5.3.1 Boltzmann transport theory

In the following it is assumed that there is no temperature gradient $\vec{\nabla}T$ within the investigated samples, and that the electrical current is only caused by an applied electrical field \vec{E} . Hence, the linear current response \vec{J} to the applied electrical field \vec{E} is given by the equation

$$\vec{J} = 2e \sum_{k \in BZ} g_k \vec{v}_k = \frac{e}{4\pi^3} \int_{BZ} g_k \vec{v}_k d\vec{k} = \hat{\sigma} \vec{E}, \quad (5.14)$$

where $g_k = f_k - f_{k,0}$ denotes the displacement of the non-equilibrium distribution function f_k from the Fermi equilibrium distribution

$$f_{k,0} = \frac{1}{e^{\frac{E_k - \mu}{k_B T}} + 1} \quad (5.15)$$

due to an applied external force. $\frac{1}{4\pi^3}$ is the electron density in momentum space for both spin directions. The velocity of the Bloch electrons \vec{v}_k is related to the band dispersion E_k via the first equation of motion

$$\frac{d\vec{r}}{dt} = \vec{v}_k = \frac{1}{\hbar} \vec{\nabla} E_k. \quad (5.16)$$

Furthermore, the time evolution of the momentum of the Bloch electrons is given by the second equation of motion

$$\vec{F} = \hbar \frac{d\vec{k}}{dt} = e(\vec{E} + \vec{v}_k \times \vec{B}). \quad (5.17)$$

The Boltzmann equation describes the time evolution of the non-equilibrium distribution function f_k , taking into account collisions:

$$\frac{\partial f(\vec{r}, \vec{k}, t)}{\partial t} + \vec{v}_k \cdot \vec{\nabla}_r f(\vec{r}, \vec{k}, t) + \vec{F} \cdot \frac{1}{\hbar} \vec{\nabla}_k f(\vec{r}, \vec{k}, t) = \left(\frac{\partial f(\vec{r}, \vec{k}, t)}{\partial t} \right)_{coll}^{tot}. \quad (5.18)$$

The terms on the left are denoted as drift terms and the term on the right is the collision term. The collision term in a generalized form must include explicitly

the distribution function and the type of scattering, which is incorporated in the scattering probabilities $W_{k,k'}$ derived from the ‘‘Golden Rule’’, and is given by [172]

$$\left(\frac{\partial f(\vec{k})}{\partial t} \right)_{coll}^{tot} = - \int \frac{d\vec{k}'}{(2\pi)^3} \{ W_{k,k'} f(\vec{k}) [1 - f(\vec{k}')] - W_{k',k} f(\vec{k}') [1 - f(\vec{k})] \}. \quad (5.19)$$

With this generalized collision term Equation 5.18 becomes a nonlinear integro-differential equation. A simplification is obtained by using the relaxation time approximation

$$\left(\frac{\partial f(\vec{k})}{\partial t} \right)_{coll}^{tot} = - \frac{f_k - f_{k,0}}{\tau_k} = -g_k \Gamma_k, \quad (5.20)$$

where τ_k is the averaged time elapsed between two consecutive scattering events experienced by a Bloch electron. Hence, Γ_k is the corresponding scattering rate. Assuming no explicit time and spatial dependence of the distribution function (stationary situation) and the validity of the relaxation time approximation, Equation 5.18 can be rewritten using the equations of motion 5.16 and 5.17:

$$\frac{e}{\hbar} (\vec{v}_k \times \vec{B}) \vec{\nabla}_k g_k + \Gamma_k g_k = -e \vec{E} \vec{v}_k \frac{\partial f_{k,0}}{\partial E}. \quad (5.21)$$

From this equation an expression for g_k can be obtained by means of the Jones Zener expansion

$$g_k^{(n)} = \left\{ \frac{-e}{\hbar \Gamma_k} (\vec{v}_k \times \vec{B}) \vec{\nabla}_k \right\}^n \cdot \left\{ \frac{\vec{v}_k}{\Gamma} \left(- \frac{\partial f_{k,0}}{\partial E} \right) \cdot e \vec{E} \right\}, \quad (5.22)$$

where $g_k = \sum_{n=0,1,2,\dots} g_k^{(n)}$. With this expression for g_k one can calculate the conductivity tensor $\hat{\sigma}$ by using Equation 5.14. Note, that the Jones Zener expressions are expansions in \vec{B} . The zero order of g_k describes the in-plane conductivity $\sigma^{(0)}$. It is independent from the magnetic field and the current is only driven by the applied electrical field \vec{E} . An applied magnetic field causes corrections in the conductivity, where the correction terms expand with \vec{B}^n . The components of the tensor $\hat{\sigma}$ are given by

$$\sigma_{i,j}^{(n)} = \frac{1}{4\pi^3} \int_{BZ} d\vec{k} \left\{ e v_i \left(- \frac{e}{\hbar \Gamma} (\vec{v}_k \times \vec{B}) \vec{\nabla}_k \right)^n \cdot \frac{e v_j}{\Gamma} \left(- \frac{\partial f_{k,0}}{\partial E} \right) \right\}. \quad (5.23)$$

For a further evaluation of the integral in Equation 5.23 some general considerations are useful. Without restrictions of any kind, \vec{B} is applied along the \hat{z} direction and \vec{E} along the \hat{x} direction for the following discussion. \hat{x} and \hat{y} direction correspond to the in-plane crystal axis, whereas \hat{z} corresponds to the out-of-plane direction (perpendicular to the CuO_2 sheets). Since the system is quasi two-dimensional, one can simplify the integration in Equation 5.23 by evaluating the integral of one CuO_2 sheet and multiplying it with a factor of $2\pi/d$, which is the value obtained from the integration in out-of-plane direction. It is usual [172]

to express the volume element $d\vec{k}$ in terms of a surface element dS_F and an element in \vec{k} -space dk_\perp , which is oriented perpendicular to the Fermi surface

$$d\vec{k} = dS_F \cdot dk_\perp = dS_F \frac{dE}{|\vec{\nabla}_k E|} = dS_F \frac{dE}{\hbar v_k}. \quad (5.24)$$

For the quasi two-dimensional cuprates the Fermi surface is one-dimensional with a certain circumference S and the surface element is equal to the curvature element ds . In addition, for moderate temperatures T or $T \ll T_F$ one can approximate the derivative $\left(-\frac{df_{k,0}}{dE}\right) \approx \delta(E - E_F)$, and hence the integral of Equation 5.23 is completely reduced to an integration over the Fermi surface circumference S :

$$\sigma_{i,j}^{(n)} = \frac{1}{4\pi^3} \left(\frac{2\pi}{d}\right) \oint_S \frac{ds}{\hbar v_k} \left\{ ev_i \left(-\frac{e}{\hbar\Gamma} (\vec{v}_k \times \vec{B}) \vec{\nabla}_k\right)^n \cdot \frac{ev_j}{\Gamma} \right\}. \quad (5.25)$$

For a further evaluation of the conductivity expression in Equation 5.25, the definition of special unit vectors might be helpful, which are oriented tangentially (\hat{t}) and normally (\hat{n}) on each point of the Fermi circumference S :

$$\hat{n} = \frac{\vec{v}_k}{v_k} \quad \text{and} \quad \hat{t} = \hat{z} \times \hat{n} = -\frac{\vec{v}_k \times \vec{B}}{v_k B}. \quad (5.26)$$

With the definition of the mean-free-path l of the Bloch electrons

$$\vec{l} = \begin{pmatrix} l_s \cdot \cos \theta_s \\ l_s \cdot \sin \theta_s \end{pmatrix} = \vec{v}_k \cdot \tau, \quad (5.27)$$

where θ denotes the angle between the \vec{E} field direction and \vec{l} , one obtains finally the expression for the in-plane conductivity

$$\sigma_{xx}^{(0)} = \frac{e^2}{4\pi^3 \hbar} \left(\frac{2\pi}{d}\right) \int_S ds l_s \cos^2 \theta_s. \quad (5.28)$$

The in-plane conductivity is proportional to the mean-free-path l_{av} , averaged over the Fermi surface circumference. For a tetragonal system with fourfold symmetry the in-plane conductivity is a scalar and is independent from the \vec{E} field direction.

The Hall conductivity $\sigma_{xy}^{(1)}$ is obtained by evaluating Equation 5.25 using $g_k^{(1)}$:

$$\sigma_{xy}^{(1)} = B \cdot \frac{e^3}{4\pi^3 \hbar^2} \left(\frac{2\pi}{d}\right) \int_S ds \left\{ l_s \sin \theta_s \frac{d}{ds} [l_s \cos \theta_s] \right\}. \quad (5.29)$$

The physical interpretation of the integral on the right side might be easier using l_x and l_y explicitly. In this case Equation 5.29 can be rewritten as

$$\sigma_{xy}^{(1)} = B \cdot \frac{e^3}{4\pi^3 \hbar^2} \left(\frac{2\pi}{d}\right) \int_S ds \left\{ l_y \frac{d}{ds} [l_x] \right\} = B \cdot \frac{e^3}{4\pi^3 \hbar^2} \left(\frac{2\pi}{d}\right) \int_{l\text{-space}} dl_x \cdot l_y. \quad (5.30)$$

With the definition of the so called ‘‘Stokes area’’ A_l in the two-dimensional l -space [173]

$$2 \cdot A_l = \hat{z} \cdot \int_{l\text{-space}} d\vec{l} \times \vec{l} = \int_{l\text{-space}} [dl_x \cdot l_y - dl_y \cdot l_x] = 2 \cdot \int_{l\text{-space}} dl_x \cdot l_y, \quad (5.31)$$

the path integral in Equation 5.29 can be transformed into an integral in the l -space, leading to the famous Ong interpretation of the Hall conductivity [173]:

$$\sigma_{xy}^{(1)} = B \cdot \frac{e^3}{4\pi^3 \hbar^2} \left(\frac{2\pi}{d} \right) \cdot A_l = B \cdot \frac{e^3}{4\pi^3 \hbar^2} \left(\frac{2\pi}{d} \right) \cdot \frac{\hat{z}}{2} \cdot \int_{l\text{-space}} d\vec{l} \times \vec{l}. \quad (5.32)$$

With the magnetic flux $\Phi = B \cdot A_l$ and the flux quantum $\Phi_0 = \frac{h}{e}$ one can express the Hall conductivity by means of the magnetic flux, which penetrates the Stokes area

$$\sigma_{xy}^{(1)} = \frac{2}{d} \left(\frac{e^2}{h} \right) \left(\frac{\Phi}{\Phi_0} \right). \quad (5.33)$$

Figure 5.1 illustrates the advantage of the transformation from an integral in the \vec{k} -space to an integral in the \vec{l} -space on the basis of a simulation result of overdoped $\text{La}_{1.78}\text{Sr}_{0.22}\text{CuO}_4$. Since the two-dimensional Fermi surface has fourfold symmetry, only one quadrant of the Brillouin zone (BZ) is shown. Equation 5.32 indicates that $\sigma_{xy}^{(1)}$ is directly proportional to the Stokes area A_l in the \vec{l} -space. A_l is generated by the set of mean-free-path vectors \vec{l}_s , which are obtained when moving along the Fermi circumference. The vectors \vec{l}_s , which are located perpendicular to the Fermi surface, are plotted into the new coordinate system with the same norm and orientation with respect to an applied external field \vec{E} , which is characterized by the angle θ . Note, that the Stokes area is an oriented area, and the sign (positive or negative) depends only on the sense of rotation, when the vector \vec{l}_s traces out the circumference of A_l . If \vec{l} rotates clockwise, A_l is positive and hence, $\sigma_{xy}^{(1)}$ is hole-like. Else $\sigma_{xy}^{(1)}$ becomes electron-like. Figure 5.1 shows the expected Fermi surface of overdoped $\text{La}_{2-x}\text{Sr}_x\text{CuO}_4$ ($x = 0.22$) based on band dispersion parameters taken from [4]. In principle, the Fermi surface has an electron-like topology, centered around the Γ point of the Brillouin zone (BZ). However, the Hall signal is always positive for moderate overdoped $\text{La}_{2-x}\text{Sr}_x\text{CuO}_4$ [21, 61]. This behavior can be explained by discussing the \vec{l} -curve in Figure 5.1 (b). The Fermi curve consists basically of two segments with different curvature. By moving along the Fermi surface (following the arrows) up to position 1, the curvature is positive and θ increases continuously. At the inflexion point 1 the curvature changes sign and remains negative in a longer segment around the $(\frac{\pi}{2a}, \frac{\pi}{2a})$ position. In this segment the angle θ turns to 1 and starts decreasing until the second inflexion point 3 is reached. Between 1 and 3 the sense of rotation of \vec{k}_F and \vec{l} is opposite to each other (note the sense of circulation of both curves in Figure 5.1) and shows again the same circulation, when position 3 is crossed. The segments in the Fermi surface with negative curvature provide a positive contribution (+) to the Hall conductivity,

whereas the positive curved parts in antinodal direction provide a negative contribution ($-$). The net contribution to $\sigma_{xy}^{(1)}$ is obtained by summing up the values of the oriented areas of the different loops

$$A_l = \sum_i A_i . \quad (5.34)$$

Note, that the local Fermi surface topology is not sufficient to explain the sign of the Hall signal. Assuming isotropic \vec{l}_s , the two loops in Figure 5.1 (b) would collapse on a single curve, resulting in a negative sign of $\sigma_{xy}^{(1)}$. The anisotropy in \vec{l} is a further important criterion, which has strong influence on the topology of the \vec{l} -curve and hence, determines the sign of R_H . In overdoped $\text{La}_{2-x}\text{Sr}_x\text{CuO}_4$ the highly mobile electrons in nodal direction govern the transport properties and consequently, R_H is positive. The discussion of the Hall conductivity is concluded with the remark that the shape of the \vec{l} -curve is independent from the \vec{E} field orientation and therefore, $\sigma_{xy}^{(1)}$ is a scalar quantity.

The magnetoconductivity $\sigma_{xx}^{(2)}$ is obtained by evaluating Equation 5.25 using $g_k^{(2)}$:

$$\sigma_{xx}^{(2)} = B^2 \cdot \frac{e^4}{4\pi^3 \hbar^3} \left(\frac{2\pi}{d} \right) \int_S ds \left\{ l_s \cos \theta_s \cdot \frac{d}{ds} \left[l_s \frac{d}{ds} (l_s \cos \theta_s) \right] \right\} . \quad (5.35)$$

Concerning the geometrical interpretation, the magnetoconductivity $\sigma_{xx}^{(2)}$ reflects the amount of curvature of the \vec{l} -curve. Hence, it is a measure of the anisotropy in \vec{l} and serves as a check for the assumed anisotropic scattering rates Γ in the simulation.

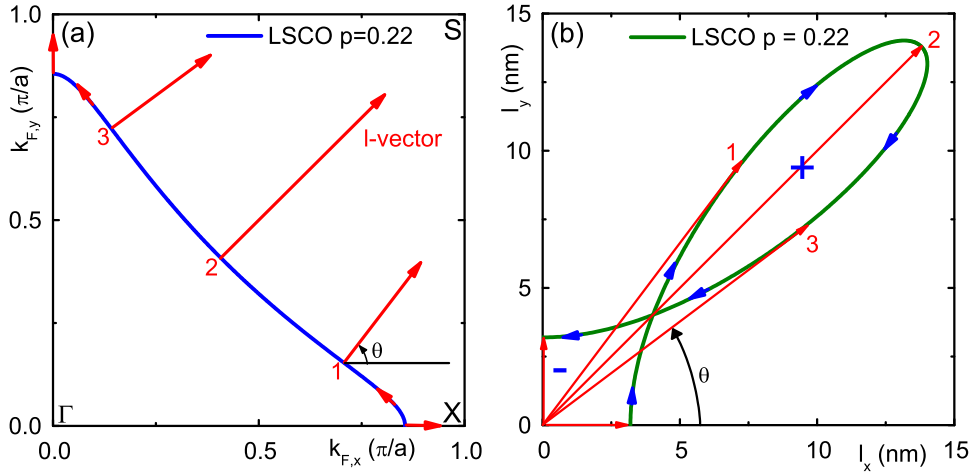


Figure 5.1: (a) Typical two-dimensional Fermi surface, obtained from overdoped $\text{La}_{2-x}\text{Sr}_x\text{CuO}_4$ with $x = 0.22$. The band dispersion parameter for the simulation is taken from [4]. (b) Illustration of the corresponding \vec{l} -curve. The Hall conductivity $\sigma_{xy}^{(1)}$ is directly proportional to the area in the \vec{l} -space, which is swept out by the \vec{l}_s -vector.

Finally, the relations between the derived conductivities and the measurable quantities ρ_{xx} , R_H and $\Delta\rho/\rho$ are given by collecting the lowest order terms in B (weak field limit $\omega_c\tau \ll 1$, i.e. $\rho_{xy} \ll \rho_{xx}$)

$$\rho_{xx} \approx \frac{1}{\sigma_{xx}^{(0)}} , \quad (5.36)$$

$$R_H \approx \frac{1}{B} \cdot \frac{\sigma_{xy}^{(1)}}{\left(\sigma_{xx}^{(0)}\right)^2} , \quad (5.37)$$

$$\Delta\rho/\rho = -\frac{\sigma_{xx}^{(2)}}{\sigma_{xx}^{(0)}} - \left(\frac{\sigma_{xy}^{(1)}}{\sigma_{xx}^{(0)}}\right)^2 . \quad (5.38)$$

The magnetoresistance consists of the magnetoconductance and the Hall angle as a negative correction term. Generally, the change in the conductivity $\sigma_{xx}^{(2)}$ is always negative due to the Lorentz force and the first term in Equation 5.38 is larger than the second one, so that the orbital magnetoresistance $\Delta\rho/\rho$ is always positive. For a further explanation the Hall angle might be useful

$$\tan \theta_H = \frac{\rho_{xy}}{\rho_{xx}} \approx \frac{\sigma_{xy}^{(1)}}{\sigma_{xx}^{(0)}} , \quad (5.39)$$

$$\cot \theta_H = \frac{1}{\tan \theta_H} \approx \frac{\sigma_{xx}^{(0)}}{\sigma_{xy}^{(1)}} . \quad (5.40)$$

For a two band model with a hole-like (indexing “h”) and an electron-like (indexing “e”) band, ρ_{xx} , R_H and $\Delta\rho/\rho$ in the weak field limit ($\omega_c\tau \ll 1$) are given by

$$\rho_{xx} = \frac{1}{\sigma_{xx}^{(0,h)} + \sigma_{xx}^{(0,e)}} , \quad (5.41)$$

$$R_H \approx \frac{1}{B} \cdot \frac{\sigma_{xy}^{(1,h)} + \sigma_{xy}^{(1,e)}}{\left(\sigma_{xx}^{(0,h)} + \sigma_{xx}^{(0,e)}\right)^2} , \quad (5.42)$$

$$\tan \theta_H = \frac{\rho_{xy}}{\rho_{xx}} \approx \frac{\sigma_{xy}^{(1,h)} + \sigma_{xy}^{(1,e)}}{\sigma_{xx}^{(0,h)} + \sigma_{xx}^{(0,e)}} , \quad (5.43)$$

$$\Delta\rho/\rho = -\frac{\sigma_{xx}^{(2,h)} + \sigma_{xx}^{(2,e)}}{\sigma_{xx}^{(0,h)} + \sigma_{xx}^{(0,e)}} - \tan^2 \theta_H . \quad (5.44)$$

5.3.2 Fermi surface topology

The doping dependent evolution of the two-dimensional Fermi surface depends strongly on whether holes or electrons are added into the CuO_2 planes. The evolution of the hole doped compounds is shown in Figure 5.2. The undoped Mott insulator is half-filled and the Fermi surface coincides with the diamond-shaped AFM Brillouin zone³. The Fermi surface of hole doped cuprates is usually described by a single band tight-binding (TB) model [4] with the particle dispersion

$$E_{\vec{k}} = -2t[\cos(k_x a) + \cos(k_y a)] + 4t' \cos(k_x a) \cos(k_y a) - 2t''[\cos(2k_x a) + \cos(2k_y a)] + \mu, \quad (5.45)$$

where t , t' and t'' are the first, second and third nearest-neighbor transfer integrals within the CuO_2 layers. The values for transfer integrals and chemical potential μ

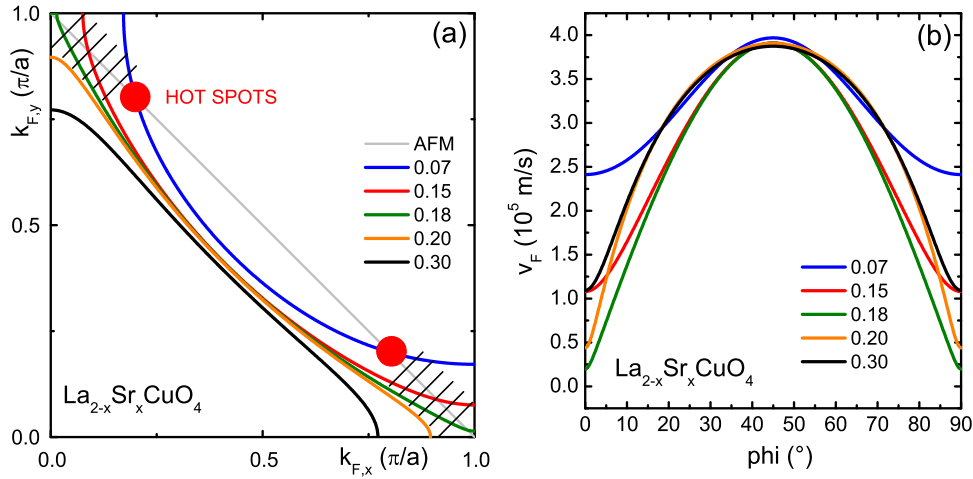


Figure 5.2: (a) Simulation of the Fermi surface evolution of hole doped $\text{La}_{2-x}\text{Sr}_x\text{CuO}_4$. The band parameters are taken from [4]. For clarifying reasons only one quadrant of the Brillouin zone is shown. (b) Calculation of the Fermi velocity from the energy dispersion. Note the anisotropy in the Fermi velocity, which is highest in nodal direction (corresponding to $\phi = 45^\circ$) for all doping levels. The charge carriers in nodal direction govern primarily the transport properties in hole doped cuprates.

are adjusted to ARPES measurements. For the simulation parameters from [4] are used. Note, that μ is an adjustable quantity determined by the band filling.

Concerning the Fermi surface topology two aspects are remarkable. In the underdoped region up to doping levels of $x \approx 0.18$ the Fermi surface has a hole-like topology. The Fermi surface is centered around the S point $(\frac{\pi}{a}, \frac{\pi}{a})$ in the Brillouin zone, and it crosses the AFM Brillouin zone close to the $(\pi, 0)$ region. In this region near the nodal direction the Fermi surface is gaped probably due to strong interactions of the quasiparticles with the spin density wave (SDW) background.

³Remember the AFM unit cell in Figure 2.4 with the lattice constant $a_m = \sqrt{2} \cdot a$. Hence, the magnetic Brillouin zone is half of the Brillouin zone obtained from the crystal lattice.

These positions on the Fermi surface are referred to as hot spots (red dots in Figure 5.2), as the quasiparticles undergo a coherent backscattering of amplitude Δ and wave vector $\vec{q} = (\frac{\pi}{a}, \frac{\pi}{a})$. Consequently, the Fermi surface in the underdoped region consists of Fermi arcs confined around the nodal position [4, 62, 174]. The truncated one-dimensional arcs, as they are mapped by ARPES experiments [174], are unique concerning their topology. So far, there are two scenarios of interpreting the Fermi arcs [7, 175]: Based on observed quantum oscillations on underdoped $\text{YBa}_2\text{Cu}_3\text{O}_{7-\delta}$ the Fermi arcs are interpreted as small, closed hole pockets, which cannot be resolved by ARPES measurements [8, 176]. In this case the estimated hole number differs from the nominal doping. The second scenario, however, assumes a large underlying Fermi surface with a spectral weight loss in antinodal direction. Yoshida et al. [4] were able to determine the underlying Fermi surface by extrapolating the momentum distribution curves (MDCs) in the gaped segments. From the large Fermi surface a charge carrier number, which corresponds to the nominal hole doping, could be determined using Luttinger's theorem. With increasing hole doping the Fermi surface shrinks towards the Γ point direction. Thus, the hot spots are shifted continuously towards the van Hove singularity at $(\frac{\pi}{a}, 0)$. At the doping level $x \approx 0.18$ the Fermi level reaches the van Hove singularity and a crossover in the topology towards a closed electron-like Fermi surface is observed [4]. At these doping levels quasiparticle spectral weight in ARPES can also be observed in antinodal direction. In Figure 5.2 (b) the simulated Fermi velocities are shown, as well. Note the strong anisotropy in v_F (factor 3) between nodal and antinodal direction for all doping levels $x \leq 0.30$, which explains the discrepancy between the measured positive Hall signal and the electron-like Fermi surface in the overdoped region. For doping levels $x > 0.30$, v_F might become more isotropic and thus, a sign change in R_H for the entire temperature range is expected.

The electron doped cuprates, however, exhibit a contrary evolution of the Fermi surface. The Fermi surface moves diagonally towards the S point in the Brillouin zone when the doping level is increased. Consequently, the hot spot regions on the Fermi surface are moving continuously towards nodal direction and disappear when the Fermi surface has completely crossed the AFM Brillouin zone boundary. In this case the Fermi surface is expected to be reconstructed to a hole-like large S-centered surface. The doping level, at which the Fermi surface is fully reconstructed, is estimated to be $x \geq 0.17$ [10]. From the discussion of the Hall signal in Section 5.3.1 by using the \vec{l} -representation, it can be concluded immediately that – independent from the \vec{l} anisotropy – the Hall signal must be positive over the whole temperature range when the Fermi surface is reconstructed.

In the underdoped region the strong AFM correlations in electron doped compounds, which have been found to exist up to optimally doping (cf. discussion in Section 2.1), lead to a Fermi surface fragmentation at the hot spot regions. Hence, the treatment of the electron doped compounds within a two-band model is more appropriate than a single band description. Due to the strong backscattering of the charge carriers with momentum transfers of $\vec{q} = (\frac{\pi}{a}, \frac{\pi}{a})$, the unit cell is doubled, and at the degeneracy points (i.e. on the AFM zone diagonal) the levels are split

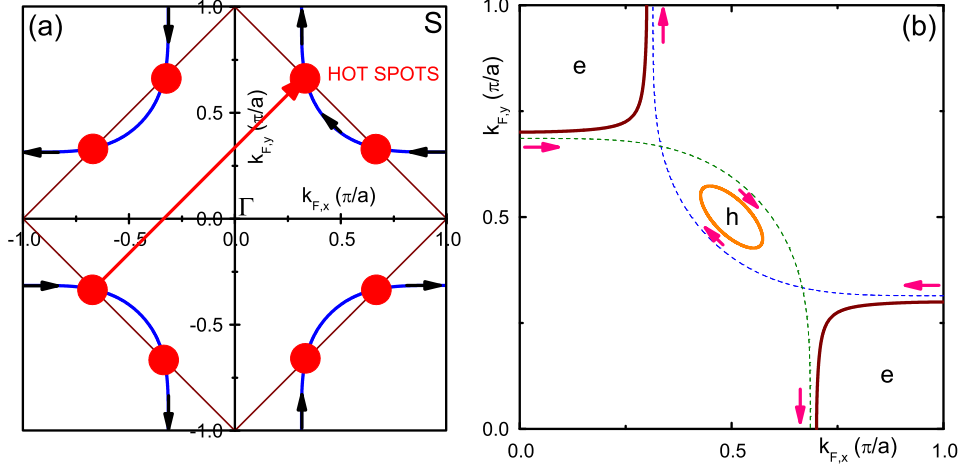


Figure 5.3: (a) Single-band Fermi surface of electron doped cuprates. Typical band parameters for the electron doped cuprates are given by [177]. Compared to the hole doped cuprates the hot spots (red dots) are shifted towards nodal direction. Electrons in the hot spot region undergo an effective backscattering by the AFM wave vector $\vec{q} = (\frac{\pi}{a}, \frac{\pi}{a})$. Note the sense of circulation of the electrons on the Fermi surface. (b) Illustration of the Fermi surface fragmentation due to the strong coupling of the electronic states with the SDW state in electron doped compounds. The new Fermi surface is obtained from the single-band dispersion by a translation of the dispersion with the AFM vector \vec{q} in the reciprocal space (dashed green line) and by an inclusion of the level splitting of 2Δ at the points of intersection. The resulting Fermi surface consists of two different parts: An electron-like pocket around $(\frac{\pi}{a}, 0)$ with counterclockwise circulation of the charge carriers and a hole pocket in nodal direction with clockwise circulation of the charge carriers. The band parameters are chosen as: $t = 0.38$ eV, $t' = 0.32 \cdot t$ eV, $t'' = 0.5 \cdot t'$ eV, $\mu = 0$ eV and $\Delta = 0$ eV for the dashed curves and $\Delta = 0.2$ eV for the solid curves.

by the energy gap 2Δ . The energy gap is directly proportional to the AFM interaction strength, which obviously depends on the Ce content x . The new two-band dispersion is given by

$$E_{\vec{k}}^{\pm} = \frac{1}{2} \{ E_{\vec{k}} + E_{\vec{k}+\vec{q}} \pm \sqrt{(E_{\vec{k}} - E_{\vec{k}+\vec{q}})^2 + 4\Delta^2} \}, \quad (5.46)$$

where $E_{\vec{k}}$ is the single band dispersion as defined in Equation 5.45. For $\Delta = 0$ (see dashed lines in Figure 5.3 (b)), the lower branch (-) is equal to the shifted band dispersion $E_{\vec{k}+\vec{q}}$, which crosses the upper branch (+) given by $E_{\vec{k}}$ at the hot spots. From the sense of circulation of the charge carriers of both branches it is easy to see that, after splitting the degeneracy at the hot spots by 2Δ , a hole-like pocket with clockwise circulation in nodal direction as well as an electron-like pocket with counterclockwise circulation in antinodal direction is formed.

The doping dependent evolution of Δ and hence, the evolution of the upper (+) and lower band (-) has been simulated by Kusko et al. [10] and has been compared with ARPES data [9]. Figure 5.4 summarizes the corresponding results. In

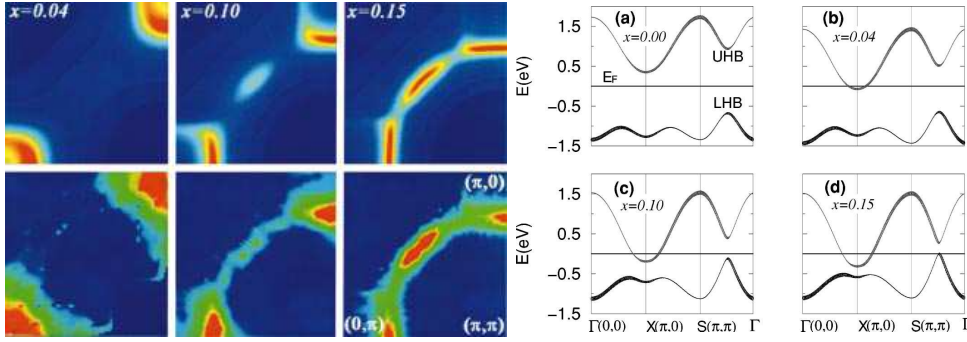


Figure 5.4: Band calculations by using a $t - t' - t'' - U$ Hubbard model [10] (**right, upper left**) and the corresponding ARPES data of $\text{Nd}_{2-x}\text{Ce}_x\text{CuO}_4$ crystals (**bottom left**) taken from [9].

the model the Fermi energy E_F is set to zero and the corresponding evolution of the upper (+) and lower band (−) is shown. For the undoped parent compound E_F lies within the band gap. Hence, the lower band is fully occupied corresponding to $1e^-$ per Cu ion. With increasing doping the band gap is closing gradually. The upper band is crossing E_F at first at low doping levels and consequently small electron-like pockets in antinodal direction appear. With further doping the electron pockets increase and change their shape from circular to squarish. In this context a peculiar feature is the loss of spectral weight in $\Gamma - X$ direction, so that the squarish Fermi surface is transformed into an arc-like segment at optimally doping. This redistribution of spectral weight, as it is seen by ARPES, is not included in the above discussed two-band model.

The lower band initially shows only a small evolution with doping ($x = 0.04$), but moves rapidly towards E_F at higher doping levels. At doping of $x = 0.10$ a small hole-like pocket in nodal direction is already visible. Concerning the spectral weight redistribution, the same evolution has been found as for the electron pockets. In other words, the well established hole pocket at $x = 0.15$ has been found to be an arc rather than a closed pocket as described in the two-band approach above. At optimally doping the imminent transition into a large hole-like Fermi surface is already observable, as the three pieces can be seen as parts of a large spherical Fermi surface, which is gaped at the hot spots. The redistribution of the spectral weight upon doping is represented clearly by the linewidth of the band dispersion in Figure 5.4 (**right**). Following the thick linewidth in the dispersion for doping $x = 0.15$, one can see the underlying uncorrelated single-band dispersion. Reaching the overdoped regime, the gaped states at the hot spots might be filled up [1], resulting in the already mentioned hole-like electronic state of the electron doped compounds.

Chapter 6

Experimental techniques

The second part of this thesis deals with the unusual transport properties in electron doped high temperature superconductors. For this purpose standard DC transport was carried out on $\text{Nd}_{2-x}\text{Ce}_x\text{CuO}_4$ single crystals of different doping and highest quality. The measured variables are the resistivity, the Hall signal as well as the transversal magnetoresistance.

In addition to the in-plane transport, the out-of-plane transport was measured for different doping levels in order to map the resistivity anisotropy in the NCCO sample system and to compare it with other sample sets.

Transport measurements are also a powerful tool in order to check the microscopic homogeneity of the crystals. Therefore, transport measurements on annealed crystals complete the characterization methods already discussed in Chapter 4.

6.1 Preparation of the single crystals

6.1.1 In-plane transport with a standard six-terminal Hall bar

For the in-plane measurements annealed and characterized single crystals with well defined T_c are cut into bars with typical dimensions of $4.0 \times 1.0 \times 0.1 \text{ mm}^3$ (length $l \times$ width $w \times$ thickness t). Depending on the size of the grown crystals the edge length may vary slightly by keeping always the aspect ratio of length to width equal to 4 : 1. The edges are oriented parallel to the crystallographic a and b axis and the tilt of the ab planes with respect to the sample surface, that is, the orientation of the c axis is better than 0.5° . The thickness of the Hall bar is controlled by gradually grinding of the ab surfaces. The downscaling in c direction is critical as microcracks within the thin crystal can arise due to the grinding and polishing procedure. However, the reduction of the Hall bar thickness is crucial, as the Hall voltage is proportional to $1/t$ at constant current. Unlike in thin film Hall bars the reduction of t in single crystals is limited for reasons of handling: Crystals with $t < 100 \text{ }\mu\text{m}$ easily break during processing. The thickness of the bars measured in this thesis ranges between $100 \text{ }\mu\text{m}$ and $200 \text{ }\mu\text{m}$.

The Hall bar was realized by attaching platinum or gold leads to the single crystal bars by using a silver paint¹. The pads together with platinum or gold leads are cured by a heat treatment at 400 °C for 1 hour in air. Note that this short heat treatment does not affect notably the oxygen state of the sample but is a precondition in order to get stable low resistance ohmic contacts. Typical values of contact resistance achieved with this technique are a few Ohm.

Initially, gold contacts were sputtered on the crystal surface. For this purpose the crystals are masked with aluminium foil leaving blank only the contact areas. On the masked crystal a 500 nm thick gold film was sputtered. Thereafter, the generated gold contacts are annealed in the same way as it is done for the silver paint. It was found that the sputtered gold contacts are less stable than the silver ones and the transition curves sometimes show a second transition, which is a clear signature for the change of the doping state due to contacting. Therefore, for the major part of the crystals the contacts are made manually by using a silver paste only.

For the current contacts the whole area of the two opposing side faces are covered by silver paint (pin 1, 2) in order to provide a homogeneous current injection and flow through the crystal. A pair of voltage leads is mounted under an optical microscope on each lateral side along the current flow direction. Therefore, the Hall bar is equipped with four voltage contacts (pin 3, 4, 5, 6) and the resistivity is measured by using both pairs, independently. The resistivity is calculated as

$$\rho_{xx} = (U_I/I) \cdot (wt/l) , \quad (6.1)$$

and the Hall coefficient R_H is given by:

$$R_H = \rho_{xy}/B = (U_H/I) \cdot (t/B) . \quad (6.2)$$

In order to minimize the uncertainty in the absolute values of ρ_{xx} and ρ_{xy} , relatively long samples and narrow voltage contacts with a width of 100 – 250 μm are used. The total error in the absolute values is estimated to be 10 %. The in-plane resistivities measured independently on both voltage pairs provide a good indication for the quality of the Hall bar. If crystals show qualitative different T dependence in the resistivity on both sides or the amplitudes differ from each other in the range of more than 10 %, the crystals are not investigated further, since some inhomogeneities or microcracks may be the reason of such behavior.

In order to measure the bare Hall signal (e.g. the transverse voltage drop over pin (4, 6)) one has to align the opposing voltage leads exactly in the same distance with respect to the current leads. In practice, this is not feasible when drawing the contacts manually and therefore, the transverse signal is superposed by a longitudinal fraction, which - depending on the doping x - can be two or three orders of magnitude higher than the transverse signal.

¹For the electrical contacts the silver paste Du Pont 4929 is used. In order to get an adequate consistency, the paste is diluted with butyl acetate before contacting.

6.1.2 Measuring technique

The quantities to be measured are the resistivity ρ_{xx} , the Hall coefficient R_H and the magnetoresistance $\Delta\rho/\rho$. These three quantities are measured within the temperature interval from 1.5 K to 300 K in magnetic fields up to 15 T. A cryostat with a variable temperature insert (VTI) and superconducting magnet system from Oxford Instruments is used for the measurements.

The crystals with leads are glued² to an electrically isolating sapphire plate³. The sapphire with sample is glued with GE varnish on a copper or brass interface, which is mounted onto the dip stick. The sample temperature is measured and controlled with precision of a few mK by using a Lake Shore temperature controller. This controller reads the T dependent resistance of a Cernox sensor and regulates the heater power of the sample heater. Both, heater and sensor are mounted very close to the sample position, providing therefore an accurate temperature measurement. Up and down sweeps in temperature result in the same transition curves, that is, no hysteresis effects are observable.

The second independent variable to measure is the magnetic flux density B . By using a superconducting switch connected in parallel to the superconducting coil, one can run the magnet in the so called “persistent mode”: For energizing the magnet, the temperature of the switch is increased above T_c by a heater and therefore, the magnet is connected to the current source. After switching off the heater the superconducting coil is disconnected from the current source and a certain field, which corresponds to the applied current, is frozen in. The coil in the persistent mode provides a very stable magnetic field and deviations from the nominal value are only due to the decay of the persistent current. Typical decay rates are better than 100 ppm per hour.

ρ_{xx} , R_H and $\Delta\rho/\rho$ can be measured at the same time by using the configuration described in Chapter 6.1.1. As it is possible to make large geometrical well defined bars from the TSFZ grown rods, there is no need to use a complicated technique such as the Montgomery [178, 179] or Van der Pauw [180, 181] method in order to measure the magnetotransport quantities. The Van der Pauw technique is used for small isotropic crystals of arbitrary shape, when the preparation of Hall bars is not feasible. The Montgomery approach, however, is applied for anisotropic systems and for the analysis of the resistivity the anisotropic sample is mapped to an isotropic one. The used measurement setup is shown in Figure 6.1. Depending on the expected amplitude of the voltage signals a standard DC or Lock-In technique is used:

²As glue GE varnish or Stycast 2850 FT, prepared with Catalyst 24 LV, is used. Especially in out-of-plane measurements, where the samples are fixed on the small lateral ac side (Figure 6.2), the use of Stycast is indispensable in order to prevent a rotation of the crystals in high magnetic fields due to the strong imposed torque. The Stycast 2850 FT is characterized by a high thermal conductivity, small thermal expansion and good working properties due to the low viscous consistency. Once hardened, the embedded crystal cannot be dismantled without destroying it.

³Dimensions of the sapphire plate are $10.0 \times 5.0 \times 0.2 \text{ mm}^3$.

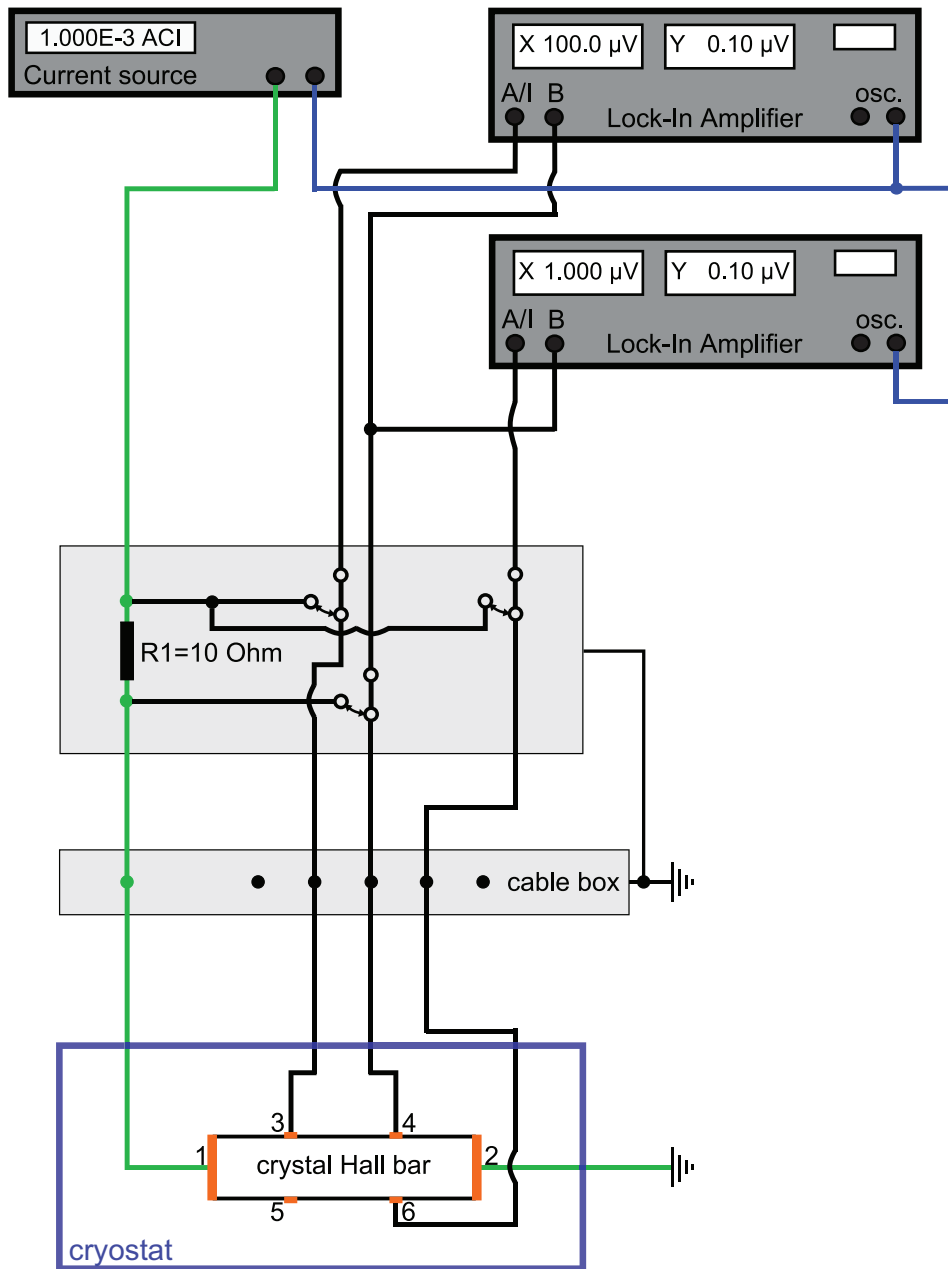


Figure 6.1: Electrical circuit for measuring ρ_{xx} and ρ_{xy} . A low frequency AC current (< 300 Hz) is biased on pin (1, 2) and the voltage drop between the pins (3, 4) and (4, 6) is measured by using modern SR830/SR850 Lock-In amplifiers. For this purpose the reference output of the HP3245A current source is connected to the reference input of the Lock-In amplifiers and the A-B mode is used. A 10Ω reference resistance R1 is connected in series with the sample in order to adjust the phase. When a DC technique is used, the Lock-In amplifiers are only substituted by low noise Keithley 2182 Nanovoltmeters and as current source a Keithley 2400 SourceMeter is used. The connecting lines represent the inner conductor of the used coaxial cables. Cryostat, cable box and measuring instruments are grounded.

- DC nanovoltmeters:

The simplest way to measure the longitudinal voltage drop U_l and the Hall voltage U_H is to bias a DC current on pin (1, 2) and to measure the longitudinal and transverse voltage with multimeters on the four other pins. Typical current values are 1 – 10 mA corresponding to current densities for the above mentioned dimensions of up to 10 A/cm². As DC current source a Keithley 2400 SourceMeter and for the voltage measurements the low noise Keithley 2010 or Keithley 2182 Nanovoltmeters are used.

In order to eliminate thermovoltages, the current is reversed during measurement. The highest resolution of both multimeter types are 10 nV and 1 nV, respectively. Certainly, the speed and noise rejection are determined by the filter and rate settings. In order to improve the noise performance analog and digital filters are activated and the rate is set to medium or slow modulus. The rate operation of the multimeters sets the integration time of the A/D converter and therefore, it affects fundamentally the accuracy and speed of the measurement. The digital filter averages a certain number of integrated single measurements and the average value is continuously corrected by the new incoming single measurement (moving average filter). Thus, one has to find a compromise between accuracy and speed. As the Hall voltage is expected to be very small (< 100 nV) especially for the overdoped crystals, and as the accuracy of the low noise multimeter is in the range of 50 – 100 nV, the Lock-In technique is also applied.

- Lock-In technique:

The main advantage of using a Lock-In is the gain of accuracy and speed during data acquisition. As it is an AC method there is no need of current reversal at each data point in order to eliminate thermal EMFs, which of course affect the low resistance measurement accuracy.

One challenge is to find the ideal measurement settings, which might vary from sample to sample. In practice it turned out that, whenever the contacts are drawn carefully resulting in good ohmic contacts, there are no problems with phase shifts caused by some spurious capacitances.

In the following the operating mode of a Lock-In amplifier is summarized in few words: On the sample an AC excitation with a given frequency, generated by an oscillator or function generator, is applied and the Lock-In detects the response of the sample at the same frequency and optimum phase. Noise signals of different frequency are rejected and will not disturb the measurement. For this purpose a Lock-In is made up of different components: A reference component, which provides a reference signal with a certain frequency and phase θ to the phase sensitive detector (PSD); the PSD component, which multiplies the incoming signal from the sample by the reference signal; a subsequent low pass, which integrates the PSD-signal over a certain time constant; a phase shifter, which allows the determination of the signal

phase with respect to the reference signal. Modern, highly sensitive Lock-In amplifiers, such as the SR830 or SR850 used in these measurements, convert the signal after a preamplification to digital form using a A/D converter, and the already discussed signal processing occurs digitally. Additionally, they measure with two independent phase sensitive detectors, where the phase shift between both PSDs is 90° . Thus, magnitude (R) and phase (θ) or real (X) and imaginary part (Y) are measured at once. Note, that the signal coming out from the low pass filter is a phase dependent DC signal which is proportional to the amplitude of the incoming AC sample signal.

The electrical circuit used for measuring small resistivities with a Lock-In amplifier is shown in Figure 6.1. In this case the AC excitation of the sample is an applied AC current. A HP3245A or homemade current source is used. The internal oscillator of the Lock-In in combination with a high ohmic series resistor is sometimes used as current source, too. The amplitude of the current varies from 1 – 10 mA. Common frequencies are < 300 Hz and have to be adjusted from sample to sample. All other settings such as time constant, sensitivity, filters and dynamic reserve are adjusted to optimize the signal resolution. The voltage pins are connected to the Lock-In inputs A-B. The signal is measured using the X and Y mode. As the resistivity of the sample is measured, only the real part X is of importance. For checking the current and phase adjustment a low ohmic reference resistance R1 of 10Ω is connected in series with the sample, which can be measured comfortable by using a switch box.

6.1.3 Collection of data

After mounting the sample on a dip stick, U_l is measured on both sides of the Hall bar during cooling down at zero field for testing the homogeneity. At low temperatures $U(I)$ curves are recorded in order to exclude a possible non-linear behavior of the contacts as well as heating effects. After these preliminary tests and after finding a reasonable value for the current, the measurement procedure can begin. Note, that the measured quantities are always dependent on both variables, temperature T and magnetic flux density B . The measurements are carried out by varying one parameter while keeping the other one constant. For the Hall measurements B is applied in c direction (normal to the Hall bar plane).

- T sweeps at constant B :
The longitudinal resistivity ρ_{xx} is measured at different magnetic fields (up to 14 T) by sweeping T with a certain rate and simultaneously measuring U_l . This is the simplest series of measurements, which already gives significant information about the evolution of ρ_{xx} as a function of T (power law of T dependence, suppression of superconductivity at high fields, upturns at low T).

- B sweeps at constant T :

In order to measure precisely the transverse magnetoresistance $\Delta\rho/\rho$ and the Hall coefficient R_H , B field sweeps at different temperatures are carried out by starting at low T up to 300 K. For $T > 40$ K field sweeps in intervals of 20 K are performed, whereas for $T < 40$ K the T intervals are reduced depending on the doping of the crystals and the related features one would like to study. As $\Delta\rho/\rho$ and particularly R_H are small compared to possible deviations of ρ_{xx} due to small T fluctuations, the stabilization of temperature is of great importance. As described in Chapter 6.1.2 the temperature is stabilized with an accuracy of 10 mK. $\Delta\rho/\rho$ and R_H can be measured simultaneously by using a longitudinal and transverse contact pair, as in general both measurements do not influence each other. The extraction of U_H from the transverse measurement is challenging, as the signal is superimposed by a longitudinal fraction due to a misalignment. Hence, the B field is swept with sweep rates of 1 T/min up to 14 T. During ramping in steps of 0.2 – 1 T the field was stabilized for 20 – 30 s and after stabilization a data point is taken⁴. Thereafter, the field is swept to the next point, stabilized and measured again. In order to avoid hysteresis effects data at the same field positions are also recorded when sweeping down to 0 T. Under field reversal the measurement is repeated by sweeping up to –14 T and a subsequent down sweep to 0 T. This B field sweep is repeated at each temperature. U_H is extracted by using the fact that ρ_{xx} has only even contributions in B :

$$\rho_{xx}(B) = \rho_{xx}(0) \cdot [1 + aB^2 + \mathcal{O}(B^4)], \quad (6.3)$$

and ρ_{xy} has only odd contributions in B

$$\rho_{xy}(B) = R_H \cdot B + \mathcal{O}(B^3). \quad (6.4)$$

Therefore, U_H is extracted according to the following equation:

$$\overline{U_H(B, I)} = \frac{1}{4} \cdot \{ [U_H(+B, +I) - U_H(+B, -I)] - [U_H(-B, +I) - U_H(-B, -I)] \}. \quad (6.5)$$

Note, that for each temperature data are taken for the up and down sweep. Therefore, U_H is the result of 8 independent data points⁵.

6.2 Out-of-plane transport

For the out-of-plane measurements the crystals are prepared and contacted in the same way as for the in-plane measurements. The crystal dimensions are 1.0×0.5 mm² in the ab plane and 0.2 – 0.3 mm in the c direction. The shape of the ab plane is of secondary importance, whereas the thickness t of the sample must be uniform

⁴When multimeters are used, the current is reversed in order to eliminate the zero point offset.

⁵For Lock-In measurements one has 4 independent data points.

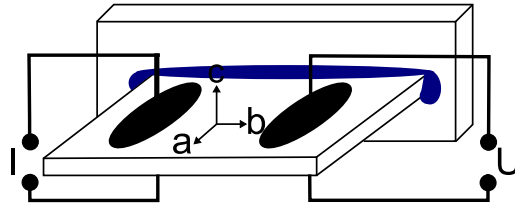


Figure 6.2: Sketch of the experimental setup for the out-of-plane measurements. The crystal is glued with Stycast 2850 in lateral position to a sapphire plate. On one contact pair the current I is applied and the voltage U is measured on the second pair.

throughout the sample and also well determined. There are only four electrical contacts applied to the crystal by a conducting paint, two on each lateral surface. The current I is applied in c direction over one contact pair and the voltage U is measured over the other contact pair (Figure 6.2). The out-of-plane resistivity is given by the ratio

$$\rho_c = (U/I) \cdot (lw/t). \quad (6.6)$$

As $\text{Nd}_{2-x}\text{Ce}_x\text{CuO}_4$ is a highly anisotropic system (cf. Section 7.1) with an anisotropy ratio

$$\rho_c/\rho_{ab} \approx 10^4, \quad (6.7)$$

the equivalent isotropic configuration corresponds to a rod of the same cross sectional area of $1.0 \times 0.5 \text{ mm}^2$ but a thickness t of $2 \cdot 10^2 - 3 \cdot 10^2 \text{ mm}$ and therefore, the current distribution can be regarded as perfectly homogeneous.

Chapter 7

Magnetotransport properties of high quality $\text{Nd}_{2-x}\text{Ce}_x\text{CuO}_4$ single crystals

In the following Chapter the doping dependent normal state transport of $\text{Nd}_{2-x}\text{Ce}_x\text{CuO}_4$ single crystals is discussed. One advantage of the electron doped compounds with respect to the hole doped compounds is their much lower upper critical field B_{c2} . As a consequence, superconducting fluctuation effects, which contribute also above T_c , are expected to be less influential as in $\text{YBa}_2\text{Cu}_3\text{O}_{7-\delta}$ or $\text{La}_{2-x}\text{Sr}_x\text{CuO}_4$ with their high B_{c2} values [182]. For the available magnetic fields up to $\mu_0 H = 15$ T the normal state at $T = 2$ K might be accessible for all doping levels, as the highest value of B_{c2} derived from resistivity measurements amounts to 8 T for the optimally doped $\text{Nd}_{1.85}\text{Ce}_{0.15}\text{CuO}_4$ ¹.

7.1 The in-plane and out-of-plane resistivity

The T dependent zero field and high field (14 – 15 T) in-plane and out-of-plane resistivity curves for $\text{Nd}_{2-x}\text{Ce}_x\text{CuO}_4$ are illustrated in Figure 7.1 and 7.2. The measured resistivity curves $\rho(T, B)$ reveal various properties of the $\text{Nd}_{2-x}\text{Ce}_x\text{CuO}_4$ single crystals, such as the critical temperature T_c , an estimation of the upper critical field B_{c2} , the residual resistivity (which provides information about the impu-

¹The debate about the real upper critical field B_{c2} in high temperature superconductors is still going on. The cuprates exhibit a complex vortex phase diagram (presence of vortex lattice, vortex liquid phases), which complicates the determination of the transition between the superconducting state and normal state. Hence, in resistivity measurements, for example, the discrimination between normal state and vortex liquid state might be difficult and the derived values represent rather the transition between vortex lattice and vortex liquid. Consequently, $B_{c2}(T)$ derived from resistivity measurements might be underestimated. Higher values of $B_{c2}(T)$ in optimally doped $\text{Nd}_{1.85}\text{Ce}_{0.15}\text{CuO}_4$ are deduced from vortex Nernst signal [183] with $B_{c2}(0) \approx 10$ T. New studies of the $B - T$ phase diagram of the electron doped $\text{La}_{2-x}\text{Ce}_x\text{CuO}_4$ compound by means of zero energy Andreev bound states [184] reveal considerably higher values of $B_{c2}(T)$ with $B_{c2}(0) \approx 25$ T.

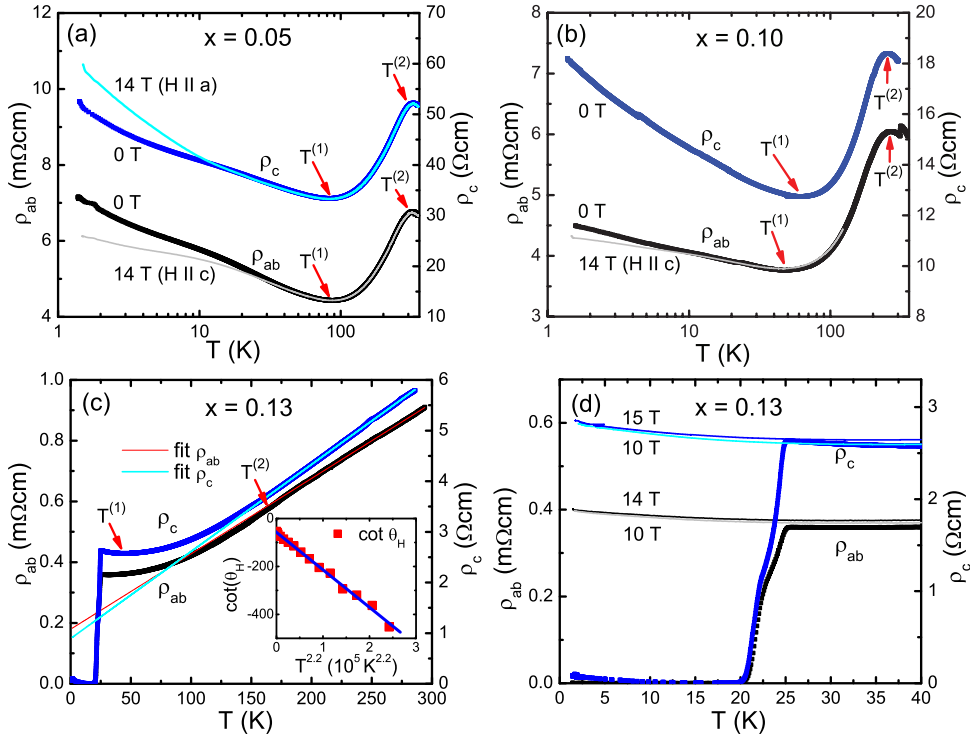


Figure 7.1: In-plane (black) and out-of-plane (blue) resistivity curves for $\text{Nd}_{1.95}\text{Ce}_{0.05}\text{CuO}_4$ (a), $\text{Nd}_{1.90}\text{Ce}_{0.10}\text{CuO}_4$ (b) as well as for $\text{Nd}_{1.87}\text{Ce}_{0.13}\text{CuO}_4$ (c, d) single crystals. The zero field and high field measurements ($\mu_0 H = 14$ T) are plotted. Note, the different T dependence of $\rho_{ab}(T)$ (linear fit) and inverse Hall angle (inset in (c)) for the doping level $x = 0.13$.

urity concentration of the crystals) and the dominant scattering mechanisms of the charge carriers. Therefore, transport measurements are an useful tool in order to characterize the single crystals.

At first glance two general features attract immediately attention when comparing the resistivity data for different doping levels. The upturn in resistivity (i.e. $\frac{d\rho_{ab}}{dT} < 0$) at low temperatures and the metallic behavior ($\frac{d\rho_{ab}}{dT} > 0$) at moderate temperatures up to 300 K. Both regimes are separated by a reversal point, which shifts towards lower temperatures with increasing doping and disappears completely for the overdoped $\text{Nd}_{1.83}\text{Ce}_{0.17}\text{CuO}_4$ sample. For doping levels of $x = 0.15$ and $x = 0.16$ the reversal point lies below T_c and appears only when superconductivity is suppressed by a strong magnetic field (Figure 7.2 (b) and (d)).

Concerning the temperature evolution of the resistivity, the in-plane and out-of-plane resistivity show surprisingly the same features (upturn, reversal point, metallic regime, T_c) for all doping levels. This is in strong contrast to the hole doped $\text{La}_{2-x}\text{Sr}_x\text{CuO}_4$ system, where a semiconducting behavior in the $\rho_c(T)$ curves for doping levels of $x \leq 0.10$ has been found at moderate temperatures up to 300 K

[60]. Consequently, also the resistivity ratio ρ_c/ρ_{ab} in $\text{La}_{2-x}\text{Sr}_x\text{CuO}_4$ evolves different with doping and temperature. It is doping independent at $T = 270$ K for doping levels of $x \leq 0.05$ and decreases with increasing doping, suggesting that the system becomes more three-dimensional in the overdoped regime. The transport results in the underdoped regime of $\text{La}_{2-x}\text{Sr}_x\text{CuO}_4$ have been interpreted in terms of an in-plane charge carrier network (possibly charge ordering), which is responsible for the strange metallic transport close to the Mott insulator limit [143], and an incoherent hopping between these networks in c direction, which is doping independent. In $\text{Nd}_{2-x}\text{Ce}_x\text{CuO}_4$, however, the resistivity anisotropy at 270 K is enhanced with respect to $\text{La}_{2-x}\text{Sr}_x\text{CuO}_4$ (by a factor of 5 at $T = 270$ K for crystals with the same nominal doping $x = 0.05$) and amounts to $7 \cdot 10^3$. For optimally doped and overdoped crystals ρ_c/ρ_{ab} increases slightly up to values of $1 - 2 \cdot 10^4$. The temperature evolution of the resistivity ratio in $\text{Nd}_{2-x}\text{Ce}_x\text{CuO}_4$ evolves moderately for all doping levels (factor < 2).

In the (far) underdoped regime the metallic behavior of the resistivity at intermediate temperatures is another peculiar feature of the electron doped compounds. Figure 7.1 (a), (b) presents the resistivity curves for the underdoped $\text{Nd}_{1.95}\text{Ce}_{0.05}\text{CuO}_4$ and $\text{Nd}_{1.90}\text{Ce}_{0.10}\text{CuO}_4$ crystals, respectively. Both curves reveal two reversal points at doping specific temperatures $T^{(1)}$ and $T^{(2)}$ and a small linear regime with positive slope in-between. For $\text{Nd}_{1.95}\text{Ce}_{0.05}\text{CuO}_4$ the characteristic temperatures amount to $T^{(1)} = 87$ K and $T^{(2)} = 322$ K (extremum) and for $\text{Nd}_{1.90}\text{Ce}_{0.10}\text{CuO}_4$ they come up to $T^{(1)} = 62$ K and $T^{(2)} = 254$ K, respectively. For $T > T^{(2)}$ the resistivity shows again a negative slope. One can get an idea of the physical reason for the strong change in ρ_c and ρ_{ab} when analyzing the optical conductivity data. Onose et al. [2] have shown that $T^{(2)}$ coincides with the pseudogap temperature T^* , at which the optical conductivity $\sigma(\omega)$ loses spectral weight at energies < 0.5 eV. Additionally, with T^* a concomitant evolution of a Drude peak in the limit $\omega \rightarrow 0$ is observed, which is interpreted in terms of a change from an incoherent to a coherent charge transport of the electron pockets in antinodal direction. The pseudogap is believed to play a crucial role in the out-of-plane transport, depending on its position in the Brillouin zone. For $\text{La}_{2-x}\text{Sr}_x\text{CuO}_4$, for instance, the out-of-plane transport – described by the hopping integral t_\perp and dominated by the charge carriers in antinodal direction – is reduced due to the pseudogap formation in antinodal direction. Hence, the gap opening in antinodal direction might explain the different evolution of ρ_c and ρ_{ab} . For $\text{Nd}_{2-x}\text{Ce}_x\text{CuO}_4$, however, the pseudogap evolves close to the nodal position and is expected to influence the out-of-plane transport only marginally. Thus, the qualitatively same evolution of ρ_c and ρ_{ab} at moderate temperatures is plausible. According to the interpretation of Onose et al. the second reversal point at $T^{(2)}$ and the following decrease in resistivity for $T < T^{(2)}$ are associated with the formation of coherent charge carriers below $T^{(2)}$.

The superconducting underdoped $\text{Nd}_{1.87}\text{Ce}_{0.13}\text{CuO}_4$ sample (Figure 7.1 (c)) exhibits at first glance a different temperature dependence in $\rho_{ab}(T)$ and $\rho_c(T)$, which

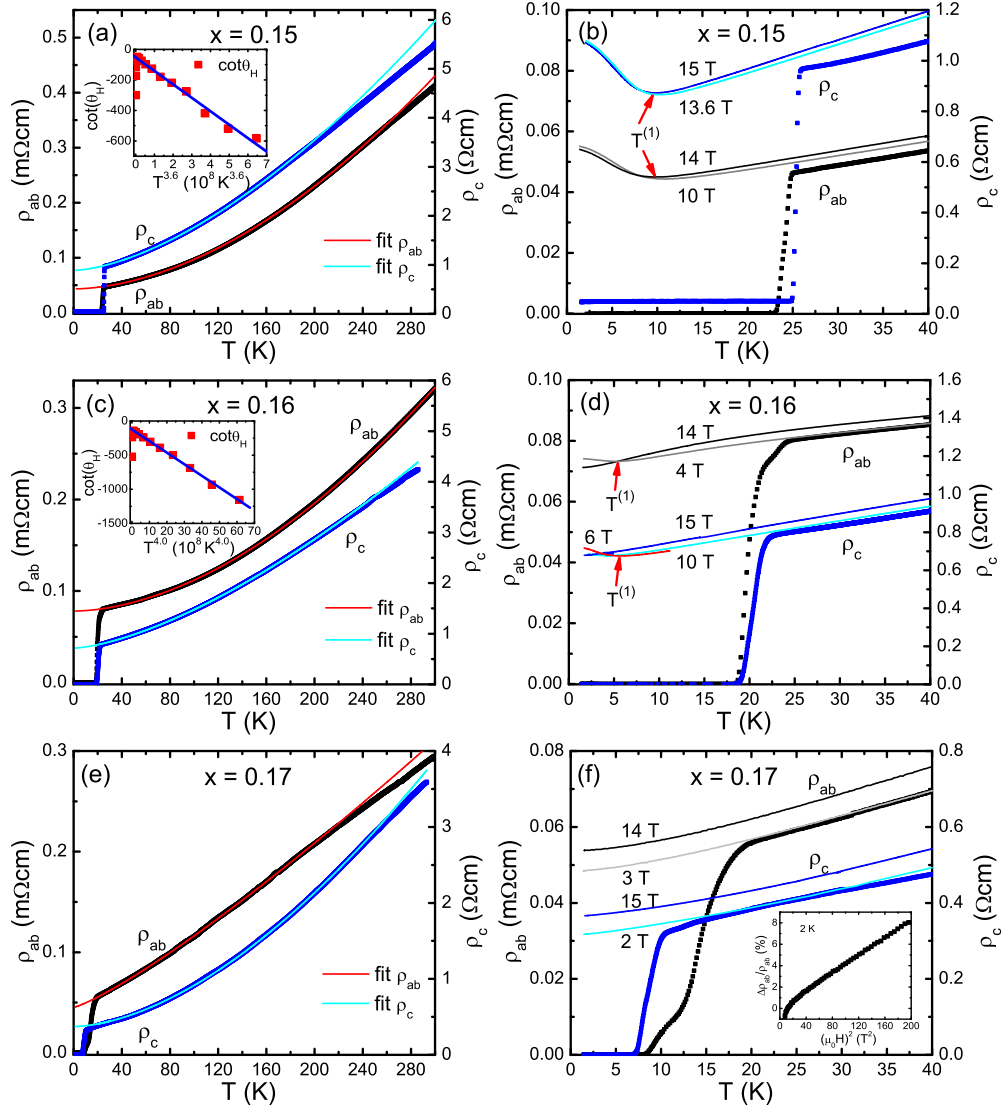


Figure 7.2: In-plane (black) and out-of-plane (blue) resistivity curves for $\text{Nd}_{1.85}\text{Ce}_{0.15}\text{CuO}_4$ (**a**, **b**), $\text{Nd}_{1.84}\text{Ce}_{0.16}\text{CuO}_4$ (**c**, **d**) and $\text{Nd}_{1.83}\text{Ce}_{0.17}\text{CuO}_4$ (**e**, **f**) single crystals. The magnetic field is applied perpendicular to the CuO_2 layers. The insets show the inverse Hall angle $\cot\theta_H$ of the in-plane measurements.

resembles to that of the optimally and overdoped crystals. Nevertheless, at closer examination the features in the T dependence of the normal state resistivity are rather related to the doping level $x = 0.10$ than to $x = 0.16$. In particular, $T^{(1)}$ is shifted to temperatures slightly above T_c and amounts to 32 K for the $\rho_{ab}(T)$ measurement and to 44 K for the $\rho_c(T)$ measurement. The difference in $T^{(1)}$ in both measurements might be due to a small variation in doping, although both samples arise from the same batch and show the same transition curves (Figure 7.1 (d)). For $T > T^{(1)}$, the curves show a positive slope up to 300 K and the second reversal point is vanished. However, there is a characteristic temperature $T^{(2)} = 160 \pm 10$ K, at which the slope (first derivative) of the $\rho_{ab}(T)$ curve reveals a kink. Above 160 K the resistivity follows an almost linear dependence (see linear fit in Figure 7.1 (c) with a slope of $2.48 \cdot 10^{-3}$ m Ω cm and an ordinate intersection of 0.18 m Ω cm), whereas for $T < T^{(2)}$ the resistivity drops initially below the linear fit and shows a complex curved behavior, which cannot be fitted by a power law. This S-shaped behavior at $T^{(2)}$ resembles the $\rho_{ab}(T)$ curve in underdoped $\text{La}_{2-x}\text{Sr}_x\text{CuO}_4$ [23], which has been interpreted in terms of pseudogap opening. Interestingly, in the out-of-plane transport the S-shaped drop in resistivity at $T^{(2)}$ is absent. The curve is linear in the temperature range from 160 K to 300 K and deviates smoothly from linearity towards higher values for $T < 160$ K. The in-plane inverse Hall angle $\cot \theta_H$, which is related to the scattering rate Γ in the same way as the resistivity, follows a $T^{2.2}$ dependence over the whole temperature range (inset in Figure 7.1 (c)). Hence, also the electron doped cuprates reveal a similar "separation" of lifetimes as the hole doped cuprates (cf. phenomenological discussion in Chapter 5).

At doping levels $x \geq 0.15$, a fundamental change in the features of the T dependence of the normal state resistivity can be observed. $T^{(2)}$ disappears and the low temperature upturn is superposed by the superconducting regime. It is only visible at high magnetic fields. For the optimally doped $\text{Nd}_{1.85}\text{Ce}_{0.15}\text{CuO}_4$ sample (Figure 7.2 (a, b)), $T^{(1)}$ amounts to 10 K. The normal state in-plane resistivity obeys a power law with $\rho_{ab}(T) = \rho_{ab,0} + AT^{1.8}$, where the residual resistivity $\rho_{ab,0}$ and A are estimated to be $4.34 \cdot 10^{-2}$ m Ω cm and $1.35 \cdot 10^{-5}$ m Ω cm/K^{1.8}. For temperatures $T > 200$ K the resistivity deviates from the power law and becomes linear. The inverse Hall angle follows a $T^{3.6}$ dependence for temperatures $T \geq 50$ K, which is twice the exponent of the ρ_{ab} dependence. A deviation from power law towards linearity at already $T = 180$ K is also observed in the ρ_c curve. For $T < 180$ K the derivative of the curve suggests a resistivity fit of the form $\rho_c(T) = \rho_{c,0} + BT + AT^2$ with $\rho_{c,0} = 0.77$ Ω cm, $B = 5.96 \cdot 10^{-3}$ Ω cm/K and $A = 3.99 \cdot 10^{-5}$ Ω cm/K².

The upturn in the overdoped $\text{Nd}_{1.84}\text{Ce}_{0.16}\text{CuO}_4$ sample (Figure 7.2 (c, d)) can be suppressed in both the in-plane and out-of-plane transport, when a magnetic field of 14 T is applied perpendicular to the CuO_2 sheets. In this case $\rho_c(T)$ decreases linearly for $T < 40$ K and $\rho_{ab}(T)$ reveals a sublinear T dependence. At intermediate magnetic fields (4 – 6 T) the upturn behavior is still visible below $T^{(1)}$ and

amounts to 5.5 K for both in-plane and out-of-plane resistivity curves. Similar to the optimally doped sample, $\rho_{ab}(T)$ obeys the relation $\rho_{ab}(T) = \rho_{ab,0} + AT^{1.8}$ with $\rho_{ab,0} = 7.81 \cdot 10^{-2} \text{ m}\Omega\text{cm}$ and $A = 8.49 \cdot 10^{-6} \text{ m}\Omega\text{cm}/\text{K}^{1.8}$ for temperatures $T > 40 \text{ K}$. At $T \geq 200 \text{ K}$, a deviation towards lower powers ($T^{1.6}$) is observed. The inverse Hall angle shows a $T^{4.0}$ dependence for $T \geq 80 \text{ K}$. Furthermore, $\rho_c(T)$ reveals the same two temperature regions with lower powers of $T^{1.5}$ and $T^{1.3}$. The residual resistivity amounts to $0.72 \text{ }\Omega\text{cm}$.

The doping level $x = 0.17$ (Figure 7.2 (e, f)) has an exceptional position within the $\text{Nd}_{2-x}\text{Ce}_x\text{CuO}_4$ sample set. This is not only confirmed by the positive Hall signal at low and moderate temperatures (see Section 7.3) but also by the normal state transport $\rho(T, B)$. For instance, there is no upturn and related to this there is no negative magnetoresistance observable for temperatures down to 1.4 K (see inset in Figure 7.2 (f)). Superconductivity is already fully suppressed for applied magnetic fields of 3 T perpendicular to the CuO_2 layers and $\rho(B, T = \text{const})$ evolves with B^2 . Moreover, $\rho_{ab}(T)$ can be fitted by $\rho_{ab}(T) = \rho_{ab,0} + AT^{1.2}$ with $\rho_{ab,0} = 4.52 \cdot 10^{-2} \text{ m}\Omega\text{cm}$ and $A = 2.83 \cdot 10^{-4} \text{ m}\Omega\text{cm}/\text{K}^{1.2}$ and flattens again for $T > 200 \text{ K}$. In comparison to the nearly linear in-plane resistivity, $\rho_c(T)$ exhibits a stronger curvature and follows a $T^{1.7}$ dependence for temperatures up to 220 K with a residual resistivity of $0.37 \text{ }\Omega\text{cm}$. For higher temperatures a crossover to linear behavior appears.

In the metallic regime the residual resistivities provide a good test for the crystal purity. $\rho_{c,0}$ decreases steadily with increasing doping from $0.89 \text{ }\Omega\text{cm}$ for the underdoped sample $x = 0.13$ to $0.37 \text{ }\Omega\text{cm}$ for the overdoped sample $x = 0.17$. For the in-plane measurements $\rho_{ab,0}$ is minimal at the doping level $x = 0.15$. In comparison to $x = 0.15$, $\rho_{ab,0}$ is increased by 80% for $x = 0.16$ and by 4% for $x = 0.17$, respectively. This demonstrates clearly the very high quality of the optimally doped sample and the difficulty to grow high purity crystals in the overdoped regime close to the solubility limit of the dopant. In literature the residual resistivity values vary considerably, what might be due to the pronounced sensitivity of the resistivity on the annealing treatment [185]. For optimally doped $\text{Nd}_{1.85}\text{Ce}_{0.15}\text{CuO}_4$, values of $\rho_0 \approx 15 \text{ }\mu\Omega\text{cm}$ ([81], thin films), $\rho_0 \approx 20 \text{ }\mu\Omega\text{cm}$ ([139], thin films), $\rho_0 \approx 10 \text{ }\mu\Omega\text{cm}$ ([2], single crystals) have been reported. On the other hand, much higher values for overdoped $\text{Nd}_{2-x}\text{Ce}_x\text{CuO}_4$ single crystals ($\approx 45 \text{ }\mu\Omega\text{cm}$ for $x = 0.17$ and $\approx 25 \text{ }\mu\Omega\text{cm}$ for $x = 0.20$) [157] have been found. For comparison, the $\text{Pr}_{2-x}\text{Ce}_x\text{CuO}_4$ system reveals considerably higher ρ_0 values for all doping levels [153].

The remarkable "coherence" between in-plane and out-of-plane transport poses the question of the transport mechanism in c direction. In principle, the metallic behavior of the in-plane resistivity within the observed temperature interval (for all doping levels around the superconducting dome) is preserved in the out-of-plane transport, suggesting therefore a coherent transport mechanism in c direction. However, the same behavior of $\rho_{ab}(T)$ and $\rho_c(T)$ is not an unambiguous hint for

a coherent transport, as it has been shown [186] that $\rho_c(T)$ can image the in-plane dependence even though the transport is incoherent. So far, the existence of a quasi three-dimensional Fermi surface was only reported for heavily overdoped Tl2201 [5]. In principle, the transport is coherent when the interlayer hopping time satisfies the relation $\tau_c = \frac{\hbar}{t_c} < \tau$, where t_c is the interlayer transfer integral and τ the in-plane scattering time. In this case an electron might tunnel through multiple layers before dephasing occurs. In the incoherent regime, i.e. $\tau_c = \frac{\hbar}{t_c} \gg \tau$, the coherent tunneling is blocked [186] as the carriers undergo multiple dephasing scattering events in the highly conductive layers before tunneling. However, one can assume a weakly incoherent scenario, where coherent tunneling takes place only between neighboring layers (single tunneling process) due to a finite t_c before dephasing of the charge carriers occurs again. In this case the transfer integral is renormalized to $t'_c = \frac{t_c^2 \tau}{\hbar}$. Note, that the transfer integral is then governed by the in-plane scattering time. In this context it has been shown [186] that, although the out-of-plane transport is (weakly) incoherent, ρ_c can be expressed via ρ_{ab} :

$$\rho_c \propto \rho_{ab} \cdot \left(\frac{a}{d}\right)^2 \cdot \left(\frac{t_{ab}}{t_c}\right)^2. \quad (7.1)$$

Here, a is the in-plane lattice constant, d the interlayer spacing and t_{ab} the intralayer transfer integral. Thus, as fully consistent with the experimental findings, ρ_c mirrors the in-plane transport and depends on the ratio of the transfer integrals.

Concerning the power law behavior of the resistivity curves, in-plane and out-of-plane curves are fitted best by using a bare $\rho_0 + AT^\alpha$ relation without a linear term (with the exception of ρ_c for $\text{Nd}_{1.87}\text{Ce}_{0.13}\text{CuO}_4$), where $\alpha < 2$ for all doping levels, which seems to be smaller for the out-of-plane measurements. In literature a pure T^2 dependence is reported at least for a small temperature regime above 40 – 50 K [81, 139, 187] and a flattening occurs at higher temperatures (≈ 200 K). Deviations from the value of 2 in the power law are assigned to some imperfections in the system and the origin of the T^2 term is believed to arise from electron-electron scattering. For this scattering mechanism in a three-dimensional Fermi liquid one obtains [172]

$$\rho(T) = \rho_0 + A_{e,e} T^2. \quad (7.2)$$

The deviations from a strict T^2 at higher temperatures are often explained using a two-dimensional expression of the electron-electron interaction [139]

$$\rho(T) = \rho_0 + A_{e,e} \left(\frac{T}{T_F}\right)^2 \ln\left(\frac{T_F}{T}\right). \quad (7.3)$$

However, the deviation from T^2 behavior might be rather explained by the parallel resistor model (application of the MIR limit, see Chapter 5) than by a proposed transition from three to two dimensions. In addition, the scattering amplitude for electron-electron interaction (fit parameter $A_{e,e}$) is in the order of $10^{-2} \mu\Omega \text{ cm/K}^2$, which is 4 orders of magnitude higher than for alkali metals. Therefore, it is questionable, if the observed T^2 dependence of the scattering rate is only

due to electron-electron interaction. It has been shown [188] that scattering on spin fluctuations leads to a quadratic dependence in T , as well.

7.2 The upturn behavior at low temperatures

For the discussion of the upturn behavior in the resistivity vs. temperature curves at low temperatures only the $\rho_{ab}(T)$ curves are used, as the $\rho_c(T)$ curves reveal the same features. The reversal point $T^{(1)}$, at which the resistivity starts to increase with decreasing temperature is strongly doping dependent (Figure 7.3 (b)) and disappears for the doping level $x = 0.17$. For $T < T^{(1)}$, ρ_{ab} follows roughly a $\log(1/T)$ dependence with some doping dependent deviations for $T \rightarrow 1.4$ K (note the $\log T$ scale in Figure 7.3 (a) and 7.1 (a)). For instance, at high doping levels of $x = 0.16$, $x = 0.15$ and $x = 0.13$ (not shown), the curves flatten towards smaller values below $T = 3$ K, $T = 5$ K and $T = 6.5$ K, respectively. However, no trend of saturation could be deduced at the lowest accessible temperature of 1.4 K from this sublogarithmic behavior.

The strongly underdoped sample ($x = 0.05$) shows a nearly $\log(1/T)$ dependence in the temperature range from 18 to 40 K and bends towards smaller values for $T < 13.5$ K. The same deviation from linearity in the upturn regime (even though not as pronounced) has also been observed for the doping level $x = 0.10$ at about $T = 12$ K. In the sublinear regime both curves reveal a strong decrease in $\rho_{ab}(T)$ when a magnetic field of $\mu_0 H = 14$ T is applied perpendicular to the CuO_2 sheets. This perpendicular, negative magnetoresistance (NMR) within the upturn regime is found for all doping levels. At 2 K, $\Delta\rho(14\text{T})/\rho$ amounts to -11.6% and -4% for $x = 0.05$ and $x = 0.10$, respectively. In the superconducting regime the zero field upturn is hidden and the remnants are observed at high magnetic fields. Thus, the field evolution of the $\rho_{ab}(B)$ curves for the corresponding doping levels is difficult to study due to the influence of superconductivity. For the optimally doped $\text{Nd}_{1.85}\text{Ce}_{0.15}\text{CuO}_4$ sample (Figure 7.3 (c)) the magnetic field sweeps peak at about 10 T, followed by a negative slope. From the small negative edge only a crude linear extrapolation is possible in order to estimate an extrapolated field of $\mu_0 H_e = 23$ T, at which the upturn is expected to be fully suppressed at $T = 1.4$ K. It cannot be excluded that $\rho_{ab}(B)$ follows a $-\log B$ dependence at higher fields, which of course would lead to higher values of H_e . Evidence for a $\log B$ behavior of $\Delta\rho/\rho$ arises from the underdoped $x = 0.05$ and overdoped $x = 0.16$ sample. For the latter one and for fields $\mu_0 H \geq 10$ T (i.e. $H > H_{c2}$), the curve follows roughly $-\log B$. The crossover to metallic behavior is reached for applied fields of $\mu_0 H_e = 10$ T.

For the doping level $x = 0.05$, $\Delta\rho/\rho$ is logarithmic in B at high fields and deviates from this behavior when approaching the zero field. An extrapolated field of $\mu_0 H_e \approx 500$ T is calculated from the negative slopes at low temperatures. One important aspect is the anisotropy of the MR in the upturn region, which can easily

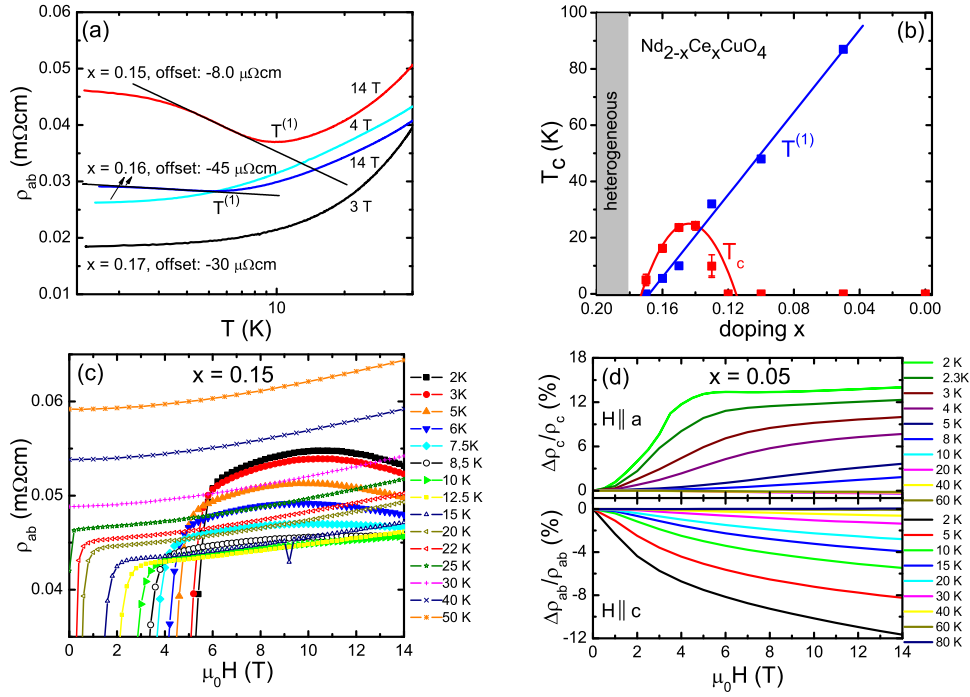


Figure 7.3: (a) Low temperature in-plane resistivity plotted vs. $\log T$. The curves are plotted with offset for a better comparison. The straight lines represent $\log 1/T$ fits. (b) Doping dependent evolution of the reversal point $T^{(1)}$ (upturn regime). (c) $\rho_{ab}(B)$ curves at low temperatures obtained from doping level $x = 0.15$. (d) Magnetoresistance data of the underdoped $x = 0.05$ sample for $H \parallel a$ (upper chart) and $H \parallel c$ (lower chart). The corresponding $\rho(T)$ curves are shown in Figure 7.1.

be investigated in the far underdoped regime ($x = 0.05$)². In contrast to the observed NMR for magnetic fields applied perpendicular to the CuO_2 sheets, the MR is positive for temperatures $T \leq 8$ K (Figure 7.3 (d)) when the magnetic field is applied parallel to the CuO_2 sheets. The positive MR consists of two regimes, a steep increase at low fields and a moderate, almost saturating behavior at higher fields. This crossover in the magnetoresistance for applied fields parallel to the CuO_2 sheets has been interpreted as a transition of the AFM spin structure from a noncollinear to a collinear one [189] (cf. Section 2.3.2 for the spin structure).

The reason for the upturn³ in the resistivity vs. temperature curves for $T \rightarrow 0$, and related to it for some unidentified localization of itinerant charge carriers is up to now not fully understood. It is widely believed that the upturn is primarily

²The upturn region at doping levels $x = 0.15$ and $x = 0.16$ is not accessible for field orientations parallel to the CuO_2 planes due to the high B_{c2}^{\parallel} fields.

³Note, that in literature [146, 156] the terminology of a metall-insulator (MI) crossover is often used. This notation might be somewhat misleading, as the resistivity change is very small (much less than one order of magnitude). For example the doping level $x = 0.05$ shows a ρ_{ab} value at $T = 2$ K ($\mu_0 H = 0$ T curve) with an increment of only 35% with respect to the minimum at $T^{(1)}$. Upon doping this magnitude is decreasing further.

a disorder-driven effect [146, 156], as shape and appearance of the upturn depend on the cuprate system [146, 190] and the detail of fabrication. For example, for $\text{Nd}_{2-x}\text{Ce}_x\text{CuO}_4$ the literature is contradicting concerning the rigid $\log(1/T)$ dependence down to lowest temperatures [191–194]. In order to find a useful criterion for the estimation of a disorder-driven metal-insulator transition, the idea from Ioffe and Regel is used [195], who argued that conventional metallic transport breaks down, when the mean free path l becomes comparable to the interatomic spacing or k_F^{-1} (see also Section 5.1.1). In other words a metal-insulator transition is expected for $k_F l = 1$. For a quasi two-dimensional system with distance $d = c/2$ between the conducting layers a simple relation between the measured resistivity ρ and the Ioffe-Regel criterion is obtained by using standard transport theory⁴: $\rho_{ab} = \frac{\hbar}{e^2} \cdot \frac{d}{k_F l}$. Note, that $\frac{\rho_{ab}}{d}$ is the sheet resistance, which is directly proportional to the von Klitzing constant $\frac{\hbar}{e^2} = 25812.807 \Omega$.

Hence, for $\text{Nd}_{2-x}\text{Ce}_x\text{CuO}_4$ a resistivity value of $\rho_{ab} = 1.558319 \text{ m}\Omega\text{cm}$ corresponds to $k_F l = 1$. With the exception of the underdoped crystals of $x = 0.05$ and $x = 0.10$, where a value of $k_F l = 0.3$ and $k_F l = 0.4$ is deduced – corresponding to ρ_{min} at $T^{(1)-}$, all other samples are below this limit in the temperature range from 1.4 K to 300 K. For doping $x = 0.15$ and $x = 0.16$ the transition at applied fields of 14 T and 4 T occurs at values of $k_F l = 35$ and $k_F l = 21$, respectively. For comparison, the residual resistivity for $\text{Nd}_{1.83}\text{Ce}_{0.17}\text{CuO}_4$ corresponds to a comparable value of $k_F l = 36$. Hence, there is a crossover to insulating behavior at resistivity values, which correspond to values of $k_F l \gg 1$, suggesting therefore the strange nature of the normal state transport at low temperatures. This is a typical behavior of so-called bad metals [196], which is also observed in hole doped $\text{La}_{2-x}\text{Sr}_x\text{CuO}_4$ [146]. Additionally, from far underdoped $\text{La}_{2-x}\text{Sr}_x\text{CuO}_4$ a metallic behavior of ρ_{ab} is known [143], although the Ioffe-Regel limit is strongly violated ($k_F l = 0.1$).

In theory two effects can be invoked in order to explain a $\log T$ correction of the conductivity and a $-\log B$ behavior of the magnetoresistance: two-dimensional weak localization and the Kondo effect.

The weak localization is a quantum correction effect to the conductivity in disordered metals [195, 197]. In principle, an electron, which undergoes elastic scattering processes on impurities, can move on various paths from point A to point B . In order to calculate the conductivity the total scattering probability for the motion from point A to B has to be evaluated. According to quantum mechanics this is given by the square of the modulus of the sum of all amplitudes of the different paths. Hence, the total probability arises from the sum of the probabilities of each single path and an interference term, which in principle disappears due to the strong differences in phase for different paths when summing up. There are, however, special self-intersecting trajectories with loops, which can be traversed in two opposite directions. In this case the amplitudes for both cycles are coherent and the interference term leads to an increase in the scattering probability, which is twice as large as the classical sum of the probabilities. Hence, due to coherent backscat-

⁴ $\sigma = \frac{ne^2\tau}{m^*} = \frac{ne^2l}{vm^*} = \frac{e^2}{\hbar} \cdot \frac{d \cdot n_{2dim}}{k_F} \cdot (k_F l)$ and with $k_F = d \cdot \sqrt{n_{2dim} \cdot 2\pi}$ follows: $\sigma = \frac{e^2}{\hbar} \cdot \frac{k_F l}{d}$

tering the conductivity decreases and the resistivity increases, respectively. For the quantitative deduction one has to account for the dimensionality of the system and the fact that coherent interference is only possible when the elastic scattering time τ_{el} is much smaller than the time scale of coherence of the charge carriers τ_ϕ , i.e. $\tau_{el} \ll \tau_\phi$. This is the reason why weak localization is only observed at low temperatures in the region of the residual resistivity, as the dephasing inelastic scattering due to electron-phonon or electron-electron interactions dominates at higher temperatures. For the correction of the conductivity the following expression is derived [195, 197]:

$$\Delta\sigma_{2dim} = \sigma(T) - \sigma_0 \propto -\frac{e^2}{\hbar} \cdot \ln\left(\frac{T_0}{T}\right). \quad (7.4)$$

As a consequence, the weak localization leads to the $\log(1/T)$ dependence in the resistivity. For small corrections ρ_{ab} is given by

$$\rho_{ab} = \rho_0 + \rho_0^2 \cdot C \cdot \ln\left(\frac{T_0}{T}\right), \quad (7.5)$$

where C is a constant and T_0 a characteristic temperature.

In addition, the negative magnetoresistance for magnetic fields applied perpendicular to the current direction results from the fact that the momentum \vec{p} has to be replaced by $\vec{p} - \frac{e}{c} \cdot \vec{A}$, where the vector potential \vec{A} causes a phase difference of $2\pi \cdot \frac{\Phi}{\Phi_0}$ between both amplitudes. This phase difference gives rise to a destruction of the positive interference, resulting therefore in a negative magnetoresistance. The magnitude is estimated to be [197]

$$\sigma_{2dim}(B) - \sigma_0 \propto \frac{e^2}{\hbar} \cdot \ln\left(\frac{eBD\tau_\phi}{\hbar c}\right), \quad (7.6)$$

where D is the diffusion constant and $L = \sqrt{D\tau_\phi}$ the diffusion length of the electrons. The product $BD\tau_\phi \propto \Phi$ reflects the magnetic flux, which penetrates the loop trajectory. Thus, the magnitude of the effect depends on the penetrating flux and hence, a strong anisotropy in the magnetoresistance is expected when the field is turned towards in-plane direction. In addition, due to τ_ϕ in the numerator a strong temperature dependence is expected, as well.

In literature, two-dimensional weak localization has often been used in order to explain the metal-insulator transition at low temperatures [2, 146, 193]. However, at least for $\text{Nd}_{2-x}\text{Ce}_x\text{CuO}_4$ there are some experimental aspects, which are strongly contrary to the conventional weak localization theory of a two-dimensional disordered metal:

- For all doping levels there are remarkable deviations from a predicted pure logarithmic divergence. At certain doping specific temperatures the upturn deviates strongly, showing a sublogarithmic behavior.
- The doping dependent scaling of the reversal point $T^{(1)}$ is difficult to understand within weak localization (Figure 7.3 (b)). The high onset temperature

of the upturn in the underdoped region is incompatible with the basic assumption of $\tau_\phi \gg \tau_{el}$.

- Indeed, there is evidence for a $\log B$ behavior of the magnetoresistance. However, it was shown by Sekitani et al. [191] that the anisotropy of MR does not follow a cosine dependence when the field is turned towards parallel position. In addition, the data show a strange positive MR at low temperatures, when the field is applied parallel to the CuO_2 layers (Figure 7.1 (b)). Thus, the upturn behavior is rather related to a spin effect than to conventional disorder induced localization.

The Kondo effect describes the interaction between the spin of itinerant charge carriers $\vec{\sigma}$ and the magnetic moment of localized magnetic impurities \vec{S} . This leads to a scattering amplitude of [197]

$$\frac{J}{n} \cdot (\vec{\sigma}\vec{S})_{\sigma'\sigma} \cdot \left\{ 1 - \frac{J}{n} D(E_F) \ln \left(\frac{\tilde{E}}{\max(|\xi|, T)} \right) \right\}, \quad (7.7)$$

where $\xi = E_k - \mu$, $D(E_F)$ is the DOS, n the impurity concentration, \tilde{E} a characteristic energy and J the exchange constant. The logarithmic term is a second order correction to the first one. For $J < 0$ the amplitude and therefore the resistivity increases as a scattering process with a flip of the electron spin is allowed. For a ferromagnetic interaction ($J > 0$) the spin flip is forbidden due to spin conservation, and the amplitude decreases. The Kondo contribution to the resistivity is given by the square of the scattering amplitude

$$\rho_K = \rho_J^{(0)} \cdot \left\{ 1 - 2 \frac{J}{n} D(E_F) \ln \left(\frac{\tilde{E}}{k_B T} \right) \right\}. \quad (7.8)$$

Thus, for $J < 0$ the resistivity diverges logarithmically with decreasing temperature. Considering the residual resistivity ρ_0 and some general T^p dependent contribution to the resistivity, one can see immediately that for decreasing temperatures the resistivity passes through a minimum before showing the logarithmic upturn. Note, that the upturn does not diverge to infinity. For $T < T_K$, with the Kondo temperature $T_K = \tilde{E} \cdot \exp(-\frac{n}{JD(E_F)})$, the logarithmic correction is large and Equation 7.8 is no longer valid. Calculations have shown that for the limit $T \rightarrow 0$ the resistivity tends to a finite value [198]. Concerning the magnetoresistance behavior a negative $\log B$ dependence with saturation for $B \rightarrow 0$ is expected [191]. An applied magnetic field polarizes the spins of the impurities, so that the probability of spin-flip scattering is diminished. In principle, the magnetoresistance should be isotropic for the Kondo effect.

The Kondo effect might explain the majority of the observed features such as the finite maximum value for $T \rightarrow 0$ and the $\log B$ dependence of the magnetoresistance with saturation. Nevertheless, there are two fundamental problems left: First, the magnetoresistance is anisotropic. Here, Sekitani et al. [191] have argued that the anisotropy can be explained by an anisotropic g value due to the crystal

field. Secondly, the unknown nature of possible Kondo scattering centers. Generally, an interaction between charge carriers and the magnetic moments of the rare earth ions can be ruled out, as $\text{La}_{2-x}\text{Sr}_x\text{CuO}_4$ with the non-magnetic La^{3+} shows the same features. In addition, assuming rare earth scatters, it is difficult to explain the doping dependent scaling of the upturn. Thus, possible scatters must lie within the CuO_2 layers. It was suggested that local spins of Cu^{2+} act as Kondo scatters [191].

When trying to explain the metal-insulator transition, one aspect has always been ignored. There is a clear doping dependency, which is not considered in both theories. The characteristic temperature $T^{(1)}$ scales nearly linearly with doping and becomes zero close to the doping level $x = 0.17$ (Figure 7.3 (b)). Hence, the upturn behavior in $\rho_{ab}(T)$ might be associated with an additional scattering channel, which arises from an unusual strong coupling of the charge carriers with AFM fluctuations. The upturn evolution seems to correlate with the Fermi surface evolution of $\text{Nd}_{2-x}\text{Ce}_x\text{CuO}_4$ [1], and a completely metallic behavior for $T \rightarrow 0$ might be obtained at doping levels $x \geq x^*$, where the Fermi surface is fully restored. In literature a QCP is often suggested at $x = x^*$, at which a magnetic quantum phase transition occurs [1, 11].

7.3 The Hall effect and magnetoresistance

7.3.1 The Hall resistivity

The Hall resistivity $\rho_{xy}(B)$, from which the Hall coefficient R_H is obtained, is shown in Figure 7.4. The determination of the Hall coefficient is not straightforward, especially at low temperatures where large magnetic fields are required in order to suppress superconductivity and to restore completely the normal state (cf. brief discussion at the beginning of this Chapter). Nevertheless, with available magnetic fields of 14 T the normal state in $\text{Nd}_{2-x}\text{Ce}_x\text{CuO}_4$ can be explored down to low temperatures. Obviously, in the superconducting regime the Hall signal is expected to disappear. However, there is a peak structure visible in all doping levels $0.13 \leq x \leq 0.17$, which increases with T and shifts towards smaller magnetic field values. The appearance correlates with the transition in $\rho_{xx}(B, T = \text{const})$. This contribution to the Hall signal is assigned to flux flow.

For $\text{Nd}_{1.87}\text{Ce}_{0.13}\text{CuO}_4$ (Figure 7.4 (a)), ρ_{xy} is linear in the magnetic field with a negative slope over the entire temperature range well above B_{c2} (≈ 8 T at 2 K, extrapolated from $\rho_{xx}(B)$). The slope decreases steadily with increasing temperature. A similar behavior is also found in the overdoped $\text{Nd}_{1.83}\text{Ce}_{0.17}\text{CuO}_4$ (Figure 7.4 (d)), though the sign is reversed. B_{c2} is estimated to be ≈ 3 T, so that the Hall coefficient can be determined easily from the linear slope of the field sweeps. Note the large positive value in $\rho_{xy}(B)$ for $T \leq 20$ K, which decreases rapidly and reaches a value very close to zero at $T = 140$ K. For higher temperatures the change to negative sign is clearly visible, although the error of the extracted Hall values is not negligible due to the low amplitudes of the measured signal (< 10 nV).

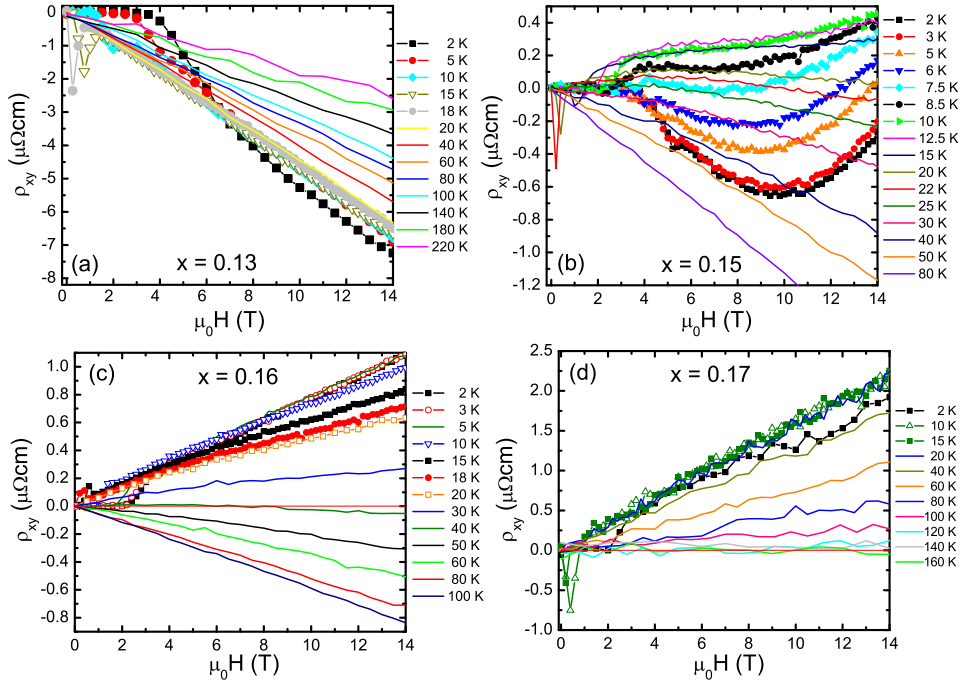


Figure 7.4: Measurements of the Hall resistivity ρ_{xy} at low temperatures for single crystals with nominal Ce-concentration $x = 0.13$ (a), $x = 0.15$ (b), $x = 0.16$ (c) and $x = 0.17$ (d). The magnetic field is applied perpendicular to the CuO_2 sheets.

For $\text{Nd}_{1.84}\text{Ce}_{0.16}\text{CuO}_4$ (Figure 7.4 (c)) the sign change is shifted to temperatures close to 40 K. At low temperatures, $\rho_{xy}(B)$ shows a clear dominance of a hole-like contribution to the Hall signal. The curves are fully linear in the magnetic field with a positive slope for temperatures up to 10 K. In the temperature range between 10 K and 50 K, $\rho_{xy}(B)$ deviates slightly from linearity and with increasing field it starts bending towards negative slope. For $T \geq 60$ K, ρ_{xy} follows a straight line again.

For optimally doped $\text{Nd}_{1.85}\text{Ce}_{0.15}\text{CuO}_4$ (Figure 7.4 (b)), the ρ_{xy} curves are linear in H for temperatures $T \geq 50$ K. Below this temperature they reveal a complex behavior. In the temperature interval $2 \leq T \leq 10$ K, $\rho_{xy}(B)$ shows a reversal point with positive slope for magnetic fields $\mu_0 H > 10$ T. This unusual behavior is only observed for optimal doping within the upturn region and is similar to the evolution of the $\rho_{xx}(B)$ curves at these temperatures. Thus, it is difficult to extract the normal state in this temperature regime due to influences arising from the mixed state. The positive linear slope at the high field end of the curves (≥ 12 T) might reflect the normal state at low temperatures (remember $B_{c2} \approx 10$ T at $T = 5$ K, estimated from the Nernst signal [183]). At $T = 8.5$ K, the Hall signal is entirely positive and remains positive for temperatures up to 20 K, while simultaneously the slope for magnetic fields > 5 T is curving towards negative values and changes sign between 15 – 20 K. Above 20 K, the contribution from the electron band prevails

more and more over the contribution from the hole band. At $T = 30$ K, ρ_{xy} becomes completely negative. The curves recorded at temperatures of 30 K and 40 K can be well described by considering the next order of the Jones Zener expansion, i.e. $\rho_{xy} \propto R_H B + R_3 B^3$. The low temperature evolution of R_H (see Figure 7.10 (b)), is deduced from the linear slopes at high magnetic fields, which is the only reasonable criterion. The temperature evolution of R_H passes continuously into the regime where ρ_{xy} is only given by a straight line. The sign change in R_H occurs at $T \approx 18$ K. We are well aware of the fact that the absolute value of R_H as well as the temperature, where R_H changes sign, might depend on the details of the evaluation. Nevertheless, the main features (positive Hall coefficient at low temperatures, sign change) are independent from analysis.

In principle, the doping levels $x = 0.15$ and $x = 0.16$ are comparable with respect to their magnetic field evolution of R_H for temperatures $T < 50$ K, although for the optimally doped crystal the $\rho_{xy}(B)$ curves show a stronger curvature, which is certainly related to the higher purity of the optimally doped crystal. For instance, $\omega_c \tau$ estimated from the magnetoresistance amounts to 0.34 and 0.20 at an applied field of $\mu_0 H = 14$ T at $T = 30$ K for the doping levels $x = 0.15$ and $x = 0.16$, respectively. Thus, deviations from the weak field limit might be visible especially in the Hall data for $x = 0.15$. Recently, similar deviations from linearity were reported for $\text{Pr}_{2-x}\text{Ce}_x\text{CuO}_4$ thin films at higher magnetic fields (between $\mu_0 H = 20 - 60$ T) [152]. For doping levels $x > 0.15$ a bending in $\rho_{xy}(B)$ towards a positive slope at high enough fields was observed for different doping levels, which was interpreted in terms of a magnetic field induced rearrangement of the Fermi surface. This is certainly not the case in the presented measurements. However, the $\rho_{xy}(B)$ data for $x = 0.15$ and $x = 0.16$ suggest not only a two band model with different T dependent mobilities, but also a strong influence of the magnetic field on the scattering mechanism of both types of carriers, or alternatively some instability of the Fermi surface against magnetic fields. Of course, such effects are not included when analyzing the data within the framework of conventional Boltzmann transport theory.

7.3.2 The transverse magnetoresistance

Another important transport quantity is the magnetoresistance, which is very sensitive to the variation of the mean free path l around the Fermi surface (Section 5.3). More precisely, it is a measure of the variance of the Hall angle over the Fermi surface [150]. The field dependence and temperature evolution of the orbital magnetoresistance for $0.13 \leq x \leq 0.17$ is illustrated using Kohler's plot. According to conventional transport theory (Chapter 5), $\rho_{ab} \propto \Gamma$ and $\Delta\rho/\rho \propto 1/\Gamma^2$, and thus, the curves in Figure 7.5 should collapse on a straight line for different temperatures. However, from the data one can immediately see that there are significant doping dependent deviations from Kohler's rule in the $\text{Nd}_{2-x}\text{Ce}_x\text{CuO}_4$ system.

For the underdoped $\text{Nd}_{1.87}\text{Ce}_{0.13}\text{CuO}_4$ crystal the transverse magnetoresistance exhibits a quadratic behavior in B over the whole temperature range (also in the

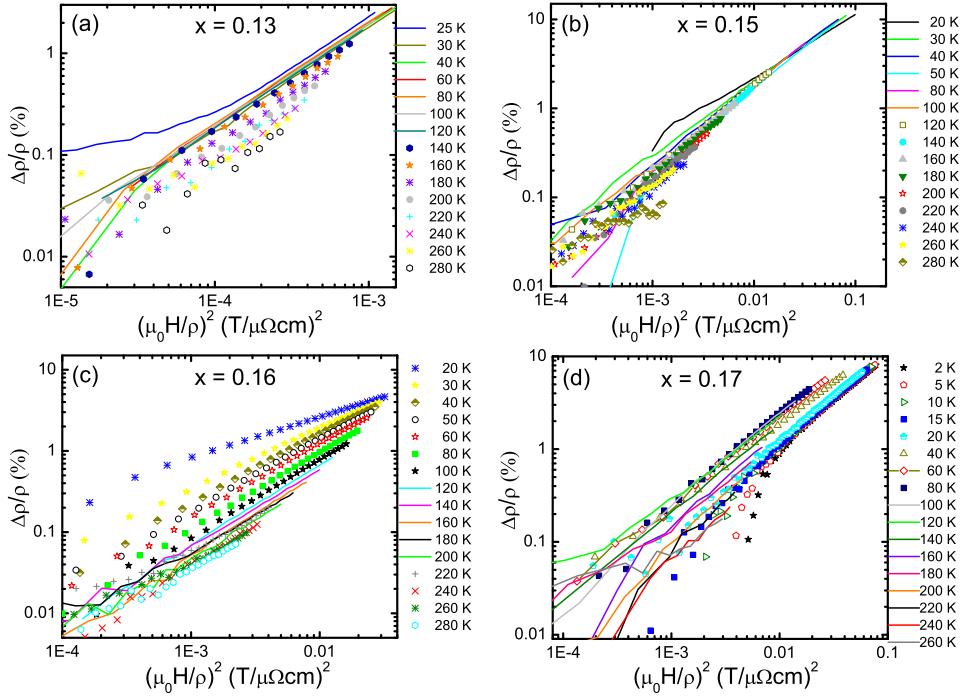


Figure 7.5: Kohler's plot of the orbital magnetoresistance for single crystals with nominal Ce-concentration $x = 0.13$ (a), $x = 0.15$ (b), $x = 0.16$ (c) and $x = 0.17$ (d). Note the logarithmic scales. The magnetic field is applied perpendicular to the CuO_2 sheets.

superconducting regime for fields far above B_{c2}). For clarifying reasons, the temperature evolution of the magnetoresistance is plotted in Figure 7.5 (a) by using a logarithmic scale. The data do not collapse on a straight line. There is rather a continuous increase in the slope with decreasing temperature (shift in the double logarithmic plot), suggesting that the in-plane lifetime τ obeys a different temperature dependence in contrast to the lifetime, which enters in the magnetoresistance. Similar behavior has been also found in different hole doped cuprates. The violation of the conventional Kohler's rule is attributed to the unusual temperature dependence of the Hall signal [150]. A better understanding for the anomaly – at least for the hole-doped cuprates – has been achieved by plotting the data versus $\tan\theta_H$. In this case the magnetoresistance data collapse on a straight line according to the relation $\Delta\rho/\rho = m^2 \tan\theta_H$ (modified Kohler's rule), where m is a temperature independent constant [5, 150]. Thus, the magnetoresistance follows the same temperature dependence as the Hall angle and from the expression of Equation 5.38, Ong et al. [150] have concluded that the Hall scattering life time $\tau_H(T)$ must change uniformly with T , independent from the position s on the Fermi surface. However, the underdoped $\text{Nd}_{1.87}\text{Ce}_{0.13}\text{CuO}_4$ does not obey the modified Kohler's rule, as well. The constant m has a large value of 7.4 at $T = 10$ K and increases with temperature like $T^{0.4}$, which might reflect a different T dependent scaling of

the mean free path l on different segments s on the Fermi surface.

A quite different behavior of the magnetotransport has been found for the optimally doped $\text{Nd}_{1.85}\text{Ce}_{0.15}\text{CuO}_4$ (Figure 7.5 (b)). Comparable to the Hall data, the magnetotransport cannot be evaluated completely in the upturn region (≤ 10 T). For temperatures $T > 10$ K, $\Delta\rho/\rho$ shows a positive, but sub-quadratic behavior. The power increases continuously and for $T \geq 50$ K Kohler's rule is approximately satisfied. This experimental result agrees with previous measurements on optimally doped $\text{Nd}_{2-x}\text{Ce}_x\text{CuO}_4$ thin films [139].

In the overdoped $\text{Nd}_{2-x}\text{Ce}_x\text{CuO}_4$ with $x = 0.16$, Kohler's rule is strongly violated as it can be seen from the strong diversification in the curves of Figure 7.5 (c). The magnetoresistance is quadratic in B for $T \geq 40$ K. At lower temperatures the dependence is similar to that described for optimal doping. The modified Kohler's rule does not work, as well. Like for $\text{Nd}_{1.87}\text{Ce}_{0.13}\text{CuO}_4$, and in contrast to the hole doped cuprates the constant m is quite high and reveals a strong T dependence.

Like in the Hall data, the doping level $x = 0.17$ also differs considerably in the magnetoresistance compared to the smaller doping levels. The B^2 dependence was found for the whole temperature range down to 2 K. There is no large spin-dependent contribution superimposed to the orbital transverse magnetoresistance, which dominates the low temperature behavior with reversal point, negative magnetoresistance, etc. Nevertheless, the (modified) Kohler's rule is also violated for this doping level.

It is clear that at low temperatures close to the superconducting regime the orbital magnetoresistance can be falsified by paraconductivity influences or a contribution related to an isotropic spin magnetoresistance. Nevertheless, as already mentioned above, the influence of superconducting fluctuations in $\text{Nd}_{2-x}\text{Ce}_x\text{CuO}_4$ might be negligible already at $T = 30 - 40$ K for all doping levels and the contribution of the isotropic spin magnetoresistance can be eliminated by subtracting the longitudinal magnetoresistance. For instance, for $\text{Nd}_{1.84}\text{Ce}_{0.16}\text{CuO}_4$ at $T = 30$ K the correction of the transverse magnetoresistance only amounts to 5% and decreases rapidly with increasing temperature.

7.4 Simulation of the normal state transport

Based on the various characteristics, already obtained from a general discussion of the transport data, a two band model was used in order to simulate the data. In the past, the quantity $\tan\theta_H$ or $\cot\theta_H$ has often been used in order to analyze the Hall problem [141, 157]. However, it is important to keep in mind that the (inverse) Hall angle is only a derived quantity [199] ($\tan\theta_H = \frac{\rho_{xy}}{\rho_{xx}}$), and models using the $\cot\theta_H$ as starting point for the T parameterization of the scattering rate Γ should be tested implicitly if they also comprise the T evolution of R_H and $\Delta\rho/\rho$. Thus, apart from the in-plane resistivity ρ_{xx} and the magnetoresistance $\Delta\rho/\rho$, R_H is used rather than $\tan\theta_H$ in order to adjust the parameters in the presented model.

7.4.1 The two-band model

The numerical simulation of the in-plane transport data is based on the band dispersion of Equation 5.46. The mean-free-path l is obtained from the analytically derived Fermi velocity \vec{v}_F and the scattering rate Γ , which is the adjustable quantity in this model and which is discussed below in more detail. The transport quantities are derived from the conductivity tensor, which was calculated up to the second order by summing up over the Fermi surface (see Section 5.3.1 for the expressions used in the calculation). The band dispersion is calculated by using the doping independent parameter values of $t = 0.38$ eV, $t' = 0.32 \cdot t$, and $t'' = 0.5 \cdot t'$, which are generally accepted values in literature [177].

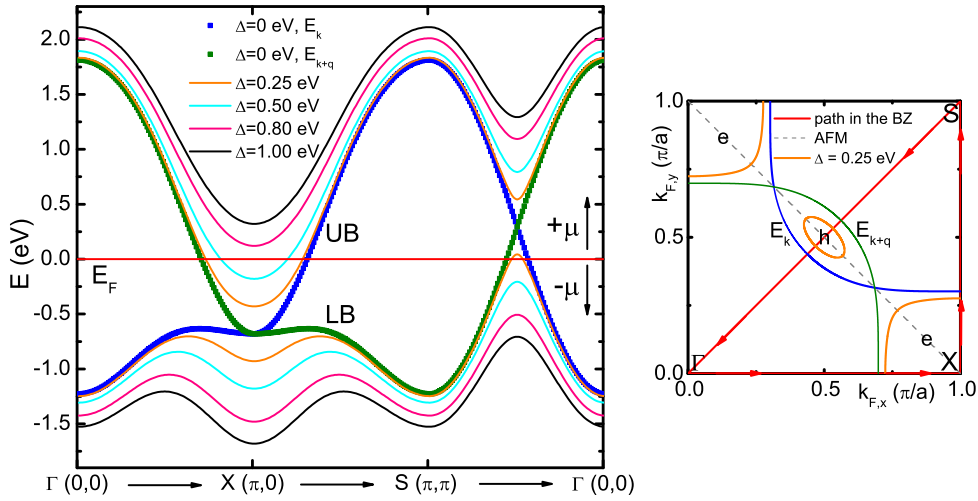


Figure 7.6: Evolution of the upper (UB) and lower band (LB) along the principal directions Γ – X – S – Γ of the Brillouin zone for different values of Δ and constant $\mu = 0.05$ eV. The Fermi energy E_F is set to zero. The band filling can be adjusted by the parameter μ .

In Figure 7.6 the simulated dispersion along the most important directions of the Brillouin zone is shown. Note, that there are two further doping dependent adjustable parameters: the chemical potential $\mu = f(x)$ and $\Delta = f(x)$, which splits the degeneracy at the AFM zone diagonal by 2Δ . For comparison, the evolution of the upper and lower band for different Δ is calculated and plotted in Figure 7.6. For the limit $\Delta \rightarrow 0$ (vanishing AFM correlations) the gap on the AFM zone diagonal is closed and the dispersion consists of the single band dispersion $E_{\vec{k}}$ (blue curve in Figure 7.6) and of the single band dispersion $E_{\vec{k}+\vec{q}}$, which is shifted by the AFM wave vector \vec{q} (green curve in Figure 7.6)⁵. The strength of the AFM interaction is reflected by Δ . In literature no clear relation between Ce content x and Δ has been reported so far [1, 10, 177]. Matsui et al. [1] have deduced a nearly linear decrease

⁵The two-band model has already been introduced in Section 5.3.2. The construction of the two bands due to the AFM superlattice structure is analog to the construction of energy bands in solid state physics using free electron parabolas.

in Δ from ARPES with a relative large value of $\Delta \approx 0.08$ eV, still visible in the overdoped $\text{Nd}_{1.87}\text{Ce}_{0.13}\text{CuO}_4$. Consequently, Δ is also varied to some extent in the fitting procedure, studying therefore its influence on the transport data.

In the simulation the Fermi energy E_F is set to zero and the quantity μ is adjusted by calculating numerically the so called band filling factor. The band filling is related to the nominal Ce doping x . For the undoped compound, for instance, a remarkable energy gap between the upper and lower band is expected ($\Delta \approx 0.8$ eV [10]), while E_F lies within the band gap. Hence, the lower band is fully occupied corresponding to a filling factor of $n_{LB} := N_{occ}/N_{tot} = 1$, where N_i denotes the number of occupied/all states in the Brillouin zone. In this case n_{UB} obviously amounts to zero. With increasing doping Δ decreases (cf. Figure 7.6) and the Fermi level may cross the upper and lower band. Therefore, the total filling is given by $n_{tot} = n_{LB} + n_{UB}$ and is related to the nominal doping x via $x = n_{tot} - 1$. Note, that the introduced quantity μ is not a real chemical potential, which in thermodynamics describes the energy gain of a system when a particle is added to the system. For analyzing the transport data the real value of the chemical potential is unimportant and only the band filling counts. Hence, the introduced quantity μ is used in order to shift the energy bands with respect to $E_F := 0$.

The Fermi surface topology with its different circulations of the hole- and electron-like pockets has already been discussed in Section 5.3.2. However, it is worth discussing briefly the most important properties of the pockets, which can be derived from the band structure. The Fermi velocity \vec{v}_F is anisotropic, as one can easily deduce from the shape of the Fermi surface of both pockets. A typical evolution of the Fermi velocity for both pockets is presented in Figure 7.7, where the values for Δ and μ correspond to those of simulation 1 and 3 for the optimally doped $\text{Nd}_{1.85}\text{Ce}_{0.15}\text{CuO}_4$ sample. The absolute value of the Fermi velocity v_F becomes minimal at angles where \vec{v}_F shows up along the AFM zone diagonal (Figure 7.7). Moving away from the AFM zone boundary v_F increases and the magnitude of anisotropy depends on the choice of Δ and μ , especially for the electron pocket. The anisotropy decreases with decreasing filling factor for the electron band. This means that the electron pocket moves towards the X point and simultaneously the Fermi surface changes its shape from square- to circular-like. Hence, the Fermi velocity becomes more isotropic and decreases mainly at the zone boundaries. For simulation 3, the anisotropy amounts to 1.53, while for simulation 1, which comprises a more circular Fermi surface, the anisotropy is lower and amounts to 1.36. For the hole pocket the evolution of the anisotropy is different. It decreases slightly with increasing hole pocket. There is a tendency to a shift in v_F to higher values when Δ is decreased and the elliptical surface is transformed into a larger almond-shaped Fermi surface. For simulation 1 the anisotropy in v_F amounts to 1.8, whereas for the smaller pocket it amounts to 2.1. Note also the higher maximum values of v_F for the electron band. Typical values are in the range of $5 - 7 \cdot 10^5$ m/s and $2 - 5 \cdot 10^5$ m/s for electrons and holes, respectively.

Generally speaking the electron pocket can be described easier than the hole one. For example, the minimum at point X of the band dispersion along the high

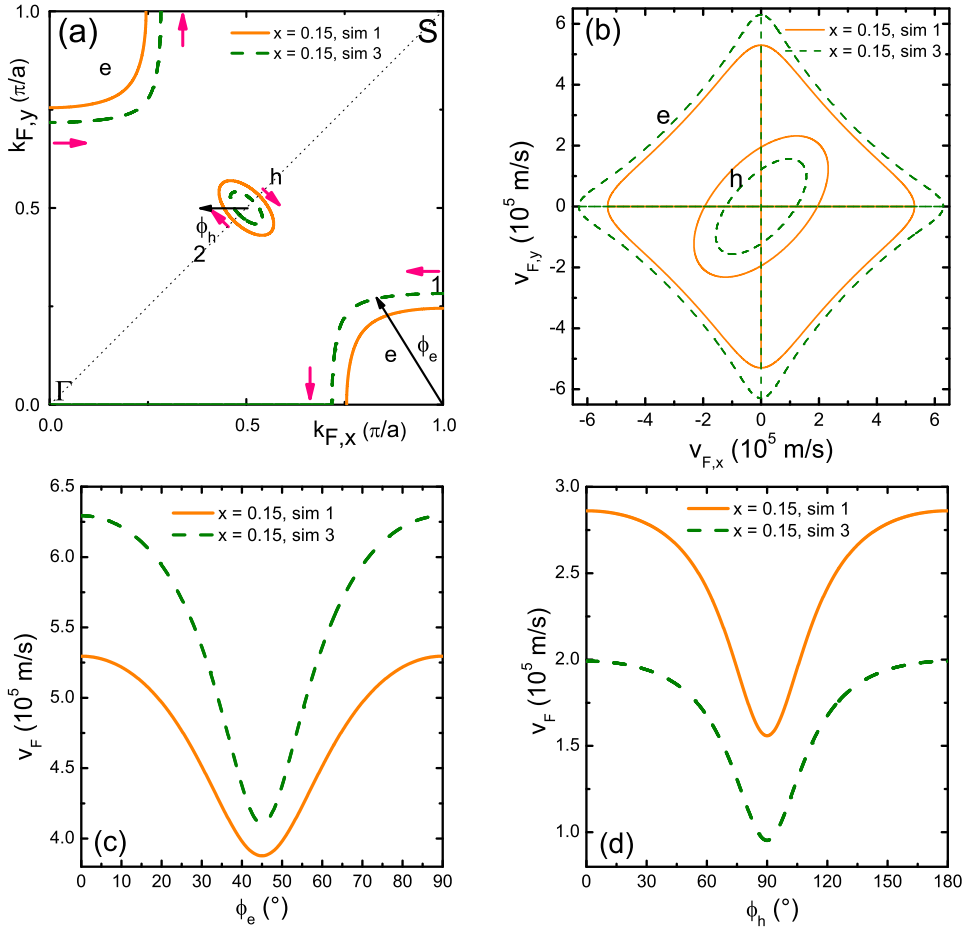


Figure 7.7: (a) Illustration of one quadrant of the Fermi surface calculated with the parameters used in simulation 1 and simulation 3 of the $\text{Nd}_{1.85}\text{Ce}_{0.15}\text{CuO}_4$ sample (see Table 7.1). Note the different angles ϕ_e and ϕ_h introduced for the numerical calculation. For the electron pocket the calculation starts at position (1) and follows the red arrows, while for the hole pocket the simulation starts at position (2) on the diagonal between Γ and S point. In (b) the Fermi velocity \vec{v}_F is shown for both pockets. The absolute values $v_F = \sqrt{v_{F,x}^2 + v_{F,y}^2}$ are illustrated separately for the electron pocket in (c) and for the hole pocket in (d).

symmetry directions can be described by a parabolic function as a first approximation at moderate values of Δ (see Figure 7.6 and 7.8). In Figure 7.8 the numerical results for the optimally doped $\text{Nd}_{1.85}\text{Ce}_{0.15}\text{CuO}_4$ sample (simulation 1) are summarized for both bands. For the upper band (electron-like) the following averaged quantities are derived by using the parabolic approximation: $k_F = 1.97 \cdot 10^9 \text{ m}^{-1}$, $m_e^* \approx 0.44 \cdot m$, $v_F = 5.2 \cdot 10^5 \text{ m/s}$ and $T_F = 4000 \text{ K}$, where m is the free electron mass. Comparable values have been also found for the electron pockets of the overdoped samples. The hole pocket, however, behaves differently. The parabolic

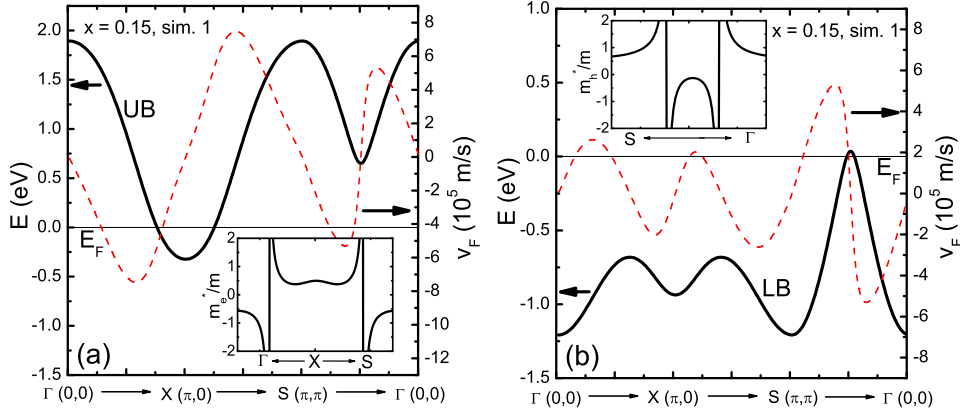


Figure 7.8: Calculation of the band dispersion E_k , Fermi velocity v_F and effective mass m^* (inset) along directions of high symmetry. The results for the upper band (UB) and lower band (LB) are illustrated in (a) and (b), respectively. The effective mass m^* is only plotted for small intervals in momentum space, where the pockets appear. The parameters are the same as in simulation 1 of the $\text{Nd}_{1.85}\text{Ce}_{0.15}\text{CuO}_4$ sample (cf. Table 7.1).

approximation along the principal axis of the hole pocket (diagonals of the Brillouin zone) fails also for moderate values of the level splitting Δ (Figure 7.6 and Figure 7.8). Nevertheless, one can make some qualitative conclusions about the effective mass of the holes in the lower band m_h^* , when comparing the curvature of both bands (UB and LB) near the band edge. The curvature of the lower band along the diagonal $\overline{S\Gamma}$ is larger and hence, the effective mass⁶ m_h^* is expected to be smaller than the effective mass of the electrons m_e^* . The calculated value amounts to $m_h^* \approx 0.15 \cdot m$ and is shown in the inset of Figure 7.8 (b). Comparable values of $m_h^* \approx 0.10 \cdot m$ have been also found for the overdoped samples. The effective mass of the hole pocket along the second principal axis (AFM zone diagonal) has not been calculated explicitly, as the contribution of this part of the Fermi surface to the transport is only small.

In the following the expression for the scattering rate Γ is introduced and discussed in combination with the experimental results. A key result recently presented by Narduzzo et al. [6] was the statement that R_H can obviously deviate from the free electron value $R_H = 1/(pe)$ by taking into account the real band dispersion, but it still remains T -independent when an isotropic Γ is assumed. Note, that even for isotropic Γ , l might be anisotropic due to the intrinsic anisotropy of the Fermi velocity $v_F = \frac{1}{\hbar} \frac{\partial E}{\partial k}$. Thus, the pronounced T dependence of R_H or in general, observed deviations from the expected T dependencies of the transport quantities, which in standard transport theory are clearly related to each other by the T dependence of Γ , reflect the strong anisotropy of Γ . In a two-band model, however, a T dependence of R_H can result directly from Equation 5.42, even if an isotropic scattering time is used and R_H^\pm for the individual bands is T independent.

⁶The effective mass is defined as $\left(\frac{1}{m^*}\right)_{ij} = \frac{1}{\hbar^2} \frac{\partial^2 E(\vec{k})}{\partial k_i \partial k_j}$.

The main evidence for invoking an anisotropic Γ in electron-doped compounds, as well, is the magnetoresistance $\Delta\rho/\rho$, which is completely underestimated for isotropic Γ . As the in-plane and out-of-plane resistivity show a power law behavior T^α (with $1 < \alpha < 2$) and no indication for a term with explicitly linear T dependence is found, the following ansatz for Γ in the model for both bands is made:

$$\Gamma_{tot}^{e,h} = \Gamma_0^{e,h} + \Gamma_T^{e,h} \cdot T^2. \quad (7.9)$$

The anisotropy of Γ_0 is parameterized for both bands separately and has the form:

$$\Gamma_0^e = G_{0,e} \cdot (1 + \chi_e \cdot \sin^2(2\phi_e)) \quad \text{and} \quad \Gamma_0^h = G_{0,h} \cdot (1 + \chi_h \cdot \sin^2 \phi_h). \quad (7.10)$$

Remember the different angles introduced in the numerical calculation. For the electron pocket the integration starts at position (1) in Figure 7.7 (a) and the angle ϕ_e becomes zero along the Brillouin zone boundary \overline{XS} , whereas for the hole pocket ϕ_h amounts to zero along the diagonal $\overline{S\Gamma}$. Hence, the sinusoidal ansatz accounts for a strong suppression of the mean-free-path $l = v\tau$ close to the hot spot regions along the AFM diagonal. Alternatively, an AV ansatz (Equation 5.8) was also used in order to reduce the number of free adjustable parameters:

$$\Gamma_0^{e,h} = \frac{\beta_{e,h}}{v_F(\phi_{e,h})}. \quad (7.11)$$

In the AV ansatz the anisotropy of Γ results from the intrinsic anisotropy of $v_F(\phi)$ with its minima along the AFM diagonal. The sinusoidal ansatz is fully equivalent to the AV ansatz, but provides a more flexible handling due to its additional parameters $\chi_{e,h}$.

The temperature dependent scattering rate $\Gamma_T^{e,h}$ is modeled in the same way:

$$\Gamma_T^e = G_{T,e} \cdot (1 + \varepsilon_e \cdot \sin^2(2\phi_e)) \quad \text{and} \quad \Gamma_T^h = G_{T,h} \cdot (1 + \varepsilon_h \cdot \sin^2 \phi_h). \quad (7.12)$$

Concerning the anisotropy of Γ_T the same arguments are valid as for Γ_0 . The magnitude and shape of $\Delta\rho/\rho$ at moderate temperatures $T > 100$ K evoke the assumption of anisotropy. In principle the ansatz according to Equations 7.9-7.12 is also plausible from the physical point of view. An increased scattering, and thus a smaller l , might be expected on those parts of the Fermi surface, where the charge carriers undergo interactions with magnetic excitations (i.e close to the hot spot regions). There are 10 or 8 free parameters depending on whether the sinusoidal ansatz or AV ansatz is chosen. Thus, a general discussion of the transport data seems to be difficult. However, there are some constraints (filling factor, Matthiesen rule), which limit the number of free adjustable parameters and there are not too many possibilities to interpret all features of the three transport quantities within the measured temperature interval.

For optimally doped $\text{Nd}_{1.85}\text{Ce}_{0.15}\text{CuO}_4$ three fits are shown in order to illustrate the impact of anisotropy and band filling. The corresponding parameters are summarized in Table 7.1. The best agreement with the data is obtained in simulation 1

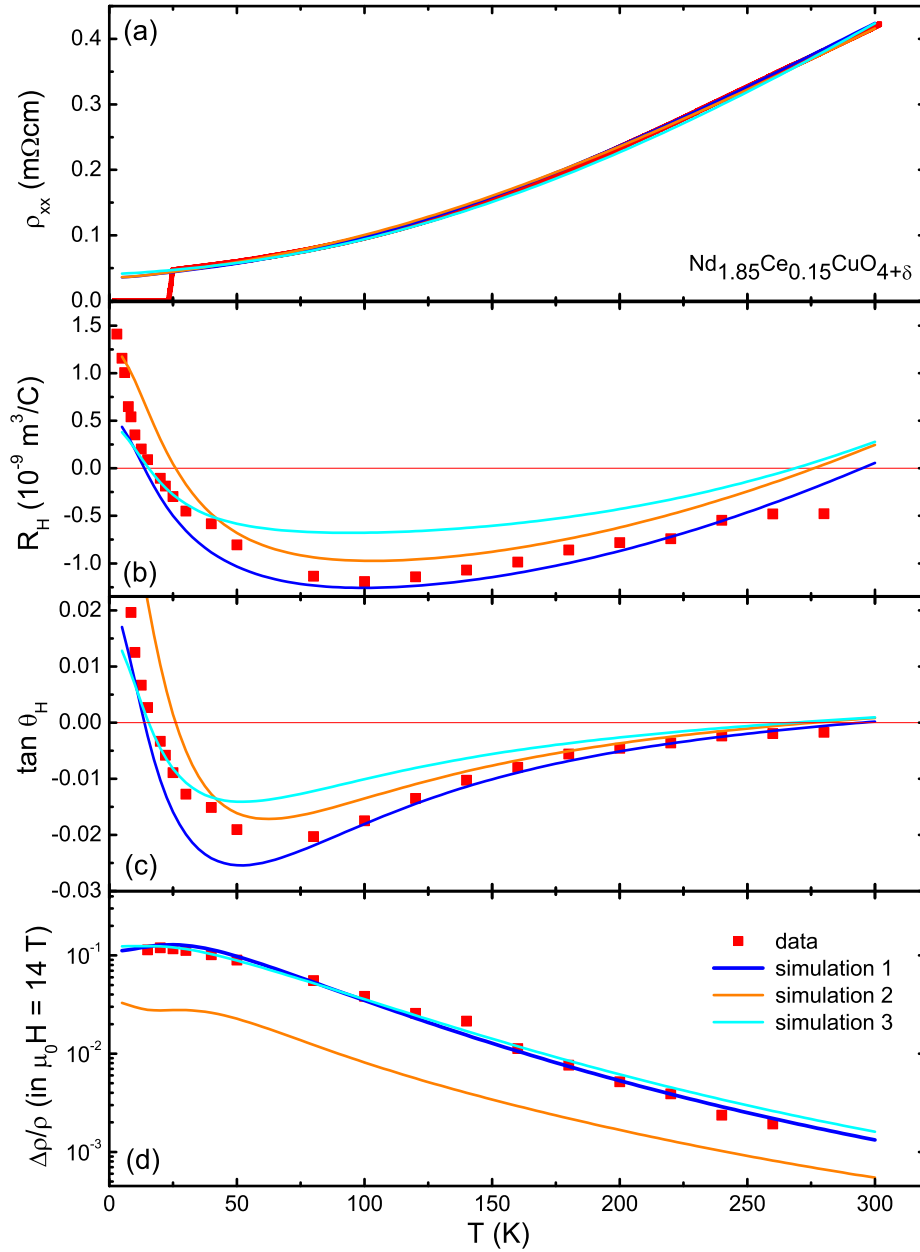


Figure 7.9: ρ_{xx} (a), R_H (b), Hall angle $\tan \theta_H$ (c) and magnetoresistance $\Delta\rho/\rho$ (d) data (red squares) plotted versus T for an optimally doped $\text{Nd}_{1.85}\text{Ce}_{0.15}\text{CuO}_{4+\delta}$ single crystal together with the simulation results. See the text for details concerning the data simulation by using the two-band dispersion, given by Equation 5.46. The corresponding parameters are summarized in Table 7.1.

(Figure 7.9). It is assumed that the charge carriers of both bands have a comparable scattering rate G_0 , which governs the residual resistivity. G_0 is adjusted simulta-

Parameter	simulation 1 (sine)		simulation 2 (AV)		simulation 3 (sine)	
	e	h	e	h	e	h
G_0 [s^{-1}]	$3.0 \cdot 10^{13}$	$2.4 \cdot 10^{13}$	–	–	$3.4 \cdot 10^{13}$	$2.4 \cdot 10^{13}$
χ	4	1.5	–	–	6	1
β [ms^{-2}]	–	–	$3.5 \cdot 10^{19}$	$8.0 \cdot 10^{18}$	–	–
G_T [$\text{s}^{-1}\text{K}^{-2}$]	$3.0 \cdot 10^9$	$6.5 \cdot 10^9$	$3.7 \cdot 10^9$	$6.5 \cdot 10^9$	$3.1 \cdot 10^9$	$8.5 \cdot 10^9$
ε	5.5	30	3	13	7.5	15
Δ [eV]		0.307		0.307		0.255
μ [eV]		0.100		0.100		0.025

Table 7.1: Summary of the parameters for the simulation of the transport data of the $\text{Nd}_{1.85}\text{Ce}_{0.15}\text{CuO}_4$ sample.

neously for both bands to the low temperature region of the in-plane resistivity. The anisotropy factors χ also affect the magnitude of the in-plane resistivity to a certain extent. The T dependence of both bands is modeled in a different way. The electron pocket seems to dominate the transport at temperatures $T > 80$ K, which is also supported by the negative Hall signal. Using $\sigma_{xy} \propto A_l$ (cf. Chapter 5) it becomes clear that the electron mean-free-path $l_e(\phi)$ must exceed the hole value $l_h(\phi)$ at higher temperatures. At low temperatures both quantities become comparable. Therefore, $G_{T,e}$ is adjusted to the in-plane data at moderate temperatures up to 300 K. The value of $G_{T,h}$ is set considerably higher (approximately for a factor 2 for all simulations) and is adjusted in relation to $G_{T,e}$ using the Hall data. Consequently, l_h is decreasing rapidly with temperature ($v_{F,h}$ is also smaller than $v_{F,e}$), so that the major part of the hole pocket becomes already incoherent at $T \approx 100$ K. This means that $l_h < a$, and with increasing temperature all carriers on the hole pocket violate the MIR criterion (cf. discussion in Section 5.2.3). However, this is not the case for the electron pocket, where a small segment close to the hot spots reaches the incoherent state at $T > 200$ K. Hence, for the hole pocket the parameter free MIR limit is introduced by using the already discussed "parallel resistor" model in the simulation. This shunting of the resistivity ρ_h is responsible for the observed reversal point in the Hall data. However, the implementation of the MIR limit for the electron pocket does not lead to satisfying results. Especially the in-plane resistivity shows a strong linearization, which cannot be compared with the reported deviations at $T > 200$ K. Nevertheless, the observed deviations from the power law towards linearity are consistent with the simulation data, which show that also the electron pocket starts approaching gradually the MIR limit for $T > 200$ K.

It is mandatory to discuss the AV ansatz (simulation 2) simultaneously in order to understand the influence of the anisotropy modulation on the transport properties. The ϕ dependent evolution of the mean-free-path $l(\phi)$ is illustrated in Figure 7.10. The values of β are adjusted in the same way as G_0 in simulation 1, keeping in mind the special form of Expression 7.11. Therefore, after dividing by v_F ,

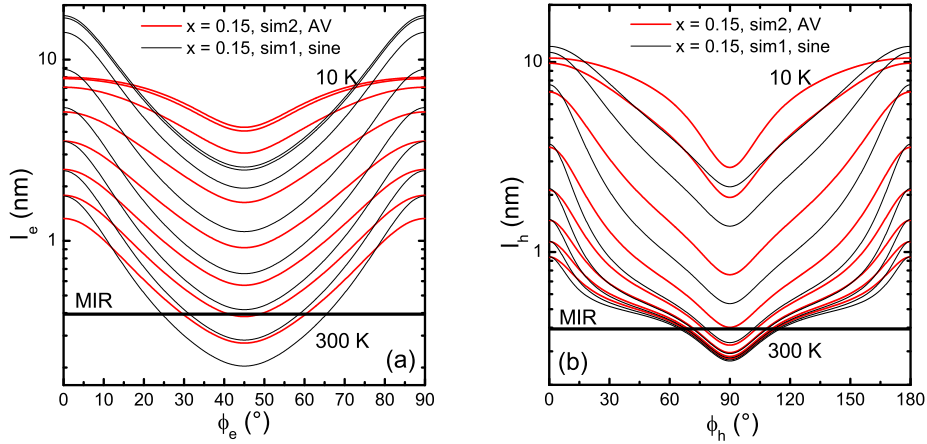


Figure 7.10: Simulation of the T dependent ($T = 10$ K, 20 K, 50 K, 100 K, 150 K, 200 K, 250 K, 300 K) evolution of the mean-free-path $l(\phi)$ of the electron (a) and hole pocket (b) using the parameters of simulation 1 and 2 of $\text{Nd}_{1.85}\text{Ce}_{0.15}\text{CuO}_4$ (MIR limit included).

the value for Γ_0^h is comparable to that in simulation 1. Γ_0^e is approximately by a factor of 2 higher than in simulation 1, which can be explained with the lower anisotropy in simulation 2. Thus, at low temperatures l_e is more isotropic in the AV ansatz, whereas in simulation 1 the electronic contribution to the transport is primarily caused by the regions close to the zone boundaries (compare the l values in Figure 7.10 (a)). For the hole pocket the best results are obtained when the anisotropy factor χ_h is comparable to that of the AV ansatz. Hence, the T evolution and anisotropy of l_h are comparable for both simulations. The parameters for $\Gamma_T^{h,e}$ do not deviate considerably from the ones of simulation 1. As it is shown in Figure 7.9 both simulations reflect the in-plane data in an equally good manner. The Hall signal and the Hall angle in simulation 2 comprise all important features (reversal point, sign change), although the magnitude of R_H and the temperature, at which the sign change occurs, cannot be fully reproduced in a correct way. However, the main evidence for the fact that simulation 2 does not reflect the physical situation in $\text{Nd}_{1.85}\text{Ce}_{0.15}\text{CuO}_4$ arises from the $\Delta\rho/\rho(T)$ curve. The magnetoresistance is underestimated by a factor of approximately 5 for $T = 50$ K and 2.5 for $T = 260$ K, respectively. Thus, the invoked, strange anisotropy in G_0 for $T \rightarrow 0$, as it is derived from the AV ansatz, is not sufficient to explain the magnetoresistance data. The sinusoidal ansatz 1 seems to reflect the transport behavior in $\text{Nd}_{1.85}\text{Ce}_{0.15}\text{CuO}_4$ in a better way, as all transport quantities are simulated successfully. The anisotropy in $l(\phi)$ is not only reflected by $\Delta\rho/\rho$, but also in an attenuated way by R_H and ρ_{xx} . The upturn in R_H at low temperatures requires a small value for χ_h while χ_e is adjusted to this value. At higher temperatures up to 300 K, ε_e is the essential fit parameter, as the electron contribution dominates the transport. ε_h affects the transport only marginally and is usually set to high values of 10 – 30 in order to improve the Hall simulation at 300 K. The small deviations of the simulations for

$T > 200$ K are most likely related to the MIR limit of the electron pockets, as discussed above. Deviations below 50 K must be interpreted considering the difficulty of extracting accurate R_H and $\Delta\rho/\rho$ data. The choice of the values for ε_h does not influence the main message of this model. It shows that the strange transport properties of $\text{Nd}_{1.85}\text{Ce}_{0.15}\text{CuO}_4$ can be understood in terms of conventional transport theory using a two-band model and assuming an anisotropic scattering rate Γ .

However, one important question in the discussion of $\text{Nd}_{1.85}\text{Ce}_{0.15}\text{CuO}_4$ is still left: The influence of Δ on the model. In simulation 1 and 2 the parameters $\Delta = 0.307$ eV and $\mu = 0.10$ eV are chosen, corresponding to a filling factor of $n_{LB} = 0.988$ and $n_{UB} = 0.106$ for the hole and electron pocket, respectively, from which an effective electron doping of $n_{tot} = 0.094$ is deduced. In simulation 3 the values amount to $n_{LB} = 0.996$ and $n_{UB} = 0.147$, respectively, leading to an effective doping of 0.143. This value for the doping is much closer to the nominal doping $n = 0.15$. However, simulations have shown that the T evolution of R_H and especially the minimum of R_H cannot be modeled in an appropriate way (compare simulation 1 and 3 in Figure 7.9). The Hall signal shifts towards positive values and the T dependence is less pronounced. One possible way to explain this discrepancy between the nominal doping $n = 0.15$ and the effective electron number n_{tot} in the CuO_2 sheets, as it is deduced from simulation 1, is the consideration of a small amount of excess oxygen in the crystal, which has already been discussed in Section 4.4.

For the overdoped $\text{Nd}_{1.84}\text{Ce}_{0.16}\text{CuO}_4$ the same considerations have been made as for the optimally doped $\text{Nd}_{1.85}\text{Ce}_{0.15}\text{CuO}_4$ in order to simulate the data. The parameters are summarized in Table 7.2 and the data are shown in Figure 7.11. Simulation 1 fits the experimental data reasonably well. The Hall signal at low temperatures and the sign change are clearly visible. The reversal point is shifted by ≈ 20 K and the deviations near room temperature are again related to the MIR limit for the electron pockets. The parameters used in simulation 1 are similar to

Parameter	simulation 1 (sine)		simulation 2 (sine)	
	e	h	e	h
G_0 [s^{-1}]	$6.5 \cdot 10^{13}$	$6.5 \cdot 10^{13}$	$7.0 \cdot 10^{13}$	$5.4 \cdot 10^{13}$
χ	6	1.5	6	1.5
β [ms^{-2}]	—	—	—	—
G_T [$\text{s}^{-1}\text{K}^{-2}$]	$2.7 \cdot 10^9$	$7.0 \cdot 10^9$	$3.2 \cdot 10^9$	$1.3 \cdot 10^{10}$
ε	4	30	3	15
Δ [eV]	0.25		0.22	
μ [eV]	0.05		0.0	

Table 7.2: Summary of the parameters for the simulation of the transport data of the overdoped $\text{Nd}_{1.84}\text{Ce}_{0.16}\text{CuO}_4$ sample.

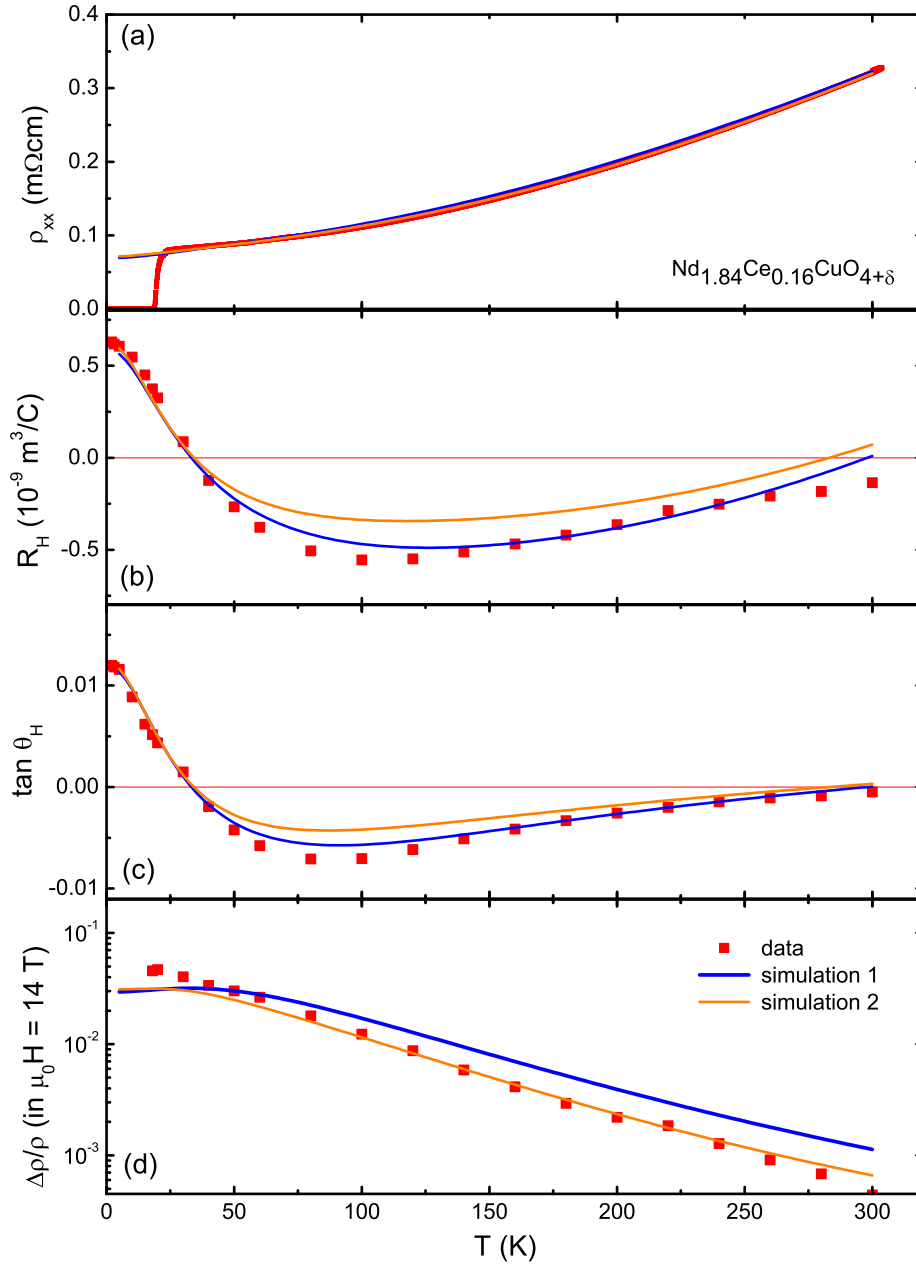


Figure 7.11: ρ_{xx} (a), R_H (b), Hall angle $\tan \theta_H$ (c) and magnetoresistance $\Delta\rho/\rho$ (d) data (red squares) plotted versus T for an overdoped $\text{Nd}_{1.84}\text{Ce}_{0.16}\text{CuO}_{4+\delta}$ single crystal together with the simulation results. The corresponding parameters are summarized in Table 7.2. See the text for details.

those used in simulation 1 for the optimally doped crystal. The main difference lies in the higher values for G_0 (both $6.5 \cdot 10^{13}$ Hz), which arise when accounting for the residual resistivity. The anisotropy factors deviate only slightly for the elec-

tron pocket. Both T dependent scattering terms are comparable. Note again the necessity of a different scattering amplitude G_T for both pockets.

We note that the magnetoresistance is not fully consistent with the data, especially in the moderate temperature regime up to 300 K, where $\Delta\rho/\rho(T)$ is overestimated by a factor of 2. Better results in $\Delta\rho/\rho(T)$ are obtained in simulation 2 at the expense of a good fit of the Hall signal. Simulation 2 differs from simulation 1 by using a smaller Δ . The values $\Delta = 0.22$ eV and $\mu = 0$ eV are assumed for the second fit, corresponding to a filling factor of $n_{LB} = 0.993$ and $n_{UB} = 0.165$, which results in an effective doping of $x = 0.158$. For simulation 1, the values of $\Delta = 0.25$ eV and $\mu = 0.05$ eV are used, corresponding to band filling factors of $n_{LB} = 0.986$ and $n_{UB} = 0.139$, respectively. Hence, the effective doping amounts only to $n_{tot} = 0.125$. Simulation 2 underestimates the real Hall data at moderate temperatures. The comparison of both fits shows again – analog to the optimally doped case – the tendency of R_H to move towards positive values with decreasing Δ .

Finally, the overdoped $\text{Nd}_{1.83}\text{Ce}_{0.17}\text{CuO}_4$ is modeled and the results are summarized in Table 7.3 and Figure 7.12. The data simulation reveals some surprises, which are discussed in the following. From ARPES measurements a Fermi surface reconstruction is reported in the overdoped regime at doping levels $x \approx 0.17$ [1, 9]. The hot spot is filled up and a large hole-like Fermi surface with volume $1 + x$, which is centered about the S point, has been reported. Further evidence for a reconstructed Fermi surface has been deduced from various transport measurements [11]. Indeed, when looking at the Hall data in Figure 7.12 (b) a collapse of the two-band model and a transition to a single hole-like band seems to be recognizable. For $T < 100$ K, the data show a remarkable positive Hall signal. At higher temperatures the Hall signal approaches the zero level and changes sign. However, as already mentioned in Section 7.3, the measured signal is very small and errors of measurement have to be taken into account. Therefore, at first a single band modeling was applied and the surprising result is that both transport quantities $R_H(T)$ and $\Delta\rho/\rho(T)$ cannot be explained sufficiently within a single band model. For the single band dispersion the parameters $t = 0.38$ eV, $t' = 0.076$ eV and $t'' = 0.038$ eV are used. The chemical potential is adjusted according to the band filling to a value of $\mu = -0.03$ eV. Note, that details in the band parameter do influence the simulation result only marginally. The anisotropic scattering rate is assumed similar to the two-band model and has the form of $\Gamma = G_0 \cdot (1 + \chi \cdot \sin^2(4\phi)) + G_T \cdot T^2$. The angle ϕ is measured from the \overline{SX} connecting line in the Brillouin zone and the integration occurs clockwise. (4ϕ) in the sine-term is used to account for possible remaining influences of the hot spot regions on the charge carriers. In addition, the MIR limit is implemented. The main result is that the shape of R_H can only be reproduced when a huge anisotropy of $\chi = 60$ of the T independent scattering rate is assumed and simultaneously, the anisotropy of the T dependent scattering rate is set to zero ($\varepsilon \rightarrow 0$). For finite ε , R_H moves to higher values at moderate temperatures and the Hall curve flattens. The Hall coefficient is completely overestimated

Parameter	simulation 1 (sine)		simulation 2 (sine)		simulation 3 (1 band)
	e	h	e	h	h
G_0 [s^{-1}]	$1.4 \cdot 10^{14}$	$3.4 \cdot 10^{13}$	$2.4 \cdot 10^{14}$	$4.4 \cdot 10^{13}$	$1.7 \cdot 10^{13}$
χ	4	4	2	3.5	60
β [ms^{-2}]	–	–	–	–	–
G_T [$s^{-1}K^{-2}$]	$2.0 \cdot 10^9$	$7.0 \cdot 10^9$	$5.0 \cdot 10^9$	$7.0 \cdot 10^9$	$8.5 \cdot 10^9$
ε	14	20	3	15	–
Δ [eV]		0.15		0.10	0.0
μ [eV]		0.02		-0.02	-0.03

Table 7.3: Summary of the parameters for the simulation of the transport data of the overdoped $Nd_{1.83}Ce_{0.17}CuO_4$ sample.

(for a factor 10 at $T = 120$ K) and a sign change cannot be obtained independently from the modeling of the l -anisotropy. As already discussed in Chapter 5, a typical non-fragmented Fermi surface for electron doped cuprates (see Figure 5.3 (a)) is always hole-like over the whole doping range, as the Stokes area A_l has a uniform positive sign. This is different for hole doping, where the Fermi surface transforms gradually into an electron-like Fermi surface in the overdoped regime (see Figure 5.2 (a)). In summary, there are two problems with simulations based on a single-band model. Firstly, the positive Hall coefficient over the whole temperature range and secondly, the magnetoresistance, which cannot be reproduced in an appropriate way. For the used parameters, $\Delta\rho/\rho(T)$ is overestimated at low temperatures, whereas at higher temperatures the simulated value drops rapidly far below the measured values (for about two orders of magnitude).

In view of the problems with a single band model, a two band model is also applied to the overdoped $Nd_{1.83}Ce_{0.17}CuO_4$ data, which improves the simulation of the experimental results. For simulation 1, a band gap of $\Delta = 0.15$ eV is assumed with a chemical potential of $\mu = 0.02$ eV. This corresponds to a band filling of $n_{LB} = 0.969$ and $n_{UB} = 0.175$, respectively. The effective doping amounts to $n_{tot} = 0.144$. The anisotropy factors χ are comparable to those used for simulating the data of doping level $x = 0.15$ and $x = 0.16$. The main difference lies in the choice of the high residual scattering rate $G_{0,e}$ for the electron pocket. However, this is necessary in order to promote the large positive Hall coefficient at low temperatures. The T dependent scattering term does not differ much from the ansatz used for optimally doped $Nd_{1.85}Ce_{0.15}CuO_4$. With this two-band ansatz the transport data can be nicely fit, although there are some inconsistencies concerning the magnitude and T evolution of the magnetoresistance. In simulation 2, Δ is changed to 0.10 eV and μ is adjusted by assuming an effective doping of $n_{tot} \approx 0.17$. The corresponding band filling amounts to $n_{LB} = 0.971$ and $n_{UB} = 0.199$, respectively. As one can see in Figure 7.12, $\Delta\rho/\rho(T)$ is slightly underestimated and R_H is overestimated with increasing temperature. Nevertheless, the evolution of both

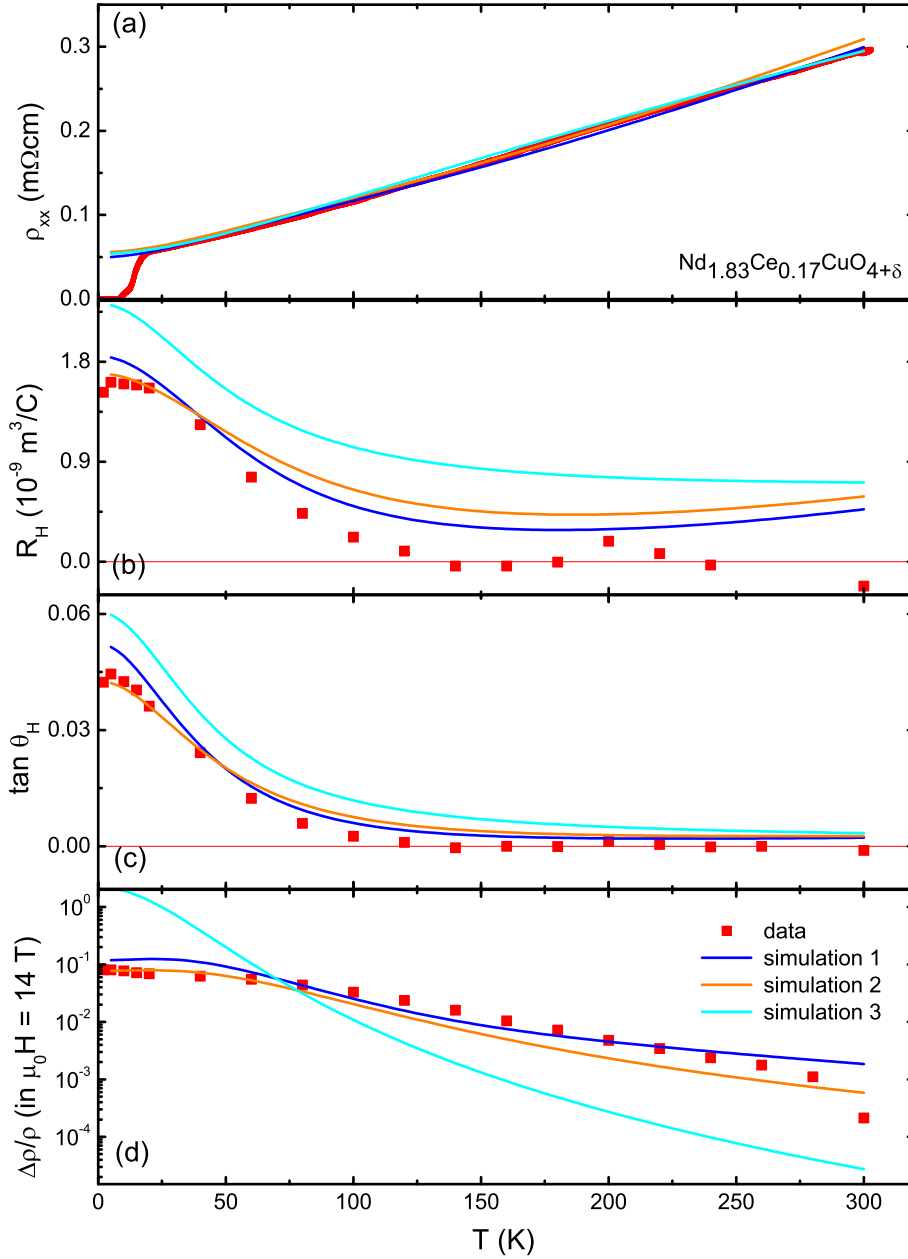


Figure 7.12: ρ_{xx} (a), R_H (b), Hall angle $\tan \theta_H$ (c) and magnetoresistance $\Delta\rho/\rho$ (d) data (red squares) plotted versus T for an overdoped $\text{Nd}_{1.83}\text{Ce}_{0.17}\text{CuO}_{4+\delta}$ single crystal together with the simulation results. The corresponding simulation parameters are summarized in Table 7.3. See the text for details.

quantities is reproduced in a correct way.

At the end of this subsection the derived quantity $\tan\theta_H(T)$, which is often used in literature rather than the coefficient R_H , is discussed briefly. In this context we

note that $\tan\theta_H$ is not too sensitive to the T evolution and details are often smeared out. Hence, the Hall angle is easier to model as the Hall coefficient, which can be also seen in Figure 7.12.

7.4.2 Discussion

At the end of this Chapter the main results are summarized and a physical interpretation of the main aspects is given:

1. The phenomenological ansatz of the scattering term $\Gamma_{tot}^{e,h} = \Gamma_0^{e,h} + \Gamma_T^{e,h} \cdot T^2$ (Equation 7.9) is plausible, where both the T independent and T dependent parts have an anisotropic amplitude. It follows from the in-plane measurements of $\rho_{ab}(T)$ (no T -linear component) as well as from the magnetoresistance (requires anisotropic amplitudes). The T^2 term might be ascribed to electron-electron scattering or/and scattering on spin fluctuations. The modeling of the anisotropy for both bands following a $\sin^2(2\phi_e)$ and $\sin^2(\phi_h)$ dependence (Equation 7.10 and Equation 7.12) accounts for presumably strong magnetic interactions of those charge carriers on the Fermi surface, which are close to the hot spots (Figure 7.13). This anisotropy is still preserved in the limit $T \rightarrow 0$. In addition, the anisotropy χ_0 seems to be larger for the electron pocket than for the hole pocket. This might be ascribed to the different curvatures of both Fermi surfaces in the vicinity of the hot spots.
2. Note, that in our two-band model AFM correlations are assumed to persist also in the overdoped region of the phase diagram at a doping level of $x = 0.17$. This is in contrast to neutron scattering experiments, where long range AFM order is reported to disappear at a doping level of $x \approx 0.13$. However, AFM fluctuations can still exist up to higher doping levels. These fluctuations must have a lifetime longer than the scattering time τ of the charge carriers in order to provide an effective scattering channel.
3. From the anisotropic scattering rate it can be followed that the transport in both bands is primarily governed by those regions of the Fermi surface, which are most far away from the hot spots, i.e close to the Brillouin zone boundary for the electron band and along the $\overline{\Gamma S}$ diagonal for the hole band. For temperatures $T > 100$ K, the electron pockets dominate the transport, whereas for $T < 100$ K there is a remarkable contribution from the hole pocket, which increases with increasing doping. The remarkable contribution of the hole carriers to the transport at low temperatures can be easily explained by their higher mobility due to the smaller effective mass m_h^* . However, the physical mechanism responsible for the strong T dependent localization of the holes at higher temperatures is unclear. The implications on superconductivity and the question whether holes or electrons are responsible for superconductivity cannot be answered at this stage.

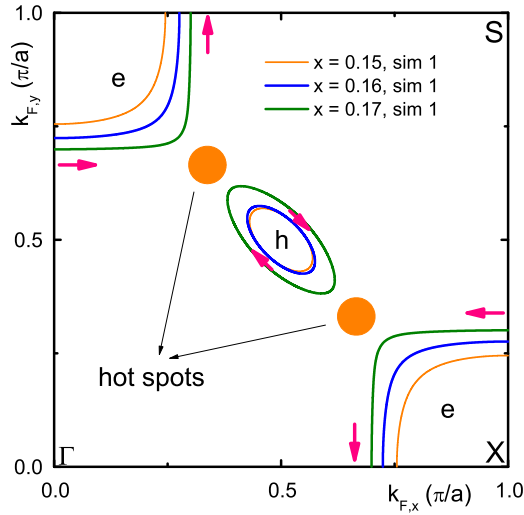


Figure 7.13: Illustration of the doping dependent underlying Fermi surfaces, which are used for the data simulation.

4. The proposed simple two-band model reproduces very well the transport data for $x \geq 0.15$. The general trend of a steep decrease in Δ ($0.307 \text{ eV} \rightarrow 0.15 \text{ eV}$, simulations 1) and a simultaneously increase of the hole pocket with increasing doping coincides with ARPES results [1, 9, 10]. Nevertheless, the underlying Fermi surfaces (Figure 7.13) do not agree with those deduced from ARPES [1] for the same doping levels. However, concerning Fermi surface topology there is a general discrepancy between ARPES and transport measurements [7], i.e. between truncated arcs or arc-like segments and closed pockets in the Brillouin zone. The Fermi surfaces for the doping levels $x = 0.16$ and $x = 0.17$ – as they are deduced from ARPES measurements by Matsui et al. [1] – are rather hole-like than electron-like, which is in clear disagreement with the transport data presented in this thesis for the same doping levels.
5. Finally, the Hall coefficient $R_H(T)$ and the magnetoresistance $\Delta\rho/\rho(T)$ are summarized in Figure 7.14 for all measured doping levels. It has been shown that for doping levels $x \geq 0.15$ the data can be understood in terms of a two-band model. The characteristic temperature dependence of the transport quantities, the deviations of R_H from the Drude value as well as the violation of the Kohler's rule can be understood in terms of a pronounced anisotropic scattering rate. In contrast, the simulation of the underdoped region turns out to be difficult, due to strong non-orbital contributions to the transport data (strong upturn behavior in $\rho_{ab}(T)$, negative magnetoresistance). The Hall data for the doping level $x = 0.13$ suggest a single band model with smaller electron pockets around the X point in the Brillouin zone. However, simulations have shown that the strong T evolution of R_H cannot be explained within the present model independent from the modeling of the scattering rate. The Hall data for the far

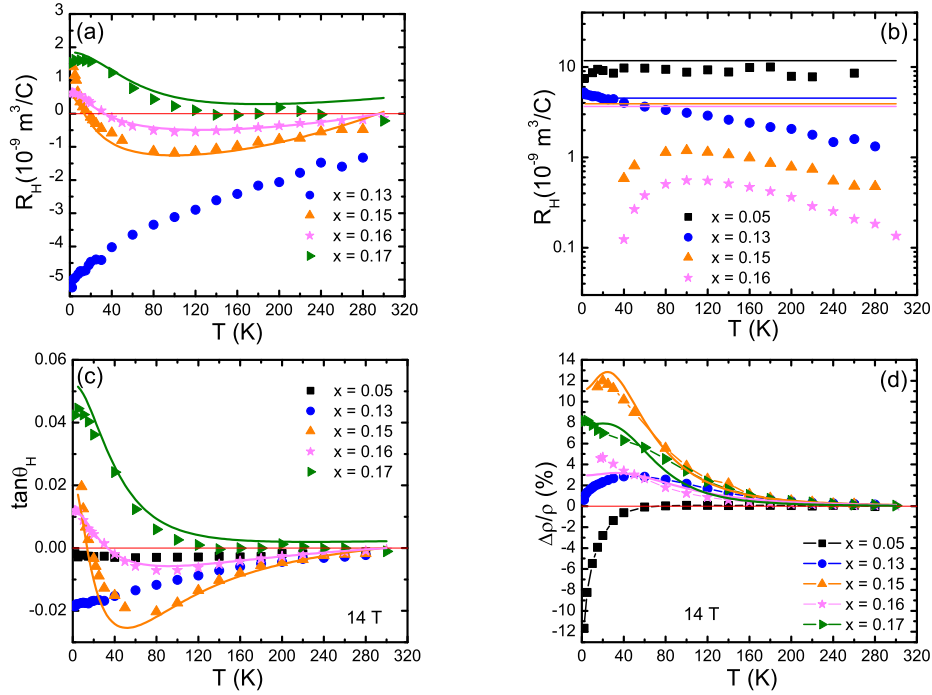


Figure 7.14: Temperature dependence of the measured Hall coefficient R_H (a) and (b), the Hall angle $\tan\theta_H$ (c) and the magnetoresistance $\Delta\rho/\rho$ (d) for $\text{Nd}_{2-x}\text{Ce}_x\text{CuO}_4$ crystals of different doping levels. The simulation results are represented by the solid lines. In (b) the absolute value of R_H is plotted and compared with the Drude value (solid horizontal lines) using the nominal carrier concentration $n = \frac{x}{\bar{v}\sqrt{2}}$.

underdoped $x = 0.05$ sample can be explained qualitatively. The Hall coefficient is almost T independent and reflects the Drude value $n = \frac{x}{\bar{v}\sqrt{2}}$ (Figure 7.14 (b)), suggesting small circular electron pockets with an isotropic scattering rate.

Chapter 8

Summary

This thesis deals with the growth and characterization of high quality single crystals of the electron doped cuprates. To this end, the main aim was the growth and characterization of a well defined sample set, which covers in narrow steps the whole phase diagram on the electron doped side of the cuprate high temperature superconductors, thus allowing a systematic study of their magnetotransport properties.

Systematic growth experiments on different electron doped 214 solid solutions have revealed that $\text{Nd}_{2-x}\text{Ce}_x\text{CuO}_4$ can be regarded as the most promising system, as high quality crystals can be grown over a wide doping range from the undoped parent compound Nd_2CuO_4 up to the overdoped metallic regime. The solubility limit has been found to be beyond the superconducting dome at a Ce doping of $x = 0.18$. Alternatively, the electron doped compound $\text{La}_{2-x}\text{Ce}_x\text{CuO}_4$ could not be grown in crystalline form due to precipitations of the Ce dopant. Furthermore, growth experiments show that the closely related systems $\text{Pr}_{2-x}\text{Ce}_x\text{CuO}_4$ and $\text{LaPr}_{1-x}\text{Ce}_x\text{CuO}_4$ are afflicted with homogeneity problems and rare earth-oxide precipitations in the overdoped regime. Hence, these systems were not included in the transport measurements. The solubility limit for Ce in $\text{Pr}_{2-x}\text{Ce}_x\text{CuO}_4$ has been found to be very close to the optimal doping level of $x = 0.15$. The high quality of the annealed crystals is indicated by the achieved sharpness of transition curves into the superconducting regime, which to our knowledge are the best values reported so far. For $\text{Nd}_{2-x}\text{Ce}_x\text{CuO}_4$ a series of high quality single crystals has been grown in steps of $\Delta x = 0.01$ within the doping interval $0.12 \leq x \leq 0.18$. For the first time it was possible to resolve the narrow superconducting dome, which shows a parabolic behavior of $T_c(x)$ with an expected maximum at $x = 0.146$. In the underdoped regime there is a small deviation from parabolicity at $x = 0.13$, where the long-range AFM disappears and superconductivity suddenly sets in, showing broad transition curves.

The strong improvement of the quality of electron doped cuprate single crystals is the result of a systematic, doping dependent investigation of the growth process and the annealing treatment, differing from earlier growth experiments. The crys-

tals are grown from a copper-rich flux composition by applying the container-free TSFZ technique, in order to avoid additional contaminations coming from crucible corrosion. The oxygen partial pressure of the growth atmosphere is the crucial, doping dependent parameter, as the dopant Ce in the solvent promotes the oxygen enrichment from the ambient atmosphere. This causes not only a change in the physical properties and hence the stability of the floating zone, but also supports the segregation of rare earth-oxides and CeO_2 at the crystallization interface.

The annealing treatment is another important aspect for all electron doped compounds. It is intimately connected with the appearance of superconductivity and a reversible epitaxial intergrowth of a parasitic rare earth oxide phase. Nevertheless, it has been shown that the macroscopic impurity phase is rather a structural by-product than a prerequisite for superconductivity. Superconductivity occurs only in the stoichiometric host crystal. The parasitic phase is the result of a severe treatment in a pure Ar atmosphere at high annealing temperatures. This treatment close to the stability limit of the crystals is inevitable in order to remove the interstitial oxygen on the apex site. Thermogravimetric experiments have shown that the as grown crystals have a doping dependent surplus of oxygen, which must occupy the apex position within the crystal structure. This additional oxygen has only a small co-doping effect (band filling). However, it is rather an effective source of disorder, which suppresses superconductivity. It has been shown in annealing experiments on an overdoped $\text{Nd}_{1.84}\text{Ce}_{0.16}\text{CuO}_4$ single crystal that the disorder effect prevails over the co-doping effect. Microscopic disorder and inhomogeneities within the crystals can be probed by means of magnetization measurements, as they act as effective pinning centers, which influence the magnetization curves. With the presented annealing treatment the $\text{Nd}_{2-x}\text{Ce}_x\text{CuO}_4$ sample set shows low irreversibility fields and no anomalies in the magnetization data, confirming therefore the microscopic homogeneity of the crystals.

On the entire $\text{Nd}_{2-x}\text{Ce}_x\text{CuO}_4$ sample set transport measurements have been carried out and discussed within a two-band model. The out-of-plane transport reveals the same features as the in-plane transport and was interpreted to be weakly incoherent. The resistivity in both directions reveals a doping dependent upturn behavior, the onset temperature of which decreases linearly with Ce doping and disappears at $x = 0.17$. The upturn behavior is rather related to AFM fluctuations than to disorder induced localization effects, which is also confirmed by the strongly anisotropic magnetoresistance. For temperatures above the upturn region the spin contribution to the magnetoresistance is negligible and the orbital magnetoresistance prevails. For doping levels $x \geq 0.15$, it was for the first time possible to explain the unusual behavior of the magnetotransport properties within standard Boltzmann transport theory by assuming a two-band model and an anisotropic scattering rate. The transport data clearly reflect the Fermi surface fragmentation at the hot spot regions due to strong interactions of the charge carriers with the AFM correlations. The simulations show that Δ , which is a measure for the AFM correlation strength, decreases steadily with increasing doping but does not drop to zero for the doping level $x = 0.17$. Thus, the Fermi surface is not yet fully reconstructed at this

doping level. For $T < 100$ K there is a remarkable contribution of a small hole pocket to the normal state transport, which can be observed at best in the temperature evolution of the Hall coefficient. The implications on superconductivity and the question whether holes or electrons are responsible for superconductivity are still open questions and could not be answered within the present thesis.

Bibliography

- [1] H. Matsui, T. Takahashi, T. Sato, K. Terashima, H. Ding, T. Uefuji and K. Yamada. Evolution of the pseudogap across the magnet-superconductor phase boundary of $\text{Nd}_{2-x}\text{Ce}_x\text{CuO}_4$. *Phys. Rev. B* **75**, 224514 (2007).
- [2] Y. Onose, Y. Taguchi, K. Ishizaka and Y. Tokura. Charge dynamics in underdoped $\text{Nd}_{2-x}\text{Ce}_x\text{CuO}_4$: Pseudogap and related phenomena. *Phys. Rev. B* **69**, 024504 (2004).
- [3] A. Damascelli, Z. Hussain and Z.-X. Shen. Angle-resolved photoemission studies of the cuprate superconductors. *Rev. Mod. Phys.* **75**, 473 (2003).
- [4] T. Yoshida *et al.* Systematic doping evolution of the underlying Fermi surface of $\text{La}_{2-x}\text{Sr}_x\text{CuO}_4$. *Phys. Rev. B* **74**, 224510 (2006).
- [5] N. E. Hussey. The normal state scattering rate in high- T_c cuprates. *Eur. Phys. J. B* **31**, 495507 (2003).
- [6] A. Narduzzo, G. Albert, M. M. J. French, N. Mangkorntong, M. Nohara, H. Takagi and N. E. Hussey. Violation of the isotropic mean free path approximation for overdoped $\text{La}_{2-x}\text{Sr}_x\text{CuO}_4$. *Phys. Rev. B* **77**, 220502(R) (2008).
- [7] N. Doiron-Leyraud, C. Proust, D. LeBoeuf, J. Levallois, J.-B. Bonnemaïson, R. L. D. A. Bonn, W. N. Hardy and L. Taillefer. Quantum oscillations and the Fermi surface in an underdoped high- T_c superconductor. *Nature* **447**, 565 (2007).
- [8] S. E. Sebastian, N. Harrison, E. Palm, T. P. Murphy, C. H. Mielke, R. Liang, D. A. Bonn, W. N. Hardy and G. G. Lonzarich. A multi-component Fermi surface in the vortex state of an underdoped high- T_c superconductor. *Nature* **454**, 200 (2008).
- [9] N. P. Armitage, F. Ronning, D. H. Lu, C. Kim, A. Damascelli, K. M. Shen, D. L. Feng, H. Eisaki, Z.-X. Shen, P. K. Mang, N. Kaneko, M. Greven, Y. Onose, Y. Taguchi and Y. Tokura. Doping Dependence of an n -Type Cuprate Superconductor Investigated by Angle-Resolved Photoemission Spectroscopy. *Phys. Rev. Lett* **88**, 257001 (2002).

- [10] C. Kusko, R. S. Markiewicz, M. Lindroos and A. Bansil. Fermi surface evolution and collapse of the Mott pseudogap in $\text{Nd}_{2-x}\text{Ce}_x\text{CuO}_{4\pm\delta}$. *Phys. Rev. B* **66**, 140513(R) (2002).
- [11] Y. Dagan, M. M. Qazilbash, C. P. Hill, V. N. Kulkarni and R. L. Greene. Evidence for a Quantum Phase Transition in $\text{P}_{2-x}\text{Ce}_x\text{CuO}_{4-\delta}$ from Transport Measurements. *Phys. Rev. Lett.* **92**, 167001 (2004).
- [12] J. Orenstein and A. J. Millis. Advances in the Physics of High-Temperature Superconductivity. *Science* **288**, 468 (2000).
- [13] W. Yu, J. S. Higgins, P. Bach and R. L. Greene. Transport evidence of a magnetic quantum phase transition in electron-doped high-temperature superconductors. *Phys. Rev. B* **76**, 020503(R) (2007).
- [14] M. R. Norman, D. Pines and C. Kallin. The pseudogap: friend or foe of high T_c . *Advances in Physics* **54**, 715 (2005).
- [15] A. J. Millis. Gaps and Our Understanding. *Science* **314**, 1888 (2006).
- [16] A. Cho. High T_c : The Mystery That Defies Solution. *Science* **314**, 1072 (2006).
- [17] H. Eisaki, N. Kaneko, D. L. Feng, A. Damascelli, P. K. Mang, K. M. Shen, Z.-X. Shen and M. Greven. Effect of chemical inhomogeneity in bismuth-based copper oxide superconductors. *Phys. Rev. B* **69**, 064512 (2004).
- [18] J. L. Tallon, C. Bernhard, H. Shaked, R. L. Hitterman and J. D. Jorgensen. Generic superconducting phase behavior in high- T_c cuprates: T_c variation with hole concentration in $\text{YBa}_2\text{Cu}_3\text{O}_{7-\delta}$. *Phys. Rev. B* **51**, 12911 (1995).
- [19] J. M. Tranquada, B. J. Sternlieb, J. D. Axe, Y. Nakamura and S. Uchida. Evidence for stripe correlations of spins and holes in copper oxide superconductors. *Nature* **375**, 561 (1995).
- [20] R. Liang, D. A. Bonn and W. N. Hardy. Evaluation of CuO_2 plane hole doping in $\text{YBa}_2\text{Cu}_3\text{O}_{6+x}$ single crystals. *Phys. Rev. B* **73**, 180505(R) (2006).
- [21] Y. Ando, Y. Kurita, S. Komiyama, S. Ono and K. Segawa. Evolution of the Hall Coefficient and the Peculiar Electronic Structure of the Cuprate Superconductors. *Phys. Rev. Lett.* **92**, 197001 (2004).
- [22] C. Niedermayer, C. Bernhard, T. Blasius, A. Golnik, A. Moodenbaugh and J. I. Budnick. Common Phase Diagram for Antiferromagnetism in $\text{La}_{2-x}\text{Sr}_x\text{CuO}_4$ and $\text{Y}_{1-x}\text{Ca}_x\text{Ba}_2\text{Cu}_3\text{O}_6$ as Seen by Muon Spin Rotation. *Phys. Rev. Lett.* **80**, 3843 (1998).

- [23] Y. Ando, S. Komiya, K. Segawa, S. Ono and Y. Kurita. Electronic Phase Diagram of High- T_c Cuprate Superconductors from a Mapping of the In-Plane Resistivity Curvature. *Phys. Rev. Lett.* **93**, 267001 (2004).
- [24] T. Uefuji, T. Kubo, K. Yamada, M. Fujita, K. Kurahashi, I. Watanabe and K. Nagamine. Coexistence of antiferromagnetic ordering and high- T_c superconductivity in electron-doped superconductor $\text{Nd}_{2-x}\text{Ce}_x\text{CuO}_4$. *Physica C* **357-360**, 208 (2001).
- [25] Y. Onose, Y. Taguchi, K. Ishizaka and Y. Tokura. Doping Dependence of Pseudogap and Related Charge Dynamics in $\text{Nd}_{2-x}\text{Ce}_x\text{CuO}_4$. *Phys. Rev. Lett.* **87**, 217001 (2001).
- [26] P. K. Mang, S. Larochelle, A. Mehta, O. P. Vajk, A. S. Erickson, L. Lu, W. J. L. Buyers and A. F. Marshall. Phase decomposition and chemical inhomogeneity in $\text{Nd}_{2-x}\text{Ce}_x\text{CuO}_{4\pm\delta}$. *Phys. Rev. B* **70**, 094507 (2004).
- [27] E. M. Motoyama, G. Yu, I. M. Vishik, O. P. Vajk, P. K. Mang and M. Greven. Spin correlations in the electron-doped high-transition-temperature superconductor $\text{Nd}_{2-x}\text{Ce}_x\text{CuO}_{4\pm\delta}$. *Nature* **445**, 186 (2007).
- [28] M. A. Dixon. The normal state electronic structure of cuprate superconductors: a covalent picture. *Physica C* **174**, 117 (1990).
- [29] P. A. Lee, N. Nagaosa and X.-G. Wen. Doping a Mott insulator: Physics of high-temperature superconductivity. *Rev. Mod. Phys.* **78**, 17 (2006).
- [30] G. M. Luke *et al.* Magnetic order and electronic phase diagrams of electron-doped copper oxide materials. *Phys. Rev. B* **42**, 7981 (1990).
- [31] T. R. Thurston, M. Matsuda, K. Kakurai, K. Yamada, Y. Endoh, R. J. Birgeneau, P. M. Gehring, Y. Hidaka, M. A. Kastner, T. Murakami and G. Shirane. Antiferromagnetic spin correlations in $(\text{Nd,Pr})_{2-x}\text{Ce}_x\text{CuO}_4$. *Phys. Rev. Lett.* **65**, 263 (1990).
- [32] H. Ding, M. R. Norman, J. C. Campuzano, M. Randeria, A. F. Bellman, T. Yokoya, T. Takahashi, T. Mochiku and K. Kadowaki. Angle-resolved photoemission spectroscopy study of the superconducting gap anisotropy in $\text{Bi}_2\text{Sr}_2\text{CaCu}_2\text{O}_{8+x}$. *Phys. Rev. B* **54**, R9678 (1996).
- [33] Z.-X. Shen, D. S. Dessau, B. O. Wells, D. M. King, W. E. Spicer, A. J. Arko, D. Marshall, L. W. Lombardo, A. Kapitulnik, P. Dickinson, S. Doniach, J. DiCarlo, T. Loeser and C. H. Park. Anomalously large gap anisotropy in the a-b plane of $\text{Bi}_2\text{Sr}_2\text{CaCu}_2\text{O}_{8+d}$. *Phys. Rev. Lett.* **70**, 1553 (1993).
- [34] C. C. Tsuei, J. R. Kirtley, C. C. Chi, L. S. Yu-Jahnes, A. Gupta, T. Shaw, J. Z. Sun and M. B. Ketchen. Pairing Symmetry and Flux Quantization in a Tricrystal Superconducting Ring of $\text{YBa}_2\text{Cu}_3\text{O}_{7-\delta}$. *Phys. Rev. Lett.* **73**, 593 (1994).

- [35] J. M. Tranquada, H. Woo, T. G. Perring, H. Goka, G. D. Gu, G. Xu, M. Fujita and K. Yamada. Quantum magnetic excitations from stripes in copper oxide superconductors. *Nature* **429**, 534 (2004).
- [36] S. A. Kivelson, I. P. Bindloss, E. Fradkin, V. Oganesyan, J. M. Tranquada, A. Kapitulnik and C. Howald. How to detect fluctuating stripes in the high-temperature superconductors. *Rev. Mod. Phys.* **75**, 1201 (2003).
- [37] T. Valla, A. V. Fedorov, J. Lee, J. C. Davis and G. D. Gu. The Ground State of the Pseudogap in Cuprate Superconductors. *Science* **314**, 1914 (2006).
- [38] S. Hübner, M. A. Hossain, A. Damascelli and G. A. Sawatzky. Two Gaps Make a High Temperature Superconductor. *arXiv:0706.4282v1* (2007).
- [39] M. R. Norman, H. Ding, M. Randeria, J. C. Campuzano, T. Yokoya, T. Takeuchi, T. Takahashi, T. Mochiku, K. Kadowaki, P. Guptasarma and D. G. Hinks. Destruction of the Fermi surface in underdoped high- T_c superconductors. *Nature* **392**, 157 (1998).
- [40] M. Eschrig. The effect of collective spin-1 excitations on electronic spectra in high- T_c superconductors. *Advances in Physics* **55**, 47 (2006).
- [41] A. Kanigel *et al.* Evolution of the pseudogap from Fermi arcs to the nodal liquid. *Nature Physics* **2**, 447 (2006).
- [42] H. Castro and G. Deutscher. Anomalous Fermi liquid behavior of overdoped high- T_c superconductors. *Phys. Rev. B* **70**, 174511 (2004).
- [43] N. E. Hussey, J. R. Cooper, J. M. Wheatley, I. R. Fisher, A. Carrington, A. P. Mackenzie, C. T. Lin and O. Milat. Angular Dependence of the c -axis Normal State Magnetoresistance in Single Crystal $Tl_2Ba_2CuO_6$. *Phys. Rev. Lett.* **76**, 122 (1996).
- [44] N. E. Hussey, M. Abdel-Jawad, A. Carrington, A. P. Mackenzie and L. Balicas. A coherent three-dimensional Fermi surface in a high-transition-temperature superconductor. *Nature* **425** (2003).
- [45] J. G. Analytis, M. Abdel-Jawad, L. Balicas, M. M. J. French and N. E. Hussey. Angle-dependent magnetoresistance measurements in $Tl_2Ba_2CuO_{6+\delta}$ and the need for anisotropic scattering. *Phys. Rev. B* **76**, 104523 (2007).
- [46] G. Blumberg, A. Koitzsch, A. Gozar, B. S. Dennis, C. A. Kendziora, P. Fournier and R. L. Greene. Nonmonotonic $d_{x^2-y^2}$ Superconducting Order Parameter in $Nd_{2-x}Ce_xCuO_4$. *Phys. Rev. Lett.* **88**, 107002 (2002).
- [47] C. C. Tsuei and J. R. Kirtley. Phase-Sensitive Evidence for d-Wave Pairing Symmetry in Electron-Doped Cuprate Superconductors. *Phys. Rev. Lett.* **85**, 182 (2000).

- [48] B. Chesca, M. Seifried, T. Dahm, N. Schopohl, D. Koelle, R. Kleiner and A. Tsukada. Observation of Andreev bound states in bicrystal grain-boundary Josephson junctions of the electron-doped superconductor $\text{La}_{2-x}\text{Ce}_x\text{CuO}_{4-y}$. *Phys. Rev. B* **71**, 104504 (2005).
- [49] B. W. Veal and A. P. Paulikas. Dependence of the hole concentration on oxygen vacancy order in $\text{YBa}_2\text{Cu}_3\text{O}_{7-\delta}$. *Physica C* **184**, 321 (1991).
- [50] A. Erb, E. Walker, J.-Y. Genoud and R. Flükiger. Improvements in crystal growth and crystal homogeneity and its impact on physics. *Physica C* **282-287**, 89 (1997).
- [51] R. Liang, D. A. Bonn and W. N. Hardy. Preparation and X-ray characterization of highly ordered ortho-II phase $\text{YBa}_2\text{Cu}_3\text{O}_{6.5}$ single crystals. *Physica C* **336**, 57 (2000).
- [52] R. Liang, D. A. Bonn, W. N. Hardy, J. C. Wynn, K. A. Moler, L. Lu, S. Larochelle, L. Zhou, M. Greven, L. Lurio and S. G. J. Mochrie. Preparation and characterization of homogeneous YBCO single crystals with doping level near the SC-AFM boundary. *Physica C* **383**, 1 (2002).
- [53] D. LeBoeuf, N. Doiron-Leyraud, J. Levallois, R. Daou, J.-B. Bonnemaïson, N. E. Hussey, L. Balicas, B. J. Ramshaw, R. Liang, D. A. Bonn, W. N. Hardy, S. Adachi, C. Proust and L. Taillefer. Electron pockets in the Fermi surface of hole-doped high- T_c superconductors. *Nature* **450**, 533 (2007).
- [54] L. Tassini, W. Prestel, R. Hackl, A. Erb and M. Lambacher. Charge ordering phenomena in high temperature superconductors. *Physica C* **460-462**, 925 (2007).
- [55] A. Jánossy, T. Fehér and A. Erb. Diagonal Antiferromagnetic Easy Axis in Lightly Hole Doped $\text{Y}_{1-x}\text{Ca}_x\text{Ba}_2\text{Cu}_3\text{O}_6$. *Phys. Rev. Lett.* **91**, 177001 (2003).
- [56] A. Jánossy, K. L. Nagy, T. Fehér, L. Mihály and A. Erb. Search for stripes in antiferromagnetic lightly hole-doped $\text{YBa}_2\text{Cu}_3\text{O}_6$: An electron spin resonance and infrared transmission study. *Phys. Rev. B* **75**, 024501 (2007).
- [57] V. Hinkov, S. Pailhès, P. Bourges, Y. Sidis, A. Ivanov, A. Kulakov, C. T. Lin, D. P. Chen, C. Bernhard and B. Keimer. Two-dimensional geometry of spin excitations in the high-transition-temperature superconductor $\text{YBa}_2\text{Cu}_3\text{O}_{6+x}$. *Nature* **430**, 650 (2004).
- [58] V. B. Zabolotnyy *et al.* Momentum and temperature dependence of the renormalization effects in the high-temperature superconductor $\text{YBa}_2\text{Cu}_3\text{O}_{7-\delta}$. *Phys. Rev. B* **76**, 064519 (2007).
- [59] Y. Ando, K. Segawa, S. Komiyama and A. N. Lavrov. Electrical Resistivity Anisotropy from Self-Organized One Dimensionality in High-Temperature Superconductors. *Phys. Rev. Lett.* **88**, 137005 (2002).

- [60] S. Komiya, Y. Ando, X. Sun and A. Lavrov. c-axis transport and resistivity anisotropy of lightly to moderately doped $\text{La}_{2-x}\text{Sr}_x\text{CuO}_4$ single crystals: Implications on the charge transport mechanism. *Phys. Rev. B* **65**, 214535 (2002).
- [61] S. Ono, S. Komiya and Y. Ando. Strong charge fluctuations manifested in the high-temperature Hall coefficient of high- T_c cuprates. *Phys. Rev. B* **75**, 024515 (2007).
- [62] T. Yoshida, X. J. Zhou, T. Sasagawa, W. L. Yang, P. V. Bogdanov, A. Lanzara, Z. Hussain, T. Mizokawa, A. Fujimori, H. Eisaki, Z.-X. Shen, T. Kakeshita and S. Uchida. Metallic Behavior of Lightly Doped $\text{La}_{2-x}\text{Sr}_x\text{CuO}_4$ with a Fermi Surface Forming an Arc. *Phys. Rev. Lett.* **91**, 027001 (2003).
- [63] P. J. Picone, H. P. Jenssen and D. R. Gabbe. Phase diagram and single crystal growth of pure and Sr doped La_2CuO_4 . *J. Cryst. Growth* **91**, 463 (1988).
- [64] C. Marin, T. Charvolin, D. Braithwaite and R. Calemczuk. Properties of a large $\text{La}_{1.92}\text{Sr}_{0.08}\text{CuO}_{4+\delta}$ single crystal grown by the travelling-solvent floating-zone method. *Physica C* **320**, 197 (1999).
- [65] R. J. Cava, A. Santoro, D. W. Johnson and W. W. Rhodes. Crystal structure of the high-temperature superconductor $\text{La}_{1.85}\text{Sr}_{0.15}\text{CuO}_4$ above and below T_c . *Phys. Rev. B* **35**, 6716 (1987).
- [66] M. G. Cramm. *Diffraktometrische Untersuchung der strukturellen Phasenumwandlungen der seltenerd-dotierten $(\text{La},\text{Sr})_2\text{CuO}_4$ Hochtemperatursupraleiter*. Ph.D. thesis, Universität Köln (1999).
- [67] V. B. Zabolotnyy, S. Borisenko, A. A. Kordyuk, J. Fink, J. Geck, A. Koitzsch, M. Knupfer, B. Büchner, H. Berger, A. Erb, C. T. Lin, B. Keimer, and R. Follath. Effect of Zn and Ni Impurities on the Quasiparticle Renormalization of Superconducting Bi-2212. *Phys. Rev. Lett.* **96**, 037003 (2006).
- [68] A. A. Kordyuk, S. V. Borisenko, M. S. Golden, S. Legner, K. A. Nenkov, M. Knupfer, J. Fink and H. Berger. Doping dependence of the Fermi surface in $(\text{Bi},\text{Pb})_2\text{Sr}_2\text{CaCu}_2\text{O}_{8+\delta}$. *Phys. Rev. B* **66**, 01450 (2002).
- [69] M. Opel, R. Nemetschek, C. Hoffmann, R. Philipp, P. F. Müller, R. Hackl, I. Tüttó, A. Erb, B. Revaz, E. Walker, H. Berger and L. Forró. Carrier relaxation, pseudogap, and superconducting gap in high- T_c cuprates: A Raman scattering study. *Phys. Rev. B* **61**, 9752 (2000).
- [70] Y. Kohsaka, C. Taylor, K. Fujita, A. Schmidt, C. Lupien, T. Hanaguri, M. Azuma, M. Takano, H. Eisaki, H. Takagi, S. Uchida and J. C. Davis. An Intrinsic Bond-Centered Electronic Glass with Unidirectional Domains in Underdoped Cuprates. *Science* **315**, 1380 (2007).

- [71] K. K. Gomes, A. N. Pasupathy, A. Pushp, S. Ono, Y. Ando and A. Yazdani. Visualizing pair formation on the atomic scale in the high- T_c superconductor $\text{Bi}_2\text{Sr}_2\text{CaCu}_2\text{O}_{8+\delta}$. *Nature* **447**, 569 (2007).
- [72] A. Maljuk, B. Liang, C. T. Lin and G. A. Emel'chenko. On the growth of overdoped Bi-2212 single crystals under high oxygen pressure. *Physica C* **355**, 140 (2001).
- [73] B. Liang and C. T. Lin. On the growth of underdoped $\text{Bi}_2\text{Sr}_2\text{CaCu}_2\text{O}_{8+\delta}$ single crystals by TSFZ method. *J. Cryst. Growth* **237-239**, 756 (2002).
- [74] B. Liang, C. T. Lin, P. Shang and G. Yang. Single crystals of triple-layered cuprates $\text{Bi}_2\text{Sr}_2\text{Ca}_2\text{Cu}_3\text{O}_{10+\delta}$ growth, annealing and characterization. *Physica C* **383**, 75 (2002).
- [75] R. Gladyshevskii, N. Musolino and R. Flükiger. Structural origin of the low superconducting anisotropy of $\text{Bi}_{1.7}\text{Pb}_{0.4}\text{Sr}_2\text{Ca}_{0.9}\text{Cu}_2\text{O}_8$ crystals. *Phys. Rev. B* **70**, 184522 (2004).
- [76] G. Kinoda and T. Hasegawa. Observation of electronic inhomogeneity in heavily Pb-doped $\text{Bi}_2\text{Sr}_2\text{CaCu}_2\text{O}_y$ single crystals by scanning tunneling microscopy. *Phys. Rev. B* **67**, 224509 (2003).
- [77] G. Triscone, J.-Y. Genoud, T. Graf, A. Junod and J. Muller. Variation of the superconducting properties of $\text{Bi}_2\text{Sr}_2\text{CaCu}_2\text{O}_{8+\delta}$ with oxygen content. *Physica C* **176**, 247 (1991).
- [78] P. G. Radelli, J. D. Jorgensen, A. J. Schultz, J. L. Peng and R. L. Greene. Evidence of apical oxygen in Nd_2CuO_y determined by single-crystal neutron diffraction. *Phys. Rev. B* **49**, 15322 (1994).
- [79] A. J. Schultz, J. D. Jorgensen, J. L. Peng and R. L. Greene. Single-crystal neutron-diffraction structures of reduced and oxygenated $\text{Nd}_{2-x}\text{Ce}_x\text{CuO}_y$. *Phys. Rev. B* **53**, 5157 (1996).
- [80] A. C. James and D. W. Murphy. *Chemistry of superconductor materials*, chap. 11 in Part 2, 427–448 (Terrell A. Vanderah, 1992), noyes publications edn.
- [81] B. Welter. *Tunnelspektroskopie an Korngrenzenkontakten aus elektronendotierten Hochtemperatur-Supraleitern*. Ph.D. thesis, TU München (2007).
- [82] M. Matsuda, K. Yamada, K. Kakurai, H. Kadowaki, T. R. Thurston, Y. Endoh, Y. Hidaka, R. J. Birgeneau, M. A. Kastner, P. M. Gehring, A. H. Moudden and G. Shirane. Three-dimensional magnetic structures and rare-earth magnetic ordering in Nd_2CuO_4 and Pr_2CuO_4 . *Phys. Rev. B* **42**, 10098 (1990).

- [83] E. Manousakis. The spin-1/2 Heisenberg antiferromagnet on a square lattice and its application to the cuprous oxides. *Rev. Mod. Phys.* **63**, 1 (1991).
- [84] M. Matsuda, Y. Endoh, K. Yamada, H. Kojima, I. Tanaka, R. J. Birgeneau, M. A. Kastner and G. Shirane. Magnetic order, spin correlations, and superconductivity in single-crystal $\text{Nd}_{1.85}\text{Ce}_{0.15}\text{CuO}_{4+\delta}$. *Phys. Rev. B* **45**, 12548 (1992).
- [85] Y. Endoh, M. Matsuda, K. Yamada, K. Kakurai, Y. Hidaka, G. Shirane and R. J. Birgenau. Two-dimensional spin correlations and successive magnetic phase transitions in Nd_2CuO_4 . *Phys. Rev. B* **40**, 7023 (1989).
- [86] S. Skanthakumar, J. W. Lynn, J. L. Peng and Z. Y. Li. Observation of noncollinear magnetic structure for the Cu spins in Nd_2CuO_4 -type systems. *Phys. Rev. B* **47**, 6173 (1993).
- [87] M. Matsuura, P. Dai, H. J. Kang, J. W. Lynn, D. N. Argyriou, K. Prokes, Y. Onose and Y. Tokura. Effect of a magnetic field on the long-range magnetic order in insulating Nd_2CuO_4 and nonsuperconducting and superconducting $\text{Nd}_{1.85}\text{Ce}_{0.15}\text{CuO}_4$. *Phys. Rev. B* **68**, 144503 (2003).
- [88] A. T. Boothroyd, S. M. Doyle, D. M. K. Paul and R. Osborn. Crystal-field excitations in Nd_2CuO_4 , Pr_2CuO_4 , and related n -type superconductors. *Phys. Rev. B* **45**, 10075 (1992).
- [89] M. F. Hundley, J. D. Thompson, S.-W. Cheong, Z. Fisk and S. B. Oseroff. Specific heat and anisotropic magnetic susceptibility of Pr_2CuO_4 , Nd_2CuO_4 and Sm_2CuO_4 crystals. *Physica C* **158**, 102 (1989).
- [90] K. Oka and H. Unoki. Phase Diagram and Crystal Growth of Superconductive $(\text{NdCe})_2\text{CuO}_4$. *Jpn. J. Appl. Phys.* **28**, L937 (1989).
- [91] A. M. Balbashev, D. A. Shulyatev, G. K. Panova, M. N. Khlopkin, N. A. Chernoplekov, A. A. Shikov and A. V. Suetin. The floating zone growth and superconductive properties of $\text{La}_{1.85}\text{Sr}_{0.15}\text{CuO}_4$ and $\text{Nd}_{1.85}\text{Ce}_{0.15}\text{CuO}_4$ single crystals. *Physica C* **256**, 371 (1996).
- [92] A. N. Maljuk, A. A. Jokhov, I. G. Naumenko, I. K. Bdikin, S. A. Zver'kov and G. A. Emel'chenko. Growth and characterization of bulk $\text{Nd}_{2-x}\text{Ce}_x\text{CuO}_4$ single crystals. *Physica C* **329**, 51 (2000).
- [93] H. Shibata, K. Oka, S. Kashiwayaa and H. Yamaguchi. Traveling solvent floating-zone growth and reduction condition optimization of $\text{Nd}_{2-x}\text{Ce}_x\text{CuO}_4$ single crystals. *Physica C* **357**, 363 (2001).
- [94] T. Uefuji, K. Kurahashi, M. Fujita, M. Matsuda and K. Yamada. Electron-doping effect on magnetic order and superconductivity in $\text{Nd}_{2-x}\text{Ce}_x\text{CuO}_4$ single crystals. *Physica C* **378-381**, 273 (2002).

- [95] K. Kurahashi, H. Matsushita, M. Fujita and K. Yamada. Heat treatment effects on the superconductivity and crystal structure of $\text{Nd}_{1.85}\text{Ce}_{0.15}\text{CuO}_4$ studied using a single crystal. *Journal of the Physical Society of Japan* **71**, 910 (2002).
- [96] T. Uefuji, S. Kuroshima, M. Fujita and K. Yamada. Superconducting phase diagram of electron-doped cuprates $\text{Nd}_{2-x}\text{Ce}_x\text{CuO}_4$. *Physica C* **392-396**, 189 (2003).
- [97] F. Schwabl. *Statistische Mechanik* (Springer-Verlag, 2000).
- [98] W. F. Hemminger and H. K. Cammenga. *Methoden der Thermischen Analyse* (Springer-Verlag, 1989).
- [99] G. Adachi and N. Imanaka. The binary rare earth oxides. *Chem. Rev.* **98**, 1479 (1998).
- [100] I. Tanaka, N. Komai and H. Kojima. Phase equilibrium in the Nd-Ce-Cu-O system. *Physica C* **190**, 112 (1991).
- [101] A. Erb. *Untersuchung zum Phasendiagramm und Kristallzüchtung im System $\text{YBa}_2\text{Cu}_3\text{O}_{7-\delta}$ - BaCuO_2 - CuO* . Ph.D. thesis, Universität (TH) Karlsruhe (1994).
- [102] K. Oka and H. Unoki. Phase Diagram of $\text{Nd}_{2-x}\text{Ce}_x\text{O}_3$ -CuO Systems. *Jpn. J. Appl. Phys.* **29**, L909 (1990).
- [103] A. N. Maljuk, A. B. Kulakov and G. A. Emel'chenko. Temperature dependence of the dissolution enthalpy of the La_2CuO_4 and $\text{Nd}_{2-x}\text{Ce}_x\text{CuO}_4$ phases and complex formation in cuprate melts. *Journal of Crystal Growth* **151**, 101 (1995).
- [104] M. Matsuda, Y. Endoh and Y. Hidaka. Crystal growth and characterization of $\text{Pr}_{2-x}\text{Ce}_x\text{CuO}_4$. *Physica C* **179**, 347 (1991).
- [105] K.-T. Wilke and J. Bohm. *Kristallzüchtung* (Verlag Harri Deutsch, 1988).
- [106] I. Shindo. Determination of the phase diagram by the slow cooling float zone method: The system MgO - TiO_2 . *Journal of Crystal Growth* **50**, 839 - 851 (1980).
- [107] T.-S. Han, K. Oka and H. Kawanaka. The optimum condition of single crystal growth of $(\text{Pr,Ce})_2\text{CuO}_4$ by the travelling-solvent floating-zone method. *Physica B* **194-196**, 2241 (1994).
- [108] K. Gamayunov, I. Tanaka and H. Kojima. TSFZ Growth of $\text{Nd}_{2-x}\text{Ce}_x\text{CuO}_4$ Single Crystals at Low Oxygen Pressure. *Physica C* **235-240**, 557 (1994).

- [109] K. Oka, H. Shibata, S. Kashiwaya and H. Eisaki. Crystal growth of $\text{La}_{2-x}\text{Ce}_x\text{CuO}_4$. *Physica C* **388-389**, 389 (2003).
- [110] J. E. Hirsch. Role of reduction process in the transport properties of the electron-doped oxide superconductors. *Physica C* **243**, 319 (1995).
- [111] M. Brinkmann, T. Rex, H. Bach and K. Westerholt. Extended Superconducting Concentration Range Observed in $\text{Pr}_{2-x}\text{Ce}_x\text{CuO}_{4-\delta}$. *Phys. Rev. Lett.* **74**, 4927 (1995).
- [112] V. Pankov, N. Kalanda, V. Truchan, D. Zhigunov and O. Babushkin. Oxygen nonstoichiometry and superconductivity of the $\text{Nd}_{2-x}\text{Ce}_x\text{CuO}_{4-\delta}$ single crystal. *Physica C* **377**, 521 (2002).
- [113] J. S. Higgins, Y. Dagan, M. C. Barr, B. D. Weaver and R. L. Greene. Role of oxygen in the electron-doped superconducting cuprates. *Phys. Rev. B* **73**, 104510 (2006).
- [114] Y. Tanaka, T. Motohashi, M. Karppinen and H. Yamauchi. Conditions for superconductivity in the electron-doped copper-oxide system, $(\text{Nd}_{1-x}\text{Ce}_x)_2\text{CuO}_{4+\delta}$. *Journal of Solid State Chemistry* **181**, 365 (2008).
- [115] Y. Onose, Y. Taguchi, T. Ishikawa, S. Shinomori, K. Ishizaka and Y. Tokura. Anomalous Pseudogap Formation in a Nonsuperconducting Crystal of $\text{Nd}_{1.85}\text{Ce}_{0.15}\text{CuO}_{4+y}$: Implication of Charge Ordering. *Phys. Rev. Lett.* **82**, 5120 (1999).
- [116] P. Fournier, X. Jiang, W. Jiang, S. N. Mao, T. Venkatesan, C. J. Lobb and R. L. Greene. Thermomagnetic transport properties of $\text{Nd}_{1.85}\text{Ce}_{0.15}\text{CuO}_4$ films: Evidence for two types of charge carrier. *Phys. Rev. B* **56**, 14149 (1997).
- [117] P. Richard, G. Riou, I. Hetel, S. Jandl, M. Poirier and P. Fournier. Role of oxygen nonstoichiometry and the reduction process on the local structure of $\text{Nd}_{2-x}\text{Ce}_x\text{CuO}_{4\pm\delta}$. *Phys. Rev. B* **70**, 064513 (2004).
- [118] G. Riou, P. Richard, S. Jandl, M. Poirier and P. Fournier. Pr^{3+} crystal-field excitation study of apical oxygen and reduction processes in $\text{Pr}_{2-x}\text{Ce}_x\text{CuO}_{4\pm\delta}$. *Phys. Rev. B* **69**, 024511 (2004).
- [119] H. Kimura, Y. Noda, F. Sato, K. Tsuda, K. Kurahashi, T. Uefuji, M. Fujita and K. Yamada. X-ray and Electron Diffraction Study of a Precipitation Phase in $\text{Nd}_{1.85}\text{Ce}_{0.15}\text{CuO}_{4+y}$ Single Crystal. *Journal of the Physical Society of Japan* **74**, 2282 (2005).
- [120] C. H. Wang, G. Y. Wang, Z. Feng, S. Y. Li and X. H. Chen. Effect of Ce doping and oxygen content on pseudogap and anisotropy in $\text{Nd}_{2-x}\text{Ce}_x\text{CuO}_{2-\delta}$. *Supercond. Sci. Technol.* **18**, 763 (2005).

- [121] H. Takagi. Superconductivity: Coppers in the right place. *Nature Materials* **6**, 179 (2007).
- [122] H. J. Kang, P. Dai, B. J. Campbell, P. J. Chupas, S. Rosenkranz, P. L. Lee, Q. Huang, S. Li, S. Komiya and Y. Ando. Microscopic annealing process and its impact on superconductivity in T'-structure electron-doped copper oxides. *Nature Materials* **6**, 224 (2007).
- [123] J. S. Kim and D. R. Gaskell. The phase stability diagrams for the systems $\text{Nd}_2\text{CuO}_{4-\delta}$ and $\text{Nd}_{1.85}\text{Ce}_{0.15}\text{CuO}_{4-\delta}$. *Physica C* **209**, 381 (1993).
- [124] T. W. Klimczuk, W. Sadowski, P. W. Klamut and B. Dabrowski. Study of superconductivity in a wide range of Ce doping in Nd-214 systems. *Physica C* **341-348**, 395 (2000).
- [125] A. Erb, B. Greb and G. Müller-Vogt. In-situ resistivity measurements during the oxygenation of $\text{YBa}_2\text{Cu}_3\text{O}_{7-\delta}$ and $\text{Gd}_{0.8}\text{Y}_{0.2}\text{Ba}_2\text{Cu}_3\text{O}_{7-\delta}$ single crystals. *Physica C* **259**, 83 (1996).
- [126] M. Fujita, T. Kubo, S. Kuroshima, T. Uefuji, K. Kawashima, K. Yamada, I. Watanabe and K. Nagamine. Magnetic and superconducting phase diagram of electron-doped $\text{Pr}_{1-x}\text{Ce}_x\text{LaCuO}_{4+\delta}$. *Phys. Rev. B* **67**, 014514 (2003).
- [127] K. Isawa, M. Nagano, M. Fujita and K. Yamada. Thermoelectric power of electron-doped superconductor, $\text{Pr}_{1-x}\text{LaCe}_x\text{CuO}_4$. *Physica C* **378-381**, 142 (2002).
- [128] Y. Tomioka, M. Naito, K. Kishio and K. Kitazawa. The Meissner and shielding effects of high-temperature oxide superconductors. *Physica C* **223**, 347 (1994).
- [129] H. Balci and R. L. Greene. Thermodynamic properties of $\text{Pr}_{1.85}\text{Ce}_{0.15}\text{CuO}_{4-\delta}$. *Phys. Rev. B* **70**, 140508(R) (2004).
- [130] T. Kawashima and E. Takayama-Muromachi. Oxygen deficiency and superconductivity in $\text{Nd}_{2-x}\text{Ce}_x\text{CuO}_4$. *Physica C* **219**, 389 (1994).
- [131] E. Wang, J.-M. Tarascon, L. H. Greene, G. W. Hull and W. R. McKinnon. Cationic substitution and role of oxygen in the n-type superconducting T' system $\text{Nd}_{2-y}\text{Ce}_y\text{CuO}_z$. *Phys. Rev. B* **41**, 6582 (1990).
- [132] G. S. P. Ghigna, M. Scavini, U. A. Tamburini and A. V. Chadwick. The atomic and electronic structure of cerium substitutional defects in $\text{Nd}_{2-x}\text{Ce}_x\text{CuO}_{4+\delta}$: An XAS study. *Physica C* **253**, 147 (1995).
- [133] B. D. Cullity and S. R. Stock. *Elements of X-ray Diffraction*. 0201610914 (Prentice Hall, 2001).

- [134] H. Takagi, S. Uchida and Y. Tokura. Superconductivity produced by electron doping in CuO_2 -layered compounds. *Phys. Rev. Lett.* **62**, 1197 (1989).
- [135] Y. Idemoto, K. Fueki and T. Shinbo. T -log diagram and copper valence of $\text{Nd}_{1.85}\text{Ce}_{0.15}\text{CuO}_{4-\delta}$. *Physica C* **166**, 513 (1990).
- [136] K. Suzuki, K. Kishio, T. Hasegawa and K. Kitazawa. Oxygen nonstoichiometry of the $(\text{Nd,Ce})_2\text{CuO}_{4-\delta}$ system. *Physica C* **166**, 357 (1990).
- [137] R. J. Cava, H. Takagi, R. M. Fleming, J. J. Krajewski, W. F. Peck, P. Bordet, M. Marezio, B. Batlogg and L. W. Rupp. Metal atom stoichiometry in the electron doped superconductor $(\text{Nd,Ce})_2\text{CuO}_4$. *Physica C* **199**, 65–72 (1992).
- [138] W. Jiang, S. N. Mao, X. X. Xi, X. Jiang, J. L. Peng, T. Venkatesan, C. J. Lobb and R. L. Greene. Anomalous transport properties in superconducting $\text{Nd}_{1.85}\text{Ce}_{0.15}\text{CuO}_{4\pm\delta}$. *Phys. Rev. Lett.* **73**, 1291 (1994).
- [139] F. Gollnik and M. Naito. Doping dependence of normal- and superconducting-state transport properties of $\text{Nd}_{2-x}\text{Ce}_x\text{CuO}_{4\pm\delta}$. *Phys. Rev. B* **58**, 11734 (1998).
- [140] J. Gauthier, S. Gagné, J. Renaud, M.-E. Gosselin, P. Fournier and P. Richard. Different roles of cerium substitution and oxygen reduction in transport in $\text{Pr}_{2-x}\text{Ce}_x\text{CuO}_4$ thin films. *Phys. Rev. B* **75**, 024424 (2007).
- [141] Y. Dagan and R. L. Greene. Hole superconductivity in the electron-doped superconductor $\text{Pr}_{2-x}\text{Ce}_x\text{CuO}_4$. *Phys. Rev. B* **76**, 024506 (2007).
- [142] I. Tsukada and S. Ono. Negative Hall coefficients of heavily overdoped $\text{La}_{2-x}\text{Sr}_x\text{CuO}_4$. *Phys. Rev. B* **74**, 134508 (2006).
- [143] Y. Ando, A. N. Lavrov, S. Komiya, K. Segawa and X. F. Sun. Mobility of the Doped Holes and the Antiferromagnetic Correlations in Underdoped High- T_c Cuprates. *Phys. Rev. Lett.* **87**, 017001 (2001).
- [144] J. Custers, P. Gegenwart, H. Wilhelm, K. Neumaier, Y. Tokiwa, O. Trovarelli, C. Geibel, F. Steglich, C. Pépin and P. Coleman. The break-up of heavy electrons at a quantum critical point. *Nature* **424**, 524 (2003).
- [145] A. W. Tyler and A. P. Mackenzie. Hall effect of single layer, tetragonal $\text{Ti}_2\text{Ba}_2\text{CuO}_{6+\delta}$ near optimal doping. *Physica C* **282-287**, 1185 (1997).
- [146] G. S. Boebinger, Y. Ando, A. Passner, T. Kimura, M. Okuya, J. Shimoyama, K. Kishio, K. Tamasaku, N. Ichikawa and S. Uchida. Insulator-to-Metal Crossover in the Normal State of $\text{La}_{2-x}\text{Sr}_x\text{CuO}_4$ Near Optimum Doping. *Phys. Rev. Lett.* **77**, 5417 (1996).

- [147] S. Nakamae, K. Behnia, N. Mangkorntong, M. Nohara, H. Takagi, S. J. C. Yates and N. E. Hussey. Electronic ground state of heavily overdoped non-superconducting $\text{La}_{2-x}\text{Sr}_x\text{CuO}_4$. *Phys. Rev. B* **68**, 100502 (2003).
- [148] H. Takagi, T. Ido, S. Ishibashi, M. Uota, S. Uchida and Y. Tokura. Superconductor-to-nonsuperconductor transition in $(\text{La}_{1-x}\text{Sr}_x)_2\text{CuO}_4$ as investigated by transport and magnetic measurements. *Phys. Rev. B* **40**, 2254 (1989).
- [149] P. W. Anderson. Hall Effect in the Two-Dimensional Luttinger Liquid. *Phys. Rev. Lett.* **67**, 2092 (1991).
- [150] J. M. Harris, Y. F. Yan, P. Matl, N. P. Ong, P. W. Anderson, T. Kimura and K. Kitazawa. Violation of Kohler's rule in the normal-state magnetoresistance of YBCO and LSCO. *Phys. Rev. Lett.* **75**, 1391 (1995).
- [151] T. Kimura, S. Miyasaka, H. Takagi, K. Tamasaku, H. Eisaki, S. Uchida, K. Kitazawa, M. Hiroi, M. Sera and N. Kobayashi. In-plane and out-of-plane magnetoresistance in $\text{La}_{2-x}\text{Sr}_x\text{CuO}_4$ single crystals. *Phys. Rev. B* **53**, 8733 (1996).
- [152] P. Li, F. F. Balakirev and R. L. Greene. High-field Hall resistivity and Magnetoresistance of Electron-doped $\text{Pr}_{2-x}\text{Ce}_x\text{CuO}_{4-\delta}$. *Phys. Rev. Lett.* **99**, 047003 (2007).
- [153] P. Li, F. F. Balakirev and R. L. Greene. Upper critical field of electron-doped $\text{Pr}_{2-x}\text{Ce}_x\text{CuO}_{4-\delta}$ in parallel magnetic fields. *Phys. Rev. B* **75**, 172508 (2007).
- [154] Y. Dagan, M. C. Barr, W. M. Fisher, R. Beck, T. Dhakal, A. Biswas and R. L. Greene. Origin of the Anomalous Low Temperature Upturn in the Resistivity of the Electron-Doped Cuprate Superconductors. *Phys. Rev. Lett.* **94**, 057005 (2005).
- [155] R. C. Budhani, M. C. Sullivan, C. J. Lobb and R. L. Greene. Thermopower and Hall conductivity in the magnetic-field-driven normal state of $\text{Pr}_{2-x}\text{Ce}_x\text{CuO}_{4-\delta}$ superconductors. *Phys. Rev. B* **65**, 100517 (2002).
- [156] P. Fournier, P. Mohanty, E. Maiser, S. Darzens, T. Venkatesan, C. J. Lobb, G. Czjzek, R. A. Webb and R. L. Greene. Insulator-metal crossover near optimal doping in PCCO: Anomalous normal-state low temperature resistivity. *Phys. Rev. Lett.* **81**, 4720 (1998).
- [157] C. H. Wang, G. Y. Wang, T. Wu, Z. Feng, X. G. Luo and X. H. Chen. Influence of doping level on the Hall coefficient and on the thermoelectric power in $\text{Nd}_{2-x}\text{Ce}_x\text{CuO}_{4+\delta}$. *Phys. Rev. B* **72**, 132506 (2005).

- [158] J. Lin and A. J. Millis. Theory of low-temperature Hall effect in electron-doped cuprates. *Phys. Rev. B* **72**, 214506 (2005).
- [159] N. P. Armitage, D. H. Lu, C. Kim, A. Damascelli, K. M. Shen, F. Ronning, D. L. Feng, P. Bogdanov, Z.-X. Shen, Y. Onose, Y. Taguchi, Y. Tokura, P. K. Mang, N. Kaneko and M. Greven. Anomalous Electronic Structure and Pseudogap Effects in $\text{Nd}_{1.85}\text{Ce}_{0.15}\text{CuO}_4$. *Phys. Rev. Lett.* **87**, 147003 (2001).
- [160] H. Matsui, K. Terashima, T. Sato, T. Takahashi, S.-C. Wang, H.-B. Yang, H. Ding, T. Uefuji and K. Yamada. Angle-Resolved Photoemission Spectroscopy of the Antiferromagnetic Superconductor $\text{Nd}_{1.87}\text{Ce}_{0.13}\text{CuO}_4$: Anisotropic Spin-Correlation Gap, Pseudogap, and the Induced Quasiparticle Mass Enhancement. *Phys. Rev. Lett.* **94**, 047005 (2005).
- [161] E. Abrahams and C. M. Varma. What angle-resolved photoemission experiments tell about the microscopic theory for high-temperature superconductors. *Proc. Natl. Acad. Sci.* **97**, 5714 (2000).
- [162] E. Abrahams and C. M. Varma. Hall effect in the marginal Fermi liquid regime of high- T_c superconductors. *Phys. Rev. B* **68**, 094502 (2003).
- [163] C. M. Varma and E. Abrahams. Effective Lorentz Force due to Small-Angle Impurity Scattering: Magnetotransport in High- T_c Superconductors. *Phys. Rev. Lett.* **86**, 4652 (2001).
- [164] M. Abdel-Jawad, M. P. Kennett, L. Balicas, A. Carrington, A. P. Mackenzie, R. H. McKenzie and N. E. Hussey. Anisotropic scattering and anomalous normal-state transport in a high-temperature superconductor. *Nature Physics* **2**, 821 (2006).
- [165] M. Abdel-Jawad, J. G. Analytis, L. Balicas, A. Carrington, J. P. H. Charnant, M. M. J. French and N. E. Hussey. Correlation between the Superconducting Transition Temperature and Anisotropic Quasiparticle Scattering in $\text{Tl}_2\text{Ba}_2\text{CuO}_{6+\delta}$. *Phys. Rev. Lett.* **99**, 107002 (2007).
- [166] L. Taillefer. Electrons scatter as they pair. *Nature Physics* **2**, 809 (2006).
- [167] A. A. Kordyuk, S. Borisenko, A. Koitzsch, J. Fink, M. Knupfer, B. Büchner, H. Berger, G. Margaritondo, C. Lin, B. Keimer, S. Ono and Y. Ando. Manifestation of the Magnetic Resonance Mode in the Nodal Quasiparticle Lifetime of the Superconducting Cuprates. *Phys. Rev. Lett.* **92**, 257006 (2004).
- [168] H. Wiesmann, M. Gurvitch, H. Lutz, A. Ghosh, B. Schwarz, M. Strongin, P. B. Allen and J. W. Halley. Simple Model for Characterizing the Electrical Resistivity in A-15 Superconductors. *Phys. Rev. Lett.* **38**, 782 (1977).

- [169] M. Gurvitch. Ioffe-Regel criterion and resistivity of metals. *Phys. Rev. B* **24**, 7404 (1981).
- [170] T. Valla, A. V. Fedorov, P. D. Johnson, Q. Li, G. D. Gu and N. Koshizuka. Temperature Dependent Scattering Rates at the Fermi Surface of Optimally Doped $\text{Bi}_2\text{Sr}_2\text{CaCu}_2\text{O}_{8+d}$. *Phys. Rev. Lett.* **85**, 828 (2000).
- [171] Y. Ando. Implication of the Mott-limit violation in high- T_c cuprates. *arXiv:0711.4213v1* (2007).
- [172] N. W. Ashcroft and I. Mermin. *Solid State Physics* (Saunders, 1976).
- [173] N. P. Ong. Geometric interpretation of the weak-field Hall conductivity in two-dimensional metals with arbitrary Fermi surface. *Phys. Rev. B* **43**, 193 (1991).
- [174] K. M. Shen, F. Ronning, D. H. Lu, F. Baumberger, N. J. C. Ingle, W. S. Lee, W. Meevasana, Y. Kohsaka, M. Azuma, M. Takano, H. Takagi and Z.-X. Shen. Nodal Quasiparticles and Antinodal Charge Ordering in $\text{Ca}_{2-x}\text{Na}_x\text{CuO}_2\text{Cl}_2$. *Science* **307**, 901 (2005).
- [175] I. Elfimov, G. Sawatzky and A. Damascelli. Fermi pockets and correlation effects in underdoped $\text{YBa}_2\text{Cu}_3\text{O}_{6.5}$. *arXiv:0706.4276v1* (2007).
- [176] M. A. Hossain, J. D. F. Mottershead, D. Fournier, A. Bostwick, J. L. McChesney, E. Rotenberg, R. Liang, W. N. Hardy, G. A. Sawatzky, I. S. Elfimov, D. A. Bonn and A. Damascelli. In situ doping control of the surface of high-temperature superconductors. *Nature physics* **4**, 527 (2008).
- [177] J. Lin and A. J. Millis. Theory of low-temperature Hall effect in electron-doped cuprates. *Phys. Rev. B* **72**, 214506 (2005).
- [178] H. C. Montgomery. Method for measuring electrical resistivity of anisotropic materials. *J. Appl. Phys.* **42**, 2971 (1971).
- [179] B. F. Logan, S. O. Rice and R. F. Wick. Series of computing current flow in a rectangular block. *J. Appl. Phys.* **42**, 2975 (1971).
- [180] van der Pauw. A method of measuring the resistivity and Hall coefficient on lamellae of arbitrary shape. *Philips Technical Review* **20**, 220 (1958/59).
- [181] O. Bierwagen, R. Pomraenke, S. Eilers and W. T. Masselink. Mobility and carrier density in materials with anisotropic conductivity revealed by van der Pauw measurements. *Phys. Rev. B* **70**, 165307 (2004).
- [182] Y. Ando, G. S. Boebinger, A. Passner, L. F. Schneemeyer, T. Kimura, M. Okuya, S. Watauchi, J. Shimoyama, K. Kishio, K. Tamasaku, N. Ichikawa and S. Uchida. Resistive upper critical fields and irreversibility lines of optimally doped high- T_c cuprates. *Phys. Rev. B* **60**, 12475 (1999).

- [183] Y. Wang, L. Li and N. P. Ong. Nernst effect in high- T_c superconductors. *Phys. Rev. B* **73**, 024510 (2006).
- [184] M. Wagenknecht, D. Koelle, R. Kleiner, S. Graser, N. Schopohl, B. Chesca, A. Tsukada, S. T. B. Goennenwein and R. Gross. Phase Diagram of the Electron-Doped $\text{La}_{2-x}\text{Ce}_x\text{CuO}_4$ Cuprate Superconductor from Andreev Bound States at Grain Boundary Junctions. *Phys. Rev. Lett.* **100**, 227001 (2008).
- [185] J. Herrmann, M. C. Andrade, C. C. Almasan, R. P. Dickey, M. B. Maple, W. Jiang, S. N. Mao and R. L. Greene. Magnetoresistivity of thin films of electron-doped high- T_c superconductor NCCO. *Phys. Rev. B* **54**, 3610 (1997).
- [186] N. Kumar and A. M. Jayannavar. Temperature dependence of the c -axis resistivity of high- T_c layered oxides. *Phys. Rev. B* **45**, 5001 (1992).
- [187] C. C. Tsuei, A. Gupta and G. Koren. Quadratic temperature dependence of the in-plane resistivity in superconducting $\text{Nd}_{1.85}\text{Ce}_{0.15}\text{CuO}_4$ - Evidence for Fermi-liquid normal state. *Physica C* **161**, 415 (1989).
- [188] O. Beom-hoan and J. T. Markert. Normal-state anisotropic resistivity of $\text{Nd}_{2-x}\text{Ce}_x\text{CuO}_{4-y}$: Evidence for scattering by anisotropic spin fluctuations. *Phys. Rev. B* **47**, 8373 (1993).
- [189] A. N. Lavrov, H. J. Kang, Y. Kurita, T. Suzuki, S. Komiya, J. W. Lynn, S.-H. Lee, P. Dai and Y. Ando. Spin-Flop Transition and the Anisotropic Magnetoresistance of $\text{Pr}_{1.3-x}\text{La}_{0.7}\text{Ce}_x\text{CuO}_4$: Unexpectedly Strong Spin-Charge Coupling in the Electron-Doped Cuprates. *Phys. Rev. Lett.* **92**, 227003 (2004).
- [190] S. Ono, Y. Ando, T. Murayama, F. F. Balakirev, J. B. Betts and G. S. Boebinger. Metal-to-Insulator Crossover in the Low-Temperature Normal State of $\text{Bi}_2\text{Sr}_{2-x}\text{La}_x\text{CuO}_{6+d}$. *Phys. Rev. Lett.* **85**, 638 (2000).
- [191] T. Sekitani, M. Naito and N. Miura. Kondo effect in underdoped n-type superconductors. *Phys. Rev. B* **67**, 174503 (2003).
- [192] N. Miura, H. Nakagawa, T. Sekitani, M. Naito, H. Sato and Y. Enomoto. High-magnetic-field study of high- T_c cuprates. *Physica B* **319**, 310 (2002).
- [193] P. Fournier, J. S. Higgins, H. Balci, E. Maiser, C. J. Lobb and R. L. Greene. Anomalous saturation of the phase coherence length in underdoped PCCO thin films. *Phys. Rev. B* **62**, R11993 (2000).
- [194] E. Maiser, W. Mexner, R. Schäfer, T. Schreiner, P. Adelman, G. Czjzek, J. L. Peng and R. L. Greene. Peculiar low-temperature properties of metallic $\text{Nd}_{2-x}\text{Ce}_x\text{CuO}_4$ caused by interactions between Nd moments and conduction electrons. *Phys. Rev. B* **56**, 12961 (1997).

-
- [195] P. A. Lee and T. V. Ramakrishnan. Disordered electronic systems. *Rev. Mod. Phys.* **57**, 287 (1985).
- [196] V. J. Emery and S. A. Kivelson. Superconductivity in Bad Metals. *Phys. Rev. Lett.* **74**, 3235 (1995).
- [197] A. A. Abrikosov. *Fundamentals of the theory of metals* (Elsevier Science Publishers B. V., 1988).
- [198] K. Winzer. Giant Kondo Resistivity in (La,Ce)B₆. *Solid State Comm.* **16**, 521 (1975).
- [199] N. P. Ong and P. W. Anderson. Comment on Anomalous Hall Effect in YBa₂Cu₃O₇. *Phys. Rev. Lett.* **78**, 977 (1997).

Acknowledgments

It was an interesting, fruitful experience and I have learned a lot. Many people have come along with me. Some of them I want to mention and thank especially at this place.

Special thanks to my "Doktorvater" Rudolf Groß for the fruitful discussions and his encouragement. He made this thesis possible and ever gave me support. Finally, he reviewed carefully the Chapters of this thesis.

I would like to thank Prof. Christian Pfeleiderer who acts as second evaluator of this thesis.

I would also like to thank Andreas Erb for his helpful feedback and for the many tips, which enhanced my work.

Many thanks to Wolfgang Prestel, who gave me very helpful support in simulating the data and for the discussions and his encouragement.

Thanks to Alain Junod, who performed the specific heat measurements described in this thesis.

I would like to thank Mark Kartsovník for his support in the lab, his patience and the many helpful tips.

Toni Helm gave me a helping hand in the lab, many thanks for that.

Thanks a lot to Georg Wild and Frank Deppe for the nice atmosphere in the office and the discussions about physics and life in general.

I would like to thank the crystal lab at the TU Munich, for helping me with the crystal preparation as well as the work shop of the Walther-Meißner-Institut, who supported me preparing tools for my work.

Thanks also to Joachim Geisman, Astrid Habel and Karen Helm-Knapp for the help in the chemistry lab and crystal lab of the Walther-Meißner-Institut.

I am very grateful to my parents Anna and Franz, who have always supported me. Thanks also to my family for always being there.

I want to dedicate this work to my wife Marion, as without her this work would have never been possible. Thanks for your love and encouraging words during the last years.

Curriculum Vitae

Michael Lambacher
Walther-Meißner-Institut
Walther-Meißner-Strasse 8
85748 Garching
Email: Michael.Lambacher@wmi.badw.de

Persönliche Angaben

Geburtsort: Schlanders, Italien
Geburtsdatum: 12.09.1979
Familienstand: Verheiratet
Staatsangehörigkeit: Italienisch

Ausbildung

1985 – 1990: Grundschule St. Magdalena, Villnöss
1990 – 1998: Mittelschule und Gymnasium, Vinzentinum Brixen
1998 – 2004: Studium der Physik an der Technischen Universität München
Diplomarbeit am Lehrstuhl Kotthaus für Festkörperphysik der Ludwig-Maximilians-Universität München: *Elektronischer Transport durch molekulare Leiter*

Doktorat

Seit 2004 am Lehrstuhl Groß für Technische Physik (E23, Walther-Meißner-Institut) der Technischen Universität München
Arbeitsgebiete: Supraleitung, Kristallwachstum von Kuprat Mischkristallen, Materialwissenschaften
Dissertation im Rahmen der Forschergruppe FOR 538 ("Doping dependence of phase transitions and ordering phenomena in copper-oxygen superconductors"): *Crystal growth and normal state transport of electron doped high temperature superconductors*

Arbeitserfahrung

2004 – 2008: Wissenschaftlicher Angestellter der Bayerischen Akademie der Wissenschaften (Walther-Meißner-Institut)
2004 – 2008: Tutor für Schüler und Studenten an der Technischen Universität München

Mitgliedschaften

Since 2003: Deutsche Physikalische Gesellschaft
Since 2004: Bayerische Akademie der Wissenschaften
Since 2004: Forschergruppe FOR 538

Sprachen

Deutsch: Muttersprache
Englisch: Professionelle Kenntnisse
Italienisch: Professionelle Kenntnisse
Latein, Griechisch: Schulkenntnisse